Integrated modelling of debris flows with Open Source GIS

Numerical simulations of triggering, mobilization, and runout of debris flows for selected study areas along the Trans-Andean road corridor Mendoza – Valparaíso

dissertation by

Martin Mergili

submitted to the Faculty of Geo- and Atmospheric Sciences
of the University of Innsbruck, Austria

in partial fulfilment of the requirements
for the degree of doctor of science

advised by

Univ.-Prof. Dr. Johann Stötter
Institute of Geography

Innsbruck, *July 2008*

Preface

Rapid mass movements in general and debris flows in particular have been a serious threat for human lives and economic values in mountain regions almost all around the world for a long time. The evolution of methods for reducing debris flow risk therefore has a long history, ranging from avoiding hazardous areas to the realization of technical countermeasures. Numerical models for the simulation and prediction of debris flows play a major role for assessing debris flow hazard in space and time. The present thesis aims at contributing to this field with a freely accessible (Open Source) model framework for the integrated modelling of debris flows.

The thesis was primarily financed with a project of the Tyrolean Science Funds, by a grant from the University of Innsbruck ("Doktoratsstipendium aus der Nachwuchsförderung der LFU"), and by the Austrian Academy of Sciences (Mountain Research: Man and Environment). Further grants were awarded by the Faculties of Natural Sciences, University of Innsbruck ("Förderstipendium") as well as by the Office for International Relations, University of Innsbruck ("Stipendium für kurzfristige wissenschaftliche Arbeiten im Ausland") and by the Government of Upper Austria ("Förderung für Auslandsstudienaufenthalte außerhalb des KIP"). Support for the participation in conferences was provided by the Faculty of Geo- and Atmospheric Sciences, University of Innsbruck.

Besides my advisor Prof. Dr. Johann Stötter, who always had an open ear for consultations and who supplied valuable thematic and methodical comments as well as a lot of organizational support, quite a couple of colleagues of various institutions have contributed to the present thesis in the one or the other way.

A special thanks goes to the Division of Geotechnical and Tunnel Engineering, University of Innsbruck. Dr. Wolfgang Fellin and his team analyzed about 50 soil samples in their laboratory and therefore contributed a substantial part of the data used in the thesis as well as providing a large number of extremely valuable comments on the models and the papers.

Prof. Alexander Ostermann and Katharina Schratz from the department of Mathematics, University of Innsbruck, provided a lot of support with mathematical issues.

A special thanks goes also to Dr. Stella Moreiras from CRICYT/IANIGLA in Mendoza for making available part of her landslide historical records and for allowing me to participate in some field excursions of her team as well as enabling the use of the working facilities of CRICYT.

Special thanks also to Mr. Jorge Espejo, former employee of the Servicio Nacional de Vialidad, Argentina, and to Prof. Arturo Hauser from the Chilean Geological Survey for providing historical documents on debris flow activity in an uncomplicated way.

Dr. Clemens Geitner was very helpful providing hints to important pieces of literature and always having an open ear for discussions. Prof. Axel Borsdorf established the contacts to the Universidad Católica and to the Universidad de Chile in Santiago.

Prof. Luis Belisario Andrade Johnson (Universidad Católica, Santiago) allowed me to participate in a field trip to the Aconcagua valley, providing a lot of important information. Furthermore I am very grateful to Prof. Francisco Ferrando and Prof. Hugo Romero (Universidad de Chile) for establishing the contacts to the Chilean Geological Survey as well as for taking me to another field excursion. Prof. Raúl Mikkan (Universidad Nacional de Cuyo) and Prof. Rodrigo Hidalgo Dattwyler provided important organizational support. My colleagues Rafael Sánchez from Santiago and Fernando Ruiz Peyré from Mendoza helped a lot with data acquisition and with important thematic and organizational information.

Furthermore I would like to thank all my friends and colleagues, particularly Elisabeth, Reinhard, Roland, Swantje, and Verena, for valuable discussions and organizational help.

Finally, a great thanks to my parents and grandparents for their support.

Martin Mergili, July 2008

Table of Content

Abstract

Debris flows are aggressive responses of catchments to extreme rainfall events or other types of triggers. They show characteristics intermediate between landslides and sediment-laden runoff, moving down slopes or channels at high velocities and posing a severe risk to people, buildings and infrastructures they interfere with. The major objective of the present thesis is to contribute to model development regarding the simulation and prediction of debris flows in order to enable action towards reducing that risk. Although numerous models dealing with different aspects of debris flows do exist on the market, publicly available tools for integrated modelling of debris flows, including triggering, mobilization and runout, are scarce.

The model framework presented here, named *r.debrisflow*, shall fill a part of this gap. It was designed as a raster module for the Open Source GIS software *GRASS*, in order to be freely available for everyone to be applied, improved, and extended. The tool is suitable for simulating debris flows triggered by heavy rainfall or extreme snow melt in study areas of few square km. It includes the following modules:

(1) infiltration and surface runoff: water input from rainfall or snow melt is distributed among vegetation, soil (Green-Ampt infiltration model), and surface runoff, which is calculated using the Manning-Strickler formula;

(2) sediment transport: detachment of soil by surface runoff is computed using a sediment transport model, and locations where runoff may evolve into a debris flow are identified;

(3) slope stability: an infinite slope stability approach is applied for detecting locations of potential slope failures, and unstable areas where debris flows may be mobilized are identified;

(4) runout and deposition: a two-parameter friction model is used for determining runout length. Areas of entrainment and deposition are distinguished using empirical thresholds of flow velocity and local slope angle.

r.debrisflow was applied to some selected study areas along the international road from Mendoza (Argentina) to Central Chile. All necessary input information was investigated on a local scale: soil samples were taken in the field and analyzed for their mechanical characteristics; soil hydraulic parameters were derived using pedotransfer functions; high-resolution terrain models were generated from different types of stereo imagery.

Scenarios of debris flows as response to rainfall events of a defined magnitude were worked out for the study areas in accordance with meteorological data. The results for the study areas were evaluated against field observations, historical archives, and the results of previous investigations. Although the findings corresponded quite well to the reference information for most of the study areas, one has to be aware of some deficiencies, in particular:

- it was not possible to determine rainfall thresholds for the occurrence of debris flows – reasons were the limitations of the infiltration model on the one hand, and insufficient reference data on the other hand;
- the parameters for the runout model had to be calibrated for each study area, limiting the capability of the model for class A predictions;
- similar problems were connected to the sediment transport model;
- the model framework is mainly suitable for rainfall events of high intensity and short duration: the infinite slope stability model yields realistic results for shallow translational failures mainly connected to such events, but large uncertainties remain in the case of debris flows deriving from deep-seated rotational failures which are rather triggered by longer periods of rainfall; therefore a better suited model approach for such failure mechanisms shall be added in the future; also more sophisticated approaches for soil water movement would be required for modelling the initiation of debris flows triggered by rainfall events of long duration.

The model results showed to be quite sensitive to a number of parameters not known at sufficient accuracy or resolution (e.g. hydraulic conductivity of the soil; vertical soil profile, influencing soil water flow and seepage forces), leading to uncertainties which were quantified by an analysis of sensitivity.

A physically-based runout model for debris flows (*r.avalanche*) was implemented into *GRASS GIS* complementary to *r.debrisflow* as a response to the limitations immanent to the two-parameter friction

model. It was tested with the same study areas. *r.avalanche* builds on a solution of the Savage-Hutter model elaborated for simple U-shaped valleys running out into a horizontal plane. The results were fairly good where topography was close to that simple shape and where flow channels were straight. For more complex study areas with curved flow channels, however, the model failed. Prospected future work shall be directed towards the development of a solution of the Savage-Hutter model for arbitrary topography and its implementation into *GRASS GIS*. Particle entrainment and the effects of the two-phase (solid-fluid) nature of debris flows shall be incorporated, too.

Resumen

Flujos detríticos se producen particularmente como respuesta a lluvias intensas o prolongadas. Son una forma intermedia entre deslizamientos y descargas saturadas de sedimentos. Se trasladan hacia abajo con alta velocidad y así presentan una considerable amenaza a la población y a las infraestructuras del área afectada.

El objetivo principal de esta tesis es contribuir al desarrollo de modelos de simulación y predicción de flujos detríticos. Los resultados deben ser usados para mejorar el manejo de riesgo. Ya existen muchos modelos para simular los subprocesos de flujos detríticos. Sin embargo hay que destacar que de estos solamente pocos son capaces de modelar todo el proceso.

El modelo presentado en esta tesis, denominado como ***r.debrisflow***, debe llenar las expectativas de una simulación integradora. Fue desarrollado como un módulo del tipo raster para el programa SIG ***GRASS*** (Open Source). De esta manera el programa es disponible gratuitamente y puede ser aplicado y mejorado por cualquier interesado.

El programa fue desarrollado especialmente para simular los flujos detríticos que se desarrollan en consecuencia a lluvias intensas y breves. El programa incluye los módulos siguientes:

(1) infiltración y descarga superficial: se modela la distribución del agua, que entra al sistema como lluvia, entre la vegetación (intercepción), el suelo (infiltración siguiendo el modelo Green-Ampt), y la descarga superficial (siguiendo la ecuación de Manning-Strickler);

(2) transporte de sedimentos por la descarga superficial: se modela la erosión del suelo por la energía de la descarga superficial y el transporte de los sedimentos. Como resultado, son identificados los áreas donde se inician los flujos detríticos;

(3) estabilidad de las laderas: se utilizó un *infinite slope stability model* que permite detectar áreas potencialmente inestables donde se pueden originar flujos detríticos;

(4) como último paso, se modela el movimiento del flujo detrítico. Un *two-parameter friction model* está aplicado para estimar la distancia recorrida por el flujo. Basándose en valores característicos de la velocidad y de la inclinación se determina la distribución de los áreas de erosión y deposición.

r.debrisflow fue aplicado en seis áreas de estudio que se encuentran a lo largo de la carretera internacional de Mendoza (oeste de Argentina) a Chile Central. Se obtuvieron las siguientes informaciones detalladas para los seis áreas del estudio: se extrajeron muestras de suelo que después fueron analizados en un laboratorio geotécnico; los informaciones sobre parámetros hidráulicos del suelo se basan en la literatura; se generaron modelos de elevación a alta resolución por diferentes tipos de imágenes estéreos.

Se simularon flujos detríticos para determinados eventos de lluvia en las áreas de estudio. Una evaluación de los resultados obtenidos en las simulaciones se realizó basándose en observaciones de campo, reportes sobre flujos detríticos, y resultados de estudios anteriores. Hay que destacar que los resultados coincidieron satisfactoriamente con la información de referencia. Sin embargo también se identificaron algunos problemas de la simulación, como los siguientes:

- no fue posible determinar umbrales de lluvia (respecto a intensidad y duración) que influyen la ocurrencia de flujos detríticos. Esto se debe al tipo de modelo de infiltración, y insuficientes datos de referencia;
- la necesaria calibración de los parámetros utilizados en el two parameter friction model consta un problema tan pronto que se trate predecir eventos en el futuro;
- el mismo problema ocurrió respecto al modelo de transporte de sedimento;
- el *infinite slope stability model* esta apto sobre todo para simular deslizamientos superficiales, que se causan por lluvias breves y fuertes. Sin embargo, falta en condiciones de lluvias prolongadas, que generan deslizamientos profundos. Hace falta incorporar un modulo que funcione bajo dichas condiciones. También sería necesario incluir un modelo de infiltración mas avanzado.

El modelo presentó una alta sensibilidad contra algunos parámetros que no se pudieron determinar detalladamente. Estas incertidumbres se cuantificaron con un análisis de sensibilidad.

10 Resumen

Un modelo determinístico para simular el movimiento de flujos detríticos (*r.avalanche*) fue implementado en el *GRASS* complementando el *r.debrisflow*. Se evaluó el *r.avalanche* en los mismos áreas de investigación. El modelo se basa en una solución del modelo Savage-Hutter que fue aplicado para valles simples con forma de U, que terminan en llanura. Los resultados para áreas de estudio con topografía simple y canalones rectas fueron satisfactorios En el caso de áreas mas complejas con canalones curvados, se presentaron dificultades. En el futuro el desarrollo del modelo debe basarse en las soluciones del modelo Savage-Hutter que funciona con topografías arbitrarias. En este proceso, también hay que incluir el fenómeno de erosión de suelo por los flujos detríticos y las complejas propiedades como flujo en dos fases (sólido y fluido).

Zusammenfassung

Murgänge stellen aggressive Reaktionen von Einzugsgebieten auf starke oder langanhaltende Regenfälle oder andere Auslösefaktoren dar. Als eine Übergangsform zwischen gravitativer Massenbewegung und sedimentbeladenem Abfluß erreichen sie oft hohe Geschwindigkeiten. Die damit verbundene Zerstörungskraft macht sie in vielen Gebrigsregionen zu einem beträchtlichen Risikofaktor für Bevölkerung, Gebäude und Infrastruktur.

Wesentliches Ziel der vorliegenden Arbeit ist es, einen Beitrag zur Entwicklung von Simulations- und Vorhersagemodellen für Murgänge zu leisten, um gezielte Aktionen hinsichtlich der Risikominimierung zu ermöglichen. Zwar existiert eine Vielzahl an Modellen zur Simulation von Teilprozessen (Hangsta-bilität, Sedimenttransport, Murbewegung, etc.), geeignete Modelle für eine integrative Simulation des Prozesses unter Einbeziehung möglichst vieler Komponenten sind jedoch seltener.

Das hier präsentierte Modellsystem, genannt ***r.debrisflow***, ist dazu gedacht, diese Lücke zumindest teilweise zu füllen. Es wurde als Rastermodul für das Open Source GIS-Programm ***GRASS*** konstruiert, um eine freie Verfügbarkeit zu gewährleisten und es einem möglichst breiten Nutzerkreis zugänglich zu machen. Das Werkzeug ist vor allem zur Simulation von Murgängen, die durch Starkregenereignisse oder extreme Schneeschmelze ausgelöst werden, geeignet. Es setzt sich aus den folgenden Modulen zusammen:

(1) Infiltration und Oberflächenabfluß: der Wassereintrag aus Regen oder Schneefall wird zwischen Vegetation (Interzeption), Boden (Infiltration, Modell nach Green-Ampt), und Oberflächenabfluß aufgespaltet. Letzter wird mit Hilfe der Manning-Strickler Gleichung berechnet;

(2) Sedimenttransport: der Abtrag von Boden durch Oberflächenabfluß wird abgeschätzt und Gebiete in denen sich daraus Murgänge entwickeln können werden ermittelt;

(3) Hangstabilität: ein sogenanntes *infinite slope stability model* wird verwendet, um potentiell auftretende Hanginstabilitäten, aus denen sich Murgänge entwickeln können, zu identifizieren;

(4) Murbewegung und -ablagerung: ein so genanntes *two-parameter friction model* wird verwendet, um die Auslauflänge der identifizierten Murgänge abzuschätzen. Empirische Grenzwerte für Hangneigung und Geschwindigkeit helfen bei der Ausweisung von Erosions- und Ablagerungsgebieten.

r.debrisflow wurde anhand von sechs Untersuchungsgebieten entlang der transandinen Straßenverbindung von Mendoza (West-Argentinien) nach Zentralchile getestet. Alle benötigten Eingangsdaten und -parameter wurden in größtmöglichem Detail erhoben. Im Gelände entnommene Bodenproben wurden im Labor analysiert. Anschließend wurden mit Hilfe von Pedotransfertabellen hydraulische Parameter abgeleitet. Hochauflösende digitale Höhenmodelle wurden aus Stereopaaren verschiedener Bildquellen erstellt.

Szenarien von Murgängen als Reaktion auf Regenereignisse verschiedener Dauer und Intensität wurden für die Studiengebiete erarbeitet. Die Modellergebnisse wurden mithilfe von Beobachtungen im Gelände, Berichten, und den Ergebnissen früherer Studien evaluiert. Grundsätzlich war die Übereinstimmung zwischen den Modellergebnissen und den Referenzinformationen recht zufriedenstellend. Auch die Grenzen der Anwendung von ***r.debrisflow*** sind jedoch hervorzuheben:

- es war nicht möglich, Schwellenwerte von Regenmengen oder -intensitäten für das Auftreten von Murgängen zu bestimmen. Einerseits ist das Infiltrationsmodell nach Green-Ampt dafür wenig geeignet, andererseits waren nicht genügend passende Referenzdaten vorhanden;
- die Parameter für das Murauslaufmedell bedurften einer Kalibrierung für jedes Studiengebiet, was eine ernsthafte Limitierung bezüglich der Möglichkeit von Vorhersagen darstellt;
- ähnliche Probleme traten mit dem Sedimenttransportmodell auf;
- das Modellsystem ist vor allem auf die Simulation von Murgängen, die durch kurze Starkregenereignisse ausgelöst werden, ausgerichtet. Solche Ereignisse führen häufig zu flachgründigen Hangrutschungen die mit dem verwendeten *infinite slope stability model* gut modelliert werden können. Für längere Regenperioden und tiefgründigeres Hangversagen wäre sowohl ein komplexeres Hangstabilitäts- als auch Wassertransportmodell nötig. Die weitere Entwicklung von ***r.debrisflow*** soll u.a. in diese Richtung gehen.

Das Modell reagiert äußerst sensibel auf die Veränderung einiger Eingangsparameter, die vor allem in ihrer räumlichen Dimension nur unzureichend bekannt sind. Deshalb war eine sorgfältige Analyse der Sensitivität des Modells auf die Veränderung solcher Parameter ein wesentlicher Bestandteil der Analysen.

Zusätzlich zu *r.debrisflow* wurde ein physikalisch basiertes Murauslaufmodell (*r.avalanche*) in *GRASS GIS* implementiert und mit denselben Studiengebieten getestet. Es basiert auf einer Lösung des Savage-Hutter Modells für einfache, U-förmige Täler die in eine horizontale Fläche auslaufen. Für Untersuchungsgebeite mit relativ einfacher Topographie und geraden Fließkanälen waren die Ergebnisse fürs erste zufriedenstellend. Das Modell versagte jedoch erwartungsgemäß für komplexere Topographien mit kurvenreichen Fließkanälen. Für die nähere Zukunft ist die Entwicklung einer Lösung des Savage-Hutter Modells für komplexe Topographien sowie deren Implementierung in *GRASS GIS* vorgesehen. Erosion durch die Mure und deren Eigenschaft als zweiphasige Bewegung (fest-flüssig) sollen ebenfalls berücksichtigt werden.

1 Introduction

1.1 Background

Debris flows are rapid mass movements of mixtures of water and debris, constituting a considerable hazard when interfering with people, buildings, or infrastructures. They are often triggered by heavy or prolonged rainfall or by extreme snow melt. Mobilization of debris flow material occurs due to translational or rotational failure of saturated or undercut slopes, or due to entrainment of soil by surface runoff or by the debris flow itself. Various models do exist for simulating sub-processes included into debris flows, for example particle entrainment, soil hydrology, slope stability, or debris flow runout. More integrated GIS-based approaches as attempted e.g. by BURTON & BATHURST (1998) or by WICHMANN (2006) are scarce. Such approaches would be extremely valuable for a quick assessment of meteorological and hydrological thresholds for potential debris flow hazard regarding specified features at risk.

Besides a review of existing knowledge and methods, the major content of the present thesis includes the development of a model framework for the integrated simulation of debris flow events (from triggering to deposition) as a *GRASS GIS* raster module named *r.debrisflow*, and a complement for physically-based modelling of debris flow runout, named *r.avalanche*. Both modules were designed for small catchments (few square kilometres) and tested with six study areas along the international road corridor from Mendoza (W Argentina) to Central Chile (Figure 1.1).

Figure 1.1: Debris flow channel directly above the international road from Mendoza to Central Chile. Photo: M. Mergili, 10/2006.

The research area for the present thesis was chosen as it occupies steep valleys of the Central Andes highly susceptible to different types of mass movements, including debris flows. Due to the importance of the road connection, historical data is available as well as meteorological records and some studies about landslides in the area (e.g. MOREIRAS 2004a; 2004b; 2005), facilitating further studies.

1.2 Specific aims

The master goal of the present thesis is to contribute to the reduction of the risk posed to human lives and economic values by debris flows.

For being operationalized, this objective has to be split up into smaller and more specific goals, which may be organized into methodological aims and thematic aims. The methodological aims are

(1) to improve the knowledge about the suitability of the Open Source GIS software *GRASS* for complex raster-based models, compared to other software, in order to facilitate the choice of the suitable software for future modellers;

(2) to improve the knowledge about the applicability of various deterministic and empirical model approaches for certain sub-processes of debris flows.

(3) and, in particular, to provide a freely accessible (Open Source) model for performing integrated modelling of debris flows, with the possibility to be applied, improved, and extended by everyone who wishes to do so;

The thematic aims are

(1) to improve the knowledge about the meteorological conditions potentially resulting in debris flows in the research area;

(2) to improve the knowledge about the sensitivity of debris flow hazard to the variability of some of the dominant conditioning factors;

(3) and, based on (1) and (2), to establish different scenarios of meteorological conditions triggering debris flows under certain assumptions in order to facilitate decisions by the authorities.

The interdependencies between all these objectives are illustrated in Figure 1.2.

1.3 Structure of the thesis

Simply spoken, the thesis is structured in the same way as a scientific article, but with longer chapters:

- Chapter 2 (State of the Art) provides a detailed review of the general concepts and the state of the art regarding debris flows in general and modelling techniques in particular;
- Chapter 3 (Research area) introduces to the research area in general and to the six selected study areas in particular;
- Chapter 4 (Materials and Methods) presents the data used for the study and gives a detailed introduction to the methods applied;
- Chapter 5 (Results) shows the results of the simulations for all of the study areas;
- and Chapter 6 (Discussion) provides a detailed discussion of the results, the capabilities and limitations of the methods, implications for risk management and needs for further research.

Maps of the study areas and some additional information are compiled in the Appendix. Also the scientific publications related to the thesis are collected there.

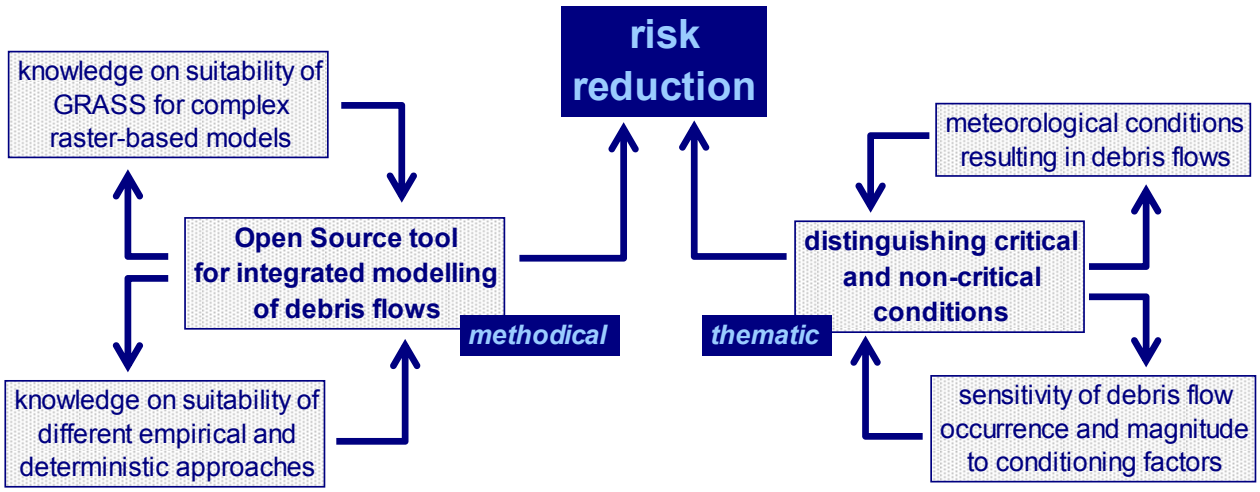

Figure 1.2: Master goal and specific aims of the thesis. Designed by M. Mergili.

2 State of the art

2.1 What are debris flows?

A definition of the term "debris flow" for the purpose of the present thesis was provided in Chapter 1. In fact, the term is much used in literature, at first glance not always referring to exactly the same process:

- Some authors rather consider it as landslide with a fluid-like runout behaviour (BURTON & BATHURST 1998; COROMINAS et al. 2003; MOREIRAS 2004a; 2004b);
- others consider it as runoff with very high sediment concentration, with sediment predominantly originating from the stream bed (O'BRIEN 2003; RICKENMANN 1999).

However, these two approaches are not necessarily antagonisms – they rather depend on whether the observer has a geotechnical or a hydrological background. As stated by RICKENMANN (1999), debris flows are phenomena intermediate between landslides and runoff. Many debris flow events in the real world share features of both types of processes, but many of them have a clear tendency to the one or the other. The Figures 2.1 and 2.2 illustrate the diversity among different types of debris flows. Some authors distinguish between debris flows on slopes (from landslides) and debris flows in channels (from erosion in and around the stream bed; e.g. WICHMANN 2006). Different processes are often tightly coupled, for example when a landslide rushes into a stream bed and the deposit is transported further downwards by the influence of stream flow either immediately or after a certain delay (e.g. during the next heavy rainfall event). Debris flow movement shows properties different from the flow of clear water, requiring specialized and complex methods to be modelled in a fully deterministic way (SAVAGE & HUTTER 1989; HUNGR 1995; IVERSON 1997).

Although the landslide perspective of debris flows and the hydraulic perspective are tightly coupled, it appears reasonable to discuss them separately first, as the concepts and methods are quite different.

Figure 2.1 (top): Large debris flow in the Maipó valley, Central Chile, mobilized by slope failure. Photo: M. Mergili, 10/2006.
Figure 2.2 (bottom): Mountain torrent in the Austrian Alps near Innsbruck, with sediment input from lateral slopes transported away as debris flows. Photo: M. Mergili, 05/2008.

2.2 The geotechnical concept of debris flows

2.2.1 Landslides

This section deals with landslides, that means downward movements of rocks and/or soils as a consequence of slope instabilities. Since landslides pose a major threat to human lives, private property and infrastructure in mountain regions all over the world, they have been investigated quite intensely. Therefore, and since the understanding about the way how landslides occur is essential for the prediction of debris flows, this issue will be discussed in detail.

Landslides include two major sub-processes: the slope failure and the runout (including entrainment of soil and deposition). After introducing to some general aspects about types of landslides, conditioning factors and triggering forces, different approaches for modelling landslide susceptibility and landslide hazard will be discussed. Many of the methods presented are applicable to all types of landslides, not only to debris flows.

Types of landslides

Some authors, e.g. NEMČOK et al. (1972) or VARNES (1978), came along with concepts for distinguishing different types of slope movement processes. NEMČOK et al. (1972) classified landslides as follows:

- creep: long-term movement without acceleration and without well-defined shear surface;
- slide: movement of coherent masses along one or more well-defined shear surfaces;
- flow: slope movement in soil or rock with mechanics similar to fluids;
- fall: sudden slope movement: the mass loses its coherence and for some moments also the contact with the underlying rock.

Conditioning factors for landslides

Though QIN et al. (2001) showed that the particular occurrence of landslides is chaotic, they do not happen randomly over time and space. Their occurrence is coupled to conditioning and to triggering factors. While conditioning factors rather determine the spatial distribution of landslide occurrence (the landslide susceptibility of an area), triggering factors determine the time at which landslides occur (Figure 2.3).

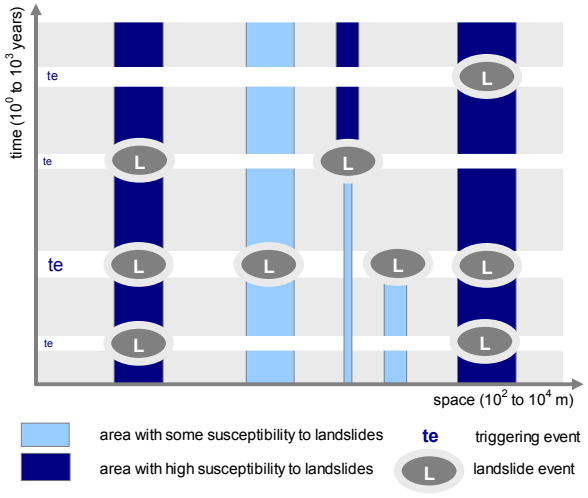

Figure 2.3: Conditioning factors (determining susceptibility) and triggering factors for landslides. Designed by M. Mergili.

Not every triggering event necessarily leads to landslides in all susceptible areas, and landslide events may alter the susceptibility of an area, e.g. by removing or, reverse, by exposing unstable material. Furthermore, conditioning factors may have a different importance under different regimes of triggering factors.

Table 2.1: A selection of major conditioning factors for landslides, without differentiation for landslide type.

Conditioning factor	Study area	Reference(s)
tectonic development	Pindos zone (Greece)	ANDRONOPOULOS (1982)
weak rocks susceptible to glacial erosion	Atlantic Pyrenees	LEBOURG et al. (2003)
rock type	China	LIU et al. (1992)
outcropping lithologies and faults	Northern Italy	BISTACCHI et al. (2000)
tectonic structures	Vietnam	LEE & DAN (2005)
structural, geomorphological and geomechanical features	Turkey	SENDIR & YILMAZ (2002)
glacially formed areas (oversteepened slopes, till)	Atlantic Pyrenees	LEBOURG et al. (2003)
unstable accumulation of granitic debris	Mendoza valley, Argentina	MOREIRAS (2004a)

Various studies do exist relating the occurrence of landslides to certain conditioning factors. The factors shown in Table 2.1 can be reduced to the following major conditioning factors:

- slope angle;
- mechanic strength of rocks and soils (presence of materials at or close to a mechanical equilibrium).

Though the conditioning factors as listed in Table 2.1 only concern rock and soils, also other components of the earth surface may play a prominent role for the tendency of a slope or catchment to produce landslides:

Slope water system. Not only the mechanical, but also the hydraulic properties of a soil, slope, or catchment play a crucial role for its stability. Basically, one may distinguish two spatial scales:

- a micro-scale, considering the soil column at one specific location regarding its hydraulic variables (water storing capacity, hydraulic conductivity, etc.). As soil hydrology is a component of most physically-based slope stability models, this issue will be discussed in more detail in Section 2.2.2;
- a macro-scale, including the entire catchment. The tendency of a point on a slope to accumulate water is considered as an essential determinant for its susceptibility to produce landslides under certain conditions. Some models (e.g. *SINMAP*, compare Section 2.2.2) therefore include the so-called topographic index, describing the ratio between upslope contribution area and local slope angle.

Vegetation and land use. Natural vegetation plays an important role regarding soil erosion and shallow movement processes. Many studies were carried out in humid areas, or regarding crop cultivations or pas-

tures. GYSSELS & POESEN (2003) found that both the shoot and the root systems of plants act against soil erosion. PRESTON & CROZIER (1999) underlined the importance of the root system for the prevention of erosion. COLLISON & ANDERSON (1996), however, argue that hydrological effects may offset the gained mechanical stability in deep residual tropical soils.

The relationship between vegetation and slope stability is characterized by forward feedbacks: after landslide events it lasts certain years, decades or even centuries until full recovery of the ecosystems. During this period, the slope is supposed to be more susceptible to landslides than with a fully developed vegetation cover. On chronically unstable slopes the succession remains in an initial stage. OHL & BUSSMANN (2004) underlined the role of the distance to undisturbed areas and therefore to existing pools of species able to invade landslides, and of ongoing local sliding processes keeping patches free of vegetation.

Anthropogenic structures. Not only natural conditions influence the occurrence of landslides, but also man-made structures disturbing the mechanical and hydrological equilibrium of a slope, for example when deep-rooted trees are replaced by shallow-rooted crops (MSILIMBA & HOLMES 2005). Also the influence of forest roads, often running over steep terrain, on slope stability was subject of a number of studies (e.g. DUTTON et al. 2005).

Triggering factors

In contrast to conditioning factors, constituting long-term states only changing over long time scales (10^0 to 10^6 and more years), triggering factors for landslides act on a much shorter time scale, from seconds or few minutes (earthquake) to days (rainfall periods).

Rainfall. Many authors have successfully tried to relate landslides to rainfall (SIRANGELO & VERSACE 1996; IIRITANO et al. 1997; GLADE 1998; BROOKS et al. 2004; FLORIS et al. 2004; CHIEN-YUAN et al. 2005; GIANNECHINI 2005; HONG et al. 2005). According to DHAKAL & SIDLE (2004) and REICHENBACH et al. (1998), rainfall sum, length, average intensity, maximum intensity and some ratios influence slope stability – however, threshold values of all these variables investigated in one area would not necessarily be valid in another area. A worldwide model was developed by REICHENBACH et al. (1998), combining rainfall intensity and duration.

Some authors emphasized the role of antecedent rainfall (REICHENBACH et al. 1998; WASOWSKI 1998; CROZIER 1999; IBSEN & CASAGLI 2004). GLADE et al. (2000) used antecedent rainfall and rainfall at the time of the event to refine the knowledge on landslide-triggering rainfall thresholds. They introduced an index of antecedent rainfall and applied statistical methods to separate landslide-triggering and non-landslide-triggering conditions. Some authors suggest to use five days antecedent precipitation (e.g. RAHARDJO et al. 2001; MOREIRAS 2005), others prefer much longer periods. AHRENDT & ZUQUETTE (2003) observed complex relationships between temporal rainfall distribution and landslides, and IBSEN & CASAGLI (2004) even observed a six month delay between a period of intense rainfall and landslide initiation in Italy. AYALEW (1999) and BELL & MAUD (2000) tried to relate landslide activity and the percentage of cumulative (present plus antecedent) rainfall of annual rainfall in study areas of Ethiopia and South Africa. 15-30 % and 12 %, respectively, would trigger small events, while 30 % and 20 %, respectively, would trigger larger landslides. REICHENBACH et al. (1998) emphasized that antecedent precipitation would be important in particular for deep-seated landslides.

Generally speaking, it is quite difficult to generalize the findings of all these studies as the rainfall-landslide relationships are spatially highly variable (BROOKS et al. 2004), based on the regional settings and the general landslide susceptibility of the slope determined by substrate and vegetation (IRIGARAY et al. 2000). An additional difficulty is that severe rainstorms often have a limited spatial extent and are not necessarily recorded by meteorological stations (MOREIRAS 2005).

Hydraulic status of the slope. Rainfall is usually only the input and therefore a surrogate for the conditions that actually influence slope stability. Also rapid snow melt (CARDINALI et al. w.j) or broken irrigation pipes (TEOMAN et al. 2004) can lead to landslide occurrences.

REICHENBACH et al. (1998) suggested to use runoff thresholds instead of rainfall thresholds, since they also reflect the system conditions and not only the raw rainfall value.

Regarding soil hydrology, VAN WESTEN (2000) distinguished three types of slope failure mechanisms:

- saturation of the upper part of the soil due to intense rainfall (particularly in tropical regions);
- perching of penetrable layers between impenetrable layers;
- ground water.

Some authors have tried to look directly into the soil for investigating the role of soil hydraulic conductivity (VIEIRA & FERNANDES 2004), of the height of the groundwater table (ONDA et al. 2004) and its seasonal changes (VAN ASCH & BUMA 1997), or the role of soil pipes (UCHIDA 2004) on slope stability, relationships which are relatively complex. Soil pipes, for example, facilitate drainage on the one hand, but reduce cohesion when filled on the other hand. Suctions above the water table, in contrast, are supposed to increase slope stability (GRIFFITHS & LU 2005), while

reduced shear resistance due to increased pore water pressure has the reverse effect (WANG et al. 2005).

In practice, it is often not possible to directly investigate soil hydrological status. Suitable models are therefore required. MILLER & SIAS (1998) described a method for modelling the groundwater level as a response to rainfall, while BOGAARD & VAN ASCH (2002) simulated the influence of soil moisture balance in the unsaturated zone on landslide activity. They emphasized the importance of evapotranspiration: A 20 % decrease in evapotranspiration caused a 20-fold increase in the velocity of the slide. A 10 – 20 % increase in evapotranspiration would probably stabilize the slide.

Mechanical instabilization. Many landslides are connected to hydrological triggering mechanisms as described above. Regarding the present thesis, such mechanisms are of specific importance, and model approaches are discussed in detail below. However, a second large complex of triggering factors is mechanical instabilization. This can be, for example, river bank failure caused by undercutting as a response to the hydraulic regime and the hydrograph (DAPPORTO et al. 2003). Much more attention has been paid to landslides triggered by earthquakes (e.g. KEEVER 2002; NAGARAJAN 2002; FUKUOKA et al. 2004). Also volcanic activity can trigger landslides, like at Mount St. Helens (SOUSA & VOIGHT 1995).

2.2.2 Methods for landslide susceptibility/hazard analysis

A large array of tools has been developed for assessing landslide susceptibility, mobilization and runout. Landslide susceptibility analysis means identifying areas prone to slope failure according to the conditioning factors, whilst landslide hazard analyses have to include landslide magnitude and frequency as well as runout. However, the terms are not always clearly separated. Since the 1990s, Geographic Information Systems (GIS) play an increasing role for both approaches. Due to the large amount of available literature and the orientation of this thesis, the following review will largely be confined to methods connected to the application with GIS. It has to be emphasized, however, that many of the methods are not necessarily connected to the use of a GIS. Particularly the equations required for physically-based (deterministic) slope stability analysis have a long tradition. Some of the statistical methods, on the other hand, are closely coupled to the application of a GIS.

SAHA et al. (2005) summarized the methods of landslide susceptibility/hazard zonation (Table 2.2). Van WESTEN (2000) discussed the use of GIS for landslide hazard modelling. He distinguished three basic types, which are applicable for different scales:

- the heuristic qualitative approach, suited for broad scale investigations (1:100,000 – 1:250,000, mainly used by regional planning agencies) is based on the opinion of one or more experts regarding the dependency of landslide hazard on predictor variables. The subjective element can be a disadvantage (reproducibility and therefore legal aspects), but also an advantage;
- the statistical quantitative approach (medium scale, 1:10,000 – 1:25,000 mainly used by consulting firms or planning agencies for the preliminary planning of infrastructural works). VAN WESTEN (2000) distinguishes between data driven multivariate statistical analysis, experience-driven bivariate statistical analysis, and predictive modelling through the application of favourability and probability functions;
- the deterministic approach (detailed scale, 1:2,000 – 1:10,000), based on physical models and mainly used by consulting firms and local planning agencies for the detailed planning of infrastructural work. The success of such a model is based on the knowledge and reproduction of the mechanism of slope failure, and on the knowledge of the physical properties of the slope. It can be coupled with a hydrological model, a model dealing with earthquakes, or a combination of both. The model can be run inside or outside GIS.

VAN WESTEN (2000) also underlined the importance of landslide occurrence maps (landslide inventories). VAN WESTEN et al. (2003) mentioned the two parts necessary for a hazard analysis: the spatial dimension (susceptibility analysis), and the temporal dimension via frequency and/or magnitude of triggering forces (rainstorms, earthquakes).

A large array of authors came along with GIS-based statistical landslide susceptibility analyses particularly since the late 1990s, most of them resulting in zonations distinguishing areas with different degrees of landslide hazard and risk. Such zonations do now exist for many study areas of different sizes all around the globe. Regarding articles published in international journals, the centres of research include South Korea (LEE & MIN 2001; DAI et al. 2001, 2004; LEE et al. 2002, 2003a, 2003b; DAI & LEE 2003; LEE 2004a), Italy (GUZZETTI et al. 2004) and the Spanish Pyrenees (e.g. BAEZA & COROMINAS 2001; COROMINAS et al. 2003; SANTACANA et al. 2003). Most of them are regions with high population densities in mountainous or hilly landscapes prone to landsliding.

Table 2.2: Methods of Landslide Susceptibility/Landslide Hazard Zonation. Modified from SAHA et al. (2005).

LHZ/LSZ method		Main feature	Selected references
Qualitative	1. Distribution analysis	Direct mapping of mass movement features resulting in a map, which gives information only for those sites where landslides have occurred in the past	NICHOL & WONG 2005; ROESSNER et al. 2005
	2. Qualitative analysis	Direct or semi-direct methods in which the geomorphological map is renumbered to a hazard / susceptibility map or in which several maps are combined into one using subjective decision rules based on the experience of the earth scientist	AL-HOMOUD & MASANAT 1998; WACHAL & HUDAK 2000; MSILIMBA & HOLMES 2005
Quantitative	3. Statistical analysis	Indirect method in which statistical analysis are used to obtain predictions of the mass-movement from a number of parameter maps	BAEZA & COROMINAS 2001; SANTACANA et al 2003, LEE & TALIB 2005
	4. Distribution-free methods	Neural networks and neuro-fuzzy methods, which do not depend on distributional assumptions of the data. Here, the weights are computed in an objective manner	LEE 2003a, b
	5. Deterministic analysis	Indirect methods in which parameters are combined in slope stability calculation	BURTON & BATHURST 1998; XIE et al. 2004a, 2004b, 2006
	6. Landslide frequency analysis	Indirect methods in which earthquakes and/or rainfall records or hydrological models are used for correlation with known landslide dates to obtain threshold values with a certain frequency	BRARDINONI & CHURCH 2004

But GIS are also frequently used for deterministic approaches (BURTON & BATHURST 1998; CLAESSENS et al. 2005; XIE et al. 2006) as well as for monitoring systems (LAZZARI & SALVANESCHI 1999).

For most GIS applications regarding landslide modelling, a raster layout is most useful, but other data models have been applied, too (BRIMICOMBE & TSUI 2000; D'AMBROSIO et al. 2003). Concerning the software used, Open Source Products distributed under the GNU General public License have gained popularity in the previous years, like *GRASS GIS* or *SAGA GIS*.

The application of GIS is connected to some problems that should not be overlooked. CARRARA et al. (1999) discussed the problems of the use of GIS in the prediction and monitoring of landslide hazard. They criticized the tendency to prefer short-time, low-cost projects, partly driven by the technological possibilities and performed rather by computer specialists than experts in geology, hydrology, etc. to long-time studies done by experts in the field. Senior experts in particular would often not like to make themselves confident with GIS operations. CARRARA et al. also mentioned the bottlenecks in hardware capacity and some general problems in acquiring, processing and displaying data. However, these latter problems may have reduced since the article was published due to the advances in both software and hardware. These critics, however, should rather be understood as an appeal to avoid the misuse of GIS than as critics on the capability of the technique itself.

In addition it has to be avoided to overestimate the capabilities of a GIS. It is quite easy to create nice-looking maps, but many slope characteristics are actually very difficult to capture in their full spatial extent (e.g. soil mechanical or hydraulic properties), and much emphasis has to be put on the choice of suitable interpolation methods as well as on a proper inaccuracy assessment.

In the following sections, the different approaches for GIS-bases landslide susceptibility and hazard analyses will be discussed in more detail, following the classification according to VAN WESTEN (2000).

Direct methods (Landslide inventory)

The most straightforward way for distinguishing areas prone to slope failures from more stable areas is to map the locations of previous landslides, using field investigations and/or remote sensing techniques. Such maps are called landslide inventories. As standalone products, their value is rather limited as they only represent one snapshot within a long history of slope evolution, and due to their purely descriptive nature, they have no power for predicting future events. On the other hand, landslide inventories are extremely valuable in landslide hazard analysis as they are required for validating the results of qualitative, statistical, and deterministic approaches. PARISE & WASOWSKI (1999) emphasize the importance of a spatio-temporal view, meaning the repeated generation of landslide inventories for one area.

Though mapping of landslides is thought to be quite an objective task, inventory maps may contain a certain degree of subjectivity, like VAN WESTEN et al. (1999) could show. They tested the convergence of different landslide inventory maps by comparing independent mappings of three different teams of geomorphologists (two from the Netherlands, one from Italy) for the Alpago area (Belluno, Italy). The results from two teams were quite similar, but those obtained by the third team varied considerably, leading to the conclusion that direct landslide susceptibility mapping is a highly subjective task depending on the expertise, experience, assessment and also opinion of the researcher.

Creating landslide inventories for larger areas from field investigations only is time-consuming and therefore expensive. Extraction from aerial or satellite imagery saves a lot of time, but such images are not al-

ways available. NICHOL & WONG (2005) suggested a method based on automated satellite imagery interpretation: they tested different methods for the fusion of IKONOS images and showed that the level of detail of the enhanced images corresponds to that of aerial images. The authors furthermore showed a way how to perform regional landslide mappings by combining broad-scale SPOT imagery with the detail of PAN-sharpened IKONOS-imagery.

Also ROESSNER et al. (2005) discussed the applicability of satellite remote sensing data, using a study area in S Kyrgysztan where no other relevant long-term data was available. They underlined the different potential of different systems for extracting features: while LANDSAT data was not practicable for isolating areas affected by landslides because limestone outcrops showed the same reflection properties, ASTER data was better suited for this task. ROESSNER et al. generated a 25 m resolution DEM from MOMS data. A geological map focussing on landslide susceptibility was prepared using an existing geological map, topography, remote sensing data and experts, applying a profile and 3D mapping tool. The authors further concluded that 15 to 30 m resolution remote sensing data would be suitable for landslide hazard assessments on a regional scale (15 m would be good for an analysis of the relevant geological structures).

Compared to the traditional methods of remote sensing, the upcoming technique of laser scanning allows the recognition of small-scale structures and the identification of vegetation-covered landslides (CHIGIRA et al. 2004, SEKIGUCHI & SATO 2004). The bottleneck with this method is still the limited availability/high cost of data sets (airborne laser scanning) and the expensive equipment (terrestrial laser scanning)

Heuristic qualitative methods

Qualitative landslide susceptibility analyses base themselves on subjectively defined rules for relating landslide susceptibility to certain predictors. A common approach is to assign ratings to the classes of the predictor maps, and to distinguish hazard classes according to the mean ratings (AL-HOMOUD & MASANAT 1998; NAGARAJAN et al. 2000; WACHAL & HUDAK 2000; MSILIMBA & HOLMES 2005). Qualitative approaches may also be combined with statistical methods: AYALEW et al. (2004) applied two levels of weights to the predictor maps: primary-level-weights are based on landslide frequency, secondary-level weights on expert opinions.

Also the Universal Soil Loss Equation (USLE) shall be mentioned in this context, though rather applicable to soil erosion than to real slope failures. It is an empirical formula combining dimensionless factors denoting the tendency of a soil to be eroded:

$$A = R \times K \times L \times S \times C \times P \qquad \text{Eq. 2.1,}$$

where A is the total annual soil loss (t ha-1 a-1), R is the Rainfall erosivity factor (MJ mm ha-1 h-1 a-1), K is the Soil erodibility factor (t ha h ha-1 MJ-1 mm-1), L is the slope length factor, S is the slope steepness factor, C the crop and management factor and P the factor for conservation supporting practices. LEE (2004b) applied the USLE for estimating soil erosion in the Boun study area, South Korea.

The most important qualitative landslide susceptibility zonation in the context of the present thesis was done by MOREIRAS (2004b), covering a section of the Río Mendoza Valley between Guido and Picheuta. Different types of landslides (in particular rock falls, slides and debris flows) were included. The study was based on overlaying maps of conditioning factors (lithology and slope angle) and a landslide inventory (MOREIRAS 2004a). Seismicity and heavy rainfall were mentioned as the major triggering factors for landslides in that region.

ESPIZUA & BENGOCHEA (2001) did a qualitative risk zonation mapping in the Río Grande Basin, also located in the Andean portion of the Province of Mendoza, Argentina. They used field data and aerial imagery and found a relationship between lithology and landslide susceptibility. Furthermore, they underlined that landslide events mainly occur in connection to snowmelt in spring, and to heavy rainstorms in summer.

Statistical methods

Statistical methods are widely used for landslide susceptibility analyses. With the increasing application of GIS-based studies, serving for the coverage of large areas, the application of statistics has increased rapidly. The standard procedure is to find a spatial coincidence between landslide incidence and one or more suspected conditioning factors. This way of analysis requires a landslide inventory that has to be obtained using field or remote sensing techniques as discussed above as well as spatial datasets representing the conditioning factors. The way how the landslide inventory is integrated plays a crucial role for the performance of the analysis, and in particular for the capability to predict the locations of future landslides. REMONDO et al. (2003) underlined the difference between landslide susceptibility analysis and landslide hazard analysis. For landslide hazard analysis it would be necessary to use two different inventories: one for the analysis itself, the other for validation. This can be attained in different ways:

- The dataset is split into two parts, one for susceptibility analysis and one for hazard analysis (e.g. SANTACANA et al. 2003),
- the landslide inventories of different study areas have to be applied for susceptibility analysis and hazard analysis, or

- different time spans have to be used. This would be the most adequate, but however the most difficult method.

REMONDO et al. (2003) also underlined the better performance of statistical methods compared to qualitative methods.

FABBRI et al. (2003) discussed the difference between hazard assessment and hazard prediction, regarding landslides in Belgium and Portugal. The authors critically reviewed the problems and restrictions and suggested a statistical method to successfully predict the location of future landsliding, based on landslide inventories. They underlined the importance of such archives and the fact that the maximum prediction horizon corresponds to the period of the past covered by the inventory. The threshold separating hazardous and non-hazardous areas should be defined in a way that all landslides of the inventory (or 95 % of them) fall within the hazardous area.

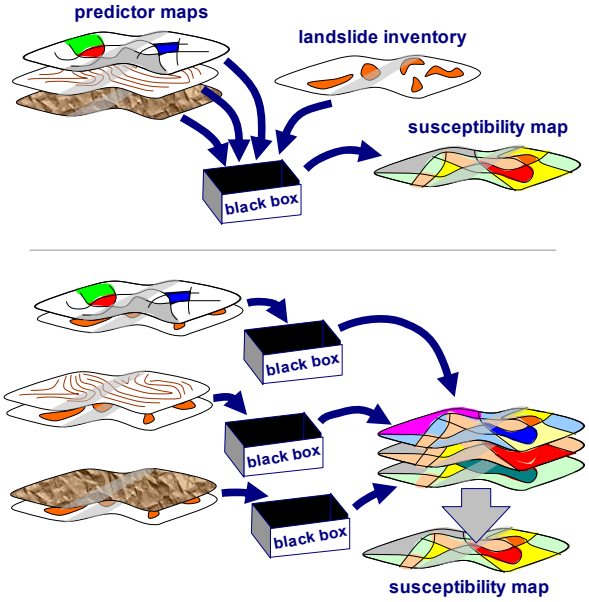

Figure 2.4: Multivariate (top) and bivariate (bottom) statistical approaches for landslide susceptibility analysis. Designed by M. Mergili.

A statistical landslide hazard analysis can either be based on the comparison of the landslide inventory to a single predictor (bivariate methods), or to a combination of predictors (multivariate methods). Figure 2.4 illustrates the difference. The most common multivariate methods are (logistic) regression and discriminant analysis. Both of them are "traditional" methods that have been successfully applied to a wide array of problems in natural and social sciences for a long time. Many bivariate methods used in landslide hazard analysis are relatively new, having developed as a response to the increased application of GIS techniques.

Multivariate statistical methods (data-driven). CARRARA (1983) mentioned discriminant analysis and multiple (logistic) regression as valuable multivariate statistical methods for landslide hazard evaluation. DAI et al. (2001), LEE & MIN (2001), DAI & LEE (2003), DAI et al. (2004), LEE (2004a), SÜZEN & DOYURAN (2004) and WANG & SASSA (2005) used logistic regression for landslide susceptibility zonations in Korea, Hong Kong, Japan and Turkey. Logistic regression, in contrast to standard multiple regression, allows the inclusion of categorical variables (ATKINSON et al. 1998). The results of the logistic regression – values between 0 and 1 – can be evaluated using the χ^2-test (DAI & LEE 2003).

Multivariate statistical analyses require large datasets of environmental information. SANTACANA et al. (2003), using discriminant analysis, captured 17 independent variables for a study area in the Spanish Pyrenees from a 15 m resolution DEM, aerial imagery and field work. Using principal component analysis, t-test and one-way test allowed to isolate the most significant predictors for landslide susceptibility. 88.5 % of the whole dataset and 95.6 % of the failed slopes were predicted correctly. BAEZA & COROMINAS (2001), using a combination of multivariate statistical methods to generate a landslide susceptibility map for the Ensija range in the Eastern Pyrenees, obtained a set of more than 30 attributes of 230 failed and unfailed slopes.

Bivariate statistical methods (experience-driven). With the increased application of GIS techniques for landslide hazard analysis, new methods of bivariate statistics were developed. They are similar in their major characteristics as all of them

- are based on discrete classes of predictors;
- require the input of data matrices (rasters) of predictors as well as a landslide inventory;
- use the number of cells classified as landslide or not landslide (inventory), or assigned to a class (predictor) as basic value;
- and produce susceptibility indices separately for each predictor.

Although bivariate methods consider the relationships between one single predictor and the occurrence of landslides, the effects of an array of predictors may be combined by adding the index values for each predictor. PISTOCCHI et al. (2002) concluded that each factor added to the analysis would improve the quality of the results, adding some more detail to the study. The most widely used bivariate methods and their applications are discussed below.

The InfoVal (Information Value) approach (compare e.g. SAHA et al. 2005) is based on weights assigned to classes of each independent variable:

$$W_i = \ln\left[(p_i / P_i) \Big/ \left(\sum_{i=1}^{n} p_i \Big/ \sum_{i=1}^{n} P_i \right) \right] \qquad \text{Eq. 2.2,}$$

where W_i is the weight of the class i of a particular independent variable, p_i is the number of cells of the class i classified as landslide, P_i is the total number of

cells of the class *i*, and *n* is the total number of classes of the considered independent variable. The term is logarithmized in order to account for the large variation in the weight values. The weights of all thematic layers are overlaid for each cell.

Also the LNRF (Landslide Nominal Risk Factor) approach is based on weighting classes of layers of independent variables:

$$LNRF = (p_i) \Big/ \left(\sum_{i=1}^{n} p_i \Big/ n \right) \qquad \text{Eq. 2.3,}$$

with factors > 1 indicating high susceptibility, values < 1 indicating low susceptibility and values = 1 indicating an average value. The weights for all layers are overlaid in the same way as with the InfoVal method. Further classification is either done subjectively or using other statistical methods.

LEE & TALIB (2005) carried out a landslide susceptibility analysis for a 293 km² study area in NW Malaysia. They used the frequency ratio method, which is a probabilistic approach:

$$LSI = \sum_{i=1}^{n} \frac{N_{l,i}/N_l}{N_i/N} \qquad \text{Eq. 2.4,}$$

where *LSI* is the dimensionless Landslide Susceptibility Index for the considered cell, N_l is the number of cells classified as landslide, N is the total number of cells. n is the number of predictor layers and i represents the class of the layer assigned to the considered cell.

Further bivariate statistical methods proving successful with landslide susceptibility analysis include the Statistical index and Weighting factor (ÇEVIK & TOPAL 2003) and the Association and correlation coefficients (FERNÁNDEZ et al. 2003).

Some authors underlined the better performance of multivariate methods, compared to bivariate methods (DUMAN et al. 2005, LEE 2004a, SÜZEN & DOYURAN 2004). Problems connected to weighting of the predictor variables were identified as a major source of the worse performance of the bivariate methods. LEE (2004a), however, stated that the likelihood ratio method was much easier to perform as no statistical software was required. DUMAN et al. (2005) underlined the better understandability of bivariate methods and the advantages in calculation speed, compared to multivariate analyses.

Probability and favourability functions. The Weight of Evidence approach, based on Bayesian Probability, analyses the spatial coincidence of an independent and a dependent variable, with both variables having a binary character. In practice, this means that the landslide status (landslide or not landslide) is overlaid with a class of a predictor layer, providing a positive and a negative weight, W^+ and W^-, respectively, for the regarded class:

$$W^+ = \log_e \frac{P\{B \mid D\}}{P\{B \mid D'\}} \qquad \text{Eq. 2.5,}$$

and

$$W^- = \log_e \frac{P\{B' \mid D\}}{P\{B' \mid D'\}} \qquad \text{Eq. 2.6,}$$

where P is the prior probability of an occurrence, B and B' stand for the presence and absence of the binary predictor, respectively, and D and D' stand for the presence and absence of a landslide, respectively. The weights are used for calculating a contrast value C:

$$C = W^+ - W^- \qquad \text{Eq. 2.7.}$$

Positive values of C indicate a positive relationship between the predictor and landslide incidence, negative values indicate a negative relationship. C is therefore used as rating for the classes of the predictors. Certain combinations of predictor layers are overlaid, and the sum of the C-values is taken as susceptibility index. This procedure can be repeated for several combinations of predictor layers. LEE et al. (2002), DUMAN et al. (2005), and ZÊZERE et al. (2004) used Bayesian approaches for landslide susceptibility analyses in Korea, Turkey, and Portugal.

Another approach is the so-called Probability method, based on a favorability function F:

$$F = 1 - (1 - 1/A_0)^{A_1} \qquad \text{Eq. 2.8,}$$

where A_0 is the total area of the considered class, and A_1 is the area of the considered class affected by landslides. The method was applied by HANTZ et al. (2003) and REMONDO et al. (2003), the latter comparing it with fuzzy logic (compare below).

Artificial intelligence methods. The term artificial intelligence includes methods attempting to imitate human thinking. It has gained importance in many fields with increasing computational capacities in the previous years and decades. Various methods have been developed, two of which are currently applied for landslide susceptibility analysis: Fuzzy Logic and Artificial Neural Networks.

The concept of fuzzy logic (compare e.g. NOVÁK et al. 1999 for a general introduction) assumes that each element of a sample may belong to more than one class, in other words: the boundaries between classes are not sharp. The membership of each element to each class is defined by so-called membership functions. In the previous years, some authors applied the theory of fuzzy logic for landslide susceptibility analyses (e.g. JUANG et al. 1992; AL-HOMOUD & AL-MASRI 1999; UROMEIHY & MAHDAVIFAR 1999; GORSEVSKI et al. 2001; ERCANOGLU & GOKCEOGLU 2002). In many of these studies the fuzzy concept was superimposed on simple bivariate methods by assigning membership values to each

class of susceptibility and to each class of each predictor (ERCANOGLU & GOKCEOGLU 2002). The same authors used a fuzzy approach for a landslide susceptibility assessment of a study area in Turkey. They isolated the most important predictors determining landslide susceptibility using a simple factor analysis. Among six factors (land use, slope angle, slope aspect, weathering depth, elevation, water conditions), slope angle proved to have the highest importance, weathering depth the lowest. The authors defined rules (fuzzy conditional statements) and fuzzy sets. Each rule defined the degree of landslide susceptibility (very low, low, moderate, high, very high) based on a class of a predictor dataset, e.g. "if land use is pastureland then landslide susceptibility is high". In the fuzzy sets membership values were assigned to each class of susceptibility and, according to the results of the factor analysis, to each predictor. The fuzzified index maps were overlaid in order to get a "composite" landslide susceptibility map. The results corresponded well to the observed patterns of landslide occurrence.

LEE et al. (2003a, b) carried out a landslide susceptibility analysis and mapping for two study areas in South Korea (Boun and Yongin) using artificial neural networks. Models based on artificial neural networks use the properties of so-called training sites (that have to be chosen by the investigator) to build relationships between an input layer and a set of hidden layers, imitating the human central nervous system, and to apply these relationships to an output layer. The authors underlined the advantages of this method compared to conventional statistical and deterministic methods: it could be easily applied to GIS data like aerial images, it could be applied in areas with imperfect or incomplete data availability, and it could deal with nonlinear and complex relationships between variables. Furthermore, it would be adaptive and capable of generalization and would provide a multi-faceted approach to a solution as well as the extraction of a good result for complex problems. The disadvantages were the complicated data handling and the difficult-to-follow internal structure of the mechanism.

Validation. An important part of every statistical landslide susceptibility or hazard analysis is the validation. It has to be verified that the majority of the landslides of the inventory are in zones classified as highly susceptible. The cumulative frequency curve, also called cumulative percentage diagram or validation diagram, is the most common way of validation (e.g. LEE et al. 2002; REMONDO et al. 2003; SANTACANA et al. 2003; LEE & TALIB 2005). It is based on an index of landslide frequency *R*:

$$R = 100\left(n_i/N_i\right)/\sum\left(n_i/N_i\right) \qquad \text{Eq. 2.9,}$$

where n_i is the number of landslides in the susceptibility level *i* and N_i is the total number of raster cells located in the susceptibility level *i*. In a validation diagram, the portion of the predicted landslides is plotted against the portion of the study area classified as susceptible. A straight diagonal line would represent a random distribution.

Deterministic methods for slope stability

Qualitative and statistical methods require large, but superficial datasets like a landslide inventory and maps of conditioning factors (TERLIEN 1998), whilst it is not necessary to understand the physical processes behind the slope failure leading to the landslide (black box, compare Figure 2.4). Deterministic (physically-based) models require the understanding of these processes, and they require much more detailed parameters determining slope instabilities (compare Table 4.2). Therefore they are usually only applicable to small areas (small catchment scale, few square kilometres). In order to be fit for predictive modelling, such approaches have to include subroutines dealing with the triggering forces (infiltration, groundwater development, seismic stress, etc.). CHAU & LO (2004) underlined the advantages of numerical modelling compared to statistical analyses: the latter would not take account of the local conditions.

An essential point for physically-based modelling of landslides is to know about the mechanics of the slope failure. The differences between shallow translational failures and deep-seated rotational failures are tremendous (PETLEY & ALLISON 1997), requiring the application of completely different model algorithms. Whilst shallow translational failures may be tackled with a simple infinite slope stability approach (compare below), deep-seated rotational failures require algorithms for the identification of failure planes and are more difficult to be implemented in a GIS. Many of the existing models for GIS-supported physically-based slope stability simulations therefore use the infinite slope stability approach. Some of the most widely used frameworks are listed in Table 2.3.

Whilst it is not possible to discuss all of these models in detail in this place, some of the major physical concepts behind slope stability and soil hydraulics will be presented

One of the basic concepts for physically-based slope stability modelling is the factor of safety, or factor of stability, *FOS*, in its most simple formulation:

$$FOS = \frac{stabilizing\ forces}{destabilizing\ forces} \qquad \text{Eq. 2.10.}$$

Values of $FOS < 1$ indicate unstable conditions. Slope failures may occur when the total shear force *T* (N) exerted on a section of a slope exceeds its shear resistance T_f (N; Figure 2.5). Shear stress can be exerted by the weight force exerted by the overlying soil, by seismic events, by seepage forces, by raindrop impact, by the force of surface runoff, or by additional mechanical stress like snow, buildings, or ani-

mals. Under average conditions, T never exceeds T_f, so that the slope is in equilibrium or stable. In non-cohesive materials, the angle at which $T_f = T$ is called angle of internal friction φ. It is mainly determined by grain texture and roughness and has to be determined experimentally, Cohesion c (N m^{-2}) increases the stability of a slope, allowing slope angles exceeding φ.

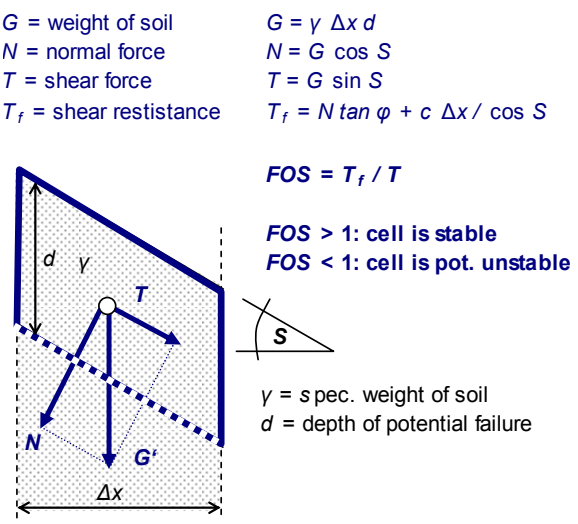

Figure 2.5: Infinite slope stability model for a section of a simple slope with dry soil. Designed by M. Mergili.

The factor of safety can be used for modelling translational as well as rotational failures, but the way it is calculated is quite different for the two mechanisms and much less complex for translational failures where infinite slope stability models are applicable:

Infinite slope stability model. It assumes a plane, infinite slope and a failure plane parallel to the slope surface (compare Figure 2.5). These conditions are never met in reality, but for shallow failures, the ratio between the depth of the failure plane and slope length is usually small, so that the method can be considered as a reasonable approximation. Strictly spoken, it only works for cohesionless soils as failures become rotational as soon as cohesion occurs. However, it is practice to use infinite slope stability models for cohesive soils (including root cohesion) too.

Various authors have used infinite slope stability models in combination with GIS, for example VAN WESTEN & TERLIEN (1996), BORGA et al. (1998, 2002), BURTON & BATHURST (1998), MILLER & SIAS (1998), COROMINAS & SANTACANA (2003), IIDA (2004), XIE et al. (2004a), or LAN et al. (2005). Therefore, an array of different formulations does exist, all of them meaning the same. Figure 2.5 shows the most simple system possible.

When taking into account vegetation and seepage, the conditions become more complicated (compare also Figure 4.9). BURTON & BATHURST (1998) expressed the factor of safety as follows:

$$FOS = \frac{\left[2c/\gamma_w d \sin(2\alpha)\right] + \left[(L-m)\tan\varphi/\tan\alpha\right]}{L} \qquad \text{Eq. 2.11,}$$

where $$L = \frac{q}{\gamma_w d} + m\frac{\gamma_{sat}}{\gamma_w} + (1-m)\frac{\gamma_m}{\gamma_w} \qquad \text{Eq. 2.12.}$$

c is the sum of soil and root cohesion obtained from effective stress tests, γ_w, γ_{sat} and γ_m (all in N m^{-3}) are the specific weights of water, saturated soil and soil at field moisture content. φ is the effective angle of internal friction of soil at the failure plane, d (m) is the soil depth and a is the local slope angle. q (N m^{-2}) is the vegetation surcharge per unit plan area, and m is the relative saturated depth.

Table 2.3: A selection of existing model frameworks dealing with deterministic modelling of slope stability.

Model	Main features	Distribution	Selected applications
CHASM	2-dimensional combined hydrological and slope stability model	commercial	WILKINSON et al. (2002)
LAPSUS-LS	extension to the landscape evolution model LAPSUS, based on critical rainfall and distribution maps, partly GIS-based		CLAESSENS et al. (2005)
GISLIP, SHESLIP	extensions to the SHETRAN sediment transport model: GISLIP computes hydrology and factor of safety (GIS-based), SHESLIP the failure patterns at coarser resolution		BURTON et al. (1998), BURTON & BATHURST (1998)
SHALSTAB	combined hydrological and slope stability model, assuming infinite slope and steady-state subsurface flow; extension to ArcView	free	GORSEVSKI et al. (2001)
TRIGRS	deterministic model for simulating rainfall infiltration and slope stability, developed by the USGS	free	CHEN-YUAN et al. (2005)
JUST-SLOPE	slope stability model for rotational failures, including ordinary method on slices and Bishop method		MALKAWI & TAQUIEDDIN (1996)
SINMAP	slope stability model based on infinite slope stability approach, allowing uncertainties; extension to ArcGIS/ArcView	free	THIEBES et al. (2007)

Also *SINMAP* (PACK et al. 1998; compare Table 2.3) is based on an infinite slope stability model:

$$FOS = \frac{c + \cos^2\alpha\left[\gamma_s\left(d_p - d_w\right) + \left(\gamma_s - \gamma_w\right)d_w\right]\tan\varphi}{d_p\gamma_s \sin\alpha\cos\alpha} \qquad \text{Eq. 2.13,}$$

where d_p is the thickness of soil above the failure plane, and d_w is the thickness of saturated soil above the failure plane. In *SINMAP*, Eq. 2.13 is combined with a probabilistic approach.

Eq. 2.11 and 2.13 yield exactly identical results. The way the same infinite slope stability model was implemented in *GRASS* for the present thesis is illustrated in Figure 4.9 (Section 4.2).

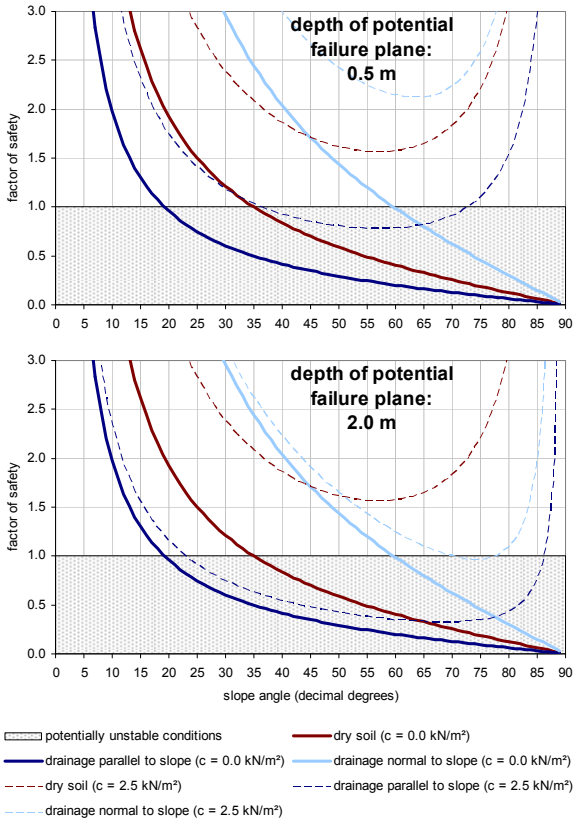

Figure 2.6: Factor of safety for different assumptions regarding soil water movement, depth of potential failure plane and cohesion.

All these formulations build on the worst-case assumption that soil water moves parallel to the slope, so that the seepage force has a destabilizing downslope component only. Roughly, this leads to the reduction of *FOS* by a factor of 2, compared to dry soil. Slope-parallel seepage usually occurs over impermeable layers. Assuming that seepage occurs exclusively normal to the slope (only stabilizing seepage force) results in doubling of *FOS*, compared to dry soil. Vertical soil water movement has no influence on the factor of safety. Figure 2.6 illustrates these patterns for cohesive and non-cohesive soils at different depths of potential failure planes. Note that the depth of non-cohesive soils has no influence on the factor of safety. The stability of cohesive soils reaches a minimum at medium slope angles.

The factor of safety for rotational failures. The infinite slope stability concept is not applicable to deep-seated rotational failures: if the ratio between failure depth and slope length is too high, the assumption of an infinite slope is not acceptable. Furthermore, the concept is not able to deal with curved slip surfaces. The algorithms required to model rotational failures therefore differ substantially from the infinite slope stability concept. Several models are applied by geotechnicians (compare e.g. SCHNEIDER-MUNTAU & FELLIN 2005), but three-dimensional GIS-based approaches are rare due to difficult implementation of the required complex algorithms and iteration procedures as well as due to the problems with 3D processes in 2D raster systems usually applied in GIS (XIE et al. 2003). The same authors criticized the concentration on the infinite slope stability concept in slope stability modelling and introduced a GIS-based model for rotational failures. They express the factor of safety as follows:

$$FOS_{3D} = \frac{\sum_Y \sum_X \left[cA + \left(d_{yx}\gamma'\cos\vartheta - u_{yx}\right)\tan\varphi\right]\cos\vartheta_{Avr}}{\sum_Y \sum_X d_{yz}\gamma' \sin\vartheta_{Avr}\cos\vartheta_{Avr}} \qquad \text{Eq. 2.14,}$$

where X and Y are the column and the row of the raster, c is cohesion, A is the area of the slip surface, d_{ij} is the depth of the slip surface, γ' is specific weight, ϑ is the normal angle of the slip surface, u_{ij} (Pa) is pore water pressure at the slip surface, φ is angle of internal friction and ϑ_{Avr} is the apparent dip of the main inclination direction of the slope failure.

One specific problem of this approach is the identification of the critical slip surface which can not be determined in an analytical way. XIE et al. (2003) assumed an ellipsoidal slip surface and used a Monte Carlo simulation to solve the problem. Central point, geometric parameters and inclination angle of the ellipsoid were used as variables. BAKER (1980) presented a method for determining the critical slip surface of any shape. WILKINSON et al. (2000) developed a model performing an automated non-circular slip surface search within the combined slope stability and hydrology model *CHASM*.

Slope stability models for rotational failures also require different approaches for the mechanical impact of the root systems than models for translational failures – root cohesion c_r can be computed as follows:

$$c_r = t_r RAR(\cos\theta\tan\varphi + \sin\theta) \qquad \text{Eq. 2.15,}$$

where RAR is the root area ratio, t_r is the average tensile strength of root or fibre per unit area of soil (N m^{-2}), and θ is the angle of shear rotation (WILKINSON et al. 2002).

The hydraulic component of slope stability models. When looking at Eq. 2.11 and Eq. 213, it appears obvious that the infinite slope stability approach as applied there is based on the assumption that slope failures occur as a response to certain hydraulic conditions, more exactly to the occurrence of seepage forces on the one hand (compare Figures 2.6 and 4.9), and to the change of effective stress due to pore water pressure u (Pa) on the other hand:

$$s = c + (\sigma - u)\tan\varphi \qquad \text{Eq. 2.16,}$$

where s (N m^{-2}) is the soil shear strength, c is the effective soil cohesion, and φ is the effective angle of internal friction (WILKINSON et al. 2002). Most applications are therefore tightly coupled to hydraulic models of subsurface water movement (compare e.g. CASADEI et al. 2003, HENNRICH & CROZIER 2004). Water flow through unsaturated soil follows the relationship

$$\frac{\partial\theta}{\partial t} = -\frac{\partial}{\partial z}\left(K\frac{\partial\phi}{\partial z}\right) - \frac{\partial K}{\partial z} \qquad \text{Eq. 2.17,}$$

where θ (m³ m^{-3}) is the volumetric moisture content, dt (s) is the length of one time step, z (m) is the vertical depth, K (m s^{-1}) is the unsaturated hydraulic conductivity, and ψ (m) is the matric suction or negative pore water pressure. WILKINSON et al. (2002), using a 3-dimensional raster approach, assumed a horizontal flow component under saturated conditions only.

An alternative approach for computing subsurface water movement, particularly near to the surface, is the infiltration model developed by GREEN & AMPT (1911; compare e.g.. XIE et al. 2004a for an application combined with slope stability; Figure 2.7). The basic idea of the approach is a sharp wetting front moving downwards during rainfall events, with saturated soil above and soil at initial moisture content (usually set to the permanent wilting point) below. The infiltration rate f (m s^{-1}) can be computed according to Darcy's Law:

$$f = K_s\frac{z_w + \psi_f}{z_w} = \frac{\mathrm{d}FF}{\mathrm{d}T} \qquad \text{Eq. 2.18,}$$

where K_s is the saturated hydraulic conductivity, z_w is the depth of the wetting front, and ψ_f (m) is the Green-Ampt soil suction parameter at the wetting front. The influence of a surface water table on pressure head is neglected. T (s) is the time interval, and FF (m) is cumulative infiltration:

$$FF = K_s T + \Delta\theta_i\psi_f \ln\left(1 + \frac{FF}{\Delta\theta_i\psi_f}\right) \qquad \text{Eq. 2.19,}$$

where $\Delta\theta$ is the moisture deficit at the wetting front. After the start of the rainfall there is a delay until the wetting front moves downwards (incipient ponding). The effects of incipient ponding can be included as following:

$$FF = F_p + K_s\left(T - T_p\right) + \Delta\theta_i\psi_f \ln\left(\frac{FF + \Delta\theta_i\psi_f}{F_p + \Delta\theta_i\psi_f}\right) \qquad \text{Eq. 2.20,}$$

where F_p is the cumulative infiltration at incipient ponding, and T_p is the ponding time. Eq. 2.20 is derived by integration of Eq. 2.19. z_p is the depth of the wetting front at incipient ponding:

$$z_p = K_s\psi_f/\left(i - K_s\right) \qquad \text{Eq. 2.21,}$$

$$F_p = z_p\Delta\theta = K_s\psi_f\Delta\theta/\left(i - K_s\right) \qquad \text{Eq. 2.22,}$$

$$T_p = F_p/i = K_s\psi_f\Delta\theta/\left(i^2 - iK_s\right) \qquad \text{Eq. 2.23.}$$

The depth of the wetting front z_w can then be computed as follows:

$$z_w = FF/\Delta\theta \qquad \text{Eq. 2.24.}$$

Some authors have used half the value of K_s in the Green-Ampt model (e.g. CHEN & YOUNG 2006, compare ERICKSON & STEFAN 2007). The way the Green-Ampt model was used for the present thesis is described in detail in Section 4.2 (compare Figure 4.8).

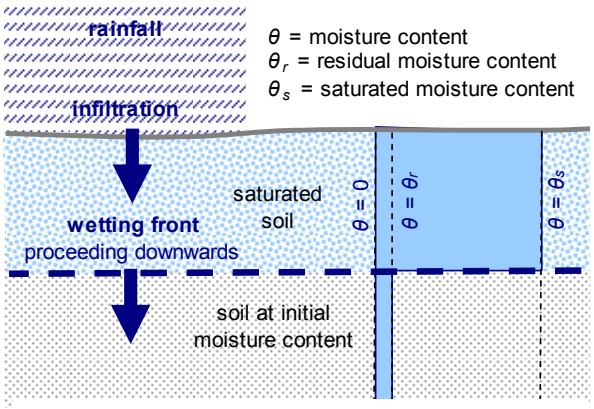

Figure 2.7: Movement of soil water according to the Green-Ampt infiltration model (soil initially at residual moisture content, compare Table 4.2). Designed by M. Mergili.

Critical precipitation. REICHENBACH et al. (1998) provided a detailed discussion on the possibility of using rainfall thresholds for the prediction of landsliding using historical data. They mentioned the limitations of data availability: one rain gauge per 50 km² and hourly records would be required for local-scale investigations, whilst daily values would be sufficient for assessments at a regional scale. The quality of the data and the length of the records had to be taken into account as well as the availability of an inventory of the landslides related to the considered meteorological event.

If the hydraulic and slope stability (factor of safety) equations are combined and solved for water input, critical precipitation may be computed in a deterministic way, e.g. as critical daily rainfall threshold P_{cr} (m day^{-1}):

$$P_{cr} = T \sin\theta \left(\frac{b}{a}\right)\left(\frac{\rho_s}{\rho_w}\right)\left(1 - \frac{\sin\alpha - C}{\sin\alpha \tan\varphi}\right) \quad \text{Eq. 2.25,}$$

where T is the saturated soil transmissivity (m² day^{-1}), a is the slope angle, b the effective unit contour length (m), a the upslope contribution area (m²), ϱ_s the wet soil bulk density (kg m^{-3}), ϱ_w the density of water, φ the effective angle of internal friction, and C the combined cohesion term:

$$C = \frac{C_r + C_s}{h\rho_s g} \quad \text{Eq. 2.26,}$$

where C_r is the cohesion of the root system, C_s the cohesion of the soil, h the perpendicular soil depth, and g the gravitational acceleration (CLAESSENS et al. 2005). Eq. 2.25 is only valid under certain boundary conditions: the slope is unconditionally stable if

$$\tan\alpha \le \left(\frac{C}{\cos\alpha}\right) + \left(1 - \frac{\rho_w}{\rho_s}\right)\tan\phi \quad \text{Eq. 2.27,}$$

or is unconditionally unstable if

$$\tan\alpha > \left(\frac{C}{\cos\alpha}\right) + \tan\phi \quad \text{Eq. 2.28.}$$

GORSEVSKI et al. (2001) used the effective steady-state rainfall rate instead of the daily rainfall:

$$\frac{q}{T} = \frac{\rho_s}{\rho_w}\left(1 - \frac{\tan\alpha}{\tan\varphi}\right)\frac{b}{a}\sin\alpha \quad \text{Eq. 2.29,}$$

where a (watershed area), b (outflow boundary length), and a (slope angle) are topographic variables, ϱ_s and ϱ_w are the densities of soil and water, respectively, and φ is the angle of internal friction. q is the ratio of steady-state effective precipitation (rainfall minus evapotranspiration) and T the transmissivity of the soil. The status of slope stability is indicated by the log of q/T. Values from -1.9 to -3.4 indicate potentially unstable slopes (and are incremented by -0.3 of the log q/T), values above -1.9 unconditionally stable slopes and values below -3.4 unconditionally unstable slopes. MONTGOMERY et al. (1998) applied a similar approach to 14 study areas in the US Pacific Northwest.

The hydraulic influence of vegetation. The influence of vegetation on slope stability includes a hydraulic and a mechanical part: while root cohesion and vegetation surcharge directly influence slope stability, interception and evapotranspiration lead to a reduction of the amount of water înfiltrating the soil. The most important hydraulic role of the vegetation besides interception is the increasing hydraulic conductivity K due to the root network. The magnitude of this effect is well documented:

$$\Delta K = \alpha + \beta RAR \quad \text{Eq. 2.30,}$$

where a and β are constants, and RAR is the root-area-ratio in per cent (WILKINSON et al. 2002). However, potential evapotranspiration and root water uptake are difficult to determine due to some hardly available input parameters.

Debris flow runout

Not all unstable soil material automatically and immediately develops into a debris flow. The further evolution of material from slope failures is largely determined by the cohesion of the material, and by its moisture content (or, from a hydrological point of view, its sediment concentration). According to O'BRIEN (2003), debris flows occur at sediment concentrations between 0.45 and 0.55 (volume of solid material per total volume of failed soil; compare Eq. 2.33 and Table 2.5). Slides are likely to occur at higher concentrations, at lower concentrations hyperconcentrated water flow will be the dominant process.

Literature on the analysis of debris flow movement is less extensive than that on landslide susceptibility and hazard analysis in general and on slope stability analysis. The existing studies on the movement and deposition of debris flow can be organized into three categories:

- empirical-statistical relationships are based on parameters derived from the analysis of previous debris flows (primarily travel distances and threshold slope angles);
- semi-deterministic approaches combine both physically-based (e.g. flow velocity) and empirically derived components (e.g. slope and velocity thresholds for entrainment and deposition);
- deterministic models attempt to simulate the physical processes behind the debris flow.

The most important aspects regarding the different approaches for landslide and debris flow runout modelling are discussed in the following sections.

Empirical-statistical relationships are sometimes coupled to deterministic GIS-based slope stability analyses (e.g. BURTON & BATHURST 1998). Empirical rules for the movement of different types of landslides have been established quite early, like by SCHEIDEGGER (1973), predicting the reach and the velocity of large catastrophic landslides depending on the volume of the landslide.

COROMINAS et al. (2003) used volume and obstruction of the flow path in order to differentiate the angles of reach of different types of landslides based on a study area in Andorra (Table 2.4). Debris flows show quite a similar behaviour as shallow slides.

RICKENMANN (1999) compiled data from debris flows all around the world and derived a statistical relationship for the total runout distance, using debris flow volume and total elevation difference between starting point and the lowest point of deposition as predictors (compare Eq. 4.35 in Section 4.2).

Table 2.4: Reach of different types of landslides according to Corominas et al. (2003).

Landslide type	Landslide volume (m³)	Obstructed flow path: angle of reach	Unobstructed flow path: angle of reach
Rock fall	1-10	54	48
	10-100	48	40
	100-1000	42	33
	>1000	36	26
Debris flow	<800	30	26
	800-2000	25	23
	>2000	23	21
Shallow slides	<800	30	26
	800-2000	25	22
	>2000	23	20

The relationships derived by COROMINAS et. al. (2003) and RICKENMANN (1999) allow for the identification of areas potentially affected by a debris flow, but they give no estimate about the patterns of scouring and deposition as no information on the subdivision of the affected area is provided. BURTON & BATHURST (1998) applied an approach proposed by VANDRE (1985) with two threshold slope angles (scouring and deposition) and a travel distance criterion (compare Eq. 4.33 in Section 4.2). The same authors assumed an even distribution of the debris flow material over the area of deposition. The disadvantage of this approach is that it is not universally applicable without calibration of the parameters to each specific study area.

The three approaches discussed above are explained in more detail in Section 4.2 since they were used for the present thesis (compare Figure 4.10).

CLAESSENS et al. (2005) also based his study on the VANDRE (1985) approach, but with refined approximations for the depth of scouring S (m), which is expressed as

$$S = \left[\rho_s \cos\theta(\tan\theta - \tan\alpha)a\right]/c_s \qquad \text{Eq. 2.31,}$$

where ρ_s (kg m^{-3}) is the soil density, θ is the slope angle, α is the threshold slope angle between scouring and deposition, a (m^2) is a dimensional correction, and c_s (N m^{-2}) is the soil cohesion, meaning that the depth of scouring becomes infinite for non-cohesive soils.

Empirical-statistical approaches for the runout of landslides and debris flows require the use of a routing algorithm when applied in combination with GIS. The most simple approach would be to use the steepest slope for determining the direction of the movement from one cell to the next. However, this would lead to a very pronounced concentration of the flow, being realistic for channels, but not for slopes or in many cases the runout zone. Therefore a certain degree of spreading has to be introduced into simulation models in order to achieve realistic results. This is most frequently done using a random walk approach (compare e.g. HUGHES 1996 for a general introduction). The flow direction for each cell and each time step is determined randomly, but with a higher probability for the steepest descent. WICHMANN (2006) provides an example for the application of a random walk procedure for the routing of debris flows.

Semi-deterministic approaches also use random walk algorithms for routing the debris flow downwards, but instead of applying simple slope or distance thresholds in order to determine runout distance, dynamic variables (e.g. flow velocity) are computed on a physical basis.

So-called friction models are most widely applied. Whilst one-parameter friction models are frequently used for simulating rock falls (e.g. MEIßL 1998), two-parameter friction models are required for modelling debris flows. A friction coefficient μ and a mass-to-drag ratio M/D (as surrogate for the power or energy of the debris flow) are used in combination with the local slope angle in order to determine flow velocity (GAMMA 2000; PERLA et al. 1980; WICHMANN 2006). The debris flow continues until velocity drops to or below zero. M/D is calibrated with flow velocity, μ with the observed runout distance. GAMMA (2000) and WICHMANN (2006) provided examples for values of both parameters. The delineation of areas of scouring and areas of deposition has to be done with empirical thresholds (slope angle and velocity), similar to the empirical-statistical approaches.

Two-parameter friction models are explained in more detail in Section 4.2 since this approach was used for the present thesis (compare Eq. 4.36 – 4.40).

Deterministic models. The first physically-based model for simulating the runout of granular masses dates back to the 1950s (VOELLMY 1958). Some theories for the motion of debris flows and flow avalanches (so-called granular flows) were developed since the 1980s, e.g. by SAVAGE & HUTTER (1989); TAKAHASHI et al. (1992), IVERSON (1997), or MCDOUGALL & HUNGR (2004). Particularly the Savage-Hutter (SH) model has gained much attention. It assumes an incompressible fluid moving down an inclined plane, being subjected to Coulomb bed friction and internal friction. The SH model is based on a system of partial differential equations of mass and momentum balance (compare Eq. 4.41 – 4.43 in Section 4.3). The model is scale-invariant, meaning that validation is possible with small-scale experiments as well as with large-scale granular flows in nature.

Solutions for a set of idealized channel topographies have been elaborated (PUDASAINI & HUTTER 2007). However, some problems remain unsolved, like en-

trainment and deposition of solid or fluid, which are difficult issues due to the complex conditions at the upper and lower boundaries of the flow. Some of the other theories (e.g. IVERSON 1997; MCDOUGALL & HUNGR 2004) are basically quite similar to the SH model, but differ in rheological assumptions, geometry, or the details of the numerical implementation (HARBITZ 1998). Among all of them, however, the SH model is the one with the most detailed validation against data from experiments or field observations.

CHAU & LO (2004) modified the model of TAKAHASHI et al. (1992) in order to model flow path and deposition of debris flows threatening the Leung King Estate (Hong Kong, China), based on a GIS. The authors added a new erosion initiation criterion to the model. The implementation of solutions of the SH model into GIS – particularly for non-trivial topographies – is a challenge since the coordinate systems often follow the topography and can not easily be converted into rectangular cartesian systems required for most GIS applications. A specific solution for a concave slope running out into a horizontal plane (WANG et al. 2004), which was used in the present thesis, will be explained in more detail in Section 4.3.

2.3 The hydraulic concept of debris flows

2.3.1 Runoff and debris flows

Water from rainfall or snowmelt not infiltrating into the soil or emerging from subsurface systems contributes to surface runoff moving downwards the steepest slope. One of the major flow variables is flow discharge Q ($m^3\ s^{-1}$), expressed as

$$Q = vA \qquad \text{Eq. 2.32,}$$

where v ($m\ s^{-1}$) is the flow velocity, and A (m^2) is the flow cross-section. v is most frequently computed using the empirical formula according to MANNING (1890) and STRICKLER (1923; compare Eq. 4.10 in Section 4.3). Surface runoff may occur in two different modes (O'BRIEN 2003):

- Overland flow (sheet flow) only occurs during or after rainfall events of very high intensity under specific conditions. The entire slope is covered by a sheet of water moving downwards;
- Channel flow is more common than overland flow. Even during intense rainfall, water usually quickly concentrates in small rills or gullies and forms ephemeral streams.

Water flow exerts a stress (the mechanical concepts are discussed below) that can lead to soil detachment (erosion). If a large amount of water moves downwards a steep channel with easily erodible soil, the sediment concentration of the flow may become high enough to convert the water flow into a debris flow (Table 2.5).

Sediment concentration C_v can be defined in several ways. The following approach will be used for the purpose of the present thesis (O'BRIEN 2003):

$$C_v = \frac{\text{volume of sediment}}{\text{volume of water} + \text{sediment}} \qquad \text{Eq. 2.33.}$$

2.3.2 Modelling erosion, transport, and deposition using GIS

General aspects

When running erosion-deposition models in GIS environments, an appropriate raster resolution has to be chosen (SCHOORL et al. 2000): using coarser resolutions the amount of erosions appears to be overestimated (an artificial mathematical effect, that is removed when increasing the spatial extent), and sedimentation appears to be underestimated (a realistic natural modelling effect). Also the temporal resolution has significant effects on the model results.

Table 2.5: Threshold sediment concentrations for various types of mass movements (from O'BRIEN 2003).

Type of movement	Sediment concentration		Flow characteristics
	by volume	by weight	
Landslide	0.65 – 0.80	0.83 – 0.91	will not flow; failure by block sliding
	0.55 – 0.65	0.76 – 0.83	block sliding failure with internal deformation during the slide
Debris flow	0.48 – 0.55	0.72 – 0.76	flow evident; slow creep sustained debris flow; plastic deformation under its own weight; cohesive; will not spread on level surface
	0.45 – 0.48	0.69 – 0.72	flow spreading on level surface; cohesive flow; some mixing
Debris flood	0.40 – 0.45	0.65 – 0.69	flow mixes easily; shows fluid properties in deformation; spreads on horizontal surface but maintains an inclined fluid surface; boulder setting; waves appear but dissipate rapidly
	0.35 – 0.40	0.59 – 0.65	marked setting of gravels and cobbles; spreading nearly complete on horizontal surface; liquid surface with two fluid phases appears; waves travel on surface
	0.30 – 0.35	0.54 – 0.59	separation of water on surface; waves travel easily; most sand and gravel has settled out and moves as bedload
	0.20 – 0.30	0.41 – 0.54	all particles resting on bed in quiescent fluid condition
Water flood	< 0.20	< 0.41	water flood with suspended load and bedload

Like slope failures, detachment by overland or channel flow is determined by mechanical laws. A water table exerts a flow shear stress τ (N m^{-2}) on the underlying soil:

$$\tau = \rho g R S \qquad \text{Eq. 2.34,}$$

where ϱ (kg m^{-3}) is the flow density, g (m s^{-2}) is the gravitational acceleration, R (m) is the hydraulic radius, and S (m m^{-1}) is the hydraulic energy gradient. Flow shear stress can be applied for deriving the stream power ω (N m^{-1} s^{-1}):

$$\omega = \tau v \qquad \text{Eq. 2.35,}$$

where v (m s^{-1}) is the flow velocity, and the effective stream power ω_{eff} (N m^{-2} s^{-1}):

$$\omega_{eff} = (\tau v)^{1.5} / d^{2/3} \qquad \text{Eq. 2.36,}$$

where d (m) is the flow depth. Some more variables do exist, consult KNAPEN et al. (2007) for a more detailed review.

There is agreement upon the fact that soil detachment is a threshold phenomenon, meaning that it only initiates if a critical value of discharge, flow shear stress, stream power, or any other variable has been exceeded, depending on the resistance of soil to detachment. The difference between the actual and the critical values of the variable is called excess, for example excess shear stress or excess stream power (KNAPEN et al. 2007), governing the magnitude of flow detachment capacity D_c (kg m^{-2} s^{-1}):

$$D_c = K_c (\tau - \tau_{cr})^b \qquad \text{Eq. 2.37,}$$

where K_c (s m^{-1}) is the concentrated flow soil erodibility, τ_{cr} (Pa) is the critical shear stress, and b is an exponent. All of the three parameters have to be derived empirically. Their variability, and therefore their spatial distribution, is extremely difficult to predict, although b is usually set to 1 (leading to a linear increase of detachment with excess shear stress). Analogous approaches do exist for other flow parameters, particularly stream power. Some authors (e.g. HAIRSINE & ROSE 1992) proposed more complex approaches.

The sediment concentration of a flow decreases its capability to detach more soil, probably due to reduced turbulence (KNAPEN et al. 2007). Some approaches do exist to account for this effect, for example:

$$D_r = D_c \left(1 - \frac{q_s}{T_c}\right) \qquad \text{Eq. 2.38,}$$

where D_r (kg m^{-2} s^{-1}) is the detachment rate, q_s is the sediment load, and T_c is the transport capacity. If D_c or D_r, respectively, become negative, deposition of the transported sediment begins.

The soil detachment and sediment transport models discussed above are based on mechanical variables like τ, but they include empirical components which have to be validated, indicating that the mechanisms behind the processes are quite complex, posing severe problems to the elaboration of fully deterministic models.

Various authors came along with predominantly or fully empirical sediment transport formulas for streams, for example SCHOKLITSCH (1962), YALIN (1963), YANG (1973), BAGNOLD (1980), LOW (1989), GOVERS (1990), RICKENMANN (1990), or ABRAHAMS et al. (2001). HESSEL & JETTEN (2007) compare some of the approaches regarding their suitability for certain flow regimes. Most of the equations were developed for channel flow except those of GOVERS (1990) and ABRAHAMS (2001), which are applicable to overland flow on gentle (<10°) slopes. Some of the equations are better suited to small grain sizes, others were developed for sand and gravel. Some include both bedload and suspended load, others only include one of the components, and they also differ in their suitability for different slope angles and sediment concentrations.

The RICKENMANN (1990) equation is best suited for relatively steep channels and high sediment loads. It only includes bedload. Since it was used for the present thesis, the approach is explained in more detail in Section 4.2 (compare Eq. 4.18 and 4.19).

2.4 Debris flow hazard and risk

2.4.1 The risk concept: hazard, exposure, and vulnerability

The discussion above referred exclusively to the natural components of debris flows. However, the purpose of all efforts to simulate and to predict the occurrence of such processes in nature is to contribute to decreasing the risk emerging from debris flows for individuals and for the society.

Figure 2.8: Risk and the society. Designed by E. Henzinger and M. Mergili.

The term *risk* is used in many fields of society and science, from gambling to traffic, from economics to natural hazards (ADAMS 1995; WISNER et al. 2004). Therefore, several definitions do exist. One of them, suitable for *risk* emerging for natural hazard, was presented by the Asian Disaster Reduction Centre ADRC (THYWISSEN 2006):

"In general, 'risk' is defined as the expectation value of losses (death, injuries, property, etc.) that would be caused by a hazard. Disaster risk can be seen as a function of the hazard, exposure and vulnerability as follows; Disaster = function(Hazard, Exposure, Vulnerability)."

where *hazard* refers to the natural component (flood, debris flow, forest fire, etc.), and *exposure* to the presence of humans or objects at the place of impact of the hazard. The term *vulnerability* has been defined in several ways, for example by WISNER et al. (2004):

"the characteristics of a person or group and their situation that influence their capacity to anticipate, cope with, resist and recover from the impact of a natural hazard"

The *risk* concept therefore contains a strong socio-economic component and is not at all restricted to the natural process (Figure 2.8).

2.4.2 The hazard: magnitude and frequency

The *hazard* connected to a process in nature (debris flow, volcanic eruption, forest fire, etc.) is primarily determined by magnitude and frequency (recurrence interval). High-magnitude events usually occur at a lower frequency than low-magnitude events. Magnitude-frequency curves are therefore a valuable tool for hazard assessment. The annuality approach, which is very common in Central Europe for dimensioning protection measures, is based on such curves.

Several studies on magnitude-frequency relationships of landslides – including debris flows – have been published (BRARDINONI & CHURCH 2004; KO KO et al. 2004; MALAMUD et al. 2004). TROPEANO & TURCONI (2004) used historical documents (newspaper articles, etc.) for a detailed study of the occurrence of different types of landslides in Italy. The findings were, among others, that more than half of the fatalities in the last 150 years (slightly above 5,000) was caused by a few major events, in particular the Vajont disaster. 6 - 23 fatalities were counted per decade, excluding major events.

2.4.3 Exposure

WEIDINGER (2007) reported about large rockslides in the Himalayas, partly in historical times, constituting a significant *hazard*. However, the events occurred in an area without human settlement and without infrastructures (they were not even observed by anybody). If happening in a populated place, an event of the same magnitude could cause the death of many thousands of people and destroy entire cities. This means that the *exposure* – and therefore also the risk – were very low, actually zero.

Figure 2.9: Debris flow blocking a road in the Ecuadorian Andes. Photo: M. Mergili, 07/2007.

Exposure has not only a spatial, but also a temporal dimension which works on different time scales. The debris flow shown in Figure 2.9 did not result in fatalities or injuries since it occurred during night, when the traffic on the road it hit was very weak. During daytime, the *exposure* would have been much higher.

2.4.4 Vulnerability

Whilst the concept of *exposure* appears pretty clear, this is not the case with the *vulnerability* concept, which has been defined in different ways leading to some confusion in the literature (compare WISNER et al. 2004 for a list of references). One definition has been given above.

2.4.5 Debris flow risk and global change

When discussing the impacts of global change on debris flow *risk* (and *risk* due to mass movements in general), it is essential not only to consider climate change and its influence on the *hazard*, but also and particularly human-induced changes like the expansion of settlements on *exposure* and *vulnerability*.

The local and regional responses of climatically driven natural hazards to climate change may be manifold, but are in detail relatively difficult to predict quantitatively (BUMA & DEHN 1998; BUMA 2000). The retreat of permafrost (e.g. TROMBOTTO et al. 1997 for the Río Blanco Basin in the Province of Mendoza, Argentina, SATTLER et al. 2007 for a study area in the Alps) and glaciers (VILÍMEK et al. 2005 investigated the role of glacial retreat on hazards regarding a lake in the Cordillera Blanca, Peru) may play a major role in the future as large masses of unstable material will become susceptible to erosion and failure.

However, regarding mass movements, the impacts of settlement expansion on *exposure* and of changing socio-economic systems on *vulnerability* are probably as least as important as the influence of climate change on the *hazard*.

3 Research area

3.1 General aspects

The research area covers the international bioceanic road corridor from the Atlantic coast in the Buenos Aires area to the Pacific coast at Valparaíso, in its section between Mendoza (Argentina) and Los Andes (Vth Region, Chile). The corridor roughly constitutes a E-W-transect through the Andes Mountain System following the major valleys (Río Mendoza valley in Argentina and the upper part of the Río Aconcagua valley in Chile). Viewed from E, the transect starts at the pediment SW of the city of Mendoza, cuts through the Precordillera Mendocina and the Cordillera Frontal in Argentina, crosses the Cordillera Principal at the Argentinian – Chilean border and descends steeply to the Aconcagua basin to the W. Figure 3.1 represents a map and Figure 3.2 a longitudinal section through the research area.

The same transect is located along a gradient from desert climate and ecosystems to mediterranean-type climate and ecosystems. This pattern is superimposed by a pronounced altitudinal gradient, ranging from 500 m asl in the Aconcagua Basin to almost 7000 m asl in the Cordillera Principal (Cerro Aconcagua: 6,962 m). The mountainous terrain implies small-scaled patterns of terrain properties (slope, aspect, hydrologic parameters) as well as intensity and duration of solar irradiation. The combination of all these factors leads to a highly complex mosaic of ecosystems on different spatial scales. Three broad vegetation types are aligned in a parallel way from W to E (PARUELO et al. 2001): Mediterranean shrublands, Andean steppes and Monte shrublands. Each type (but the Mediterranean scrublands in particular) shows pronounced internal variations according to the regional and local climate, slope, substrate, mechanical stability, and the intensity of anthropozoogenic use.

The area is very sparsely populated, except for the lower section of the upper Aconcagua valley.

3.2 Geology

3.2.1 The research area in the global geological system

The earth surface is a complex system of crust plates separated (or connected) along various types of transition zones. The plates may either consist of thick, but relatively light continental crust, or of thin, heavier oceanic crust, or they may include both types. The transition between the plates may form diverging margins (new crust is produced at the margin of the plates), converging margins (crust is removed by subduction of one plate beneath another), or transform faults. Diverging margins usually occur at the ocean floor as the thin crust there is more easily penetrable for the magma. Converging margins may include two oceanic plates (forming island arcs), but frequently they occur at the edges of continents, where the heavier oceanic crust is subducted beneath the lighter continental crust, forming a trench and a mountain range. The global budget of crust production and destruction is balanced over any time span, but the size of single oceans or continents increases or declines (PRESS et al. 2003). The size of Atlantic Ocean, for example, increases in size as it contains a huge diverging margin and hardly any converging ones. The size of the Pacific Ocean, in contrast, declines. Though it contains some diverging margins, the whole edge of the Ocean itself consists of a huge system of converging plate margins, leading to the formation of island arcs and huge mountain ranges, showing pronounced seismic and volcanic activities (Figure 3.3). Therefore the margin of the Pacific Ocean is called "ring of fire". The Andes Mountain System, ranging from Venezuela to the Antarctic Peninsula, is one of the core parts of this "ring of fire", culminating in the research area of the present study.

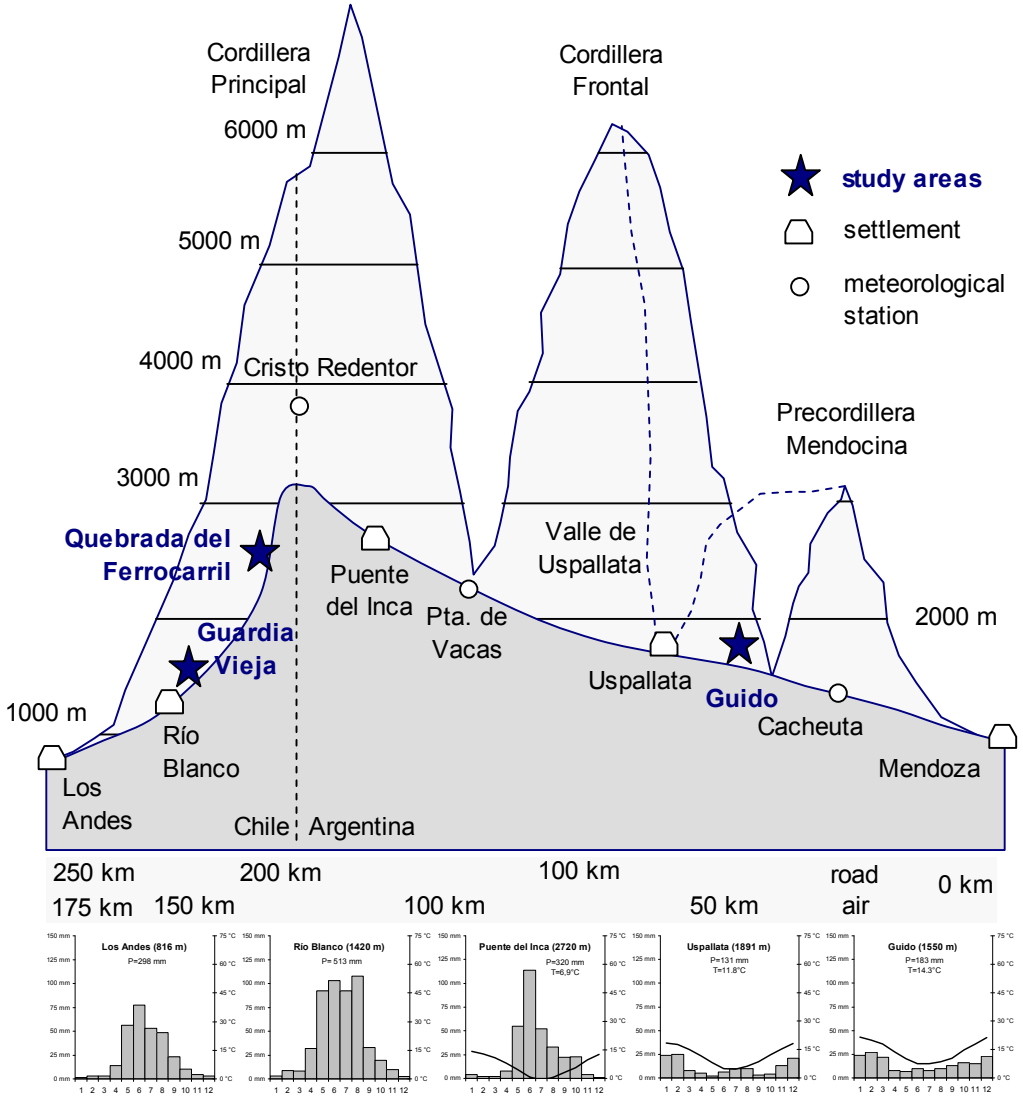

Figure 3.1 (top): Map of the study area, Designed by M. Mergili, relief derived from SRTM data (CIAT 2004).
Figure 3.2 (bottom): Cross section through the research area and climate diagrams. Profile derived from SRTM data (CIAT 2004); for sources of meteorological data compare Section 4.1.6.

Figure 3.3: The Volcán Láscar in Northern Chile is an evidence for the activity of the so-called "ring of fire". Photo: M. Mergili, 09/2006.

3.2.2 Geotectonic units in the research area

The research area contains a wide variety of rock types of sedimentary, plutonic and volcanic origin, having developed since the lower Paleozoic. Four major units may be distinguished: the Precordillera Mendocina, the Uspallata valley, the Cordillera Frontal, and the Cordillera Principal. All of them developed in their own way, anyway sharing some common features.

3.2.3 Precordillera Mendocina, Valle Uspallata and Cordillera Frontal

The areas today known as Precordillera Mendocina (Figure 3.4), Valle de Uspallata and Cordillera Frontal once formed a large continuous peneplain (Figure 3.5). The basement of the Precordillera Mendocina and the Cordillera Frontal consists of sedimentary and metamorphic rocks of varying characteristics and origin: schists, wackes, amphibolites, limestones, diabases, peridotites, and talc from the Cambrian and Ordovician are present as well as Devonian sandstones and claystones (FERNÁNDEZ GARCÍA & MIKKAN 2003; MOREIRAS 2004b).

Folding and uplift took place already in the Paleozoic, maybe with the Caledonian, but definitely with the Variscian orogenetic period between the Upper Devonian and the beginning Mesozoic. A Permo-Triassic volcanoclastic succession accompanied the orogenesis, producing a very heterogeneous formation known as Choiyoi Group. It was intruded by a granitic body during the Triassic – dated with 244±10 Ma(K/Ar) – today outcropping in the Guido area (FERNÁNDEZ GARCÍA & MIKKAN 2003; MOREIRAS 2004b; compare Figure 3.33).

The following geological stages were characterized by changing terrestrial sedimentation, intrusive bodies and volcanic deposits of varying characteristics. The uplift to the current position began in the lower Eocene (Precordillera Mendocina), and in the upper Pliocene (Cordillera Frontal), respectively. In the case of the Cordillera Frontal, the major share of the uplift took place until the lower Pleistocene and is still an ongoing process, but at a slower rate (FERNÁNDEZ GARCÍA & MIKKAN 2003).

Figure 3.4 (top): The Precordillera Mendocina close to Villavicencio. Photo: M. Mergili, 04/2006.
Figure 3.5 (bottom): Aerial view of the Cordillera Frontal and the Río Mendoza valley. The remnants of old land surfaces at the top are clearly visible. Photo: M. Mergili, 04/2006.

The Precordillera Mendocina and the Cordillera Frontal are separated by a pronounced tectonic depression of about 1,800 m asl, named after the village of Uspallata (Figure 3.6). Its base is of Paleozoic age, with origins tightly coupled to the rocks building up the Precordillera and the Cordillera Frontal. Separated from these ranges by tectonic faults, the valley was filled with Mesozoic and Cenozoic sediments (FERNÁNDEZ GARCÍA & MIKKAN 2003). The same tectonic fault continues southwards along the Mendoza valley, separating Precordillera Mendocina and Cordillera Frontal (Figure 3.7).

Whilst the Precordillera culminates at 3,500 m asl, the maximum elevation of the Cordillera Frontal exceeds 6,000 m in the Cordillera del del Tigre (N of Mendoza valley), and 5,500 m in the Cordón del Plata (S of Mendoza valley).

Figure 3.6 (top): Valle Uspallata and Cordillera Frontal, seen from the top of the Precordillera Mendocina (Cruz de Paramillo). In the background Cerro Aconcagua (Cordillera Prncipal). Photo: M. Mergili, 04/2006.
Figure 3.7 (bottom): The Cordillera Frontal is built up by a large variety of rock types. Photo: M. Mergili, 11/2006.

3.2.4 Cordillera Principal

The rocks forming the Cordillera Principal are generally younger than those building up the Cordillera Frontal and the Precordillera Mendocina. They consist of Mesozoic sedimentary rocks, mainly gypsum and carbonaceous rocks deposited in various environments during the Jurassic and the Cretaceous, intermixed with a complex system of intrusive and volcanic rocks with ages ranging from the Mesozoic to the Quaternary. The most common outcropping volcanic rocks are of andesitic chemistry.

The geotectonic development of the Cordillera Principal is interpreted as follows (FERNÁNDEZ GARCÍA & MIKKAN 2003):

(1) The pre-andine basement shows the same characteristics and is closely related to the Cordillera Frontal;

(2) the geoliminar stage (medium Jurassic up to medium Cretaceous) was characterized by the presence of a geosynclinal-like structure, which, however, lacked some of the typical features of other geosynclinals. One may distinguish an internal W domain with intense volcanic activities, and an external E domain with predominant terrestrial, but also marine sedimentation. Therefore, in general, volcanic rocks are more common in the W part (Chile), whilst sedimentary rocks predominate in the E part (Argentina) of the Cordillera Principal;

(3) during the late liminar stage (upper Cretaceous to Pliocene) the major tectonic processes forming the S Andes took place. Five different orogenetic movements may be distinguished, while

(4) the post-liminar stage (Quaternary) is characterized by glacial and volcanic processes and deposits. The large volcanoes S of the Mendoza and Aconcagua valleys, like Tupungato, Marmolejo or Maipó, originate from this stage, which is of less importance in the research area itself.

The evolution of the Cordillera Principal is an ongoing process, expressed in numerous seismic events as well as volcanic and geothermal activities. The highest peak in the Southern hemisphere, Cerro Aconcagua (Figure 3.8), is located in the Cordillera Principal. RAMOS (1996) provides a detailed discussion of the geology of the Aconcagua area.

Figure 3.8: Aerial view of Cerro Aconcagua, the highest peak of the Americas (6,962 m). Photo: M. Mergili, 09/2006.

3.3 Climate

3.3.1 The research area in the global climate system

In order to understand the climatic conditions in the research area it is useful first to have a look at its position in the global climate system (Figure 3.9).

Due to the gradient of the radiation budget from the meteorological equator to the poles, the troposphere is warmer at the equator and therefore less dense, leading to a higher position of the tropopause there, compared to the poles where the air is colder and therefore more compressed. This situation implies a density gradient from the equator to the poles in the upper troposphere, leading to a strong poleward wind system called jet-streams. In the mid-latitudes the jet-streams are forced westwards by the Coriolis effect, preventing them from reaching the poles, instead creating a zone of prevailing westerly winds in the mid-latitudes, which also affects the lower troposphere. This constellation leads to the phenomenon that the W parts of the continents at the corresponding latitudes receive plenty of precipitation all over the year. The farther eastwards one moves, or the higher the

mountains to the W are, the more limited is the precipitation (SCHÖNWIESE 1994).

Besides this system of westerly winds, another system exists in between, around the meteorological equator. The very warm air directly at the meteorological equator rises up during noon and afternoon, cooling down and producing the zenithal rainfall typical for the inner tropics, if there is sufficient moisture available. The pressure deficit (low pressure area) in the lower troposphere triggers winds from N and S, the so-called tradewinds. As they converge at the meteorological equator, this area is called Inner Tropical Convergence Zone (ITCZ). All these processes result in a downward air movement and the generation of very persistent high pressure cells in the outer tropics, and to very hot and dry conditions there (SCHÖNWIESE 1994).

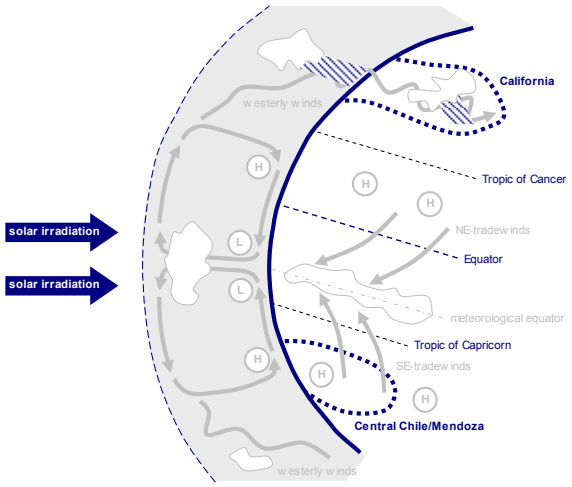

Figure 3.9: Sketch of the global climate system. Designed by M. Mergili.

The ITCZ, and the entire global climate system, oscillate at a seasonal frequency. This means that the areas around the tropic circles receive a lot of zenithal rainfall during summer whilst they are located within the high pressure cells in winter. The areas in between the mid latitudes and the outer tropics receive westerly winds during winter, while they are located in the high pressure cells during summer (SCHÖNWIESE 1994).

The processes discussed above explain the general climatic patterns in the research area, located within the zone of westerly winds during winter, and in the zone of tradewinds and descendant air movement during summer. The W part therefore receives winter rainfall from the moist pacific air masses whilst the summers are dry. The E part is rather arid during the whole year. In winter, the moist air masses from the Pacific Ocean loose their water content over the Andes Mountain System and reach Mendoza as the foehn-like so-called Zonda wind (SCHÖNWIESE 1994; FERNÁNDEZ-GARCÍA & MIKKAN 2003). There are, however, several local effects, particularly that of elevation, modifying the patterns imposed by the rules of the global climate system

3.3.2 A climatic transect from Mendoza to Los Andes

The city of Mendoza receives an annual precipitation of about 200 mm. When moving towards the E slopes of the Precordillera Mendocina, vegetation indicates an increase in precipitation, but a rain gauge is lacking on these slopes. The farther moving westwards in the valleys, the less precipitation occurs, indicated by the gauges of Cacheuta (211 mm annual mean), Guido (202 mm), and then Uspallata in the rain shade of the Precordillera Mendocina with 116 mm only (compare Figure 3.2). The rain shade effect of the Precordillera indicates that the moisture comes predominantly from the SE tradewinds. Much of the precipitation is caused by convective rainfall events mainly during summer.

The rain gauge in Punta de Vacas receives a mean annual sum of 130 mm. Though located E of the main range of the Andes, precipitation shows a clear winter maximum that indicates a predominance of moist air masses from the W. Puente del Inca, already located in the Cordillera Principal close to the border to Chile, receives 294 mm, and Cristo Redentor at the international border even 359 mm. When crossing the border, the seasonal distribution of the precipitation remains clearly dominated by a winter maximum and at the mid altitudes of the W slope of the Andes, where moist winterly air masses hit the mountains, an increase in winter precipitation can be observed (Río Blanco station: 572 mm). A significant decrease over a short distance occurs directly westwards and Los Andes, located in a basin at the foothills of the Andes, receives much less precipitation (288 mm) due to the rain shade effect of the Coast Ranges. Viña del Mar and Valparaíso directly at the coast of the Pacific Ocean receive about 500 mm.

The predominance of winter precipitation in the high-altitude areas implies that a considerable share of annual precipitation occurs as snowfall. FERNÁNDEZ-GARCÍA & MIKKAN (2003) report an average annual duration of snow cover of 41 days for Puente del Inca and 64 days for Cristo Redentor. Particularly at the Cristo Redentor station at 3,829 m, snow fall can occur at any time of the year. The presence of snow over a certain period of the year leads to frequent obstructions of the international road traffic between Argentina and Chile on the one hand and to a certain potential of winter tourism on the other hand (compare Section 3.6).

For the sources of precipitation data please compare Section 4.1.6. The locations of the rain gauges are shown in the Figures 3.2 and 4.5.

3.3.3 The influence of the ENSO phenomenon

ENSO (El Niño – Southern Oscillation) stands for a well-known phenomenon that includes weakening

and strengthening of the Humboldt current due to changes in the thermohaline circulation system of the South Pacific Ocean as well as the related climatic consequences. There is no place here for looking at the background of ENSO – it has to be referred to the literature (e.g. DIAZ & MARKGRAF 2000). The climatic manifestations of the phenomenon, however, have to be discussed shortly as they are important for the topic of the present thesis.

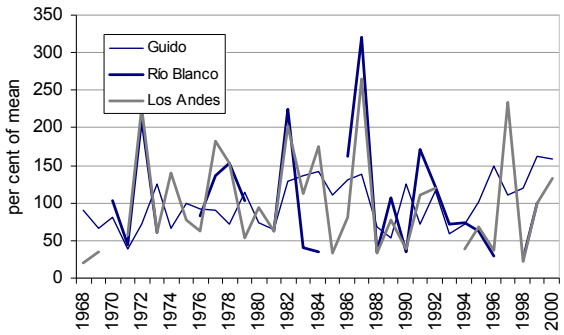

Figure 3.10: Annual variability of precipitation recorded at selected rain gauges within the research area. The peaks at Río Blanco and Los Andes coincide with El Niño years. The data sources described in Section 4.1.6 were used.

Weakening of the Humboldt Current and the connected Upwelling leads to increased movement of air masses from the Pacific Ocean to the South American continent (SCHÖNWIESE 1994). Such events occur every few years (but on irregular intervals) and are called El Niño. These are the only years when the Atacama desert farther N receives a significant amount of rainfall. In Central Chile precipitation in El Niño years may exceed 300% of the annual means (compare Figure 3.10). In 1987, an extreme El Niño year, an annual precipitation of 1775 m was recorded at the Río Blanco rain gauge in the upper Aconcagua valley (average: 572 mm), more than 1200 mm fell during July and August only, causing major damages due to inundations in the lower Aconcagua valley, and due to a debris flow that is subject of the present thesis (Guardia Vieja study area, compare below). The effect of El Niño is also recordable in the upper section of the Mendoza valley (parts of the Cordillera Frontal and the Cordillera Principal), whilst it has no influence in the Precordillera (MOREIRAS 2005). The precipitation patterns recorded at the Guido station do not indicate an influence of El Niño (compare Figure 3.10).

Years with strengthening of the Humboldt current and decreased precipitation do occur as the contrary of El Niño. This phenomenon is called La Niña (SCHÖNWIESE 1994).

3.4 Geomorphology

The landscape of the research area has been shaped over geological timescales by the interaction of a large array of geomorphological processes, triggered and constrained by the underlying geology and the prevailing climates of different periods. Some of the processes were only acting during the past, others are still going on. The dominant types of processes shaping the landscape are fluviatile, glacial, periglacial and gravitative as well as various processes intermediate between these types. The dominant large-scale landforms are deeply incised river valleys following tectonic faults (compare Figures 3.5 and 3.7).

3.4.1 Fluviatile processes and landforms

The today's shape of the valleys is largely a consequence of the interaction of different types of fluviatile processes, often in connection with other forces. The most striking feature of the Mendoza valley are the almost continuous river terraces between Punta de Vacas and the Potrerillos area (Figure 3.11). FERNÁNDEZ GARCÍA & MIKKAN 2003 use the term fluvio-glacial for the evolution of the terraces. Although this term is commonly used in another context, the terraces are certainly related to glaciations in the Pleistocene. The presence of glaciers in the headwaters of the basin led to an increased supply of sediment that was deposited in the lower parts of the valley. After the glaciers had retreated, the river cut into the terraces until reaching an equilibrium.

Figure 3.11: River terraces in the Mendoza valley. Photo: M. Mergili, 04/2006.

Aside from the main valleys, the permanent, periodic and episodic streams descending from the lateral valleys have incised gullies and built up alluvial fans of different sizes (FERNÁNDEZ GARCÍA & MIKKAN 2003), often together with other types of processes, for example debris flows.

3.4.2 Glacial processes and landforms

Due to the rather continental climatic conditions, today's glaciation of the Andes is poor at the latitude of Mendoza and largely restricted to peaks exceeding 5,500 to 6,000 m (Figure 3.12). Two major glacial advances during the Pleistocene are documented for the

Mendoza valley (FERNÁNDEZ GARCÍA & MIKKAN 2003):

- the first advance occurred in the time span between 200,000 and 120,000 years BP, corresponding to the Illinoian glaciation in North America. Moraines are conserved downwards until Punta de Vacas. This glaciation caused the U-shape of the uppermost Mendoza valley (Figure 3.13).
- The second glaciation was of much smaller extent. Moraines are located in the area of Puente del Inca, but the glaciers from the side valleys did not unify in the main valley. The hilly terrain of Horcones (Figure 3.14) was formerly considered as moraine from this glaciation, but reinterpreted later as the deposit of a mass movement.

A detailed study on quaternary glaciations in the Mendoza valley was carried out by ESPIZÚA (1993). CORTE & ESPIZÚA (1981) compiled an inventory of the glaciers in the catchment of the Río Mendoza.

Figure 3.12: The Cordillera Principal is poorly glaciated. Only the highest peaks, like the Nevado del Plomo (6,050 m) carry glaciers of notable sizes. Photo: M. Mergili, 04/2006.

Regarding the Aconcagua valley, there is some controversy regarding the interpretation of landforms as moraines or as deposits from mass movements (CAVIEDES 1972; ABELE 1984). The lowermost deposits most likely constituting moraines are located directly downstream of Guardia Vieja at about 1,500 m asl (FERNÁNDEZ GARCÍA & MIKKAN 2003) or near to Salto del Soldado at 1,300 m asl (CORTE & ESPIZÚA 1981).

3.4.3 Periglacial processes and landforms

Periglacial processes play a major role in the high Andes of Mendoza. Particularly rock glaciers are common since this type of landform is favoured by arid or semi-arid conditions compared to real glaciers (Figure 3.15). TROMBOTTO et al. (1997) reported about the monitoring of mountain permafrost in the Río Blanco Basin (S of the Mendoza valley). 60 % of the basin can be considered as periglacial. Rock glaciers are the most important geomorphological features, but the lowermost occurrences are not in equilibrium with the current climate. Also cryoplanation is present in the basin.

Figure 3.13 (top): The U-shaped uppermost section of the Río Mendoza valley, seen from Paso Bermejo. Photo: M. Mergili, 04/2006.
Figure 3.14 (middle): Horcones and Cero Aconcagua. Photo: M. Mergili, 02/2005.
Figure 3.15 (bottom): Rock glaciers in the Cordillera Principal – seen form Paso Bermejo. Photo: M. Mergili, 04/2006.

3.4.4 Gravitative processes and landforms

The broad-scale landforms of the Mendoza and Aconcagua valleys have been shaped primarily by glacial and fluviatile processes. Many of the medium-scale and fine-scale landforms are derived from landslides of different types and scales. Some large rockslides and rock avalanches rushed into the valleys during the Pleistocene and formed dams, partly leading to the filling of lakes (FERNÁNDEZ GARCÍA & MIKKAN 2003):

- Near Polvaredas in the Mendoza valley, two large rockslides – one from each side – dammed the

valley, leading to the development of a lake, the sediments of which are still visible upstream. It is not yet clear when the slides occurred, and there is some controversy about the question which of them occurred first (Figure 3.16);

- the village of Las Cuevas was built directly adjacent to the deposit of a rock avalanche (Figure 3.17);
- the Laguna del Inca (Portillo, uppermost part of the Aconcagua valley) was dammed by a large rock avalanche. The deposits on which the Hotel was built also cover part of the valley below (Figure 3.18);
- the Salto del Soldado barrier downstream of Riecillos is also the result of a large rockslide (Figure 3.19).

Concerning the latter two cases – and landforms in the Aconcagua valley in general – there is some controversy in the literature whether the deposits constitute landslide deposits or till. CAVIEDES (1972) interpreted many of the deposits as till, but currently there is much more accordance with ABELE (1984) who interpreted them as landslide deposits.

Figure 3.16: Two merging landslide deposits near Polvaredas. Photo: M. Mergili, 10/2006.

Whilst the large landslides described above had a strong influence on the landforms on a local scale and, if they dammed a lake, some kilometres upstream, the numerous small events of landslides, rock falls and debris flows occurring at comparatively high frequency and in many places probably exert a larger influence over the entire valley. MOREIRAS (2004a; 2004b; 2005) prepared a landslide inventory for a 30 km section of the Mendoza valley and collected data about historical events for investigating the major conditioning factors and triggering thresholds for landslides. She included different types of landslides (in particular rock falls, slides and debris flows) in her studies. Seismicity and heavy rainfall were mentioned as the major triggering factors for landslides in this region. Most rainfall-triggered landslide events occur with daily rainfall values of 6.4 to 12.9 mm only.

Figure 3.17 (top): Rock avalanche at Las Cuevas. Photo: M. Mergili, 04/2006.
Figure 3.18 (middle): Laguna del Inca and Portillo. The hotel in the background is built on the deposits of a rock avalanche. Photo: M. Mergili, 05/2006.
Figure 3.19 (bottom): Salto del Soldado, the deposit of a large rockslide. Photo: M. Mergili, 10/2006.

Regarding lithology, three classes were distinguished, one including granites and volcanic rocks (Choiyoi group, rhyolitic porphyry), one Carboniferous and Paleozoic rocks, and the third class including Triassic volcanic and sedimentary as well as Tertiary sedimentary rocks. The Choiyoi group produced half of all landslides in the inventory, partly due to the fact that it covers 54% of the study area, partly due to the presence of weak volcanites prone to instability. Also weak sedimentary rocks are rather susceptible to landslides. Jointed granites particularly tend to rock falls. Unstable accumulation of granitic and porphyric debris has led to a considerable tendency towards debris flows. Also metamorphous rocks have produced scree slopes prone to small debris flows. Jointing of the porphyry and granitic rocks, combined with tec-

tonic activities, leads to the formation of sliding surfaces, also promoting the accumulation of water.

Regarding slope, most of the landslides occurred on slopes steeper than 30° (85% in the Cordillera Frontal, 77% in the Precordillera). However, debris flows in particular also occurred on slopes between 15 and 30°. Landslide susceptibility potentially increases with steeper slopes, but in detail the relationships are more complex, as fall processes tend to occur on steeper slopes whilst flow processes are usually associated with intermediate slopes and small-scale debris flows and alluvial plain processes occur on the least steep lower slopes. Particularly for the Cordillera Frontal not only slope angle, but also aspect (as a surrogate for solar irradiation and therefore the moisture budget) plays a role, as landslide susceptibility was markedly higher on S-facing slopes with more snow and moister conditions in general.

MOREIRAS grouped the different combinations of lithology and slope classes into four categories of landslide susceptibility (high, moderate, low, very low), using the landslide inventory as reference. The map was validated using a historical archive of damages to the road and the railroad for the last 50 years. 83 % of the landslides were located within the high susceptibility zone, 14 % were within the moderate susceptibility zone.

Most of the Cordillera Frontal portion of the study area was located within the high to moderate susceptibility zones, mainly due to steeper slopes, higher abundance of rock outcrops, and the presence of permafrost above 3,200 m. The high susceptibility zone was particularly associated with steep slopes and permafrost (e.g. the front of rock glaciers), talus cones or alluvial fans. The moderate (associated with alluvial fans) to low susceptibility zones prevailed in the Precordillera. Rock falls and debris flows were the most frequent types of landslides there.

Besides the investigations by MOREIRAS, some more authors have dealt with mass movements in the Mendoza valley, regarding specific prehistoric events (EZPIZÚA & BENGOCHEA 1991) as well as recent slope dynamics (MIKKAN 1997) and risk zonations (ESPIZÚA et al. 1993). Studies on mass movements in the upper portion of the valley (Puente del Inca area) were carried out within the map:gac project (Multinational Andean Project: Geosciences for Andean Communities; e.g. FAUQUÉ et al. 2004; HERMANNS 2004).

Reports and publications from the Chilean Geological Survey do exist dealing with debris flows interfering with the international road in the Aconcagua valley (HAUSER 2000a; 2000b; 2005; Figure 3.20; Section 3.7.1). A more general introduction to hazards along the course of the valley is given by FERNÁNDEZ GARCÍA & MIKKAN (2003).

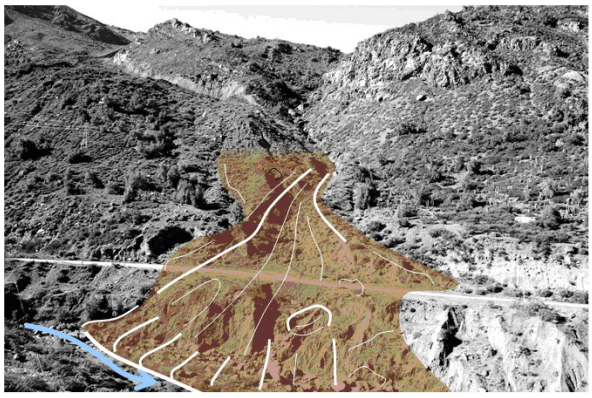

Figure 3.20: Sketch of debris flow blocking the old international road downstream of Guardia Vieja in August 1987. Background photo: M. Mergili, 09/2006; drawing by M. Mergili according to HAUSER (2000a).

3.5 Ecosystems

The Andes Mountain System plays an important role for the division of climate zones. Closely connected to the climatic regimes, the same is true for the spatial distribution of the broad-scale ecosystems.

3.5.1 Mediterranean ecosystems of Central Chile

The W side of the mountains, receiving precipitation during winter, but hardly during summer, supports a mediterranean shrubland, analogous to other regions in the world located at comparable latitudes at the W side of the continents. The ecosystems of Central and S California, of Mediterranean Europe, of the Cape region of South Africa, and of parts of SW and S Australia share many features with the natural ecosystems of Central Chile (DALLMAN 1998; BRECKLE 2002). The most important of these features is the abundance of shrubs and small trees with hard (sclerophyllous) evergreen leaves that may withstand the summerly drought and with deep and extensive root systems able to explore the sparse resources of water during summer.

Figure 3.21: Matorral at the slopes of the Aconcagua valley with the succulent *Trichocereus chilensis* in the foreground. Photo: M. Mergili, 04/2006.

The Mediterranean forests and shrublands of Chile extend from 32° to 37° S and are concentrated in the coastal ranges, the central valley and the Andean foothills, where they reach an altitude of slightly more than 1000 m asl. The major structural elements of the scrubland (matorral) are sclerophyllous shrubs and small trees (e.g. *Colliguaya odorifera*, *Cryptocarya alba*, *Lithraea caustica*, *Peumus boldus*, *Quillaja saponaria*), spiny, sometimes drought-deciduous shrubs (*Acacia caven*, *Trevoa trinervis*), and succulents (*Puya bertheroniana*, *Trichocereus chilensis*). The herbaceous undergrowth may attain 40 % ground cover and contains many geophytes. Lianas are more common in Central Chile than in other mediterranean-type ecosystems of the world. While natural wildfires are common in all the other mediterranean regions worldwide, they play only a minor role in Central Chile due to the lack of summer lightning. Man-made fires, however, play a major role. Towards S, with increasing precipitation, the upper edge of the matorral is more and more joined by coniferous trees, which are all relictual (*Austrocedrus chilensis*, *Araucaria araucana*) and deciduous forest elements of the genus *Nothofagus*.

The so-called Matorral Esclerófilo Andino (DEL CAMPO TELLO et al. 2001) is of interest for the present study. It occupies the lower slopes and valleys of the Andes (Figure 3.21) and can be subdivided into at least seven communities, with continuous transitions in between. Some of the communities share some features with the high-Andean steppes (see below).

3.5.2 Semidesert ecosystems of Central Argentina (Monte shrubland)

The E side ecosystems, receiving a small share of the winter precipitation W of Uspallata, have to show much better adaptations to the drought than those on the W side, since water is a sparse resource over the entire year. The most obvious indicator of a morphological adaptation is the wide spacing of the shrubs, indicating the tough competition for water carried out by the deep and extensive root systems. The shrubby morphology of most of the plants is an adaptation to the lack of available water, too, as the compact growth form helps to conserve moisture and to keep the humidity within the canopy high (the same is true with heat in high mountain shrubs). The leaves of many of the shrubs are sclerophyllous, but can be shed in the case of extreme drought periods. There are striking similarities between the semidesert ecosystems of SW North America and the valleys and E forelands of the Central Andes. Besides their ecological similarity, they also share the same dominant species, *Larrea divaricata* – a very particular phenomenon over such distances. Some other species, like *Cercidium floridum* in North America and *Cercidium praecox* in Argentina, are very closely related (BRECKLE 2002).

The ecosystem diversity of the so-called Monte shrub-steppe is much less pronounced than in the Chilean matorral. The forelands, as far as they are not converted into crop cultivations, often constitute uniform landscapes of sparsely spaced shrubs of *Larrea divaricata* (jarilla), *L. cuneifolia* and *L. nitida* (Figure 3.22). *Zucchagnia punctata* is common, too. *L. nitida* requires most moisture and is therefore restricted to less arid zones and to water courses. *L. divaricata* largely occupies flood plains and alluvial fans and *L. cuneifolia* is most common on steeper slopes (WALTER & BRECKLE 1984).

Geo- and Therophytes, making use of the temporarily concentrated abundance of water, are common in the mediterranean and in the semidesert ecosystems (BRECKLE 2002). The same is true for succulent plants with the ability to store water in their tissues, represented by the Cactaceae and the Bromeliaceae families in South America.

Figure 3.22 (top): Monte shrubland in the Uspallata valley, built up by different species of *Larrea*. Photo: M. Mergili, 04/2006.
Figure 3.23 (bottom): High-Andean steppe in Horcones with tussock grasses and dwarf shrubs (background: Cerro Aconcagua). Photo: M. Mergili, 02/2005.

3.5.3 High mountain ecosystems

High mountain ecosystems in the Central Andes have to face cold temperatures during night and winter as well as drought due to little precipitation and high potential evapotranspiration during the day. Tussock grasses and cushion plants are best adapted to these conditions, resembling the Puna vegetation farther N

(compare BRECKLE 2002; Figure 3.23). The Estepa Alto-Andina de la Cordillera de Santiago (DEL CAMPO TELLO et al. 2001) occupies the belt from the upper edge of the matorral up to the upper vegetation limit beyond 3000 m asl. It is associated with steep, rocky terrain, high solar irradiation, high temperature differences, lack of moisture, and strong winds. Since it is difficult for plants to establish and to survive under these conditions, some areas have a desert-like appearance. Most plants are xerophytic, many have compact growth forms (cushions or tussocks) in order to minimize the contact with the atmosphere. At least five communities may be distinguished (DEL CAMPO TELLO et al. 2001). On the E slope of the Andes, a continuous transition from the High-Andean steppes to the Monte shrubland can be observed.

3.6 Economic activities and land use

The economic activities in the research area are largely concentrated along linear structures (traffic and power lines) and some few spots. The remaining area is largely not or only extensively used. The only larger village is Uspallata (8,000 inhabitants approximately). Small villages are (from E to W): Potrerillos, Polvaredas, Punta de Vacas, Penitentes, Puente del Inca, Horcones, Las Cuevas, Caracoles, Portillo, Guardia Vieja, Río Blanco and Vilcuya. There is some dispersed settlement in the lower part of the Chilean side. The closest larger centres are Mendoza in Argentina, and Santiago de Chile in Chile.

3.6.1 Traffic

The international road from Mendoza to Los Andes (Ruta 7 in Argentina, Ruta 60 in Chile) is the most distinctive anthropogenic feature in the valley, carrying considerable quantities of truck and car traffic crossing the border between the two countries or accessing the touristic centres on both sides. The culmination point of the highway is the Cristo Redentor statue at 3829 m asl, but since 1980 a 3 km long tunnel exists at an elevation of 3000 m. The road is currently (2007) running as two-lane highway over most of its length (Figure 3.24). A large share of the activities in the valleys depends on the international traffic:

- the customs: there is one big centre serving for the border crossing formalities on each side of the border, one in Horcones (Argentina) and one in Caracoles (Chile);
- the highway patrol, controlling the truck traffic;
- some basic touristic infrastructures for the truck drivers;
- and the road maintenance centre in Uspallata (Dirección de Vialidad).

There used to be a railroad connection, too, but it was abandoned in the 1980s with the general decline of railway traffic in South America (Figure 3.25). There are, however, plans to reestablish the railway line between the two countries. The population of some villages supported by the railroad from Argentina to Chile declined rapidly after the traffic was suspended.

Figure 3.24 (top): Intense truck traffic near Portillo (Aconcagua valley). Photo: M. Mergili, 04/2006.
Figure 3.25 (bottom): The abandoned railway station of Guido (Aconcagua valley). Photo: M. Mergili, 10/2006.

3.6.2 Tourism

The research area represents a zone of great scenery, including the highest mountain of the world out of Asia and bearing possibilities for various outdoor activities both in summer and in winter. This kind of preconditions implies a considerable potential for touristic use which, up to now, has only partly been explored. Various types of activities are offered by agencies or can be followed individually:

- the classical sightseeing tourism is predominantly followed on the Argentinian side, with Mendoza as the base. It follows linear structures (the road) with some spots, usually at Uspallata, Puente del Inca, Horcones (Aconcagua view), Las Cuevas, and Cristo Redentor. It supports the local gastronomy at the touristic spots and the tourism industry in Mendoza city or in Uspallata;
- trekking is done in the Aconcagua National Park, either in the vicinity of the mountain, or with the purpose of climbing the mountain itself. A fee is collected by the National Park Administration;

- rafting on Mendoza river is popular in the Precordillera section of the area, upstream of the Potrerillos dam. The activity is operated by specialized local agencies;
- skiing is possible during the winter months (June to August/September) in the higher parts of the Cordillera Principal. The activities are concentrated around Penitentes (Argentina) and Portillo (Chile). Skiing is an upper class activity in South America which, in contrast to the Eastern Alps, is not embedded in the local tradition, but is based on one or more hotels of international style (Portillo; compare Figure 3.18) with the profit being invested in other places;
- spa tourism is possible at some spots (particularly Cacheuta) of the Río Mendoza valley, where thermal sources are present. There used to be a hotel in Puente del Inca which was propelled into the Mendoza river by a landside. Bathing in the thermal pools of Puente del Inca was possible until a few years ago, when they were closed in order to protect the natural bridge (Figure 3.26). A remainder of a former spa tourism is the Gran Hotel in Uspallata.

3.6.3 Exploitation of natural resources

Agriculture plays a minor role in the research area. Intensive farming depends on irrigation and is only carried out around Los Andes and in the immediate vicinity of settled places along the course of the valleys. Extensive cattle grazing run by the villagers is common along the majority of the valleys, except for the highest portions. Mining plays a certain role in the Aconcagua valley (particularly in the Río Blanco area). The most valuable resource provided by the mountains besides the scenery serving for a touristic use, however, is water. The Andes Mountain System provides the water allowing the existence of Mendoza city and the flourishing agriculture in the lower Aconcagua valley. The resource water is also used for the production of electricity (Potrerillos dam, Figure 3.27).

Figure 3.26: The thermal pools of Puente del Inca were closed for protecting the natural bridge. Photo: M. Mergili, 02/2005.

Figure 3.27: The Potrerillos reservoir. Photo: M. Mergili, 04/2006.

Summarized, the economy in the area is largely supported by activities serving for overcoming the mountains as barrier (traffic) on the one hand, and by making use of resources only provided by the mountains (tourism, mining) on the other hand. Economic activities not directly related to the mountainous terrain only play a minor role.

3.7 Study areas

Six study areas were selected within the research area (compare Figures 3.1 and 3.2), constituting relatively small and simple catchments with a documented history of debris flows interfering with the international road and with a meteorological station nearby. The general features of the study areas are discussed below, proceeding from W to E. The specific data obtained for the study areas and used for the present thesis is described in Section 4.1. Detailed maps of all the study areas are represented in App. 1.1. 3D views with draped orthophotos are shown in Chapter 5.

When selecting the study areas it was necessary to make a choice – some thematically very interesting and also hazardous areas (for example Quebrada Seca or Quebrada del Camino) had to be kept out for several reasons like their large size or lacking reference data.

3.7.1 Guardia Vieja

Downstream of the village of Guardia Vieja, the Aconcagua valley is narrowed by a large body of sediment the origin of which has been interpreted in different ways (CAVIEDES 1972 as till; ABELE 1984 as landslide deposit). The plain of Guardia Vieja few kilometres upstream constitutes a former lake dammed by that mass before it was cut by Río Juncal. The unconsolidated sediments have a very undulating surface with a system of ridges and steep, unstable slopes (Figure 3.28). Though it looks relatively harmless on a first glance, the system reacts very aggressively to periods of intense rainfall. During the El Niño event in 1987 it produced a massive debris flow starting from a system of rotational failures and cut-

ting the international road (compare Figure 3.20) which was later rebuilt on the other side of the valley (HAUSER 2000a).

The study area *Guardia Vieja*, which extends from 1,500 m to 2,650 m asl, covers an area of about 2.7 km².

Figure 3.28: The *Guardia Vieja* study area. Photo: M. Mergili, 10/2006.

Figure 3.29: One of the unstable slopes producing debris flows in the *Guardia Vieja* study area. Photo: M. Mergili, 10/2006.

3.7.2 Quebrada del Ferrocarril

Downstream of Portillo, the international road has to overcome a steep slope, a problem that was resolved by building a series of 180 degree loops (compare Figure 3.24). A system of gullies descends from the adjacent mountain ending up directly at the road. These gullies are prone to produce debris flows particularly in periods of intense snow melt in the upper parts of the system (Figures 3.30 and 3.31). Most of the debris flows are supposed to be initiated due to detachment by channel flow. At least one branch of the gully system has a very actively developing head moving upwards. Since 2000, several events have been recorded cutting the international traffic (HAUSER 2000b; 2005). Regarding one specific debris flow event in November 2000, HAUSER (2000b) reported about outflow of melting water which had collected in an abandoned railway tunnel, triggering a massive debris flow obstructing the road traffic (Figure 3.32).

The study area occupies a surface of about 2.6 km² and extends from 2,350 m to 4,000 m asl.

Figure 3.30 (top): Debris flow gullies ("*Quebrada del Ferrocarril*") near to Portillo. Photo: M. Mergili, 11/2006.
Figure 3.31 (middle): Debris flow gullies ("*Quebrada del Ferrocarril*") near to Portillo. In the background the international road. Photo: M. Mergili, 11/2006.
Figure 3.32 (bottom): In this site, massive outflow of water collecting by snowmelt caused a debris flow interfering with the international road. Photo: M. Mergili, 11/2006.

3.7.3 Guido (four study areas)

The Guido "village" consists of an abandoned railway station not accessible by road (compare Figure 3.25). The meteorological station is located 3 km downstream on the right side of the river. Guido is situated about 100 km W of Mendoza and 25 km SE of Uspallata, in a place where the Río Mendoza and the international road perform a sharp curve ("*Curva de Guido*"). The study areas follow the river and the road at a length of about 5 km, from km 1114 to km 1119 of the road Nr. 7, where several sections are highly

susceptible to debris flows, rock falls and landslides in general. Whilst the road runs at the right side of Río Mendoza, the abandoned railway line, which is also prone to mass movements, runs on the left side. Due to the lack of appropriate historical information on this side, the present study was confined to the right side of Río Mendoza.

Figure 3.33 (top): The Mendoza valley slightly upstream of *Guido*. Photo: M. Mergili, 10/2006.
Figure 3.34 (bottom): The study area *Las Murallas*. Photo: M. Mergili, 10/2006.

The geological situation is rather uniform. The area consists of granite (Figure 3.33) which is partly in a state of intense weathering. The terrain is generally steep, and the bedrock outcrops pose a severe threat to the road (rock falls). Packs of partly relocated residuals of weathering constitute a system of steep slopes and gullies with the capability to produce debris flows threatening the road as a response to rainfall events, for example during a heavy rainstorm in April 1996 (ESPEJO 1996; MOREIRAS 2004a). Only a small share of the area is mixed with rocks of the Choiyoi group (compare Section 3.2.3). According to MOREIRAS (2004a), most debris flows are caused by saturation of the terrain.

Four study areas were selected in the *Guido* area. Their names used below are no official ones, but were given to the study areas by the author for the purpose of the present thesis. Except for *Las Murallas*, the soils in the study areas were considered as uniform (all belonging to class 11; compare Table 4.2). Though this is a rough generalization, the available information did not allow for a more detailed subdivision.

Las Murallas

The study area *Las Murallas* ("The Walls") consists of two parts (Figure 3.34):

- a uniform steep slope of granitic residuals with strong indicators for the occurrence of shallow slides evolving into debris flows. The lower part of the slope has been reshaped to a stair-like structure in order to protect the road, but also these structures are already being partly eroded;
- the second part includes a system of debris-covered gullies appearing relatively stable and not prone to erosion in their upper parts, but severely eroded in their lower section, with steep unstable slopes directly adjacent to the road. It is located adjacent to the first part directly at the transition from the granitic intrusion to the rocks of the Choiyoi group, therefore representing more complex lithological conditions than the other study areas around Guido.

The study area occupies a surface of about 0.9 km² between 1,500 m and 2,300 m asl.

Figure 3.35 (top): The study area *Castillo de Rocas* with the international road at the very bottom. Photo: M. Mergili, 10/2006.
Figure 3.36 (bottom): Debris flow gully in the study area *Castillo de Rocas*. Photo: M. Mergili, 10/2006.

Castillo de Rocas

The study area *Castillo de Rocas* ("Rock Castle") represents a relatively complex system of gullies, deriving from the highest peaks in the area and ending up in a large cone consisting of a mixture of slope sediments

and debris flow deposits directly at the edge of the road which is protected by a retention wall that, however, only prevents small events from obstructing the traffic (Figures 3.35 and 3.36). About 0.8 km² are occupied by this study area, extending from 1,500 m to 2,500 m asl.

Quebrada Escondida

Only few hundreds of meters down valley of *Castillo de Rocas*, the study area *Quebrada Escondida* ("Hidden Canyon") represents a very compact system consisting of a steep, sediment-covered gully cut into the bedrock and, directly below, a cone showing a very active, eroding central part and ending up in some smaller and younger deposits indicating the latest debris flow events (Figure 3.37). Due to its simplicity, the study area is ideal for model evaluation. One disadvantage is that the upper part (the gully) is not accessible without special equipment. However, its characteristics were captured using a telephoto lens, and due to the uniform nature of the Guido geology, the geotechnical characteristics are not supposed to differ from those of the surrounding areas. The study area extends from 1,500 m to 2,300 m asl and covers a surface of 0.2 km².

La Ampolleta

The study area *La Ampolleta* ("Sand Glass"), the only one downstream of the Guido station and therefore located closest to the meteorological station, includes some of the highest peaks of the area. In its relatively flat upper part not yet reached by the side erosion from the Mendoza valley, it shows a very poor channel network. The channels only become clear in the steep intermediate section, where the recent occurrence of shallow slope failures is evident in some places. The lower section of the study area constitutes a cone with a complex system of fluviatile and debris flow deposits of different generations, some of them active, some not, indicating the long history of debris flows in the area. The lower part of the deposits is cut by the road (Figure 3.38). The study area covers a surface of 2.3 km² from 1,500 m to 2,750 m asl.

Figure 3.37 (top): The study area *Quebrada Escondida*. Photo: M. Mergili, 10/2006.
Figure 3.38 (bottom): The study area *La Ampolleta*. Photo: M. Mergili, 10/2006.

4 Materials and methods

Table 4.1: Sets of data and parameters used in the study.

database	format	use	sources
imagery	spatial (raster)	derivation of orthophotos, elevation models, soil class and land cover maps	regional, national and international authorities; own images
elevation and relief	spatial (raster)	all model components	stereo matching of imagery
soil	spatial (classes) and tabular	infiltration model, slope stability model	mapping; soil sampling and laboratory analysis; literature values
land cover and surface	spatial (classes) and tabular	hydraulic and slope stability model components	mapping; literature values
meteorological	tabular	input data for model validation	meteorological services
historical events	tabular	reference for model validation	official reports; existing recompilation; newspaper archives

4.1 Data and data preparation

The sets of input data and parameters for the study are presented in detail below and summarized in Table 4.1. Their use for the models *r.debrisflow* and *r.avalanche* is discussed in the sections 4.2 and 4.3.

4.1.1 Imagery database

Aerial and satellite imagery were used for the study as well as digital photos taken in the field:

- Colour and greyscale LANDSAT imagery (resolution: 28.5 and 14.25 m, respectively) were obtained (NASA LANDSAT PROGRAM 2001);
- greyscale images of SPOT5 at a spatial resolution of 2.5 m, taken in 2006 and 2007, were obtained from SpotImages;
- digital photos were taken during field surveys in 2006;
- aerial images at a scale of 1:60,000 were obtained from SAF (Servicio Aerofotogramétrico) for the entire Chilean part of the study area (Aconcagua valley). A calibration protocol of the camera was available so that the photo geometry (fiducial coordinates, distortion) was known exactly. The images were taken in May 1977. The scanned images had a spatial resolution of 3.1 m. The images were cloudless, but there was a considerable portion covered by snow in the higher parts of the area, including one portion of the study area *Quebrada del Ferrocarril*;
- aerial images at a scale of 1:20,000 were purchased from the Regional Government of the Province of Mendoza for the study areas in the Argentine part (Mendoza valley). The images were taken in August 1983. No calibration protocol was available for the camera, so that the fiducial coordinates had to be estimated and the distortion had to be set to zero. The scanned images had a spatial resolution of 0.9 m. All images were free of clouds or snow.

Orthophotos were derived from the SPOT and aerial imagery, using the LANDSAT and ASTER (compare below) datasets as reference.

4.1.2 Elevation and relief database

The relief of a slope or a catchment is one of the key determinants for its tendency to produce landslides and debris flows. Relief is most frequently represented as a raster-based digital elevation model (DEM) and its derivates (slope, topographic index, etc.). Low resolution DEMs, suited for studies at a regional scale, are available almost worldwide for free (SRTM mission, about 90 m), or at relatively low cost (ASTER, 30 m).

Higher resolution DEMs (resolution $\leq$ 10 m, 5 m if possible) were needed for the present study. Since techniques of Airborne Laser Scanning were not applicable (high cost), the following options were chosen:

- stereo-matching of aerial imagery by autocorrelation based on the parallax between the images, somehow the digital way of stereoscopic viewing. The method produced very satisfactory results for areas with good contrast and without snow;

- stereo-matching of pairs of digital photos taken from the opposite slope (compare App. 2.1), based on exactly the same principle as stereo matching of aerial images. The advantage was that daytime and season could be chosen individually. The applicability of the approach was strongly coupled to the presence of an accessible opposite slope;
- stereo-matching of SPOT satellite imagery. The same method as for aerial imagery was applied because only parts of images and no orbital information were available. Good results were obtained at a spatial resolution of 10 m, at a resolution of 5 m a large quantity of holes limited the quality of the DEMs. However, the DEMs were a valuable source of information for areas not covered by aerial or terrestrial imagery.

Stereo-matching was done with the *OrthoEngine* module of *PCI Geomatica*. The DEMs derived from the different sources were combined in order to use the dataset with the best quality for each part of each study area (Figure 4.1).

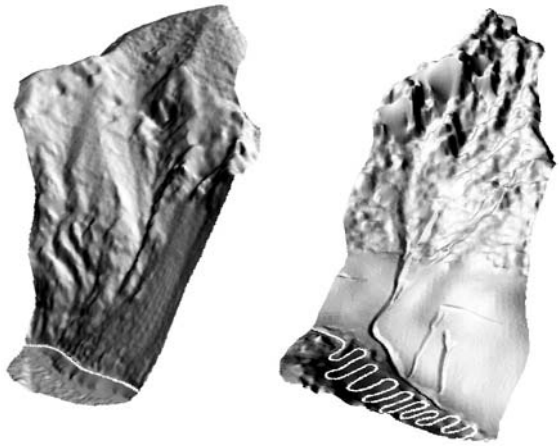

Figure 4.1 (left): 5 m DEM for the study area *Castillo de Rocas*, stacked together from DEMs derived from aerial and SPOT imagery.
Figure 4.2 (right): 5 m DEM for the study area *Quebrada del Ferrocarril*, stacked together from DEMs derived from aerial imagery and an ASTER DEM, and modified using GPS records as reference.

The ground control points (GCPs) for image matching were obtained using a combination of LANDSAT imagery, an ASTER DEM, and topographic maps at scales of 1:100,000 and 1:50,000 (particularly for the Chilean part). This means that the horizontal accuracy of the resulting DEM is not better than 15 m, but this is acceptable as only the representation of the terrain details (relative relief) are of interest, and not the absolute x, y, and z coordinates.

It was not possible to create an elevation model at the desired spatial resolution over the entire study area *Quebrada del Ferrocarril*. However, the debris flows there occur in well-defined channels which were modelled into the ASTER DEM manually using GPS records (Figure 4.2).

4.1.3 Soil database

In the present thesis, the term soil refers to sediment cover which does not necessarily contain decomposed organic matter.

Soil samples were extracted at critical points in gullies, in the sites of shallow slope failures, or at steep slopes. Some samples were also taken on debris flow deposits. Most of the samples were extracted from the upper part of the soil, directly under the shallow cover of coarse gravel occurring frequently (Figure 4.3). Maps representing the sampling sites for all the study areas are shown in App. 1.1. Grain size distribution and the corresponding texture class were determined for all the samples in a geotechnical laboratory. Stone content s_m (grains > 2 mm; per cent of mass) and the characteristic grain diameters *D30*, *D50*, and *D90* (all in mm) were derived.

For some of the samples, specific weight γ (N m^{-3}) as well as the mechanical parameters cohesion c (N m^{-2}) and angle of internal friction φ (degree) were determined, too.

Figure 4.3 (top): Extraction of soil samples. Photo: M. Mergili, 09/2006.
Figure 4.4 (bottom): Triaxial test for determining c and φ in the geotechnical laboratory of the University of Innsbruck. Photo: M. Mergili, 04/2007.

Table 4.2: Parameters for the soil classes identified in the study areas. avg = average or mode; min = minimum; max = maximum. For references and for a description of the soil classes and variables compare text.

class	n		text. class	D30 mm	D50 mm	D90 mm	s Vol.-%	γ_d kN m^{-3}	c kN m^{-2}	φ deg.	θ_r m^3 m^{-3}	θ_s m^3 m^{-3}	ψ m	K m s^{-1}	n_{bas}
0								rock							0.025 0.025 0.025
11	18	avg	S	0.86	2.06	10.83	32.9	19	9	39.7	0.045	0.43	0.050	3.27E-5	0.032
	(3)	min	LS	0.30	0.70	5.00	15.5	18	0	36.2	0.057	0.43	0.061	8.31E-6	0.028
		max	S	2.50	4.50	30.00	66.3	20	23	43.0	0.045	0.43	0.050	3.27E-5	0.035
12	4	avg	LS	0.76	8.00	13.25	36.0	20	10	39.5	0.057	0.43	0.061	8.31E-6	0.032
	(1)	min	LS	0.40	1.50	8.00	27.0	20	10	39.5	0.057	0.43	0.061	8.31E-6	0.028
		max	LS	1.50	25.00	15.00	51.0	20	10	39.5	0.057	0.43	0.061	8.31E-6	0.035
13	3	avg	SL	0.63	2.67	20.00	43.2	22	0	41.3	0.065	0.41	0.110	3.03E-6	0.035
	(1)	min	SL	0.30	2.00	15.00	38.6	22	0	41.3	0.065	0.41	0.110	3.03E-6	0.030
		max	SL	1.00	3.50	25.00	48.6	22	0	41.3	0.065	0.41	0.110	3.03E-6	0.040
21	8	avg	SL	0.35	1.83	15.50	32.8	21	18	38.7	0.065	0.41	0.110	3.03E-6	0.035
	(2)	min	SL	0.10	0.65	6.00	18.6	21	0	36.9	0.065	0.41	0.110	3.03E-6	0.030
		max	LS	0.65	2.50	25.00	38.8	21	35	40.5	0.057	0.43	0.061	8.31E-6	0.040
31	14	avg	SL	0.23	1.03	11.68	26.3	20	0	38.2	0.065	0.41	0.110	3.03E-6	0.032
	(2)	min	L	0.04	0.30	6.00	15.4	19	0	37.1	0.078	0.43	0.089	9.44E-7	0.028
		max	LS	0.60	2.50	20.00	40.0	20	0	39.2	0.057	0.43	0.061	8.31E-6	0.035

The analysis techniques for c and φ require sample sizes up to 30 kg, particularly for samples characterized by large grain sizes. For logistic reasons, only a few that large samples were extracted. Figure 4.4 illustrates the equipment for the triaxial test for determining c and φ. Table A1.1 in App. 1.2 shows all the results of the laboratory tests.

Classes of similar soil characteristics were compiled for all of the study areas, using the results of the laboratory tests as well as orthophotos, DEMs, and digital photographs taken in the field in order to enable an approximation of the spatial distribution of the soil characteristics. Soil depth had to be set to infinite due to missing spatially distributed information. The soil parameters were assumed constant over the entire depth of the soil since no drilling holes were available and steep cut slopes were hardly accessible. Average, minimum, and maximum of the parameters over all the samples located within the same class were computed. Regarding texture classes, mode was used instead of average. Table 4.2 shows the parameters for all the soil classes. The average values were used in the model, except for pairs of c and φ. These parameters can not be treated independently since they are descriptors (offset and slope) for the result of one single set of laboratory tests. The pair of c and φ leading to the least stable conditions was used for each soil class.

The basic value for Manning's n n_{bas} was also defined based on the soil classes (ARCEMENT & SCHNEIDER 2000). Since the values are only rough estimates, a random value ranging in between minimum and maximum was assigned to each cell.

Hydrological parameters were derived from the texture classes and assigned to each soil class, using published relationships: residual water content θ_r and saturated water content θ_s (both in per cent of volume), hydraulic conductivity K (m s^{-1}), and suction head ψ (m). The values shown in Table 4.2 were compiled from MAURER (1997; data from CARSEL & PARRISH 1988) and CHEN & YOUNG (2006; data from RAWLS et al. 1983). The spatial distribution of all soil classes is illustrated in App. 1.1 for all of the study areas.

Table 4.3: Grain size classes and hydraulic conductivities according to CARSEL & PARRISH (1988) and RAWLS et al. (1983).

grain size class	saturated (CP)	saturated std.dev.	Green-Ampt (R)	ratio R/CP
S	8.25E-05	4.33E-05	3.27E-05	0.40
LS	4.05E-05	3.16E-05	8.31E-06	0.20
SL	1.23E-05	1.56E-05	3.03E-06	0.25
L	2.89E-06	5.06E-06	9.44E-07	0.33
SCL	3.63E-06	7.61E-06	4.17E-07	0.11
SC	3.36E-07	7.75E-07	1.67E-07	0.50
CL	7.17E-07	1.94E-06	2.78E-07	0.39
SIL	1.25E-06	3.41E-06	1.81E-06	1.44
C	5.56E-07	1.17E-06	8.33E-08	0.15
SICL	1.97E-07	5.33E-07	2.78E-07	1.41
SI	6.94E-07	9.14E-07	–	–
SIC	5.83E-08	3.00E-07	1.39E-07	2.38

Table 4.3 illustrates the difference between values of saturated hydraulic conductivity listed by CARSEL & PARRISH (1988), and of hydraulic conductivity for the Green-Ampt infiltration model compiled by RAWLS et al. (1983), which were used for the present thesis. The values from CARSEL & PARRISH were only used for the analyses of parameter sensitivity (compare Section 4.5 and Chapter 5). The ratio in the right column of Table 4.3 should be 0.5, since hydraulic conductivity for the Green-Ampt model is half of saturated hydraulic conductivity (ERICKSON & STEFAN 2007) – other values than 0.5 indicate a deviation between the two datasets.

4.1.4 Land cover and surface database

Land cover (in the study areas principally identical to the natural vegetation) asserts a strong influence on hydrological and mechanical slope processes (compare Chapter 2). The spatial distribution of the land cover classes in the study areas was mapped using aerial images, digital photos, and ground truthing during field surveys. Characteristic values of interception capacity *ICP* (mm), rooting depth d_r (m), vegetation surcharge for Manning's n (n_{add}), and root cohesion c_r (kN m^{-2}) were assigned to each class according to values from the literature (ARCEMENT & SCHNEIDER 2000; BRAUD et. al. 2001; SCHMIDT et al. 2001; BATHURST 2002). Some of the parameters had to be estimated from the values for comparable vegetation types in other areas of the world because information was missing, The published values for most of the parameters scattered over a wide range. The maxima and minima are represented in Table 4.4. In the model *r.debrisflow* (compare Section 4.2), random values are computed for n_{add}, based on the maxima and minima for each land cover class. These values are then summed up with n_{bas} for each cell. For the other values, the average was used. The spatial distribution of the land cover classes for all of the study areas is illustrated in App. 1.1.

Independently from the land cover classes, two hydrological surface classes (HSCs) were distinguished for each study area, regarding runoff behaviour:

- HSC1 includes all cells containing a large, clearly recognizable flow channel. For each cell, the width of this flow channel was defined, based on the orthophotos and field studies;
- HSC2: slopes are dissected by several small, more or less parallel channels on a sub-cell scale, where runoff concentrates quickly after its initiation, surface runoff occurs as unconcentrated overland flow, or no surface runoff occurs at all. Spatially distributed average channel densities were assigned to the cells of this class and expressed as ratio of the total cell size.

4.1.5 Historical events database

Information on debris flow events in the past was required for model validation and evaluation, fulfilling the following requirements:

- sufficient spatial resolution and accuracy to allow for the identification of the slope or the gully where the event took place;
- a temporal resolution corresponding to that of the meteorological data used, but at least specification of the day of the event;
- and specification of the type of the event, and in the ideal case, also the amount of material moved or deposited.

In practice, these requirements are not always fulfilled. Different sources of information emphasize different points. Table 4.5 represents the events used for the validation of the results of the present study. Only records with sufficient information are listed. Please note the lacking correlation between rainfall and volume deposited on the road in the *Guido* area. The following sources were used:

- published literature: HAUSER (2000a) provided information about a debris flow event in the Aconcagua valley;
- official reports: efforts and costs for reestablishing traffic after debris flows interfering with the international road were documented, constituting a detailed source of historical data, including information on the quantity of debris deposited on the road. Unpublished reports from the Chilean Geological Survey (HAUSER 2000b; 2005) and from the road maintenance agency in Uspallata (ESPEJO 1996) were used.

Table 4.4: Parameters for the land cover classes identified in the study areas. For references and description of the variables compare text.

class	*ICP* (mm)		n_{add}		d_r (m)		c_r (kN m^{-2})	
	min	max	min	max	min	max	min	max
1 bare ground (rock or debris) or very sparse shrubland	0.0	0.0	0.030	0.075	0.0	0.0	0.0	0.0
11 Monte or *Artemisia* shrubland	0.0	0.7	0.030	0.270	0.0	2.0	0.0	3.5
21 Quillay-Coliguay matorral	0.5	1.5	0.140	0.270	1.0	2.0	0.7	3.5
22 Piche-Pingopingo matorral	0.2	1.0	0.140	0.270	0.5	1.0	0.7	3.5
23 eroded matorral	0.0	0.2	0.040	0.095	0.0	0.0	0.0	0.0
31 *Chuquiraga* or tussock high-Andean Steppe	0.1	0.2	0.050	0.090	0.1	0.5	0.7	3.5

Table 4.5 (top): Historical events used for model validation (compare Section 4.1.6 for the corresponding meteorological data).

Table 4.6 (bottom): meteorological stations and available datasets in the research area. RHN = Red Hidrológica Nacional (AR), SMN = Servicio Meteorológico Nacional (AR), OMC = Oficina Meteorológica de Chile, DGA = Dirección General de Aguas (Ministerio de Obras Públicas, CL); *P* = precipitation, *T* = temperature, *H* = relative humidity, *E* = evaporation, v_w = wind speed. All datasets are available on a daily base (sums or averages, respectively).

date	location	study area(s)	rainfall on day of event	antecedent precipitation	removed vol. (m³)	source
13.08.1987	old rd. dstr. Guardia Vieja	Guardia Vieja	148.0 mm	309.5 mm	45,000	HAUSER (2000b)
08.03.1996	R7 1113-1117	Guido	9.2 mm	2.5 mm	15,000	ESPEJO (1996)
21.03.1996	R7 1115-1126,2	Guido	40.0 mm	4.0 mm	600	ESPEJO (1996)
18.11.2000	R60 curves 2-6	Qd. Ferrocarril	0.0 (snow melt)	0.0 mm	10,000	HAUSER (2005)
21.01.2003	R60 curves 2-10	Qd. Ferrocarril	0.0 (snow melt)	0.0 mm	8,000	HAUSER (2005)
17.11.2004	R60 curves 2-10	Qd. Ferrocarril	0.0 (snow melt)	0.0 mm	14,000	HAUSER (2005)

station	elev.	source	*P* (mm)	*T* (deg. C)	*H* (rel.)	*E* (mm)	v_w (km h^{-1})
Cacheuta	1270	RHN	12/83 – 03/06	x	x	x	x
Potrerillos	1370	RHN	11/83 – 03/06	x	x	x	x
Guido	1550	RHN	02/57 – 03/06	01/65 – 03/06	01/65 – 03/06	09/93 – 03/06	03/67 – 03/06
Uspallata	1891	RHN	11/83 – 03/06	06/93 – 03/06	06/93 – 03/06	09/93 – 03/06	x
Uspallata	1891	SMN	01/62 – 07/99	01/62 – 07/99	x	x	x
Polvaredas	2290	RHN	12/83 – 03/06	x	x	x	x
Punta de Vacas	2460	RHN	12/92 – 03/06	12/92 – 03/06	12/92 – 03/06	09/93 – 03/06	01/93 – 03/06
Puente del Inca	2750	SMN	01/61 – 12/76	01/61 – 12/76	x	x	x
Cristo Redentor	3829	SMN	01/61 – 12/80	01/61 – 12/80	x	x	x
Portillo	2850	OMC	02/66 – 03/66	x	x	x	x
Juncal	2250	OMC	xx/43 – xx/52	x	x	x	x
Saladillo - Río Blanco	1420	OMC	xx/41 – 12/00	x	x	x	x
Riecillos	1293	DGA	xx/29 – 02/06	x	x	x	x
Vilcuya	1100	DGA	12/64 – 02/06	12/64 – 02/06	x	x	x

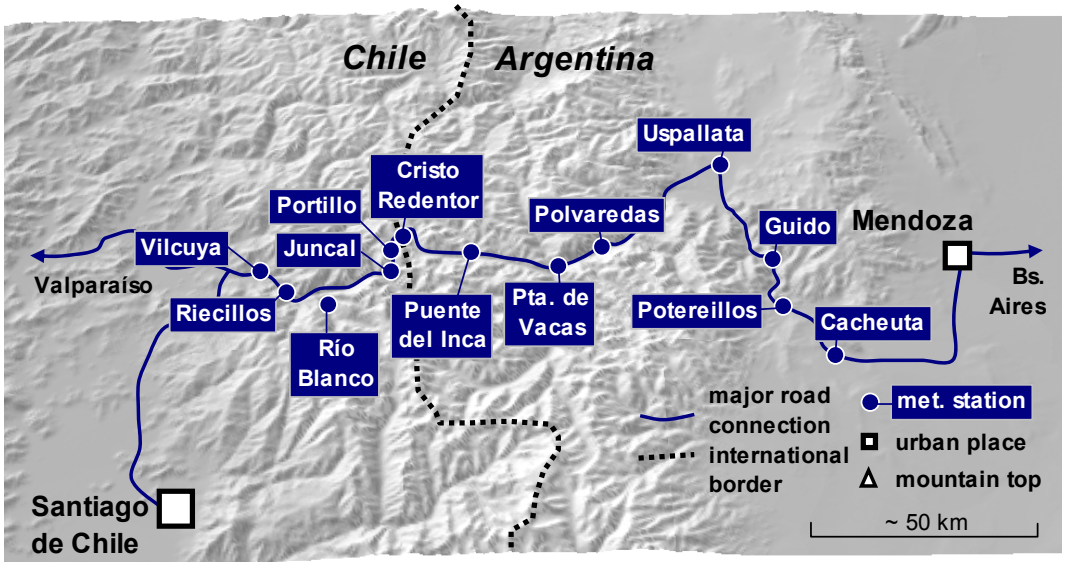

Figure 4.5: The meteorological stations in the Mendoza and Aconcagua valleys. Terrain represented with SRTM data (CIAT 2004; compare Figures 3.1 and 3.2).

A comprehensive existing archive of landslides interfering with the international road and the railroad in the Mendoza valley, compiled by Stella Moreiras from the IANIGLA research institute (MOREIRAS 2004a), was not directly applicable for validation purposes due to its broad spatial scale, but was very useful as orientation.

Newspaper archives were used as an additional source of information, but the majority of the information on debris flows did not have the precision required for model validation.

4.1.6 Meteorological database

Precipitation and temperature data

The following meteorological variables were required for simulating historical or worst-case events:

- precipitation P (mm) as water input;
- and temperature T (degree Celsius) for the delimitation of rainfall and snowfall and for the estimation of the quantity of snowmelt.

Relative humidity of the air H, evaporation E, and wind speed v_w were not required to run the model, but were obtained as additional information, where available. Table 4.6 shows the meteorological data available for the research area, Figure 4.6 illustrates the spatial distribution of the stations.

All data was available on a daily base (sums or averages) but, however, containing gaps of days or months.

Spatial differentiation

None of the study areas has a meteorological station inside. Therefore the data from the nearest station was used. No vertical gradients were applied to precipitation. In contrast, temperature was differentiated vertically using gradients.

Guardia Vieja: the Saladillo – Río Blanco station lies about 4 km SW of the study area. It only provides precipitation. Temperature values were derived using the Vilcuya station (18 km W) and vertical gradients (compare below).

Quebrada del Ferrocarril: the closest usable rain gauges were Saladillo – Río Blanco (16 km to the W) and Riecillos (21 km to the W). Since the events under investigation were all triggered by rapid snowmelt, temperature was the more important variable. It was derived from the Vilcuya station (31 km W) using vertical gradients (see below).

Guido represented the best situation concerning meteorological data among all of the study areas. The Guido meteorological station is located about 3 km downstream of the old Guido railway station. The study areas are therefore located at distances between 2 km and 7 km from the meteorological station which provides the most comprehensive dataset of all the stations in the research area (compare Table 4.6). Since neither snowfall nor snowmelt played any role at the time of the debris flow events under investigation, the standard vertical temperature gradient of 0.65 °C per 100 m was applied to the *Guido* study areas without any further tests.

Vertical temperature gradients. All over the research area, the availability of temperature data is much sparser than that of precipitation data, particularly in the Aconcagua valley, where only Los Andes, Vilcuya, and the high altitude border station Cristo Redentor serve with temperature measurements. Cristo Redentor only covers the period from 1964 to 1980 (compare Table 4.6), whilst all the considered debris flow events took place between 1987 and 2004.

Gradients of daily maximum and minimum air temperatures from Vilcuya to Cristo Redentor were calculated based on the period 1970 to 1980. These gradients were used for deriving temperature maps of the study areas for the periods of interest. The horizontal distance of 38 km between these two stations may have introduced some uncertainties and inaccuracies to be kept in mind.

Table 4.7 shows the computed temperature gradients. Two meteorological situations where distinguished, based on the occurrence of precipitation at the Riecillos station. The temporal distribution of the temperature gradients was also tested for seasonal variations which, however, were not significant at all. The gradients were therefore only differentiated according to the occurrence of precipitation.

Table 4.7: Temperature gradients (°C m^{-1}) in the Aconcagua valley, based on the stations Vilcuya and Cristo Redentor (period 1970 to 1980). Values denote averages and standard deviations (in brackets). Precipitation records were taken from the Riecillos station.

situation	daily max.	daily min.
undifferentiated	0.704 (0.120)	0.434 (0.130)
days with prec.	0.644 (0.183)	0.541 (0.355)
days without prec.	0.709 (0.227)	0.424 (0.169)
May to October	0.725 (0.352)	0.430 (0.215)
June to November	0.692 (0.346)	0.436 (0.237)

Temporal resolution

Daily values of precipitation and temperature are not sufficient to serve as input for physically-based models of processes like debris flows. The data had to be broken down into shorter time intervals.

Temperature. A sinusoidal curve was interpolated between daily maximum and minimum temperatures:

$$T_t = \frac{T_{\max} + T_{\min}}{2} + \sin\left[15 \cdot (t - t_{\min} - 6)\right] \cdot \frac{T_{\max} - T_{\min}}{2}$$

Eq. 4.1,

where T_t is the temperature at the considered time, T_{max} and T_{min} (all in degree Celsius) are the daily maxima and minima, respectively, and t_{max} and t_{min} (hours, starting from midnight) are the times when they were measured. The factor 15 is needed for conversion from hours into decimal degrees. t_{min} was set to 4:00 a.m., and t_{max} to 4:00 p.m for the present study (Figure 4.6).

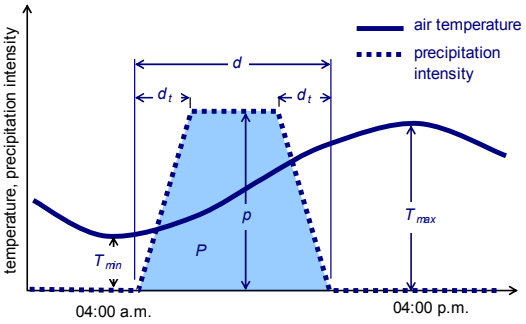

Figure 4.6: Concept for breaking down daily meteorological records into short time intervals. Designed by M. Mergili.

Precipitation. Breaking down daily precipitation P (mm) into short time intervals was more problematic. Different scenarios were established for the events under investigation, based on qualitative information and the known climatic characteristics of the areas. Those hypothetical events can be described by a duration d_p, (hours) and a maximum intensity i_p (mm per hour):

$$i_p = \frac{P}{d_p - d_{p,t}} \qquad \text{Eq. 4.2,}$$

Transition periods $d_{p,t}$ were assumed at the start and the end of the events (compare Figure 4.6). The events used for validation and the chosen scenarios are discussed in detail in Section 4.4.

4.2 The model framework r.debrisflow

4.2.1 General model layout

Part of the major objectives of the present thesis, stated in Chapter 1, is to test the suitability of the Open Source GIS product *GRASS* for integrated modelling of complex phenomena like debris flows, combining different types of approaches. The ideas for most of the model components were taken over from existing models, partly in a modified form. The model framework was named *r.debrisflow* (the r indicates that it is a *GRASS* raster module). It was kept relatively simple in its first version presented here, but was also designed in a way for allowing to be extended with more sophisticated modules in the future (compare Section 6.5).

r.debrisflow was implemented using a 2.5D raster data model (the vertical dimension plays an important role, but is only quantified by attributes). It combines physically-based, deterministic modules and modules based on empirical relationships. *r.debrisflow* couples a hydraulic model, a slope stability model, a sediment transport model, and a debris flow runout model:

- The deterministic hydraulic model distributes the water from precipitation or snow melt among vegetation (interception), soil (infiltration), and surface (runoff). It then approximates the soil water status and the runoff variables;
- the deterministic slope stability model computes the factor of safety for each cell, based on an infinite slope stability model, and identifies potential starting areas of debris flows;
- the sediment transport model (based on an empirical approach) provides an estimate for erosion and deposition by surface runoff, allowing to assess the tendency of bedload-rich runoff to develop into a debris flow;
- the debris flow runout model finally routes the debris flow downwards to the area of deposition, based on a two-parameter friction model.

The modules are executed in a defined sequence for a user-defined number of time steps during and after a rainfall or snow melt event. Slope stability and runout are computed at the end of the last time step.

Not all modules have to be executed – the following combinations (modes of simulation) are possible when running *r.debrisflow*:

- *1*: full mode: all modules are executed;
- *2*: geotechnical mode A: the sediment transport model is excluded, and only debris flows starting from slope failures are modelled – for conditions where it is known that debris flows only develop from slope failures;
- *3*: geotechnical mode B: the runoff and sediment transport models are excluded – like (*2*), but excluding the influence of runoff on infiltration: for conditions where it is known that no surface runoff develops;
- *4*: hydraulic mode: the slope stability model is excluded and only debris flows developing from sediment-laden runoff are modelled – for conditions where it is known that slope failures play no role for the mobilization of debris flows;
- *5*: fully saturated mode: it is assumed that the entire soil in the study area is saturated. With this precondition, the slope stability model and the runout model are computed;
- *6*: runout only mode: only the runout model is computed with defined areas of debris flow initiation – for testing the plausibility of the runout model for events of known patterns of debris flow initiation and deposition.

The general model layout is illustrated in Figure 4.7.

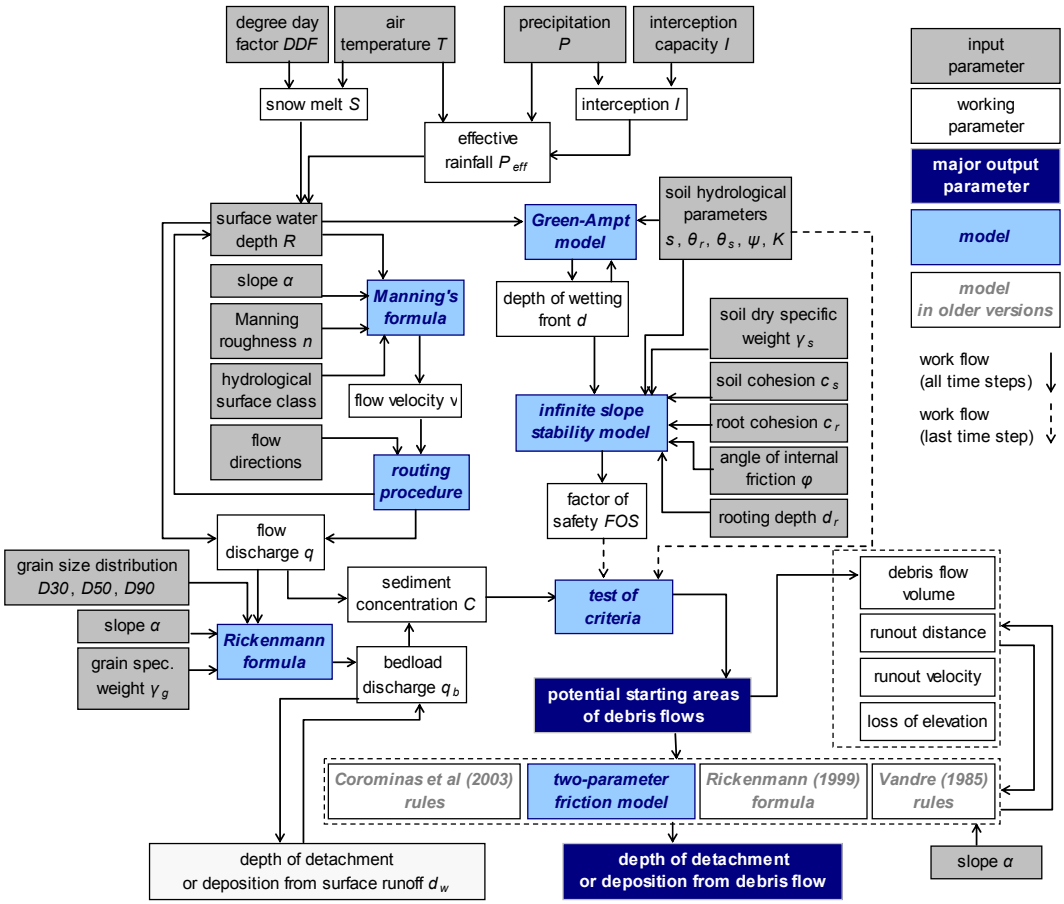

Figure 4.7: General model layout of *r.debrisflow*. Designed by M. Mergili

r.debrisflow considers the slope or catchment under investigation as six-layered system characterized by the following variables:

- the overlying atmosphere is described by air temperature T (degree Celsius) and precipitation P (m);
- snow cover is defined as snow depth d_s (m);
- land cover is defined by a raster layer representing nominal land cover classes. Minimum and maximum values of interception capacity ICP (m), root cohesion c_r (N m^{-2}), and rooting depth d_r (m) have to be assigned to each class.

  A hydrological surface class and the width of the flow channels at a sub-cell scale are defined for each cell as well as the vegetation surcharge of Manning's n n_{add};
- the surface water table is characterized by depth R (m) and flow velocity v_{flow} (m s^{-1});
- soil, here rather understood as sediment cover than as mixture of residuals from weathering and decomposed organic matter, is basically represented by a nominal soil class raster layer. A texture class, dry specific weight γ (N m^{-3}), stone content s (m^3 m^{-3}), the hydraulic parameters θ_r, θ_s (m^3 m^{-3}), ψ (m) and K (m s^{-1}), and the mechanical parameters soil cohesion c_s (N m^{-2}) and angle of internal friction φ are assigned to each soil class as well as minimum and maximum values for n_{bas}. Soil depth d (m) is defined independently from the soil classes. All parameters are considered constant over the entire depth of the soil column;
- bedrock is considered unconditionally stable. Its permeability for water is accounted for by the parameter p_r, denoting the ratio of total effective rainfall and snow melt which percolates through the rock. p_r is not defined as raster map, but globally for the considered study area.

The following sections give a more detailed introduction to the physical and mathematical background of *r.debrisflow*.

4.2.2 Hydraulic model components

Precipitation and snow melt

Precipitation P (m) and air temperature T (°C) are read from the prepared datasets. Precipitation is considered as rainfall P_r if it exceeds a user-defined temperature threshold T_{crit}, usually ranging between 0°C and 2°C. Snow melt M (m) is computed using a simple degree-day approach with air temperature as the only input:

$$\Sigma M = ddf \cdot T_{ddf} \qquad \text{Eq. 4.3,}$$

where ΣM is the daily snow melt (m d^{-1}), and *ddf* is the degree-day factor (m °C^{-1} d^{-1}). T_{ddf} is the temperature in °C at a defined time of the day. In order to estimate snow melt of shorter time intervals, daily snow melt is distributed over the considered day, following a linear relationship with temperature:

$$M = T_0 \, \Sigma M / \Sigma T \qquad \text{Eq. 4.4,}$$

where T_0 is the temperature during the cosidered time step, ΣT is the daily temperature sum, based on the length of one time step Δt (s). Only temperatures above T_{crit} are included in the sum.

Interception

The interception capacity of the vegetation I_{pot} (m) is extracted from the land cover dataset. For each time step Δt (s) rainfall is retained as interception $I_{\perp t}$ (m) until the interception capacity is reached ($\Sigma I_{\perp t} = I_{pot}$). The excess rainfall is added to the soil water table R (m) as effective rainfall $P_{r,eff}$ (m).

Water from snow melt is considered not interceptable by vegetation. This worst-case assumption was chosen due to the often unknown vertical distribution of I_{pot}.

Evapotranspiration

Potential evapotranspiration E_{pot} (m) is set to zero. This is a worst-case assumption again which was chosen for two reasons:

- also the most simple equations for evapotranspiration require highly dynamic parameters that are usually not available at sufficient accuracy and resolution (humidity, irradiation, etc.);
- the model is designed primarily for short and intense rainfall events, where evapotranspiration is rather negligible. Regarding snow melt, neglect of evapotranspiration may lead to more significant inaccuracies.

Infiltration

Infiltration, runoff, and sediment transport have to be calculated at much shorter time steps Δt_{short} than the other processes, meaning that the entire sequence has to be repeated for various times within each basic time step Δt. Δt_{short} is determined according to Eq. 4.16.

The water input from effective rainfall and the snow melt are added to the surface water table of the cell at the beginning of each short time step:

$$R_0 = R_{prev} + \frac{\Delta t_{short}}{\Delta t}\left(P_{eff,t} + M_t\right) \qquad \text{Eq. 4.5,}$$

where R_{prev} is the depth of the surface water table at the end of the previous time step. The infiltration of water into the soil is a complex process influenced by an interplay of factors like the depth of the surface water table, the soil parameters, and the local topography. It was chosen to use the GREEN & AMPT (1911) approach, assuming a sharp wetting front as the interface between saturated soil above and soil at initial moisture content below (Figure 4.8). The hydraulic parameters governing infiltration are derived from the grain size class of the soil (compare Tables 4.2 and 4.3). Infiltration capacity f (m s^{-1}) can be stated as

$$f = K\left(1 + \frac{R_0 + \psi}{d_0}\right) \qquad \text{Eq. 4.6,}$$

where K (m s^{-1}) is the hydraulic conductivity, R_0 (m) is the depth of the surface water table before infiltration, ψ (m) is the matric suction at the wetting front, and d_0 (m) is the depth of the wetting front before infiltration. Eq. 4.6 is derived from Darcy's law (XIE et al. 2004a; CHEN & YOUNG 2006).

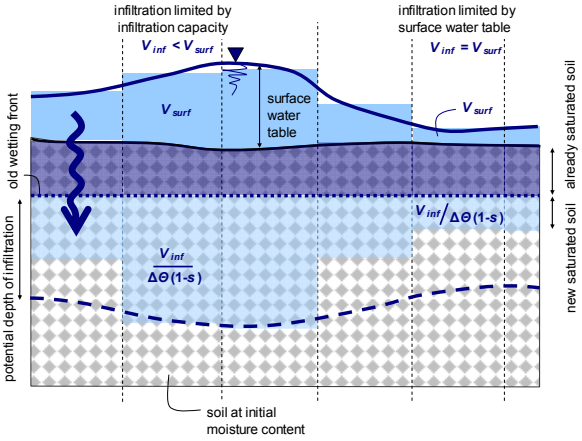

Figure 4.8: Infiltration into the soil according to the GREEN & AMPT (1911) model, as applied for the present study. V_{surf} = volume of surface water before infiltration, V_{inf} = infiltrated volume. Designed by M. Mergili.

Two possible cases have to be distinguished. f has to be corrected for volumetric stone content s, which does not affect the maximum possible depth of infiltration, but the volume that fits into the soil until this depth. For each time step it is tested which case is applicable:

- case 1: $R_0 > f \, \Delta t_{short} \, (1\text{-}s)$ – inflow to the cell exceeds maximum possible infiltration and depth of surface water table after infiltration R_f (m) is expressed as

$$R_f = R_0 - f \Delta t_{short} (1 - s) \qquad \text{Eq. 4.7,}$$

Infiltration is limited by the infiltration capacity, and the depth of the new wetting front d (m) is computed as follows:

$$d = d_0 + \Delta t_{short} \, f / \Delta\theta \qquad \text{Eq. 4.8,}$$

where $\Delta\theta$ is the moisture deficit of the soil (difference between saturated water content θ_s and initial water content θ_i; all in $m^3\ m^{-3}$);

- case 2: $R_0 \leq f\ \Delta t_{short}\ (1\text{-}s)$ – inflow to the cell is equal or smaller than maximum possible infiltration capacity. In this case, the entire inflow infiltrates,

$$d = d_0 + R_0/[\Delta\theta(1-s)] \qquad \text{Eq. 4.9,}$$

and no surface water table remains, meaning that no surface runoff will develop from the considered cell.

For case 1, s has no direct influence on d, for case 2, d increases with increasing s. The application of this method has to be considered as an approximation:

- The Green-Ampt approach, in its strict sense, was developed for horizontal surfaces, but is also applied for slopes. CHEN & YOUNG (2006) showed that on slopes until 45°, the effect of slope angle is small, compared to other sources of inaccuracy;
- stone content is not accounted for in the original model. Therefore it was decided to disregard its influence on infiltration capacity, but its role as limiting the infiltrable volume was taken into account. More research would be necessary in order to clarify the inaccuracies connected to this simplification (compare Section 6.2).

Slope-parallel seepage is neglected in the model. The infiltration is computed separately for soil below flow channels and soil in between flow channels. In between flow channels, ΣIF and OF are zero (compare Eq. 4.14 and 4.15).

The integral form of the Green-Ampt approach (compare Eq. 2.19 and 2.20 in Section 2.2) is not used as the model is run in short time steps with varying rainfall intensities.

Surface runoff

After computing infiltration, the ponded water of the depth R_f is assumed to concentrate in the flow channels immediately and to run off superficially. Strictly spoken, $R_f = A_{flow}/P_{wet}$, where A_{flow} (m^2) stands for the cross section of the flow, and P_{wet} (m) is the wetted perimeter, but in the model, R_f is approximated by flow depth. Runoff velocity v_{flow} ($m\ s^{-1}$) is computed using the Manning formula:

$$vf_{low} = \frac{1}{n_{man}} R_f^{\frac{2}{3}} (\sin\alpha)^{\frac{1}{2}} \qquad \text{Eq. 4.10,}$$

where a is the local slope angle in degrees and n_{man} is the surface roughness (determined by vegetation, soil texture, and obstacles), which is computed using

$$n_{man} = m(n_{bas} + n_{sdd}) \qquad \text{Eq. 4.11,}$$

where m is a factor accounting for meandering, n_{bas} is the basic n value, and n_{add} is a surcharge for vegetation, obstacles, etc. (compare Tables 4.2 and 4.4). m is automatically set to 1.0 since the model presented here is designed for steep terrain with poor meandering of the channels.

The water discharge per unit width q ($m^2\ s^{-1}$) is computed as follows:

$$q = v_{flow} R_f = \frac{1}{n_{man}} R_f^{\frac{5}{3}} (\sin\alpha)^{\frac{1}{2}} \qquad \text{Eq. 4.12.}$$

Surface runoff is computed separately for each hydrological surface class HSC:

- $HSC = 1$ (defined channel): the water is routed through the channel, with only one possible downward direction from each cell;
- $HSC = 2$ (slope with numerous small channels or no channels at all): the water is routed downwards assuming the defined channel densities on a sub-cell scale and a random walk weighted for slope angle:

$$w = \alpha^{u_1} \qquad \text{Eq. 4.13,}$$

where w is the weight assigned to each potential flow direction and u_1 is a user-defined exponent (values of 3 to 4 appear reasonable) – on gentle slopes, inaccuracies of the DEM or landforms on a sub-cell scale may exert a stronger effect on flow direction than on steep slopes.

For both cases, inflow ΣIF (m) is computed with the Manning formula in the same way:

$$\Sigma IF = \sum_{i=1}^{i=n} R_{f,i} \frac{v_{flow}\Delta t_{short}}{d_{h,i}} = \sum_{i=1}^{i=n} \frac{1}{n_{man,i}} \frac{\Delta t_{short}}{d_{h,i}} R_{f,i}^{\frac{5}{3}} (\sin\alpha_i)^{\frac{1}{2}} \qquad \text{Eq. 4.14,}$$

where n is the number of contributing upslope cells, $d_{h,i}$ (m) is the horizontal distance between the centre of the cell i and the centre of the considered cell. Outflow OF (m) is computed in an analogous way:

$$OF = R_f \frac{v_{flow}\Delta t_{short}}{d_h} \qquad \text{Eq. 4.15,}$$

where d_h (m) stands for the horizontal distance between the centre of the considered cell and the centre of the downslope cell. The length of one short time step Δt_{short} (s) is defined as

$$\Delta t_{short} = a\, d_{cell}/v_{max} \qquad \text{Eq. 4.16,}$$

where a is a factor ≤ 1 set to 0.5, d_{cell} (m) is the cell size and v_{max} ($m\ s^{-1}$) is the maximum runoff velocity over the entire area. Too short time steps would unnecessarily increase computing time. Δt_{short} is defined by the program automatically according to Eq. 4.16, using the maximum flow velocity of the previous time step over all cells. Δt_{short} is set to 20 s if

d_{cell}/v_{max} exceeds a threshold value. If no runoff occurs at all, Δt_{short} is set to 120 s.

The depth of the water table R for each cell is computed as follows:

$$R = R_f + T + M + \Sigma IF - OF \qquad \text{Eq. 4.17,}$$

where T is the effective rainfall, M is the snow melt, ΣIF stands for the total inflow from all the upslope cells directly draining into the considered cell, and OF stands for the outflow (all values in meters).

4.2.3 Sediment transport model

Basic assumptions

Surface runoff, independently of occurring as overland flow or channel flow, has a certain capacity to transport sediment. If the actual load is below transport capacity, soil from the bed is eroded, whilst sediment is deposited in the reverse case. The following assumptions are set in the model:

- only bedload is considered as relevant regarding the magnitude of sediment transport and the evolution of debris flows. Suspended load is neglected;
- runoff is considered to follow hydraulic principles to a certain threshold of sediment concentration; at higher sediment concentrations it is considered as debris flow.

Detachment and sediment concentration

The RICKENMANN (1990) equation is used in the model for estimating sediment transport because it is best suited for relatively steep channels and high sediment concentrations. It only includes bedload.

The original equations, mainly derived from laboratory tests, yielded very high values of detachment when applied to the study areas. Furthermore, the equation does not say anything about detachment rates. For these reasons, the dimensionless calibration parameters ST_1, ST_2, ST_3, and ST_4 had to be introduced:

$$q_b = ST_1 \frac{12.6}{(s-1)^{1.6}} \left(\frac{D90}{D30}\right)^{0.2} (q - q_{cr})(\sin\alpha)^2 \qquad \text{Eq. 4.18,}$$

where q_b (m² s⁻¹) is the volumetric bedload transport per unit width, s is the ratio between grain and fluid densities, $D90$ and $D30$ (m) are the grain sizes where 90% and 30% per weight, respectively, are finer, q (m² s⁻¹) is the fluid discharge per unit width, and a (degree) is the local slope angle. q_{cr} (m² s⁻¹) is the threshold discharge for sediment transport:

$$q_{cr} = ST_2 0.065(s-1)^{1.67} g^{0.5} D50^{1.5} (\sin\alpha)^{-1.12} \qquad \text{Eq. 4.19,}$$

where $D50$ (m) is the median grain size, and g (m s⁻²) is the gravitational acceleration. Erosion (detachment of soil) or deposition d_w (m), depth of bedload l (m), and sediment concentration C (m³ m⁻³) can then be derived:

$$d_w = ST_3(l_0 - q_b/v) \text{ for } l_0 < q_b/v \qquad \text{Eq. 4.20,}$$

$$d_w = ST_4(l_0 - q_b/v) \text{ for } l_0 > q_b/v \qquad \text{Eq. 4.21,}$$

$$l = l_0 - d_w = q_b/v \qquad \text{Eq. 4.22,}$$

$$C = l/(l + R) \qquad \text{Eq. 4.23,}$$

where l_0 (m) is the depth of bedload at the start of the time step. Negative values of d_w (Eq. 4.20) indicate detachment, positive values (Eq. 4.21) indicate deposition. Only saturated soil is allowed to be detached. All the sediment deposited is considered as saturated, and the depth of the wetting front below the flow channel(s) is corrected for detachment and deposition. Eq. 4.20 to 4.22, which are not part of the original RICKENMANN model, are based on two rough generalizations:

- the bedload moves at the same velocity as the water;
- the bedload discharge immediately reaches an equilibrium (only if $ST_3 = ST_4 = 1$).

4.2.4 Slope stability model

The hydraulic model components supply saturated depth d (m). It is assumed that

- slope failures only occur at the depth d (the wetting front);
- if total soil depth is known, slope failures are also allowed to occur at the soil-bedrock interface, but only if the entire soil is saturated (mathematically identical to slope failures at the wetting front).

An infinite slope stability model (Figure 4.9) is used for the calculations. Therefore a wide ratio between slope length and depth of the failure plane is required in order to yield an acceptable approximation – a condition that is usually met for shallow, but not for deep-seated failures.

Furthermore, infinite slope stability models assume a translational failure mechanism, which usually only occurs in cohesionless soils. For cohesive soils, the model may still derive reasonable approximations of the factor of safety, but is – strictly spoken – not really applicable.

As discussed above, the infiltration model only considers vertical seepage. Infinite slope stability models, in contrast, usually assume a slope-parallel flow, exerting a destabilizing seepage force F_s (N) parallel to the slope (compare Eq. 4.31). In reality, the direction of the seepage depends on the local conditions, particularly on the presence or absence of an imperme-

able layer. Fully including the slope-parallel seepage into the slope stability calculations is therefore a worst-case assumption. The slope stability model is executed after the computation of the infiltration has been completed (last time step), so that a slope-parallel seepage can be assumed without contradiction to the vertical seepage computed with the Green-Ampt model.

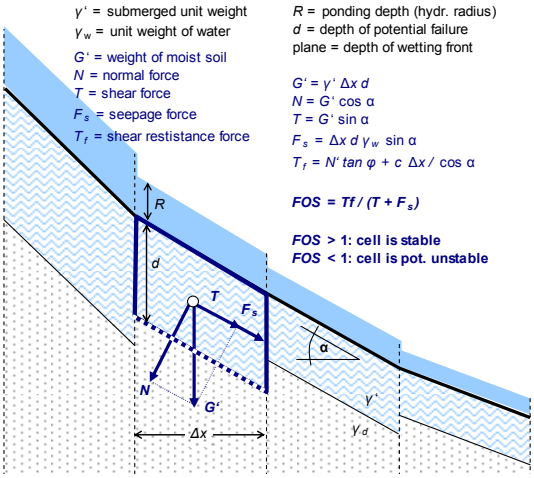

Figure 4.9: Mechanisms for infiltration and shallow slope failure as applied in the present study. For a detailed explanation compare text. Designed by M. Mergili.

The dimensionless factor of safety *FOS* is stated as

$$FOS = T_f / (T + F_s) \qquad \text{Eq. 4.24,}$$

where T_f is the shear resistance force of the soil, T is the shear force, and F_s is the seepage force (all in N; compare Figure 4.9). Shear resistance s (N m^{-2}) follows Coulomb's law:

$$s = c + \sigma(\tan\varphi) \qquad \text{Eq. 4.25,}$$

and the corresponding shear resistance force is

$$T_f = N' \tan\varphi + c \cdot \Delta x / \cos\alpha \qquad \text{Eq. 4.26,}$$

where N is the normal force, φ (degree) is the angle of internal friction, c (N m^{-2}) is the cohesion (soil cohesion c_s plus root cohesion c_r), Δx (m) is the length of the considered slope segment in downslope direction, and a (degree) is the slope angle. N and T (N) are computed from the weight of the moist soil G' (N):

$$G' = \gamma' \cdot \Delta x \cdot d \qquad \text{Eq. 4.27,}$$

$$N = G' \cos\alpha \qquad \text{Eq. 4.28,}$$

$$T = G' \sin\alpha \qquad \text{Eq. 4.29,}$$

where γ' (N m^{-3}) is the specific weight of saturated soil and d (m) is the depth of the potential failure plane:

$$\gamma' = \gamma_d + \gamma_w[\theta_s(1-s)-1] \qquad \text{Eq. 4.30.}$$

γ_d is the specific weight of dry soil, and γ_w is the specific weight of water (both in N m^{-2}). γ_d is derived from grain specific weight (to be specified by the user; 26.5 kN m^{-3} for quartzitic material), and θ_s and s as surrogates for pore volume.

The seepage force exerted by the soil water is stated as

$$F_s = \Delta x \cdot d \cdot \gamma_w \sin\alpha \qquad \text{Eq. 4.31.}$$

Dry and cohesionless soils ($F_s = 0$; $c = 0$; $\gamma' = \gamma_d$) are stable when $a < \varphi$, and unstable when $a > \varphi$.

The forces exerted by the surface water table R (m) are neglected in the model.

4.2.5 Debris flow runout

Initiation

Debris flows are supposed to occur within a certain range of sediment concentrations, usually between $C_{min} = 0.45$ and $C_{max} = 0.55$.

- At the end of the last time step, all cells identified as potentially unstable (with $FOS < 1$) during at least one time step are considered to fail at the deepest failure plane identified for the cell during the event. Failed soil with a sediment concentration of $C_{soil} < C_{max}$, where $C_{soil} = 1\text{-}\theta(1\text{-}s)$, is considered to evolve into a debris flow. In reality, debris flows with higher sediment concentration do occur, particularly in non-cohesive soils. The model therefore assumes that all failed soil with $c_s = 0$ develops into a debris flow also at at higher sediment concentrations;
- for every cell where runoff is modelled to evolve into a debris flow, sediment concentration C is tested against C_{min} after each time step. If $C > C_{min}$, the material is retained from sediment load. All retained material is routed downslope as debris flow at the end of the last time step.

Before routing the debris flow downwards, the volume and the size of each patch of cells of potential debris flow initiation are calculated. If one of these variables or the depth of potential initiation is below user-defined thresholds, the patch or the cell, respectively, is excluded from runout.

Routing procedure

The debris flow is not simply routed downwards the steepest slope. Similar to surface runoff, the routing algorithm is determined by the hydrological surface class:

- $HSC = 1$ (defined channel): the debris flow is routed through the channel with only one possible downward direction from each cell. As soon as deposition occurs in a channel, the corresponding cells are considered as $HSC = 2$ for the further simulation;

- $HSC = 2$ (no clearly defined channel): a random walk weighted for downslope angle is applied for routing the debris flow. The weight w is determined automatically as a function of the steepest slope. It is expressed as:

$$w = \alpha^{u_2} / \beta^{u_2 - 1} \qquad \text{Eq. 4.32,}$$

where the exponent u_2 has to be specified by the user (values between 3 and 5 appear reasonable). β (degree) is the slope angle where deposition starts (compare below; $w = 0$) for upslope angles. Similar to runoff, this algorithm accounts for the higher tendency of debris flows to take another than the steepest slope specified in the DEM on gentle slopes than on steep slopes.

Each cell containing starting material for a debris flow is passed through the routing procedure individually. Routing continues until the debris flow has stopped, according to the criteria specified in the next section.

Runout distance and deposition

Empirical-statistical approaches were used in the very first model versions (compare App. 2.2 and 2.3). However, these methods did not prove to be well applicable to the study areas without a lot of calibration. Therefore, in the latest model versions they were complemented and partly replaced by a two-parameter friction model.

Empirical-statistical approaches. The empirical approach of VANDRE (1985) is used in the first model versions for approximating debris flow runout distance and for determining the spatial patterns of entrainment and deposition (Figure 4.10), governed by the parameters β, ε, and υ:

- at a slope angle exceeding β, the debris flow continues unconditionally, and all soil material down to the depth of failure or erosion is entrained;
- at slope angles between β and ε, the debris flow continues until the distance criterion (see below) is fulfilled, and
- at slope angles lower than ε, the debris flow stops unconditionally.

The flow stops, too, if the following distance criterion is fulfilled:

$$\Delta s_{dep} > \upsilon \cdot \Delta z_{scr} \qquad \text{Eq. 4.33,}$$

where υ is a dimensionless empirical factor, Δs_{dep} (m) is the horizontal distance travelled on slopes between β and ε (area of deposition), and Δz_{scr} (m) is the vertical distance travelled on slopes exceeding β (area of entrainment). β, ε, and a have to be specified by the user. BURTON & BATHURST (1998) set $\upsilon = 0.4$, $\beta = 10°$, and $\varepsilon = 4°$. However, it has to be verified for each study area whether these values are applicable or not.

The patterns of deposition – depending on the specification by the user – are assumed either as even distribution or as wedge-shaped, increasing towards the front of the area of deposition. In the latter case, depth of deposition d_{dep} (m) is stated as:

$$d_{dep} = 2V_{dep} \cdot d_x / \Delta s_{dep}^2 \qquad \text{Eq. 4.34,}$$

where V_{dep} (m²) is the volume of material available for deposition per unit width (failed/detached soil plus entrained soil), and d_x (m) is the upslope distance to the point where deposition starts. It is assumed that the deposit has the same density as the same material at its place of origin.

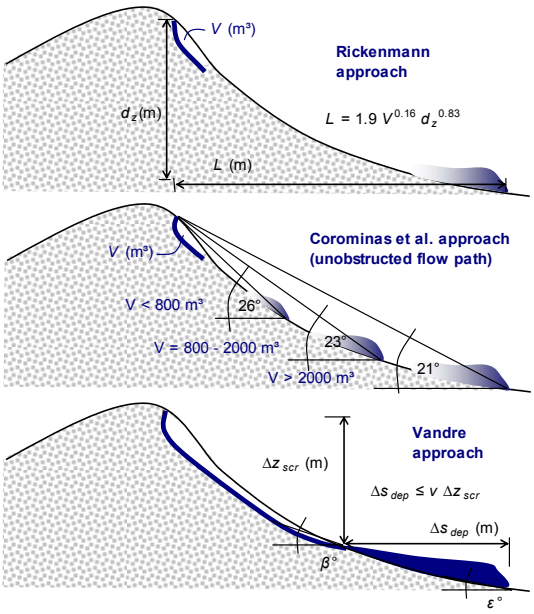

Figure 4.10: Debris flow movement and deposition model. For a detailed explanation see text. Designed by M. Mergili.

Complementary, the model also calculates the reach of the debris flow L (m) according to:

- the formula of RICKENMANN (1999; compare Figure 4.10):

$$L = 1.9 V^{0.16} d_z^{0.83} \qquad \text{Eq. 4.35,}$$

where V (m³) is debris flow volume, and dz (m) is the total elevation difference between starting point and the lowest point of deposition;

- and the rules specified by COROMINAS et al. (2003; compare Figure 4.10).

These approaches do not allow for estimating the spatial distribution of entrained and deposited volumes, but they serve for testing the plausibility of the choice of the parameters β and ε.

Two-parameter friction model. Complementary to the empirical-statistical approaches, runout is computed using a semi-deterministic two-parameter friction model developed by PERLA et al. (1980) which was modified by GAMMA (2000) and applied

by WICHMANN (2006) in a raster-based GIS environment. It is not only applicable to debris flows, but also to snow avalanches.

The deterministic element of the approach is the velocity of the debris flow v (m s^{-1}) which is computed for each raster cell i:

$$v_i = \sqrt{\zeta_i \left(\frac{M}{D}\right)_i \left(1 - e^{\eta_i}\right) + v_{i-1}^2 e^{\eta_i} \cos(\Delta\alpha_i)} \quad \text{Eq. 4.36,}$$

where M/D (m) is the mass-to-drag ratio of the debris flow, and v_{i-1} is the debris flow velocity of the previous cell. The factor ζ_i and the coefficient η_i are derived as follows:

$$\zeta_i = g(\sin\alpha_i - \mu\cos\alpha_i) \quad \text{Eq. 4.37,}$$

$$\eta_i = \frac{-2L_i}{(M/D)_i} \quad \text{Eq. 4.38,}$$

where g is gravitational acceleration (9.81 m s^{-2} on the earth surface), a_i is local slope angle, μ is the dimensionless friction coefficient, and L (m) is slope length (cell size corrected for slope angle). Δa is the difference between the slope angle of the previous cell and the slope angle of the considered cell which is set ot 0 for convex slopes or channels (WICHMANN 2006). For concave slopes, v_{i-1} is corrected as the flow loses energy:

$$v_{1-1} = v_{i-1,0}\cos(\alpha_{i-1} - \alpha_i) \text{ if } a_{i-1} > a_i \quad \text{Eq. 4.39.}$$

The first term in Eq. 4.36 determines if the flow accelerates ($\zeta > 0$) or decelerates ($\zeta < 0$), the second term provides the contribution of flow velocity to the final velocity. M/D, being a surrogate for the inertia of the flow, exerts a major influence on flow velocity, while its impact on runout distance is small. The latter is primarily determined by the topography and μ (GAMMA 2000; WICHMANN 2006). The simulation is stopped as soon as v_i becomes undefined (square root of negative value, compare Eq. 4.36).

One problem regarding the calibration of this model is that different combinations of the two parameters to be calibrated (M/D and μ) may result in the same runout distance. A common way for calibration is therefore to set M/D to values leading to realistic velocities, and then calibrating μ in order to correlate simulated and observed runout distances.

WICHMANN (2006) used values of M/D = 75 m. The following relationship for μ was found to be useful for computing the maximum runout length (GAMMA 2000):

$$\mu = 0.13A^{-0.25} \quad \text{Eq. 4.40,}$$

where A (km²) is the catchment size for the considered cell. It is assumed that μ would decrease with increasing A because the water content of the debris flow would increase. This relationship was used in *r.debrisflow*, but with user-defined factor and exponent in order to allow calibration for other conditions. Following GAMMA (2000), the range of values of μ would be restricted to a maximum of 0.3 and a minimum of 0.045, overruling Eq. 4.40.

The two-parameter friction model does not say anything about the patterns of particle entrainment and deposition. Instead of designing a more complex scheme like WICHMANN (2006), simple thresholds of slope and velocity are used for delineating these processes in *r.debrisflow*, where entrainment (as far down as to the wetting front) is only assumed if both parameters are above the threshold, whilst deposition is assumed to take place only if both parameters are below the thresholds. The calibration of the thresholds is connected to the same problems as the calibration of M/D and μ (different combinations of parameter values).

4.2.6 Implementation into GRASS GIS

r.debrisflow was designed as a raster module for the Open Source GIS software *GRASS*, based on the programming language *C*. It was developed under a *UNIX* environment.

Functions for facilitating preparation of the input datasets (compare Tables 4.2 and 4.4), running the model, and displaying and exporting the model results were put together in the shell script *r.debrisflow.sh*.

For detailed instructions regarding the operation of *r.debrisflow* and *r.debrisflow.sh* and for a comprehensive table with the required input information please consult App. 3.1.

4.3 The model framework r.avalanche

Within *r.debrisflow*, debris flow runout is computed using a two-parameter friction model following PERLA et al. (1980), GAMMA (2000) and WICHMANN (2006). Although such models have their advantages, they also show some shortcomings – the influence of landslide mass on runout, for example, is not included on a physical base, but only indirectly by the mass-to-drag ratio M/D. It is therefore not possible to use such models for class A predictions.

r.avalanche was developed complementary to *r.debrisflow* in order to overcome this problem. It provides a fully deterministic model for the motion of granular flows (suitable not only for debris flows, but also for other types of mass movements like flow avalanches). *r.avalanche* builds on a solution of the Savage-Hutter (SH) model (compare Section 2.2) for simple concave topographies with an only vertically curved flow line, running out into a horizontal plane (WANG et al. 2004; Figure 4.11). The current release of *r.avalanche* is therefore only suitable for a simple terrain with straight channels. Future development,

however, shall be directed towards overcoming this problem (compare Section 6.5).

A curvilinear coordinate system is used instead of a simple rectangular system (compare Figure 4.11).

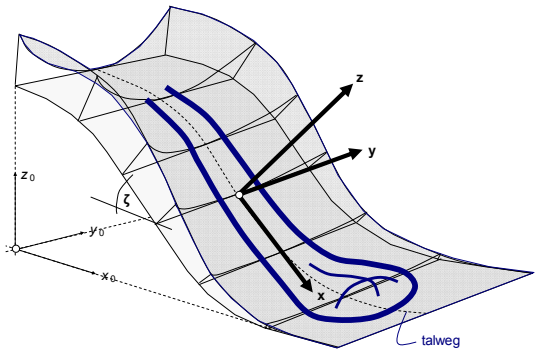

Figure 4.11: The topography for which the solution of the SH model used in *r.avalanche* was elaborated (modified from WANG et al. 2004).

4.3.1 Model layout

r.avalanche requires far less input than *r.debrisflow* as it only simulates one part of the process. In contrast, the mathematical-technical concept behind *r.avalanche* is much more complex. A full description of the way how the SH model was solved for this specific topographic situation would go beyond the scope of this thesis – a detailed description is given by WANG et al. (2004). The most fundamental aspects are summarized below.

Eq. 4.41 to 4.43 are the basis of the SH model:

$$\frac{\partial h}{\partial t}+\frac{\partial}{\partial x}(hu)+\frac{\partial}{\partial y}(hv)=0 \qquad \text{Eq. 4.41,}$$

$$\frac{\partial}{\partial t}(hu)+\frac{\partial}{\partial x}\left(hu^2\right)+\frac{\partial}{\partial y}(huv)=hs_x-\frac{\partial}{\partial x}\left(\frac{\beta_x h^2}{2}\right),$$

Eq. 4.42 top Eq. 4.43 bottom

$$\frac{\partial}{\partial t}(hv)+\frac{\partial}{\partial x}(huv)+\frac{\partial}{\partial y}\left(hv^2\right)=hs_y-\frac{\partial}{\partial y}\left(\frac{\beta_y h^2}{2}\right).$$

h is the avalanche thickness, and u and v are the depth-averaged downslope and cross-slope velocities. s_x and s_y are the net driving accelerations:

$$s_x=\sin\varsigma-\frac{u}{\sqrt{u^2+v^2}}\tan\delta(\cos\varsigma+\lambda\kappa u^2)-\varepsilon\cos\varsigma\frac{\partial b}{\partial x},$$

Eq. 4.44 top Eq. 4.45 bottom

$$s_y=-\frac{u}{\sqrt{u^2+v^2}}\tan\delta(\cos\varsigma+\lambda\kappa u^2)-\varepsilon\cos\varsigma\frac{\partial b}{\partial y},$$

where ζ is the downslope inclination angle of the reference surface, $\varkappa$ is the local curvature of the reference surface, b is the elevation above the reference surface, and ε and λ are factors (compare Table 4.8 and Section 4.3.2). β_x and β_y are defined as

$$\beta_x=\varepsilon\cos\varsigma K_x \qquad \text{Eq. 4.46,}$$

$$\beta_y=\varepsilon\cos\varsigma K_y \qquad \text{Eq. 4.47.}$$

K_x and K_y are the earth pressure coefficients in downslope and cross-slope directions.

$$K_{x,act/pass}=2\left(1\mp\sqrt{1-\cos^2\varphi/\cos^2\delta}\right)\sec^2\varphi-1,$$

Eq. 4.48 top Eq. 4.49 bottom

$$K_{y,act/pass}=\frac{1}{2}\left(K_x+1\mp\sqrt{(K_x-1)^2+4\tan^2\delta}\right).$$

φ is the angle of internal friction, and δ is the bed friction angle. Active stress rates (subscript *act*) are connected to dilatation of the material, passive stress rates are connected to compression – it depends on acceleration or deceleration of the flow whether active or passive stress rates are valid (compare WANG et al. 2004). Eq. 4.48 and 4.49 are only valid as long as the flow moves predominantly in downslope direction.

The system of equations described above is only valid for cohesionless and incompressible granular materials which can be considered as fluid continuum. It has to be emphasized that all variables are dimensionless, meaning that the model is scale-invariant and small-scale laboratory tests can be used as reference for large-scale problems in nature.

The differential equations Eq. 4.41 to 4.43 were solved using a NOC (Non-Oscillatory Central Differencing) scheme, a numerical scheme useful to avoid unphysical numerical oscillations. Cell averages are computed using a staggered grid, meaning that the system is moved half of the cell size with every time step (the values at the corners of the cells and in the middle of the cells are computed alternatively). The numerical scheme derived by WANG et al. (2004) was used for *r.avalanche*.

The degree of diffusion of the flow material is governed by using slope limiters, restricting the gradients of flow depth to a certain range. The so-called minmod limiter has already been used by WANG et al. (2004) and also for the present thesis since it is known as the most diffusive one, reducing numerical oscillations.

The simulation is run for a number of time steps until a certain break condition is fulfilled. The time steps have to be kept short enough to fulfil the CFL (Courant-Friedrichs-Levy) condition required for obtaining smooth solutions:

$$CFL_x=\max_{alli,j}\frac{\left|u_{i,j}\right|+\sqrt{(\beta_x)_{i,j}h_{i,j}}}{\Delta x_i} \qquad \text{Eq. 4.50,}$$

$$CFL_y=\frac{\max_{alli,j}\left[\left|v_{i,j}\right|+\sqrt{(\beta_y)_{i,j}h_{i,j}}\right]}{\Delta y} \qquad \text{Eq. 4.51,}$$

where Δx and Δy are the cell sizes in x and y direction and i and j are the coordinates of the cells in x and y direction, respectively. The length of one time step Δt has to be smaller than 0.5 times the minimum from CFL_x and CFL_y. Δt is determined dynamically while running ***r.avalanche***, based on the CFL condition from the previous time step. Instead of 0.5, a factor of 0.2 was chosen in order to add some tolerance.

4.3.2 Implementation into GRASS GIS

Analogous to ***r.debrisflow***, ***r.avalanche*** was developed as a raster module for GRASS GIS, using the ***C*** programming language. An additional shell script (***r.avalanche.sh***) facilitates data management (input and display). Raster maps and a set of parameters compiled in a text file serve as input (Table 4.8). For a detailed manual please consult App. 3.2.

The implementation of the SH model and its solution by WANG et al. (2004) into GIS bears two problems:

(1) the solution provides dimensionless values – in the GIS, however, it is necessary to use dimensional values;

(2) the solution is valid for a curvilinear reference system only, in contrast to a GIS which usually uses a simple rectangular system.

Dimensionalization of the variables

The first problem was solved using equations from PUDASAINI (2003). They are based on the variables L, H, and R (compare Table 4.8). L is the typical avalanche length, H is the typical avalanche depth, and R is the typical radius of curvature (all in meters). Dimensional variables are derived using

$$\hat{x} = Lx \quad \text{Eq. 4.52,} \qquad \hat{y} = Ly \quad \text{Eq. 4.53,}$$

$$\hat{h} = Lh \quad \text{Eq. 4.54,} \qquad \hat{u} = u\sqrt{gL} \quad \text{Eq. 4.55,}$$

$$\hat{v} = v\sqrt{gL} \quad \text{Eq. 4.56,} \qquad \hat{t} = t\sqrt{L/g} \quad \text{Eq. 4.57,}$$

$$\hat{\kappa} = R\kappa \quad \text{Eq. 4.58,}$$

where the variables denoted with a cap are the dimensional counterparts of the variables discussed above and g is gravitational acceleration (9.81 m s^{-2} on the earth surface). ***r.avalanche*** proved to work best when setting x, y, and h to the dimensional values (in m) while setting L, H, and R to 1. The factors $\varepsilon = L/H$ and $\lambda = L/R$ (PUDASAINI 2003) were therefore 1. This contradicts the statement by WANG et al. (2004) that the factors should be far lower than 1, but appears appropriate when using dimensional values from the beginning with h being much smaller than the length of the flow.

Adaptation of the coordinate system

The solution of WANG et al. (2004) builds on a curvilinear coordinate system based on a horizontally straight "talweg" which shall be the predominant flow direction. Three steps are performed for converting the original rectangular coordinate system in which the input raster maps are provided into the coordinate system for the simulation:

(1) the coordinate system is rotated around the z axis so that the expected predominant flow direction derived from the starting material and the elevation model is aligned with the new x direction. This rotation is based on two user-defined pairs of coordinates in the flow channel (compare Table 4.8);

(2) a reference surface is created, based on the defined "talweg" and an inclination of zero in y (cross-slope) direction;

(3) based on this reference surface, the cell size Δx for each x parallel to the reference surface is computed. The elevation h (m) – defined as the distance between terrain surface and reference surface perpendicular to the reference surface – is derived. This has to be done iteratively, varying the horizontal shift until the tested value of h converges with terrain height (Figure 4.12).

After completing the calculation, the entire system is reconverted into the rectangular coordinate system used in the current GRASS GIS mapset in order to enable a proper display of the results.

Table 4.8: Input information required for running *r.avalanche*.

map/parameter	symbol (unit)	input format	description
catchment	– (boolean)	raster map	catchment of interest map
elev	z (m)	raster map	elevation map
delta	δ (degree)	raster map	basal angle of friction map
riskobj	– (boolean)	raster map	objects at risk (1 = present, 0 = absent)
dinit	h_0 (m)	raster map	starting material map
phi	φ (degree)	value	angle of internal friction of the debris flow material
L	L (m)	value	typical avalanche length (recommended: 1; compare text)
H	H (m)	value	typical avalanche depth (recommended: 1; compare text)
R	R (m)	value	typical radius of curvature (recommended: 1; compare text)
deltatout	Δt_{out} (s)	value	interval between writing output
tmax	t_{max} (s)	value	time of simulation until it stops
vmin	v_{min} (m s^{-1})	value	velocity at maximum flow depth at which simulation stops
xchan1, ychan1	– (m)	values	coordinates of first point in flow channel (for rotating coordinate system)
xchan2, ychan2	– (m)	values	coordinates of second pt. in flow channel (for rotating coordinate system)

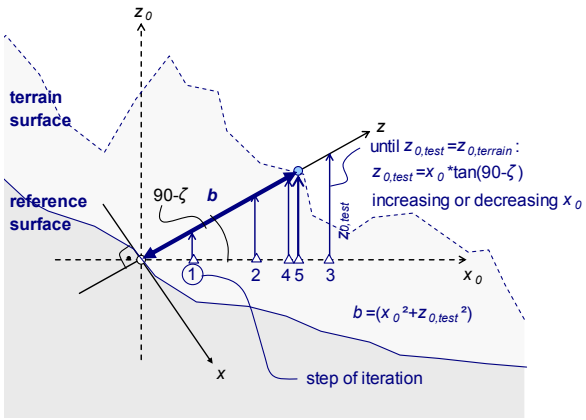

Figure 4.12: Iterative determination of *b* based on the coordinate system defined by the reference plane. Designed by M. Mergili.

Figure 4.13: Longitudinal profiles through a debris flow or avalanche running over simple topography, comparing the influence of different bed friction angles. All units are in meters, avalanche depth is 15-fold exaggerated.

4.3.3 Test with simple artificial topographies

Before being used for the study areas, *r.avalanche* was tested for two simple topographies exactly corresponding to those it was developed for:

(1) a simple plane slope with an inclination of 35°, running out into a horizontal plane. The simulation was run with four combinations of φ (32° and 37°) and δ (23° and 28°). Maps and cross sections illustrating the results are shown in the Figures 4.13 to 4.15 – only the results for φ = 32° are represented since no significant influence of φ was found in the results, what is in line with WANG et al. (2004);

(2) and an inclined U-shaped valley running out into a horizontal valley – the results are illustrated in Figure 4.16.

In general, the results corresponded well to those shown by WANG et. al. (2004), except for some oscillations which appear unphysical and are probably caused by numerical issues.

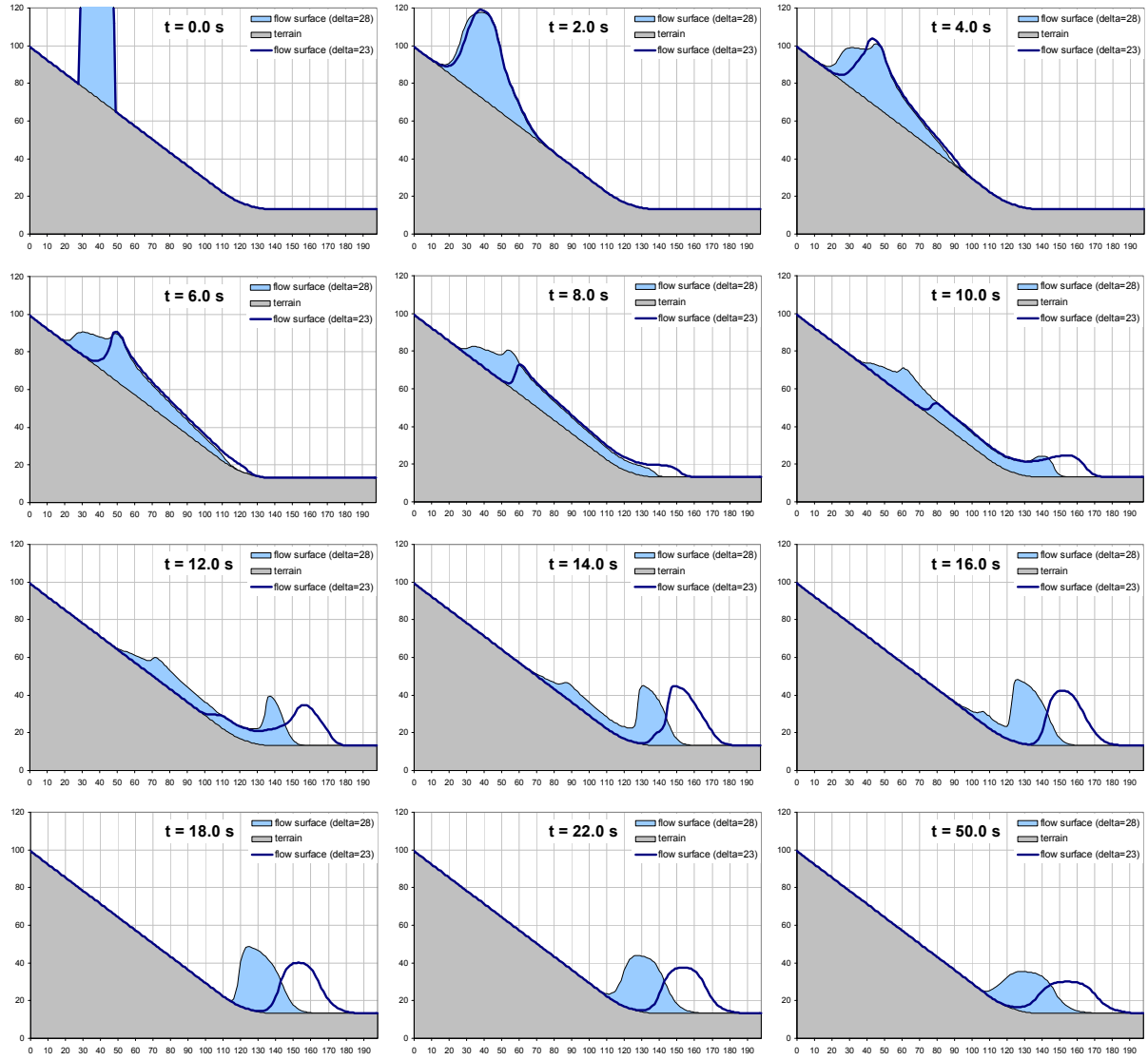

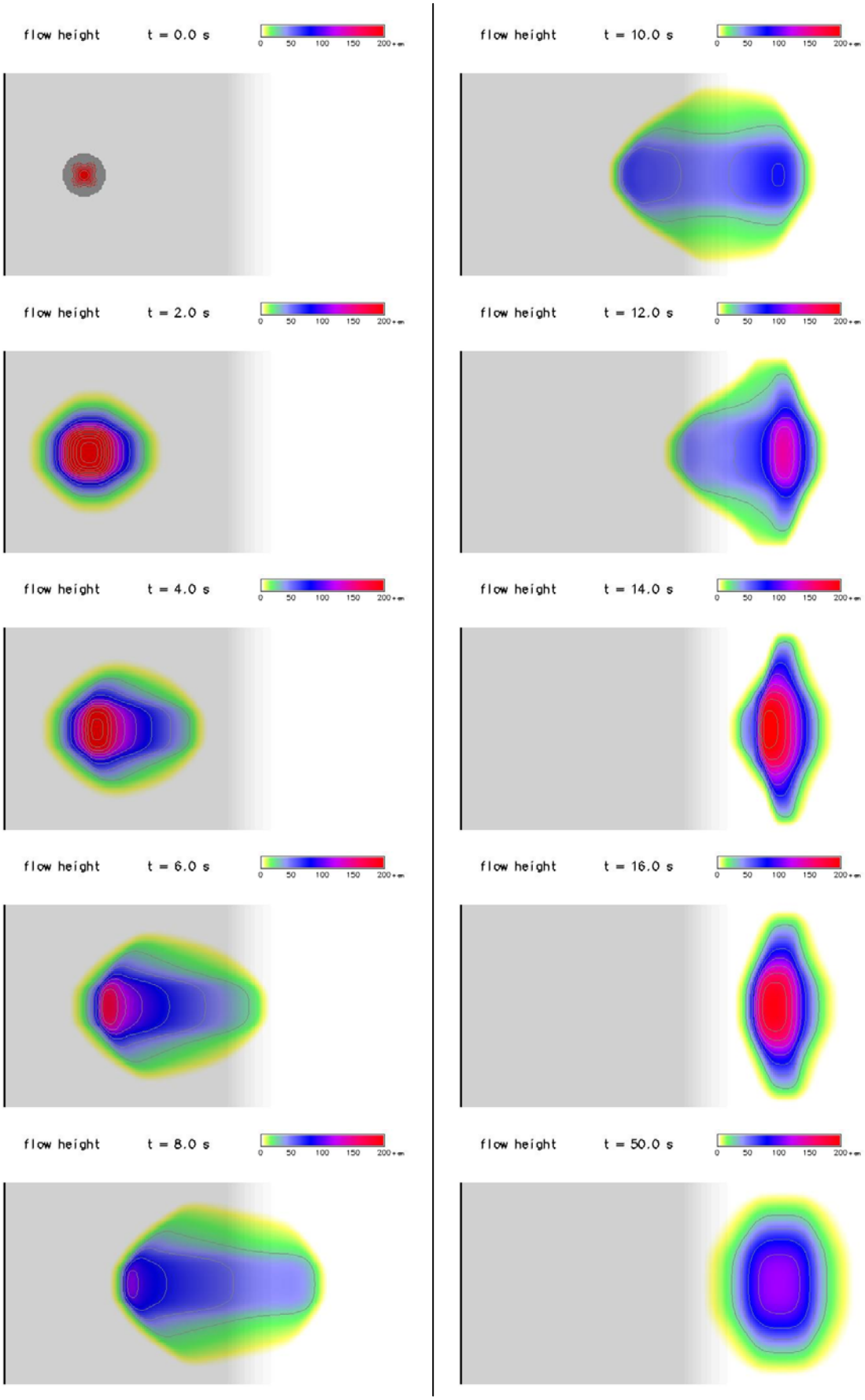

Figure 4.14: Debris flow runout over simple topography (inclined plane running out into a horizontal plane, compare Figure 4.13) with a bed friction angle $\delta = 23°$.

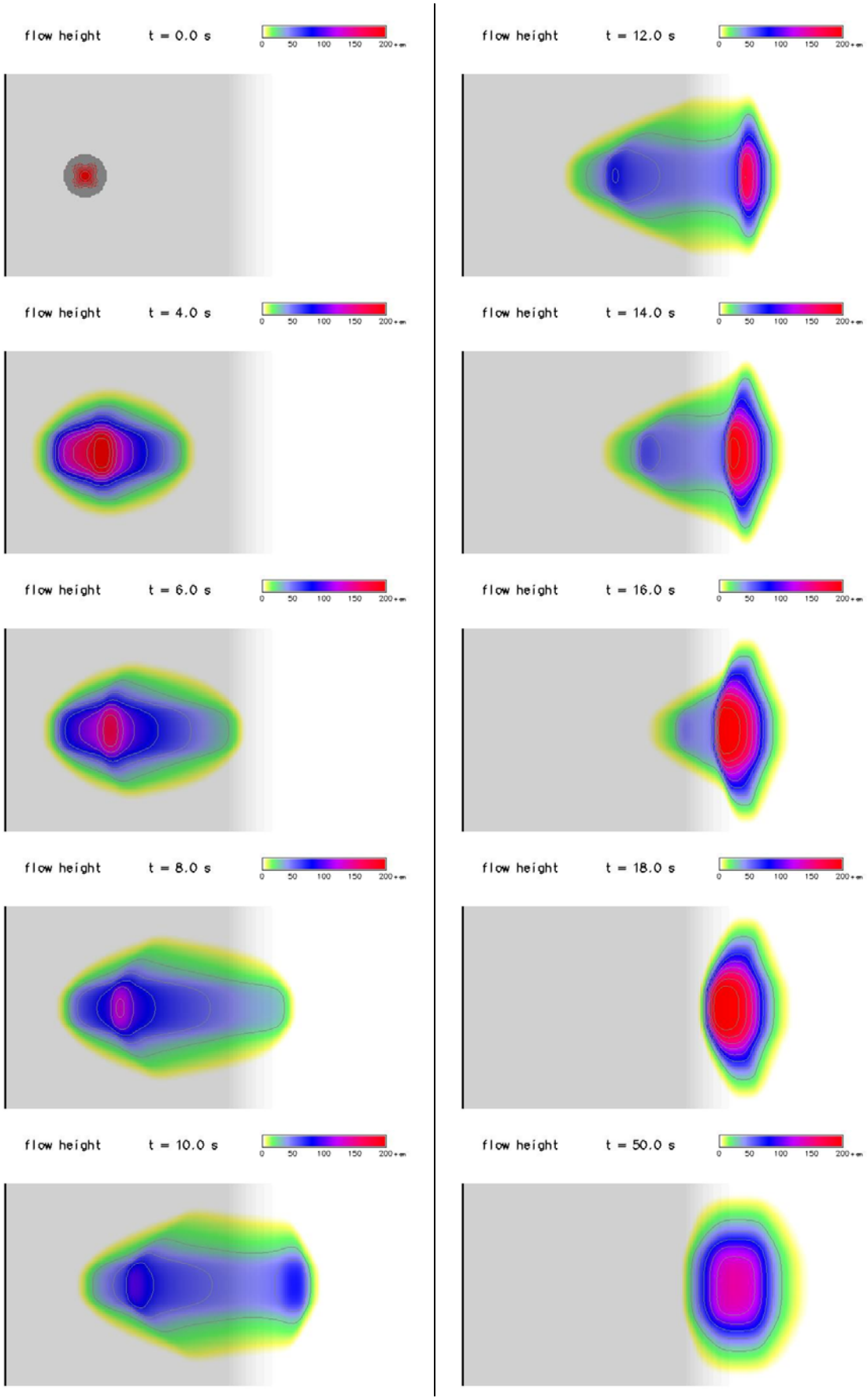

Figure 4.15: Debris flow runout over simple topography (inclined plane running out in horizontal plane) with a bed friction angle δ = 28° - the shorter runout distance compared to a bed friction angle of 23° is clearly recognizable (compare Figures 4.13 and 4.14).

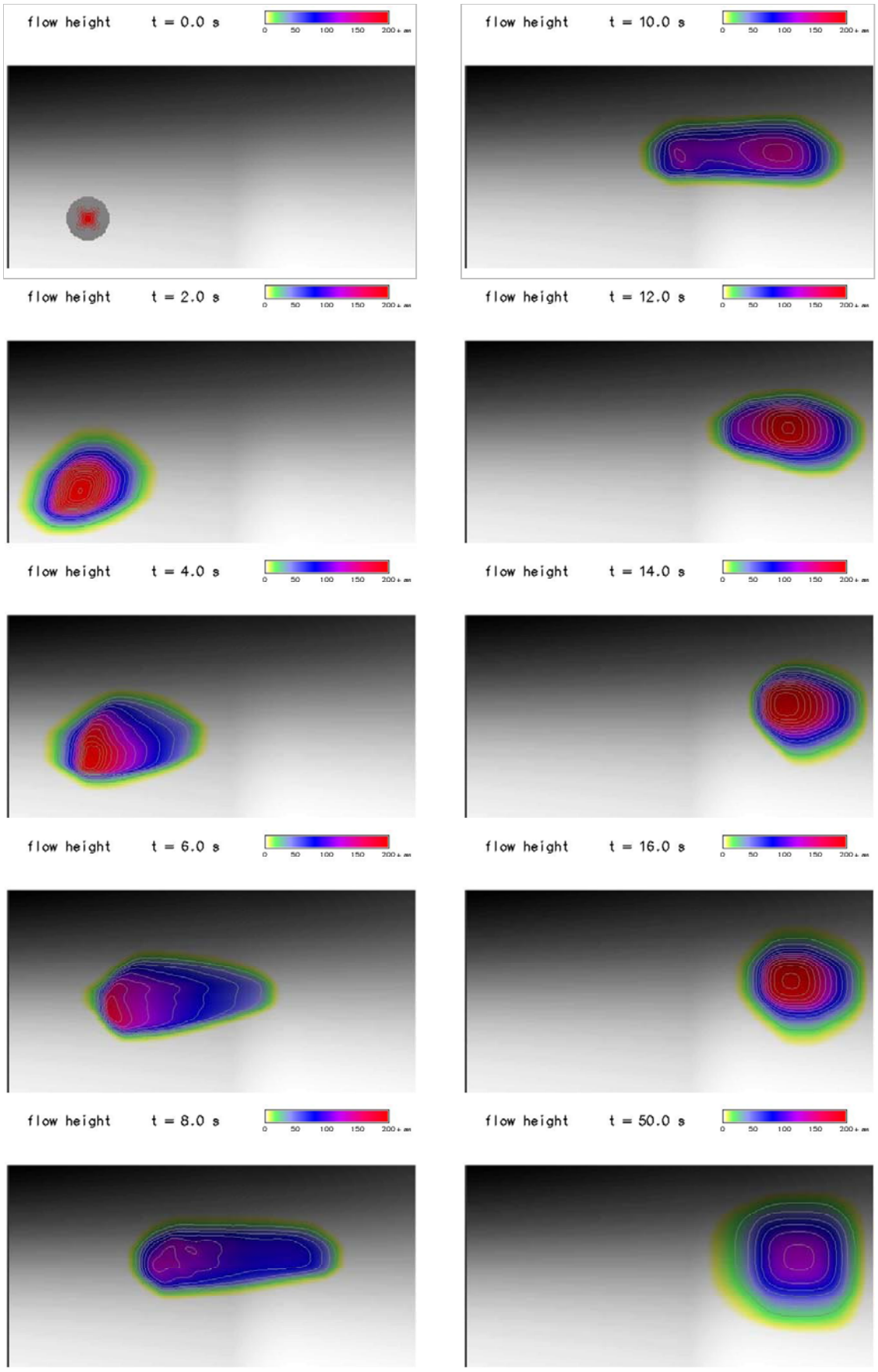

Figure 4.16: Debris flow runout through an inclined U-shaped valley running out into a horizontal valley, simulated with *r.avalanche*.

4.4 Model evaluation

4.4.1 r.debrisflow

Like all simulation models of processes in nature, the one discussed here is based on a number of assumptions. Not all required parameters are fully known. This means that the model results had to be validated with data on real debris flows and to be tested for its sensitivity to variations of uncertain parameters.

The information available for the study areas of the present thesis allowed the following steps for evaluating the model results:

- for some specific events, the sediment volumes to be removed from the international road according to official reports were compared to the volumes deposited on the road calculated by the model;
- for some events, the patterns of deposition provided by the model were validated with the patterns shown on published photos;
- landslide scars, flow channels, and the maximum extent of debris flow deposits recorded in the field and from aerial images were compared to the model results.

Model scenarios

Table 4.9 shows the scenarios used for model evaluation regarding rainfall-triggered debris flows. The scenarios of type r are based on real historic events (compare Table 4.6), while those marked with wc assume worst case meteorological conditions for the *Guido* area, based on the highest value for daily precipitation ever recorded at the Guido meteorological station. For all simulations for the *Guido* area, it is assumed that the moisture content of the soil at the start of the scenario corresponds to θ_r (compare Table 4.2).

It was decided not to use meteorological scenarios for the snow melt-triggered debris flows in the study area *Quebrada del Ferrocarril*. Though technically possible with *r.debrisflow* (compare Section 4.2), the uncertainties with the snow melt model would have been to large and too difficult to assess; furthermore, most of the debris flows were triggered by the kinetic energy of surface runoff, and computing surface runoff in the model for the required long time span would have resulted in unacceptably long computing times. Therefore, only the runout model was used for this study area with observed areas of initiation (compare Section 5.1).

For *Guardia Vieja* it did not make much sense to use the full model, either, due to the long duration of the rainfall. Instead, the maximum depth of saturation was computed manually and applied to the slope stability and runout models (compare Section 5.2).

For all of the study areas, each model component used was first tested for the plausibility of the results before running the scenarios.

Analysis of sensitivity

The occurrence or non-occurrence of debris flows as a response to a given meteorological constellation depends on an array of parameters. These parameters are often uncertain, particularly regarding their spatial distribution. For the land cover parameters, this problem was partly tackled by working with a range of values.

However, a careful analysis of sensitivity was needed for assessing the dependency of debris flow occurrence in the study areas on variations of the key parameters or of certain assumptions.

It would have been too much effort to test the sensitivity to all parameters used in the model. Therefore, only the following key parameters and assumptions were varied when running the model framework *r.debrisflow* for the analyses of sensitivity:

- soil and root cohesion c_s and c_r;
- angle of internal friction φ;
- memberships of cells to different land cover classes;
- soil hydraulic properties;
- pre-wetting of the soil prior to the considered rainfall event;
- degree of percolation of rainfall through exposed bedrock;
- parameters for the runout model;
- influence of soil water (buoyancy, seepage forces) on slope stability;
- spatial resolution.

Table 4.10 summarizes the analyses of sensitivity applied to each study area.

4.4.2 r.avalanche

r.avalanche was tested against field observations using different starting volumes and a range of values for bed friction angle δ, the latter having the most prominent influence on the simulation results as shown by WANG et al. (2004) and in Section 4.3.3. Tests for the sensitivity of the model to changes of spatial resolution were performed, too.

The model was not used for all study areas, but only for those with suitable, relatively simple topographies and more or less straight flow channels (*La Ampolleta*, *Castillo de Rocas*, *Guardia Vieja*). With *Quebrada Escondida*, the problems arising when using the model for curved flow channels are shown.

Table 4.9 (top): Scenarios used for model validation with rainfall-triggered debris flows. *P* = sum of rainfall, *d* = duration of rainfall; d_t = period of transition between no rainfall and steady-state rainfall; *p* = maximum rainfall intensity; LA = La Ampolleta; QE = Quebrada Escondida; CR = Castillo de Rocas; LM = Las Murallas; QF = Quebrada del Ferrocarril; GV = Guardia Vieja; r = real debris flow-triggering event (regarding rainfall sum); wc = worst-case scenario (compare Table 4.6 and Figure 4.6).

Table 4.10 (bottom): Choice of parameters and assumptions for the analyses of sensitivity. For names of study areas please consult Table 4.9.

scenario	*P*	met. station	type	*d*	d_t	*p*	study areas					
	mm			min	min	mm h^{-1}	LA	QE	CR	LM	QF	GV
458/–	458	Río Blanco	r	undef.	undef.	undef.						x
100/80	100	Guido	wc	80	2 x 10	100	x	x	x	x		
100/140	100	Guido	wc	140	2 x 10	50	x	x	x	x		
40/40	40	Guido	r	40	2 x 10	80	x	x	x			
40/80	40	Guido	r	80	2 x 10	40	x	x	x	x		
40/140	40	Guido	r	140	2 x 10	20	x	x	x	x		
10/180	10	Guido	r	80	2 x 10	10	x	x	x			

parameter/assumption	description of test	LA	QE	CR	LM	QF	GV
angle of internal friction φ	assuming a decrease in angle of internal friction			x			
soil cohesion *c*	assuming an increase in soil cohesion			x	x		
soil hydr. conductivity *K*	assuming values of *K* according to CARSEL & PARRISH (1988)	x					
land cover class	assumption that no vegetation exists in the study area		x				
root cohesion	assumption that no root cohesion is active			x			
influence of vegetation	assumption that no slope failures are possible in vegetated soil						x
percolation through rock	assuming that 50 % of rainfall on bedrock percolates out of the considered system through fissures and cracks		x				
water storing capacity of the soil, f(θ_r, θ_s, *s*)	assuming upper and lower thresholds						x
preferential flow f_p	assumption that preferential flow through macropores accounts for 75 % of total seepage (following SUKHIJA et al. 2003)	x					
pre-wetting of soil	assumption that relative saturation of the soil is 50 % at the start of simulation						x
spatial resolution	increase or decrease of spatial resolution for simulation to 5 m for standard of 10 m and to 10 m for standard of 5 m		x	x	x	x	x
influence of soil water	excluding the influence of soil water on slope stability (setting the specific weight of water to zero)	x	x	x	x		x
parameters for runout model	assuming different values of slope and velocity thresholds for entrainment/deposition, mass-to-drag ratio, friction coefficient and maximum depth of deposition					x	

5 Results

The simulation models *r.debrisflow* and *r.avalanche* were introduced in detail in Chapter 4. They were tested with a set of study areas (compare Chapter 3) for selected rainfall scenarios and assumptions of uncertain parameter values (compare Tables 4.9 and 4.10). The following sections provide a detailed summary of the simulation results for each study area. The thin black lines shown in the maps delineate observed potential starting areas of debris flows, the bold black lines delineate observed or reported deposits.

Important aspects directly concerning one or a few study areas are discussed directly with the results. Broader aspects and implications are treated in detail in the general discussion in Chapter 6.

5.1 Quebrada del Ferrocarril

The study area *Quebrada del Ferrocarril* (Figure 5.1) is located near the ski resort of Portillo upslope of Juncal in the uppermost portion of the Aconcagua basin, close to the Argentine border (compare Chapter 3). Three voluminous debris flows triggered by snow melt were reported in the previous years (HAUSER 2000b; 2005). The flows in the area are channelized debris flows, mobilized by surface runoff and subsequent slope erosion. The simulations for this study area were performed with defined starting areas according to field evidence. The runout model was tested with various combinations of parameters (Table 5.1). Entrainment of soil was allowed down to a depth of 1 m.

Figure 5.1: The study area *Quebrada del Ferrocarril* (compare Section 3.7). The thin white lines represent potential starting areas of debris flows according to field evidence, the bold white lines show debris flow deposits. Elevation model and orthophoto derived from ASTER, GPS points, and aerial imagery. Design: Martin Mergili, 04/2008.

Table 5.1: Parameter settings and scenarios for the study area *Quebrada del Ferrocarril*. soil = soil parameters, lcov = land cover parameters, n/sed = Manning's n and parameters for sediment transport, pflow = preferential flow (per cent of total seepage), runout = parameters for runout model, res = spatial resolution, A = hydraulic model, B = sediment transport model, C = slope stability model, D = debris flow runout model; std = standard parameters, test = changed parameters for analysis of sensitivity.

		Parameter settings						Used modules			
		soil	lcov	n/sed	pflow	runout	res (m)	A	B	C	D
Test of plausibility and analysis of sensitivity (defined areas of mobilization)											
1	Standard parameters					std	5				x
2	Friction coefficient μ					test	5				x
3	Mass-to-drag ratio *M/D*					test	5				x
4	Slope and velocity thresholds for entrainment/deposition					test	5				x
5	Friction coefficient μ					test	5				x
6	Spatial resolution					test	10				x

5.1.1 Test of plausibility and analysis of parameter sensitivity for predefined starting areas

1 Initial settings. When using the defined starting areas (Figure 5.2), the standard parameters for computing runout length according to GAMMA 2000 (compare Eq. 4.40), and slope and velocity thresholds for entrainment/deposition of 15° and 10 m s^{-1}, respectively, the simulation yielded a significant underestimation of runout length – debris flows were modelled to stop in the upper and intermediate sections of the channels, not at all reaching the international road (Figures 5.3 and 5.4).

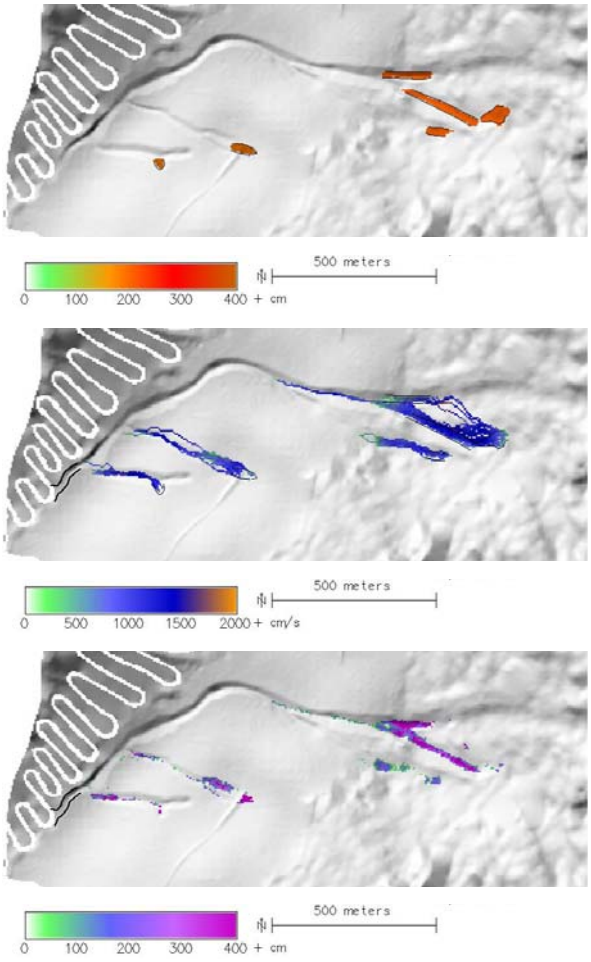

Figure 5.2 (top): Defined starting areas.
Figure 5.3 (middle): Maximum velocity of debris flows.
Figure 5.4 (bottom): Deposition from debris flows – in contrast to observations, the international road is not reached at all.

2 Friction coefficient. The major parameter determining runout length of debris flows in two-parameter friction models is the bed friction angle μ. Because debris flows in the area are triggered by run-off from rapid snow melt, they may contain much water and even some snow, significantly reducing bed friction. The Figures 5.5 to 5.7 show the simulation results for a constant bed friction angle of $\mu = 0.045$, which is the minimum value for channelized debris flows according to GAMMA (2000). The sediment balance (compare Figure 5.7), referring to each raster cell, is expressed as a vertical depth or height and has to be multiplied with the horizontal surface area of the cell in order to be quantified as a volume.

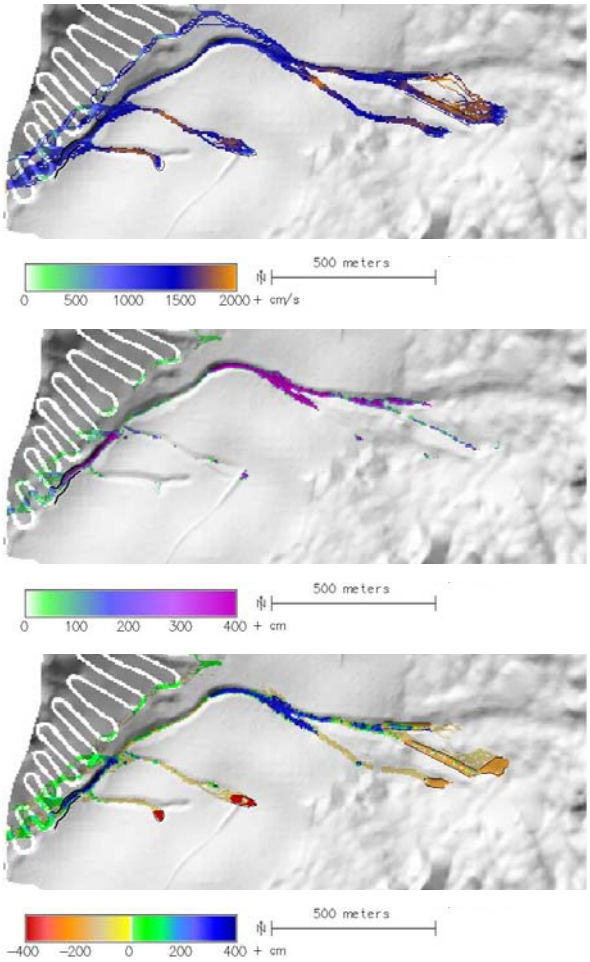

Figure 5.5 (top): Maximum velocity of debris flows.
Figure 5.6 (middle): Deposition from debris flows.
Figure 5.7 (bottom): Sediment balance from debris flows.

Runout length now corresponded much better to observations – it was reported that the lowermost curves of the road were hit by the debris flows, too (HAUSER 2000b). The modelled deposition in the intermediate portion of the channel was realistic but, however, the deposits are so thick (their maximum thickness was restricted to 4 m in the simulation) that part of the debris flows broke out of the channel directly invading the international road. Though this scenario is not unrealistic when looking at the local topography, no field evidence or report of such a behaviour of debris flows was found.

The simulation yielded the following results: In addition to the 36,100 m³ of defined starting mass, 41,700 m³ were entrained. out of a total of 77,800 m³, 5,100 m³ were deposited on the international road, but largely in places where it was not expected when looking a the reference information (compare Table 5.2).

3 Mass-to-drag ratio. When giving more power to the debris flow by increasing the mass-to-drag ratio from $M/D = 75$ to $M/D = 250$, the outbreak behaviour was not observed any more due to higher flow velocities and less deposition, but the majority of the debris flow stopped too far upwards, another portion was deposited farther downwards and the reported patterns of deposition were not matched by the simulation results (Figure 5.8). Only the outbreak of the debris flow upslope from the reported deposit is in line with HAUSER (2005). According to the simulation, 37,200 m³ of soil were entrained, 1,200 m³ out of 78,300 m³ were deposited on the international road (compare Table 5.2).

With this setting of parameters, the maximum velocity of the debris flows exceeded 20 m s^{-1} over a large portion of the uppermost sections of the channel system (Figure 5.9). Due to the steepness of these parts such high velocities appear realistic. COSTA (1984) reported about debris flow velocities up to 20 m s^{-1} for channels with a slope of maximum 20°).

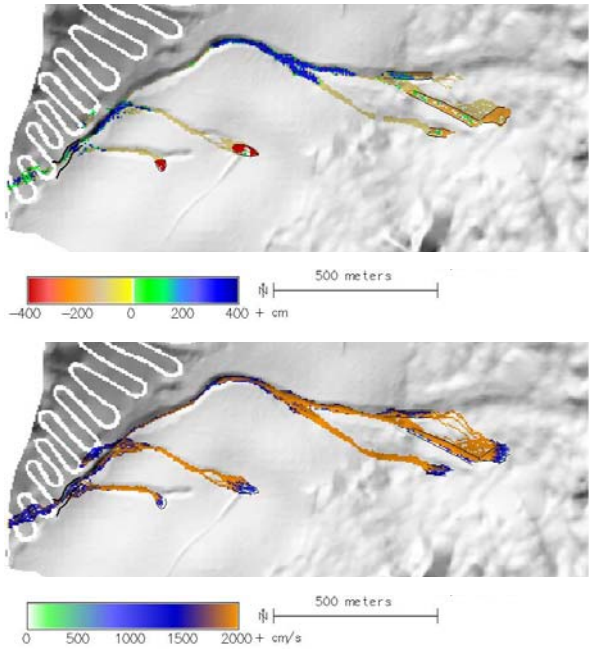

Figure 5.8 (top) Sediment balance from debris flows.
Figure 5.9 (bottom) Maximum velocity of debris flows.

4 Slope and velocity thresholds. Realistic simulation results were yielded when setting $M/D = 75$ and $\mu = 0.045$, but decreasing the slope threshold for entrainment and deposition to from 15° to 8° while keeping the velocity threshold at 10 m s^{-1}.

48,000 m³ of soil were entrained according to the simulation, leading to a deposit of 84,000 m³. The 9,800 m³ deposited on the international road (compare Table 5.2) are within the range reported by HAUSER (2005; 8,000 – 14,000 m³). Also the patterns of deposition correspond well to the reports. Some of the material was deposited in the intermediate part of the channel, but most ended up in the lower part upslope of the road, where maximum depths of debris flow material of 4 m were reported (HAUSER 2000b). A lot of the material reached the road at Curve 6 (where the large observed deposit is shown in the maps), and invaded also the lowermost curves. The invasion of Curve 10 farther upwards is also recognizable, but less pronounced than in the simulation discussed above. However, all in all, the reach of the debris flow might be somewhat overestimated (Figures 5.10 to 5.13).

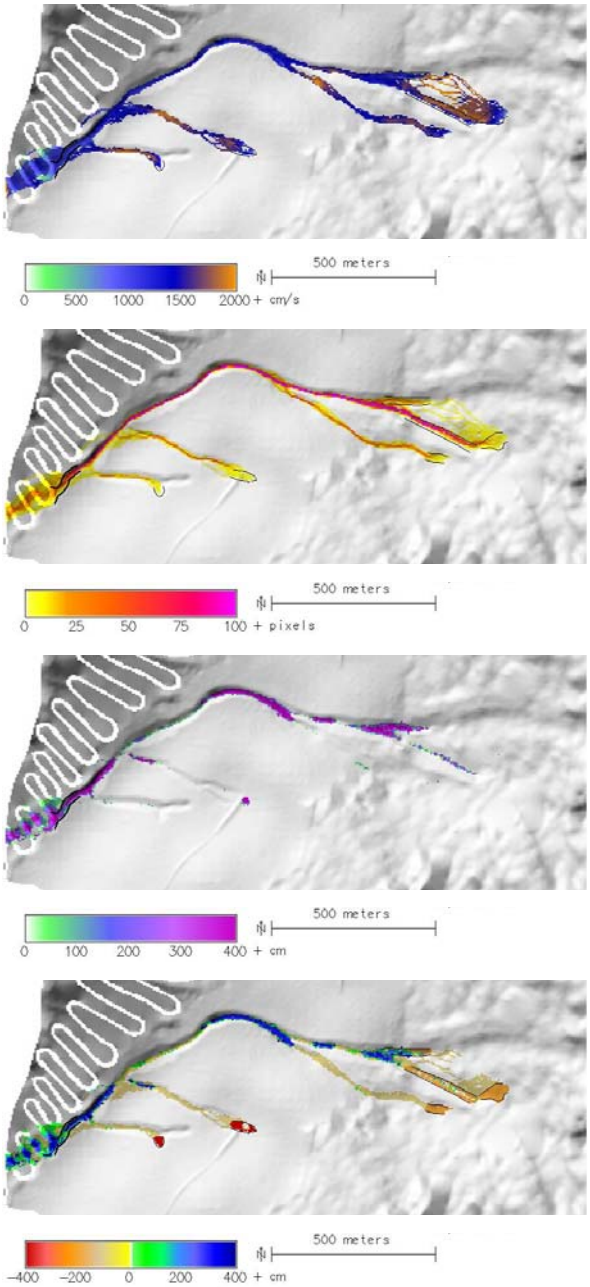

Figure 5.10 (top): Maximum velocity of debris flows.
Figure 5.11 (top middle): Index for the magnitude of debris flow impact.
Figure 5.12 (btm. middle): Deposition from debris flows.
Figure 5.13 (btm.): Sediment balance from debris flows.

5 Increased friction coefficient. When increasing the friction coefficient to $\mu = 0.1$, more of the debris

flow material stopped in the channel above the road. Curve 6 was invaded massively, but the lower curves only to a smaller extent. Though these patterns look quite realistic, only 2,300 m³ out of the total of 76,000 m³ (entrained: 39,900 m³) were simulated to be deposited on the road (Figure 5.14; compare Table 5.2).

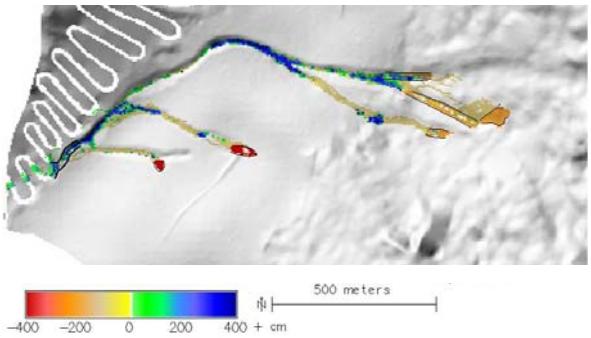

Figure 5.14: Sediment balance from debris flows.

6 Lower spatial resolution. Decreasing the spatial resolution from 5 m to 10 m and using the parameters of Analysis 4 did result in some changes of the model output, but the magnitudes remained unchanged. With 34,700 m³ of defined starting material, 65,800 m³ were simulated to be entrained and 100,500 m³ to be deposited, 12,000 m³ on the international road (compare Table 5.2).

The invasion of Curve 10 of the road was much more pronounced than with 5 m resolution, leading to the larger amount of material deposited on the road (Figure 5.15). The patterns of maximum flow velocity largely remained unchanged (Figure 5.16).

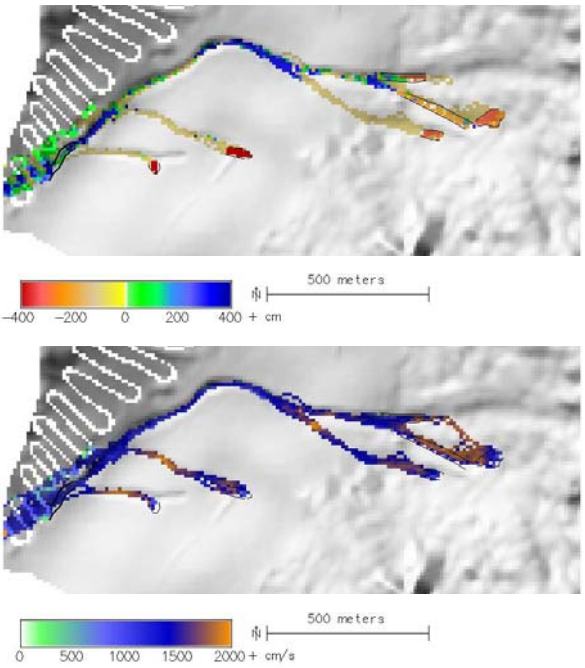

Figure 5.15 (top): Sediment balance from debris flows.
Figure 5.16 (bottom): Maximum velocity of debris flows.

5.1.2 Summary

Table 5.2: Simulated sediment balances (m³) with different parameter settings.

scenario/test	start m³	entrainm. m³	deposit m³	on road m³
1 standard	36,100	14,300	48,700	0
2 μ (1)	36,100	41,700	77,800	5,100
3 *M/D*	36,100	37,200	73,300	1,200
4 thresh.	36,100	48,000	84,000	9,800
5 μ (2)	36,100	39,900	76,000	2,300
6 res. 10 m	34,700	65,800	100,500	12,000

The sediment volumes modelled to be included in debris flows using different parameter settings are summarized in Table 5.2. The patterns of deposition observed in the field were simulated quite well when carefully calibrating the parameters. One has to be very cautious when evaluating the results due to the large uncertainties with starting areas and entrainment of soil.

5.2 Guardia Vieja

The study area *Guardia Vieja*, located in the upper Aconcagua valley, hosts a large variety of debris material (probably moraine) which easily becomes fluidized in connection to major rainfall events like during El Niño in winter 1987, when 45,000 m³ of debris were deposited on the international road which was later rebuilt on the other side of the valley (HAUSER 2000a).

Since 1987, vegetation has partly regrown and the area was reshaped by further smaller debris flows, so that the starting areas and the deposits are difficult to identify in the field. However, some clearly visible unstable areas do exist (Figure 5.17), and the major deposit partly covering the road is shown in HAUSER (2000a; compare Figure 3.20).

The 1987 event was triggered by long-term rainfall (compare Tables 4.6 and 4.9). For the purpose of the present study it was assumed that all water would infiltrate and form a sharp wetting front – a rough generalization necessary due to lacking information of greater detail. A selection of parameter settings was tested (Tables 5.3 and 5.4).

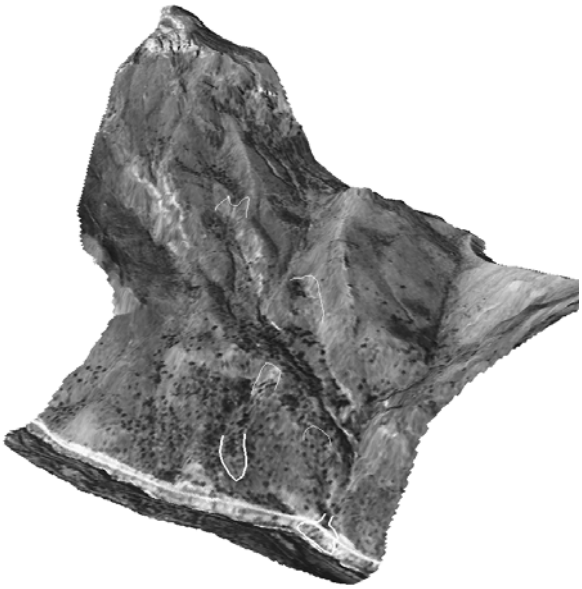

Figure 5.17: The study area *Guardia Vieja* (compare Section 3.7). The thin white lines represent potential zones of debris flow initiation according to field evidence, the bold white lines show debris flow deposits. Elevation model and orthophoto derived from aerial imagery. Design: Martin Mergili, 04/2008.

Table 5.3 (top): Parameter settings and scenarios for the study area *Guardia Vieja*. soil = soil parameters, lcov = land cover parameters, n/sed = Manning's n and parameters for sediment transport, pflow = preferential flow (per cent of total seepage), runout = parameters for runout model, res = spatial resolution, A = hydraulic model, B = sediment transport model, C = slope stability model, D = debris flow runout model; std = standard parameters (compare Section 4.1), cal = calibrated parameters, test = changed param. for analysis of sensitivity.

Table 5.4 (bottom): average, maximum, and minimum depth of wetting front and wetting front in pre-wetted soil which simulations 4 – 6 and 8 are based on (compare Table 5.3). For the choice of parameters compare Table 4.2).

		Parameter settings						Used modules			
		soil	lcov	n/sed	pflow	runout	res (m)	A	B	C	D
Test of plausibility (with precipitation = 457.5 mm in 5 days; all as rainfall)											
1a	Slope stability model	std	std			std	10			x	
1b	Debris flow runout model					cal	10				x
Scenarios											
1	Scen. 1: p=457.5 mm in 5 days	std	std			cal	10			x	x
2	Scen. 2: defined starting areas	std	std			cal	10			x	x
Analysis of sensitivity (with precipitation = 457.5 mm in 5 days; all as rainfall)											
3	Deep wetting front	test	std			cal	10			x	x
4	Shallow wetting front	test	std			cal	10			x	x
5	Slope failure only where no or badly eroded vegetation	std	test			cal	10			x	x
6	Pre-wetting of soil	test	std			cal	10			x	x
7	Increased maximum depth of deposition	std	std			test	10			x	x
8	Spatial resolution (with defined areas of initiation)	std	std			cal	5				x
9	Dry soil	std	std			cal	10			x	x
Debris flow runout based on SH model (r.avalanche)											
10	Defined starting areas	φ = 37.1°	δ = 23°				5				
11	Defined starting areas	φ = 37.1°	δ = 18°				5				

assumption	precipitation (mm)	θ_r	θ_s	stone content	depth of wetting front (m)
average	457.5	0.065	0.41	0.263	1.8
maximum	457.5	0.082	0.32	0.400	3.2
minimum	457.5	0.042	0.52	0.154	1.1
pre-wetted (based on average)	457.5	0.238 (50 % relative sat.)	0.41	0.263	3.6

5.2.1 Test of plausibility with Scenario 1: rainfall event of 457.5 mm in 5 days

1a Slope stability model. The major rainfall event in July 1987 extended over a couple of days, and the sub-day resolution of the rainfall intensity is unknown – in contrast to the Argentine study areas, where short-duration rainfall events were assumed, this was not possible for the Guardia Vieja area. Soil water movement over a long time span is much too complex to be modelled using the Green-Ampt approach. Therefore, as an approximation and for the purpose of the present study, it was assumed that all the precipitating water, if not retained by vegetation, would infiltrate into the soil. Surface runoff was neglected as well as further percolation of the infiltrated water.

Using the average soil hydraulic parameters for the prevailing soil class, a saturated depth of 1.8 m was computed for the end of the rainfall period (Table 5.4). The Figures 5.18 and 5.19 illustrate the distribution of the factor of safety for such a constellation and the connected starting areas for debris flow processes.

The areas identified as potentially unstable showed a very weak correlation with observed locations of slope failure. The following reasons may explain this phenomenon: (1) the slope failures leading to debris flows were of rotational, deep-seated character, not suitable to be described by an infinite slope stability model; (2) some scars may have been reinvaded by vegetation, making an identification difficult; (3) the elevation model used was derived from aerial imagery from 1977, prior to the big event from 1987 reshaping the study area to some extent; (4) the quality of the elevation model is not very high, shown by the parallel patterns between stable and potentially unstable areas, which rather represent artefacts than the real conditions in the field; and (5) the soil properties are spatially much more variable than in the Argentine study areas, so that levelling them to one single value may have led to distortions. 2,654,000 m³ of soil were identified as unstable, 2,641,000 m³ were considered as starting material of debris flows.

1b Runout model. The conceptual runout model was applied to the failed soil as modelled above, using the standard parameters M/D and μ after GAMMA (2000). The model was run in a way that the debris flows were allowed to entrain soil down to a depth of 1 m, given that flow velocity exceeded 10 m s^{-1} and the downward slope was steeper than 15°. Deposition was allowed on cells with flow velocities less than 10 m s^{-1} on slopes less steep than 15°. Total depth of deposition was limited to 10 m for each cell. 41,000 m³ of soil were simulated to be entrained, leading to a total deposit of 2,682,000 m³. Figure 5.20 shows the patterns of deposition from debris flows. 61,000 m³ ended up on the road, according to the model, but most of the debris flow material did not reach the bottom of the Aconcagua valley.

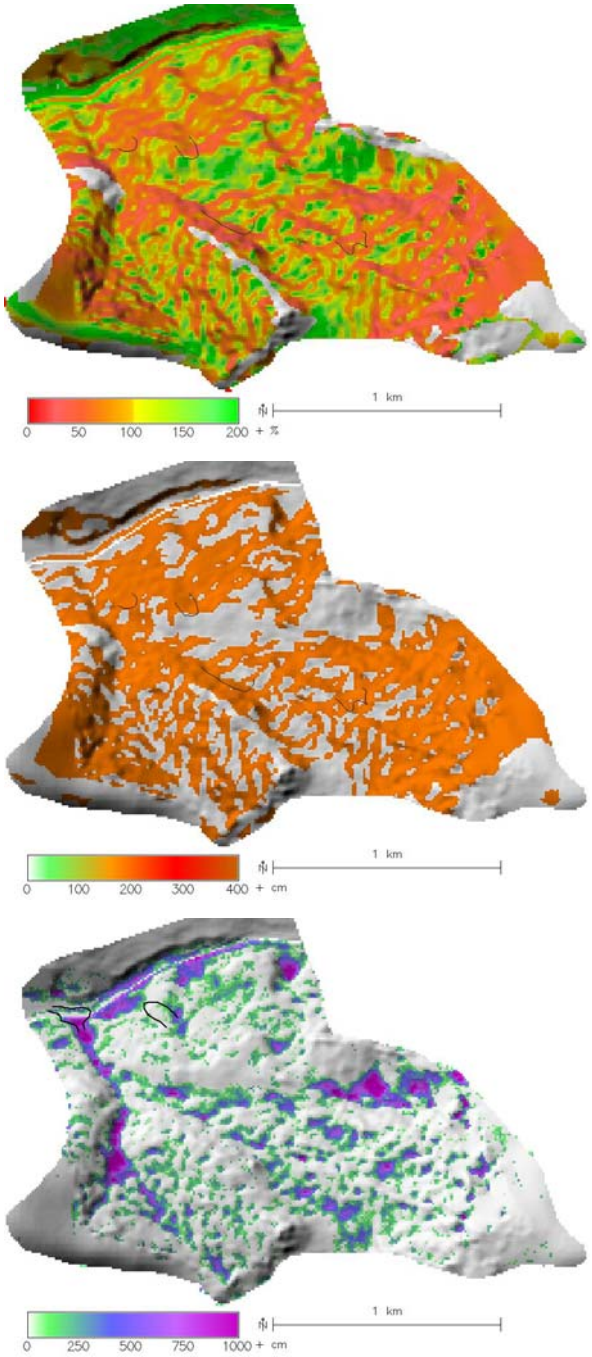

Figure 5.18 (top): Factor of safety.
Figure 5.19 (middle): Potential starting areas of debris flows.
Figure 5.20 (bottom): Depth of deposition from debris flows.

It appears that μ was too high for the conditions in this catchment. When setting μ to 0.1 for the entire catchment, the patterns of deposition at the major outlet corresponded well to reports, but the volume of sediment simulated to end up on the road (106,000 m³) was notably higher than the reported quantity of 45,000 m³ (HAUSER 2000a; Figures 5.21 and 5.22). The remaining deposits modelled in the bottom of the Aconcagua valley are difficult to vali-

date as they are not shown in Figure 3.20 and were not any more observable in the field 20 years after the event. The fact that some of the material was modelled to be deposited farther upwards in the catchment corresponds to the observed patterns – however, a more detailed validation is difficult as much of the catchment has been overgrown by vegetation or reshaped by landslides, smaller debris flows, and runoff.

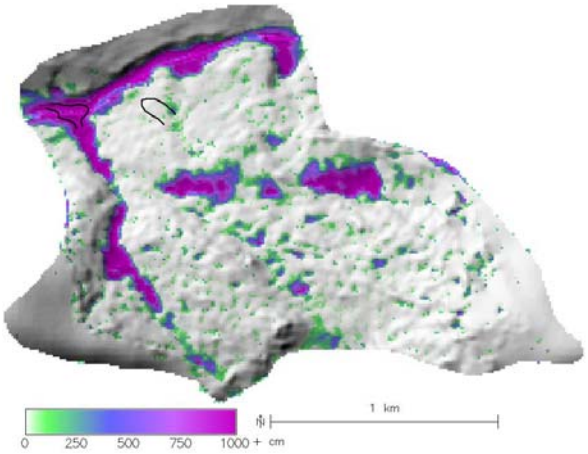

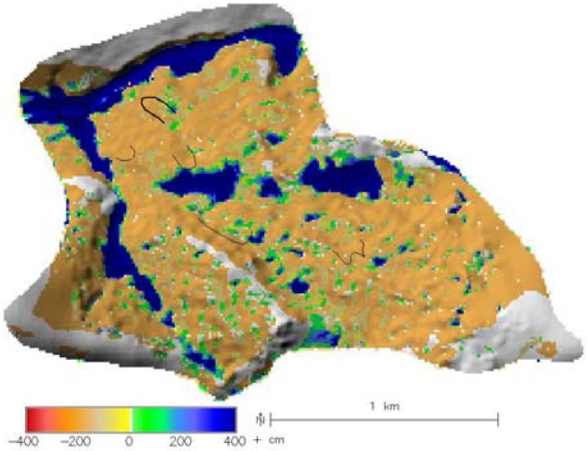

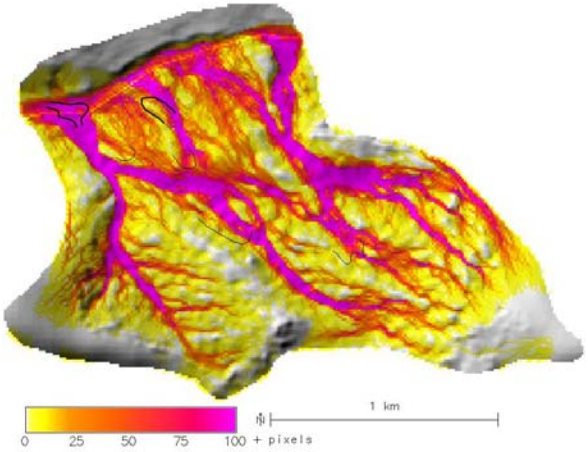

Figure 5.21 (top): Deposition from debris flows.
Figure 5.22 (middle): Sediment balance from debris flows.
Figure 5.23 (bottom): Debris flow index.

Figure 5.23 shows the debris flow index (number of starting cells hitting each cell), and Figure 5.24 represents the maximum velocity of debris flows moving over each cell. The values, exceeding 20 m s^{-1} on the steepest slopes, appear reasonable though it is not possible to validate them due to lacking availability of reference information.

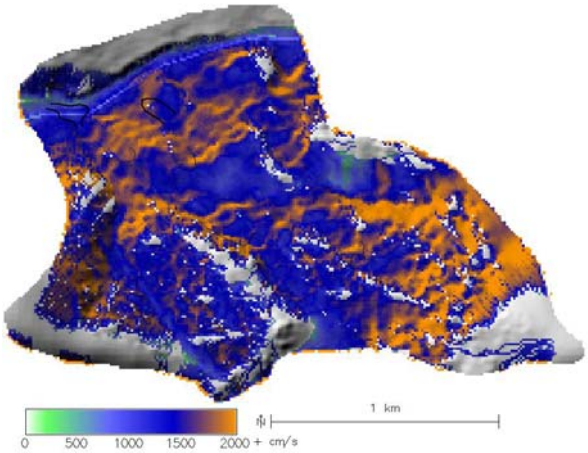

Figure 5.24: Simulated maximum velocity of debris flows.

5.2.2 Scenario 2: Defined starting areas

Visible areas of unstable slopes were mapped in the field and from an orthophoto, and the possible depth of failure was estimated (Figure 5.25). The runout model was run with the standard parameters used above. The total moved volume simulated was far less than for the rainfall scenario: slightly less than 140,000 m³ of soil were defined as starting areas and 110,000 m³ were entrained, resulting in a total deposit of 250,000 m³, 12,000 m³ on the international road, being far less than the reported quantity (45,000 m³). This indicates that in the 20 years since the event, many failure patterns have been modified or overgrown and that the failures leading to the massive debris flows of 1987 are not clearly visible any more. However, Figure 5.26 shows that the simulated spatial patterns of deposition correspond very well to the observed ones, at least when regarding the major outlet of the catchment.

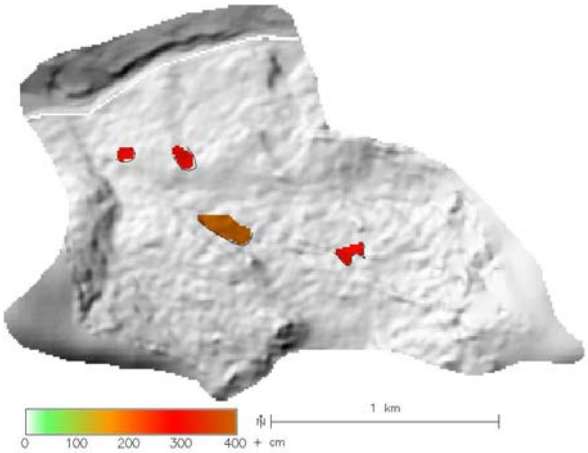

Figure 5.25: Defined depth of debris flow mobilization.

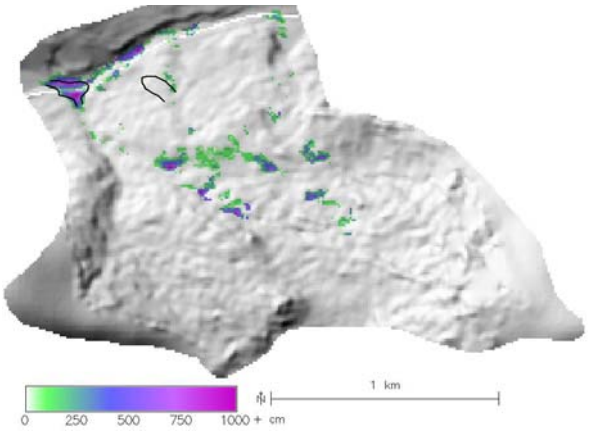

Figure 5.26: Deposition from debris flows.

5.2.3 Analysis of sensitivity

3 Maximum depth of saturation. When setting the water storing capacity of the soil to a minimum (compare Table 5.4), the depth of saturation connected to the 457.5 mm rainfall event was 3.2 m, keeping in mind the simplifications discussed above. Consequently, this led to a larger debris flow volume whilst the starting areas remained unchanged, compared to Scenario 1 (in cohesionless soil, the potential depth of failure has no influence on the factor of safety).

4,369,000 m³ of soil were identified as unstable by the model, 4,345,000 m³ as starting material for debris flow processes, entraining further 303,000 m³. 120,000 m³ out of a total 4,648,000 m³ were deposited on the international road. Figure 5.27 illustrates the sediment balance. All parameters for the runout model were applied as mentioned above.

4 Minimum depth of saturation. When assuming the maximum water storing capacity (compare Table 5.4), a 1.1 m deep wetting front resulted from the 457.5 mm rainfall event, leading to a simulated potentially unstable soil volume of 1,704,000 m³ and a debris flow starting volume of 1,693,000 m³. Together with 213,000 m³ of entrained soil, slightly more than 1,906,000 m³ of sediment were deposited, according to the model, 75,000 m³ on the international road. All parameters for runout were left unchanged. Figure 5.28 shows the corresponding sediment balance.

5 Stabilizing role of vegetation. The results of all simulations described above were influenced by rooting depth (compare Table 4.4). In all cases, the depth of the wetting front exceeded rooting depth and root cohesion became unimportant for slope stability. When assuming an infinite rooting depth for all classes of intact vegetation, the amount of unstable areas decreases considerably (Figure 5.29). When assuming the average depth of the wetting front (1.8 m), 807,000 m³ of soil were simulated as potentially unstable, and 794,000 m³ as initial debris flow volume. Including the entrained soil volume of 346,000 m³, a deposit of 1,140,000 m³ was modelled (48,000 m³ on the international road). Figure 5.30 shows the corresponding sediment balance.

6 Pre-wetting of soil. The massive debris flows occurring in August 1987 were connected to a major rainfall period. Some weeks before there was also a large amount of rainfall hitting the Aconcagua valley. It was assumed that – as a remainder from that previous rainfall event – the relative saturation of the soil at the beginning of the rainfall period considered here would have been 50 per cent, based on the soil characteristics from Scenario 1. The saturated depth would be 3.6 m under such conditions – not so much more than that for Scenario 5, so that the figures and maps would largely correspond to those for that simulation (compare Figure 5.27) and do not have to be shown separately.

7 More limited depth of deposition. In all simulations discussed up to now, depth of deposition from debris flow was limited to 10 m. When increasing the limit to 20 m and using the standard values of the remaining parameters for Scenario 1, less material remained in the upper sections of the channels (Figure 5.31). 133,000 m³ of soil were deposited on the road, according to this simulation.

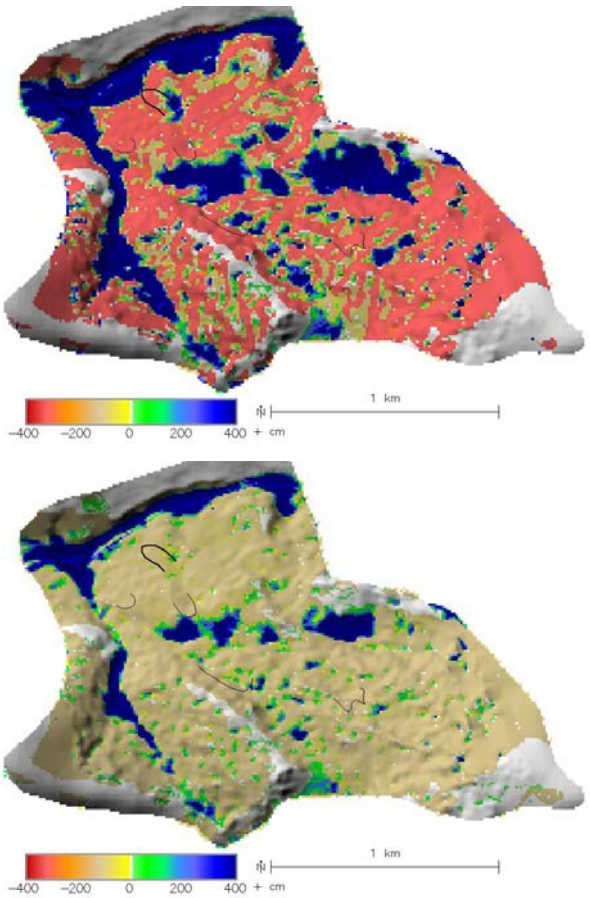

Figure 5.27 (top): Sediment balance from debris flows (maximum depth of saturation).
Figure 5.28 (bottom): Sediment balance from debris flows (minimum depth of saturation).

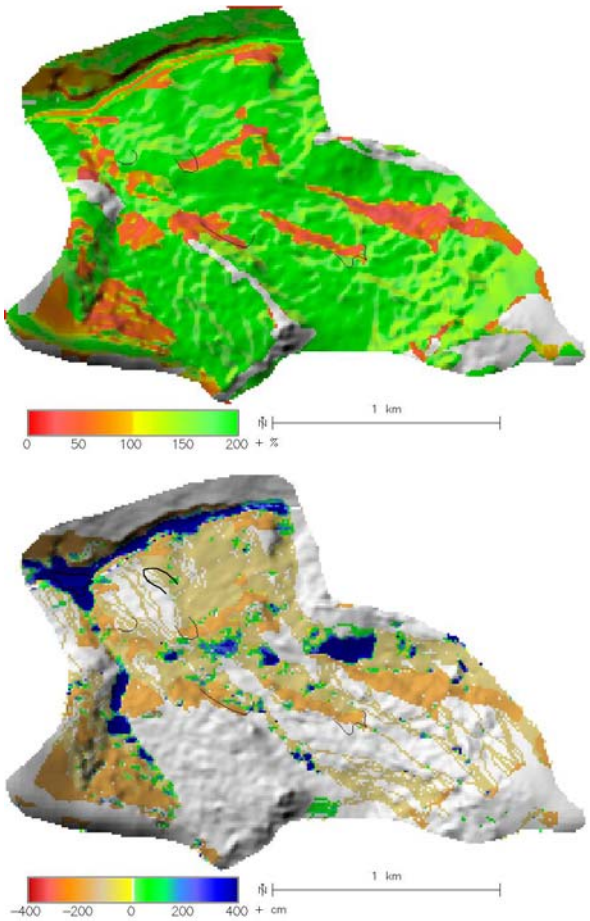

Figure 5.29 (top): Factor of safety (infinite root depth).
Figure 5.30 (bottom): Sediment balance from debris flows.

8 Higher spatial resolution. Choosing a higher spatial resolution (5 m instead of 10 m) only resulted in minor changes of the model output, as it was tested with defined starting areas (compare Scenario 2). In addition to the 140,000 m³ of mobilized soil, 95,000 m³ were entrained. 9,400 m³ out of a total 235,000 m³ were deposited on the road, according to the model.

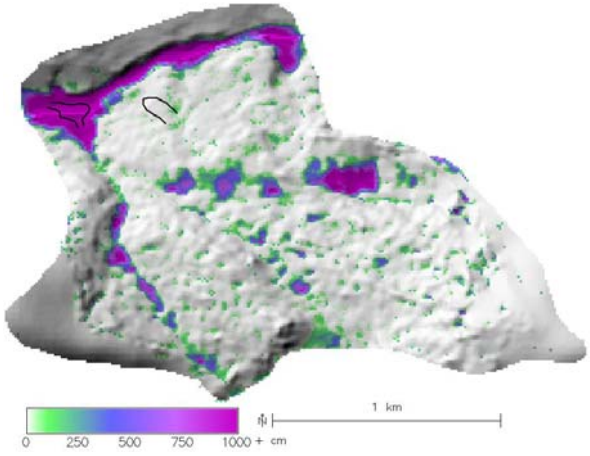

Figure 5.31: Deposition from debris flow with an allowed maximum of 20 m.

9 Dry soil. Assuming the potential failure plane from Scenario 1, but excluding the role of soil water for slope stability led to reduced unstable areas (786,000 m³) and starting volume (731,000 m³) identified by the model. Together with 490,000 m³ of entrained soil, 1,220,000 m³ were deposited, 55,000 m³ on the international road (Figures 5.32 and 5.33).

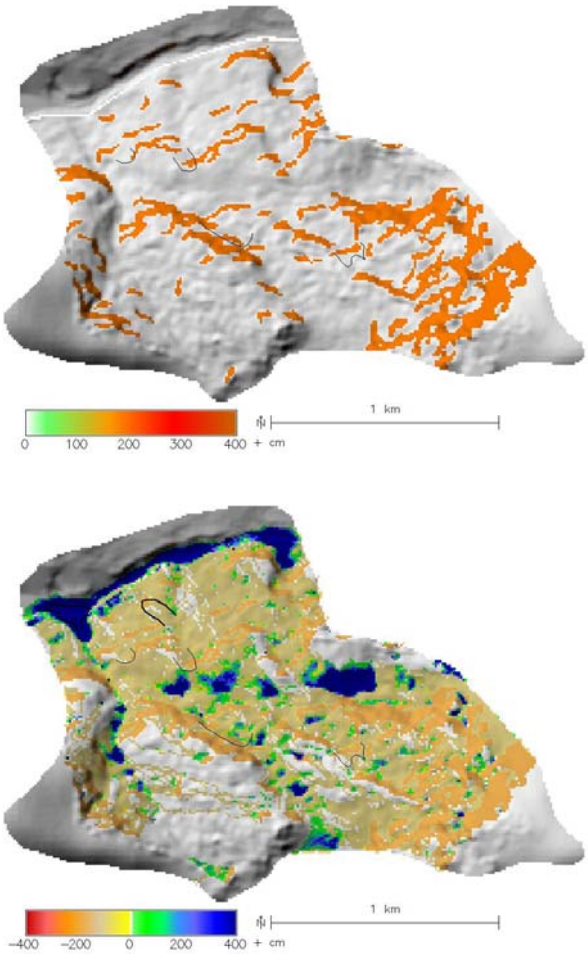

Figure 5.32 (top): Starting material of debris flows (dry soil).
Figure 5.33 (bottom): Sediment balance from debris flows.

5.2.4 Debris flow runout according to the SH model (r.avalanche)

r.avalanche was run with defined starting areas of debris flows. Two simulations were performed, one with a bed friction angle $\delta = 23°$, one with $\delta = 18°$.

10 Bed friction angle $\delta = 23°$. With a bed friction angle of 23°, much of the debris flow material stopped very early, far away from the main valley and the international road. Part of the material, however, moved father downwards and stopped in a realistic position (compare Figure 3.20; HAUSER 2000a). The volume of the modelled deposit, however, is much smaller (what is not surprising as, according to the results discussed above, the defined starting flow mass is probably too small). The debris flow reached maximum velocities of 34 m s^{-1}, according to the

model (Figure 5.34). The sediment volume on the road increased steadily until the end of the simulation, reaching about 1,350 m³ (Figure 5.35). Figure 5.38 shows a time series of debris flow runout.

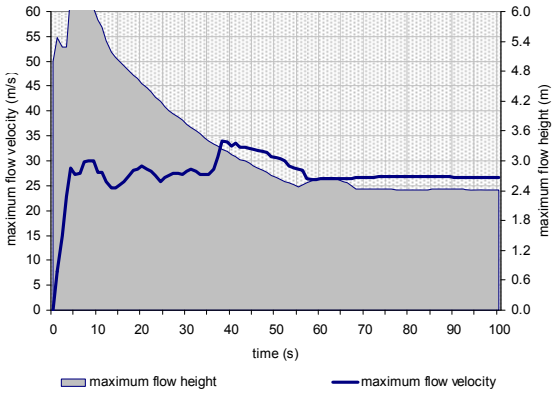

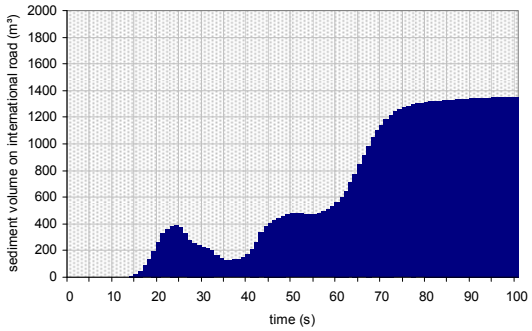

Figure 5.34 (top): Maximum flow depth and velocity of debris flow at maximum depth (δ = 23°).
Figure 5.35 (bottom): Debris flow volume on the international road (δ = 23°).

11 Bed friction angle δ = 18°. As expected, the portion of the debris flow material simulated to remain in the higher parts of the catchment was much smaller than with higher δ. In contrast, most of the material moved far up the opposite slope – farther than the reported deposit which, in general, did not invade the opposite side of the river (compare Figure 3.20).

The modelled flow velocity rose up to almost 59 m s^{-1} (Figure 5.36). Figure 5.37 shows how the mass passes the international road – during the flow, the road is covered by a maximum of more than 1,600 m³ of debris, at the end this value decreases to less than 400 mm. A series of flow depths during runout is shown in Figure 5.39.

5.2.5 Summary

Table 5.5 summarizes the volumes involved in debris flows according to the different simulations for the study area *Guardia Vieja*. The modelled volumes deposited on the international road tended to be higher than that one reported by HAUSER (2000a), but ranged within a realistic magnitude. The patterns of deposition appeared reasonable. The clearly recognizable slope failures in the field are probably a severe underestimation of the starting areas of the 1987 debris flow event – in general, much uncertainty remains, regarding the patterns and the quantity of debris flow material. The hydraulic processes leading to slope instabilities as well as slope stability itself were probably modelled insufficiently for this study area, indicated by the fact that the deposit computed for dry soil corresponded much better to observations than that one computed with the effects of the seepage force included.

r.avalanche only partly proved successful for this study area. The volumes deposited on the road were severely underestimated. Reasons may be (1) the uncertainties with the source areas; (2) the curvature of the flow channel which, though relatively smooth, may pose a problem to the implementation of the SH model used for *r.avalanche* (compare Section 4.3); and (3) deficiencies of the DEM used.

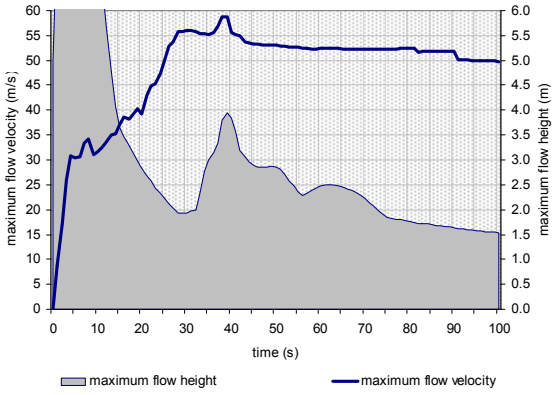

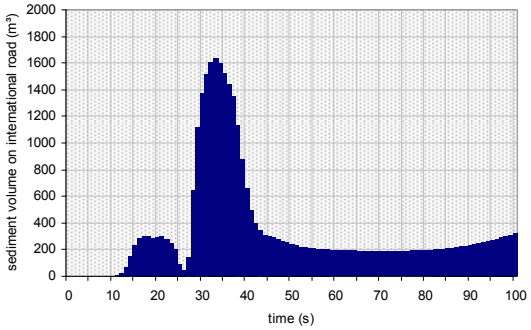

Figure 5.36 (top): Maximum flow depth and velocity of debris flow at maximum depth (δ = 23°).
Figure 5.37 (bottom): Debris flow volume on international road (δ = 23°).

Table 5.5: Simulated sediment balances (1000 m³) with different settings.

scenario/ test	pot. failure	start	entrainm.	deposit	on road
1: p = 457.5	2,654	2,641	246	2,887	106
2: defined	0	139	113	252	12
3: deep	4,369	4,345	303	4,648	120
4: shallow	1,704	1,693	213	1,906	75
5: veg. excl.	807	794	346	1,140	48
7: incr. dep.	2,654	2,641	240	2,881	133
8: res. 5m	0	140	95	235	9
9: dry soil	786	731	490	1,220	55

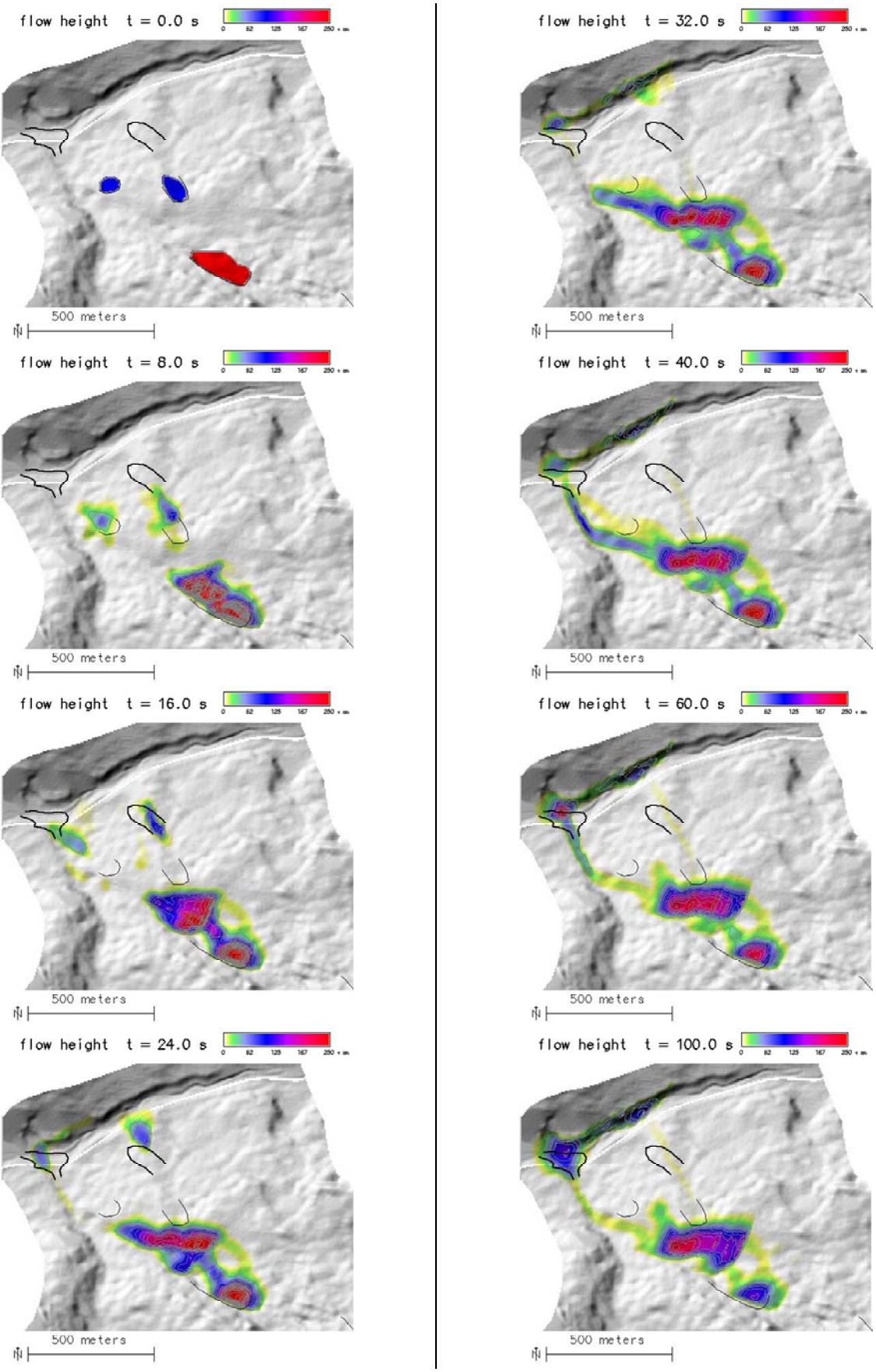

Figure 5.38: Movement of debris flow with a bed friction angle δ = 23°.

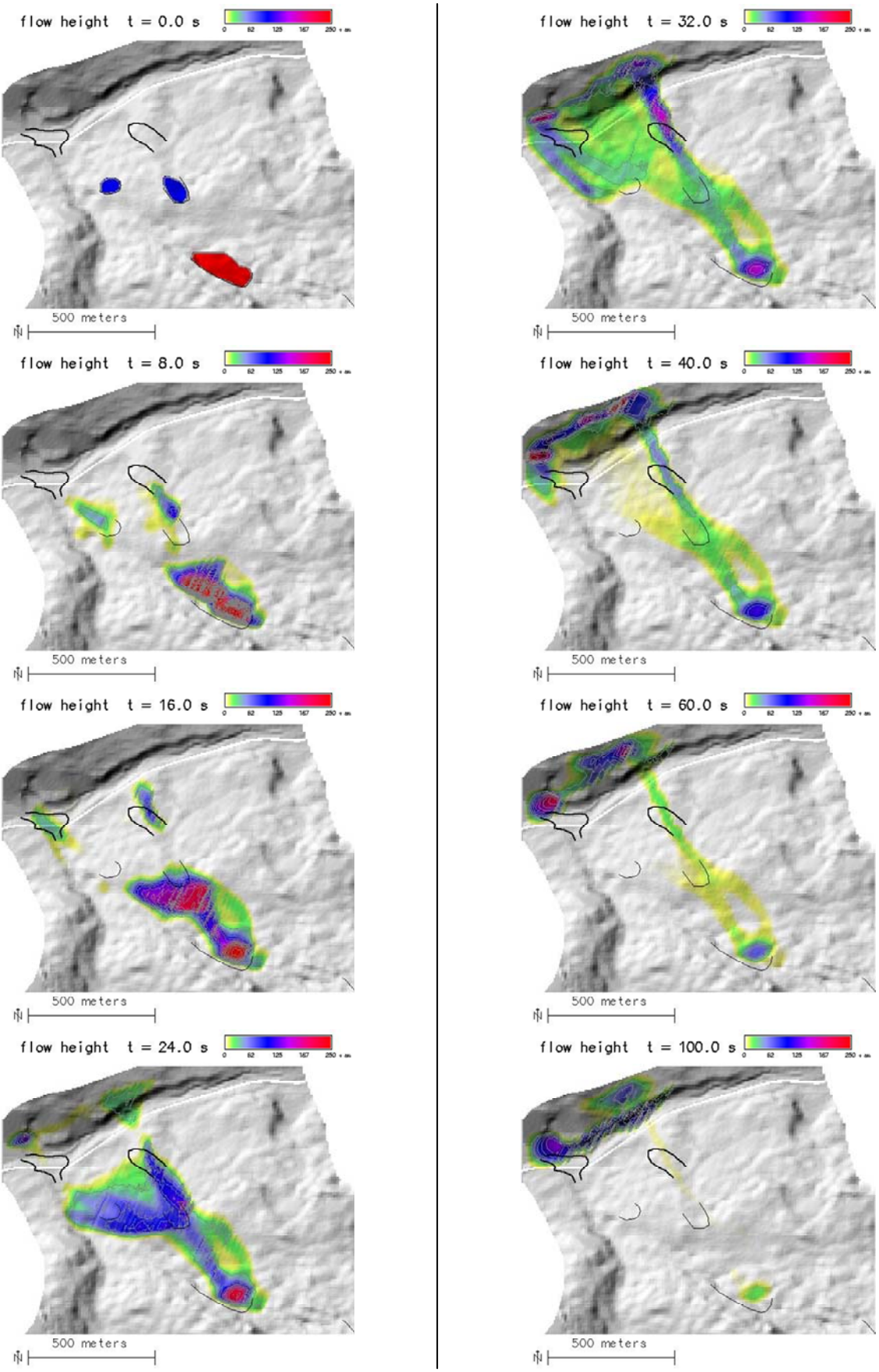

Figure 5.39: Movement of debris flow with a bed friction angle δ = 18°.

5.3 Castillo de Rocas

Castillo de Rocas (Figure 5.40; compare Section 3.7) is the first of the study areas around *Guido* to be discussed. Debris flows in the area were reported particularly in 1996 (ESPEJO 1996; MOREIRAS 2004a). The model components were first tested for the plausibility of the results with the standard parameter settings as described in Chapter 4. Where necessary, the parameters were modified in accordance with reports and field evidence. Certain meteorological scenarios were then tested for their capacity to trigger debris flows. Finally, the model results were tested for their sensitivity to changes of uncertain parameters.

Figure 5.40: The study area Castillo de Rocas (compare Section 3.7). The thin white lines delineate potential starting areas of debris flows, according to field evidence, the bold white lines show debris flow deposits. Elevation model derived from aerial and SPOT5 imagery, draped orthophoto from SPOT5. Design: Martin Mergili, 04/2008.

Table 5.5: Parameter settings and scenarios for the study area "Castillo de Rocas". soil = soil parameters, lcov = land cover parameters, n/sed = Manning's n and parameters for sediment transport, pflow = preferential flow (per cent of total seepage), runout = parameters for runout model, res = spatial resolution, A = hydraulic model, B = sediment transport model, C = slope stability model, D = debris flow runout model; std = standard parameters (compare Section 4.1), cal = calibrated parameters, test = changed parameters for analysis of sensitivity, h_i = defined starting depth.

		Parameter settings						Used modules			
		soil	lcov	n/sed	pflow	runout	res (m)	A	B	C	D
Test of plausibility (with precipitation = 100 mm in 80 minutes; all as rainfall)											
1a	Hydraulic model	std	std	std	0		5	x			
1b	Slope stability model	std	std				5			x	
1c	Sediment transport model	std	std	std, cal	0		5	x	x		
1d	Debris flow runout model					std, cal	5				x
Scenarios											
1	Scenario 1: p=100 mm in 80 min.	std	std	std	0	cal	5	x		x	x
2	Scenario 2: p=100 mm in 140 min.	std	std	std	0	cal	5	x		x	x
3	Scenario 3: p=40 mm in 80 minut.	std	std	std	0	cal	5	x		x	x
4	Scenario 4: p=40 mm in 40 min.	std	std	std	0	cal	5	x		x	x
5	Scenario 5: p=40 mm in 140 min.	std	std	std	0	cal	5	x		x	x
6	Scenario 6: p=10 mm in 80 min.	std	std	std	0	cal	5	x		x	x
Analysis of sensitivity (with precipitation = 100 mm in 80 minutes; all as rainfall)											
7	Spatial resolution	std	std	std	0	cal	10	x		x	x
8	Angle of internal friction	test	std	std	0	cal	5			x	x
9	Soil cohesion	test	std	std	0	cal	5			x	x
10	No root cohesion	std	test	std	0	cal	5			x	x
11	Dry soil	std	std	std	0	cal	5			x	x
Debris flow runout based on the SH model											
12	Defined starting areas (h_i = 1 m)	φ = 43.0°	δ = 28°				5				
13	Defined starting areas (h_i = 1 m)	φ = 43.0°	δ = 33°				5				
14	Defined starting areas (h_i = 1 m)	φ = 43.0°	δ = 33°				10				

5.3.1 Tests of plausibility

The hydrological model components (runoff, infiltration), the sediment transport model, the slope stability model, and the debris flow runout model were run with the standard parameters as described in Section 4.1. The results were tested for their plausibility against field evidence and reports. Where necessary, the parameters were modified. All tests of plausibility were performed with a precipitation of 100 mm in 80 minutes as input (Scenario 1).

1a Surface runoff and infiltration models. Some of the model parameters governing runoff and infiltration were not known at sufficient accuracy, particularly regarding their spatial distribution. The major uncertain parameter to be tuned was preferential soil water flow, which exerts a major effect on infiltration, but is hard to quantify. SUKHIJA et al. (2003) found that in soils derived form fractured granites, 75 per cent of percolation occurred due to preferential flow, and only 25 per cent due to piston flow. However, since their investigations considered long-term water movement under unsaturated conditions, their findings were not applicable for the present study. Plausibiltity of the model was tested based on the assumption that no preferential flow would occur.

Manning's n was varied between maximum and minimum (compare Table 4.4) by assigning a random value to each cell. Regarding the remaining hydraulically relevant soil and land cover parameters, the averages denoted in Tables 4.2 and 4.4 were applied.

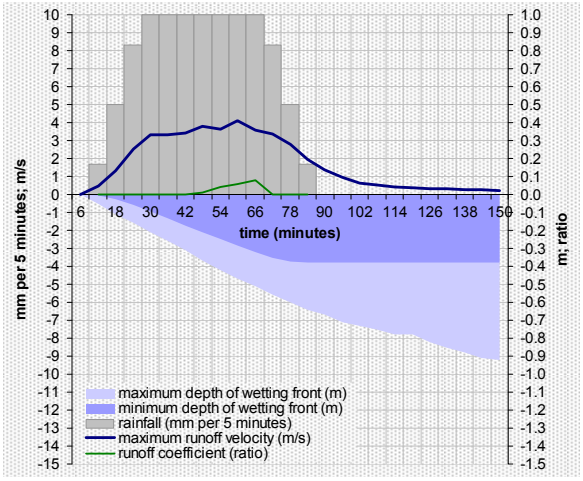

Figure 5.41: Temporal record of some major variables of the hydraulic model parts.

Figure 5.41 illustrates the temporal curve of maximum runoff velocity, runoff coefficient, and depth of wetting front compared to rainfall intensity. At the end of the scenario, the modelled wetting front was located at a soil depth between 0.38 m and 0.92 m. Runoff velocity approached a maximum of 4.1 m s^{-1}, increasing steadily during the period of high rainfall intensity. This pattern was connected to runoff coefficient. It averaged at 0.02 over the entire scenario, increasing significantly with increasing depth of wetting front and reaching a maximum of 0.08 – a phenomenon tightly coupled to the Green-Ampt infiltration model. The Figures 5.42 and 5.43 show depth and velocity of runoff at their maxima during the scenario.

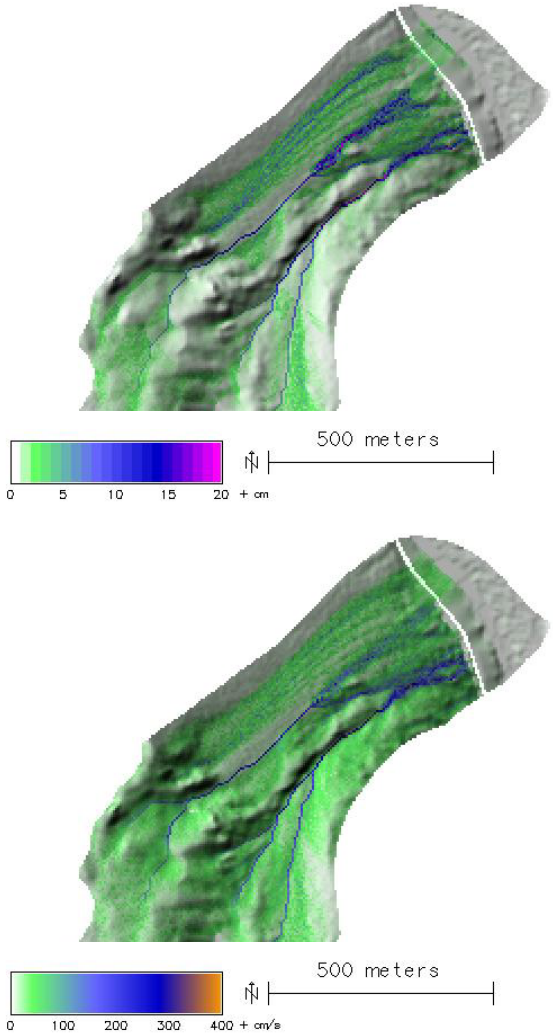

Figure 5.42 (top): Modelled runoff depth at t = 60 min.
Figure 5.43 (bottom): Modelled runoff velocity at t = 60 min.

Runoff behaviour is tightly coupled to infiltration and therefore also to the water status of the soil. Figure 5.44 illustrates the spatial distribution of the depth of the wetting front below the flow channels (compare Section 4.2 for an explanation) at the end of the scenario. The deepest zones of the wetting front are located below the major flow channels of the catchment and near to the base of bedrock outcrops where runoff enters soil-covered slopes.

The values presented above and their spatial distribution appear plausible, but the available information for the study area does not allow for a direct validation. However, the modelled runoff coefficients are in line with the range of values given by BRAUD et al. (2001) for vegetation types similar to those present in the study catchment.

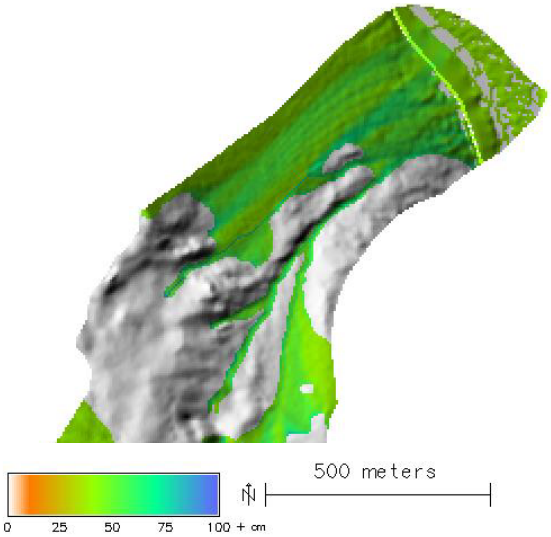

Figure 5.44: Depth of wetting front below flow channels at the end of the scenario.

1b Slope stability model. The slope stability model was to be expected relatively robust because the major input parameters were measured more or less directly (elevation model, laboratory tests). Root cohesion was the only parameter derived from values from the literature.

Figure 5.45 shows the spatial distribution of the factor of safety for the study area. The distribution of zones of potential slope failure ($FOS < 1$) corresponded well to field observations (areas identified as potentially unstable in the field are delimited by black lines in Figure 5.45).

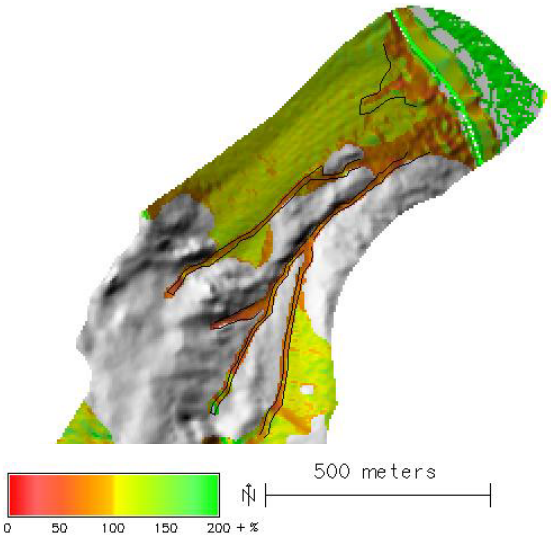

Figure 5.45: The factor of safety.

For raster cells with $FOS < 1$, the entire saturated soil column was considered to be potentially unstable (a total of 44,700 m³). Only patches of potentially unstable soil of at least 1000 m² were considered to fail (total: 40,600 m³). Since the soil in the study area was considered non-cohesive, the entire failed soil was identified to develop into debris flows (Figure 5.46; compare Section 4.2).

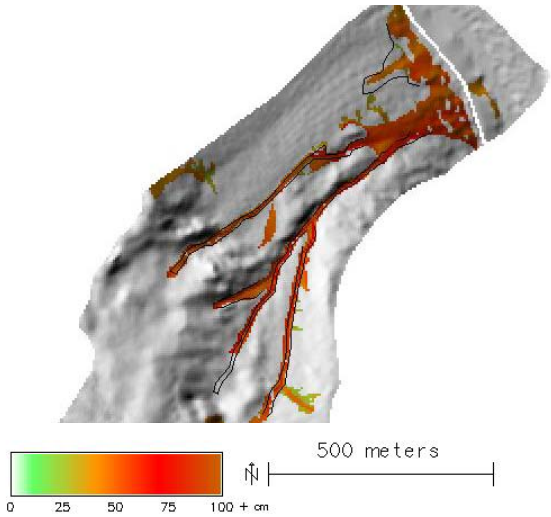

Figure 5.46: Depth of debris flow mobilization from slope failure.

1c Sediment transport model. When applied with the same hydraulic parameters derived above and exactly as described in Eq. 4.18 to 4.22 (setting ST_1 to $ST_4 = 1.0$), the detachment of soil by and the deposition of sediment from runoff appeared far to high. This was not necessarily surprising since

- the parameters of the RICKENMANN (1990) model have been calibrated for less steep slopes than those present in the study area;
- the surface of the flow channels is frequently covered by coarser material than that farther down from which the parameters have been determined.

Extensive detachment was modelled at the bottom of bedrock outcrops with a lot of clear water entering the soil-covered zone. Farther down, hardly any detachment could occur due to the already high sediment load.

Certain combinations of the parameters ST_1, ST_2, ST_3, and ST_4 were tested. $ST_1 = 1.0$, $ST_2 = 0.5$, $ST_3 = 0.005$, and $ST_4 = 0.005$ gave plausible results, regarding detachment and starting material of debris flows (Figures 5.47 and 5.48).

Alternatively, stream power (compare Eq. 2.35) was computed for each time step as indicator for areas prone to develop debris flows from sediment-laden runoff (Figure 5.49).

Comparison of the modelled starting areas of debris flows and stream power with the Figures 5.45 and 5.46 shows that most of the critical areas for the mobilization of debris flows from sediment-laden runoff are located in zones with low factor of safety. Since the choice of parameters for the sediment transport model is poorly supported by field evidence (missing reference data), only zones with FOS < 1 were considered as areas of potential debris flow initiation. This would also be in line with a statement of MOREIRAS (2004a) that debris flows in the *Guido* area are predominantly triggered by saturation. The sedi-

ment transport model was not used for the other study areas around Guido, either.

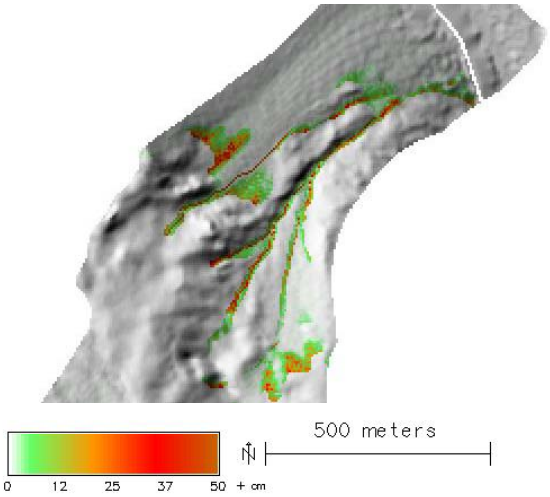

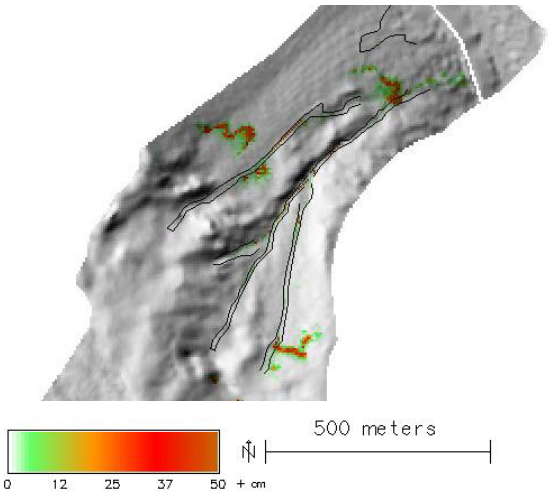

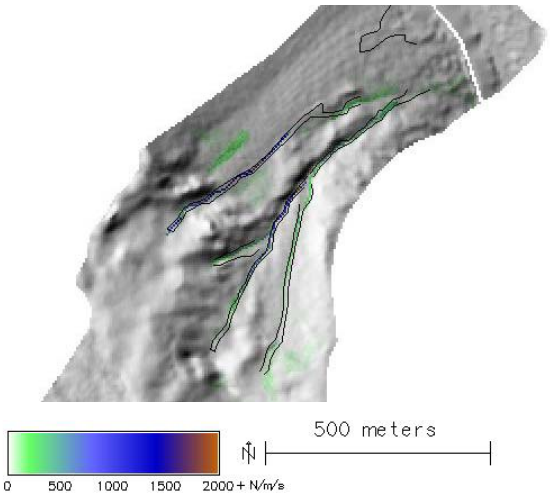

Figure 5.47 (top): Detachment by surface runoff.
Figure 5.48 (middle): Depth of debris flow starting material from runoff load.
Figure 5.49 (bottom): Stream power (t = 60 min.).

1d Debris flow runout model. The two-parameter friction model was tested for the *Castillo de Rocas* area with μ computed according to GAMMA (2000), and with slope and velocity thresholds for entrainment and deposition of 15° and 10 m s^{-1}, respectively. The M/D ratio was set to the standard value of 75 m. Figure 5.50 shows that the runout zone is squeezed, compared to field observations, with almost all material deposited on and directly upwards from the road. Some of the material also reached the bottom of the main valley, not corresponding to field evidence.

In order to overcome these problems, the minimum value for μ was set to 0.15 instead of 0.045 following WICHMANN (2006), and the entrainment – deposition thresholds were increased drastically to 27.5° and 17.5 m s^{-1}. Now the simulation results corresponded much better to the observations, but an overestimation of sediment deposited farther upwards became evident (Figure 5.51). The best result was yielded when reducing the thresholds to 20° and 15 m s^{-1}, respectively, whilst leaving the other parameters unchanged (Figure 5.52).

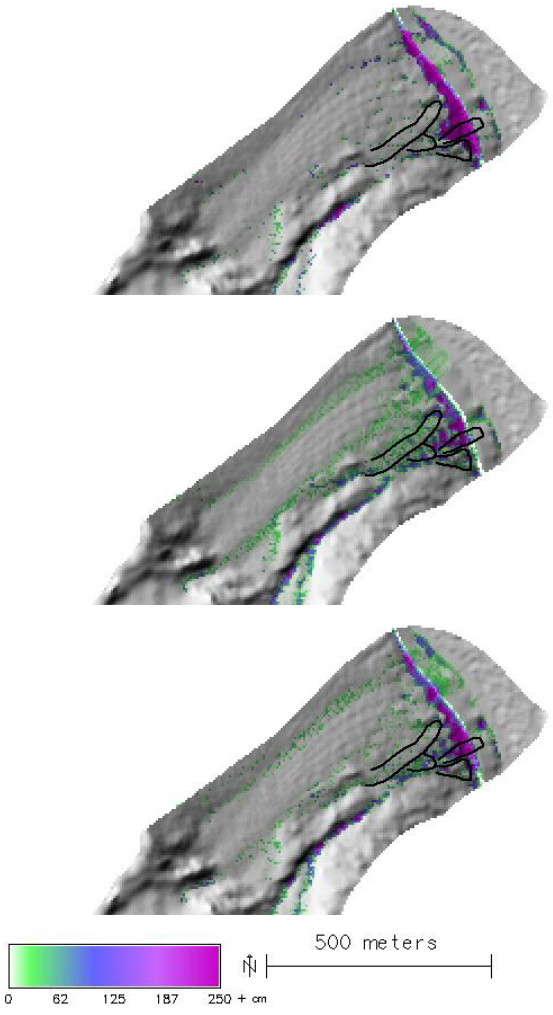

Figure 5.50 (top): Deposition from debris flows with standard parameters.
Figure 5.51 (middle): Deposition from debris flows with first calibration of parameters.
Figure 5.52 (bottom): Deposition from debris flows with final calibration of parameters.

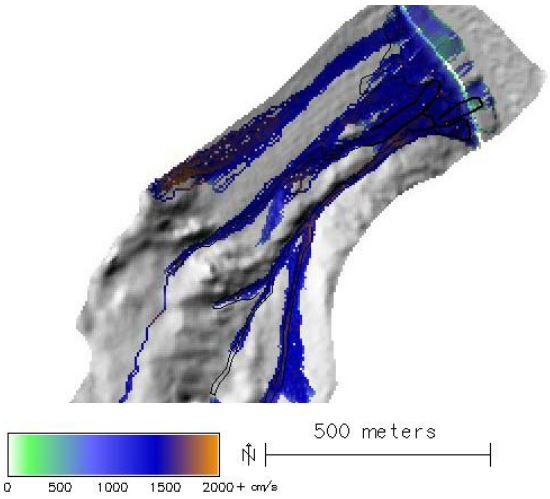

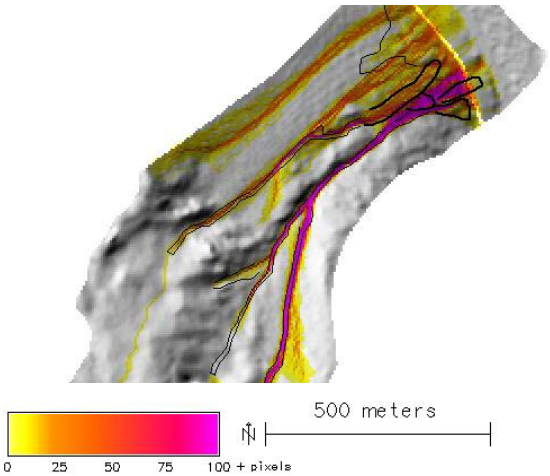

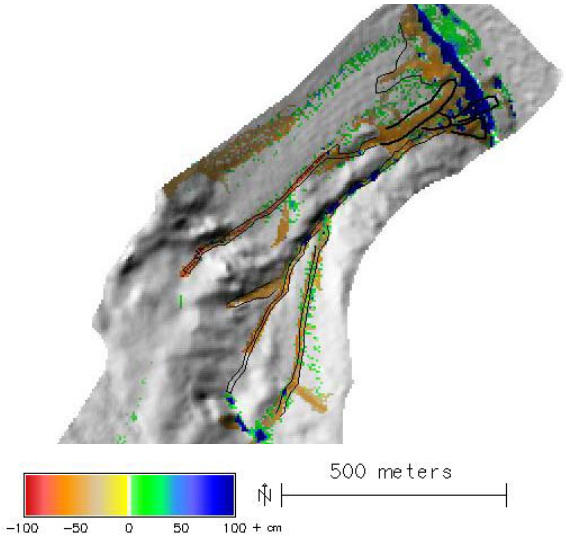

Figure 5.53 (top): Maximum velocity of debris flows.
Figure 5.54 (middle): Debris flow index (compare text for an explanation).
Figure 5.55 (bottom): Sediment balance from debris flows.

The modelled deposit now corresponded quite well to the observed one – at least regarding the broad patterns. The exact location, however, could not be modelled successfully. One reason for this is the relatively smooth topography in parts of the runout zone: small inaccuracies of the elevation model may result in different flow paths, compared to the real world. Furthermore, the northernmost debris flow deposit was not modelled successfully: it occupies very steep terrain (up to 30 degrees and more), what is probably caused by the fact that the debris flow had crossed a narrow and curved pass between rocks slightly above the deposit where it lost much of its energy. Such local effects can not be modelled successfully with this type of runout models and would require advanced physically-based approaches. It is clear, however, that all these considerations are based on the assumption that the starting areas and volumes of the debris flows were modelled correctly.

Figure 5.53 shows the maximum velocity of debris flows, exceeding 20 m s^{-1} only in some portions of the very steepest slopes, moving over most of the area with around 15 m s^{-1} and decelerating when passing the international road. Figure 5.54 illustrates the debris flow index (number of cells with starting material passing each cell).

The findings presented above would also be the results for Scenario 1 (100 mm of rainfall in 80 minutes). According to the simulation with the calibrated runout parameters, 1,800 m^3 of soil were entrained. 3,600 m^3 out of a total of 42,300 m^3 were modelled to be deposited on the international road crossing the lowermost part of the area. Figure 5.55 shows the sediment balance from debris flows for such a scenario (deposit minus entrainment minus starting material).

5.3.2 Rainfall scenarios

2 Rainfall scenario: 100 mm in 140 minutes. When decreasing rainfall intensity while increasing duration and maintaining sum, the runoff coefficient dropped to zero while the depth of wetting front increased, ranging between 39 cm and 1.22 m. Maximum runoff velocity (2.8 m s^{-1}) and stream power were reduced, compared to Scenario 1 (Figures 5.56 to 5.58).

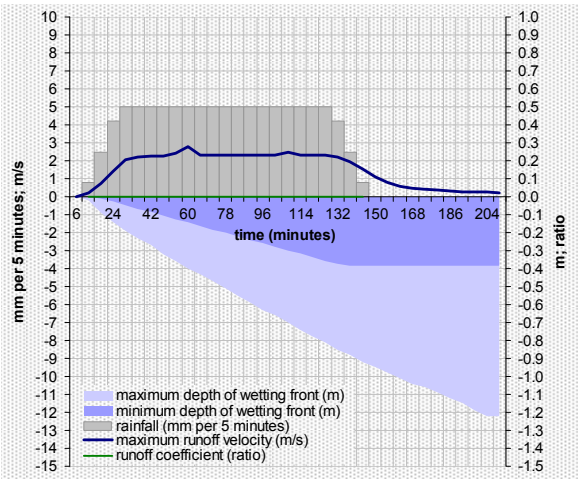

Figure 5.56: System variables (Scenario 2).

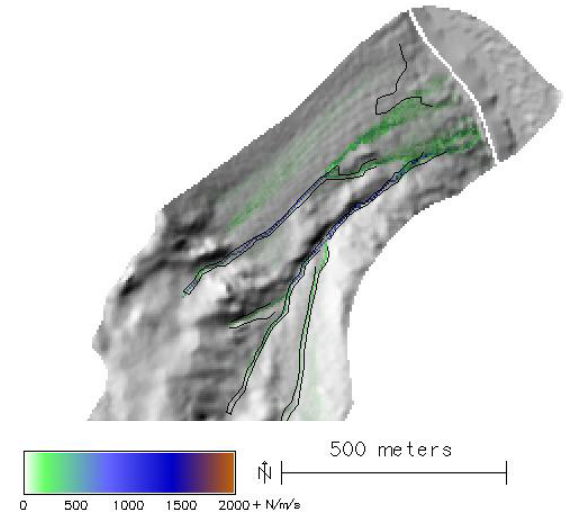

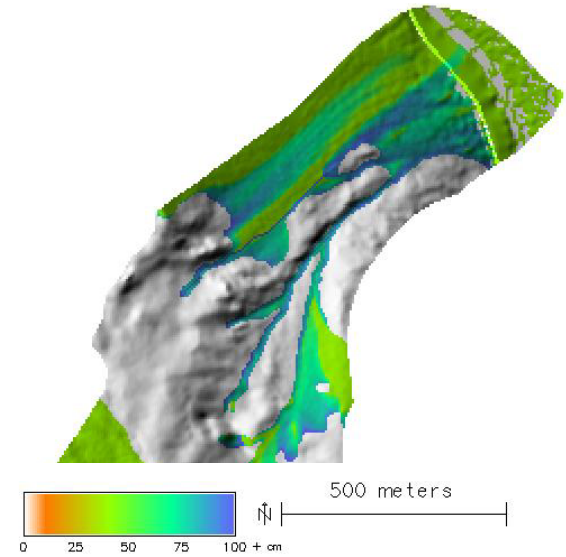

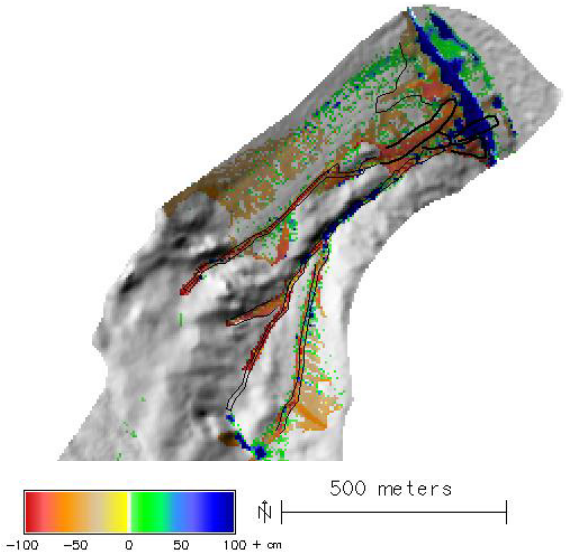

Figure 5.57 (top): stream power (t = 120 min).
Figure 5.58 (middle): Depth of wetting front at the end of the scenario.
Figure 5.59 (bottom): Modelled sediment balance from debris flows connected to a rainfall scenario of 100 mm in 80 minutes.

The distribution of unstable areas (with *FOS* < 1) was the same as for Scenario 1. The consequence of the deeper wetting front was a larger volume of potential slope failure The simulation detected 72,200 m³ of potentially unstable soil, 67,200 m³ of which were considered to be included into debris flow processes. Together with 1,300 m³ of entrained soil, 68,400 m³ of sediment were deposited, according to the model, 5,400 m³ on the international road. Figure 5.59 shows the sediment balance from debris flows.

3 Rainfall scenario: 40 mm in 80 minutes. When reducing rainfall sum to 40 mm instead of 100 mm, the depth of the wetting front ranged between 15 cm and 90 cm whilst runoff velocity peaked at 2.1 m s^{-1} (Figures 5.60 and 5.61). Compare Scenario 4 for an explanation of the spatial patterns of the depth of the wetting front.

27,400 m³ of soil were mobilized as debris flows, according to the model (potential slope failure: 25,900 m³), entraining further 200 m³. 1,900 m³ of sediment were deposited on the road (total deposit: 26,100 m³). Figure 5.62 illustrates the resulting sediment balance.

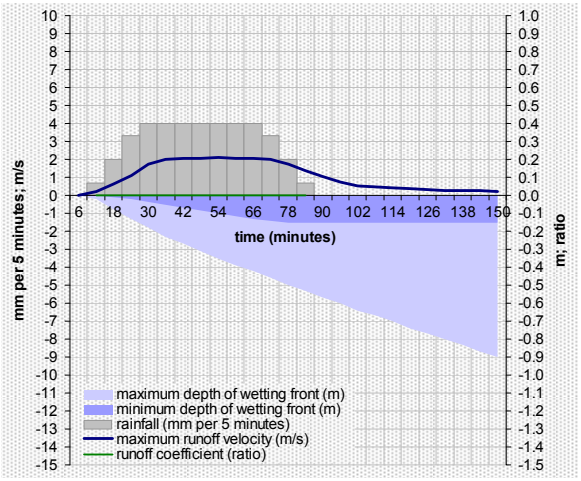

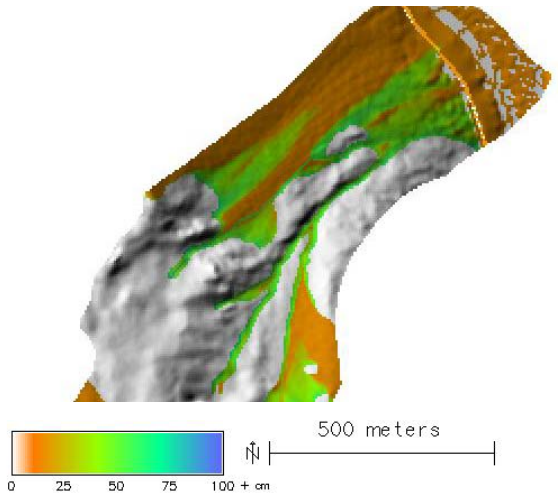

Figure 5.60 (top): System variables.
Figure 5.61 (bottom): Depth of wetting front below flow channels at the end of the scenario.

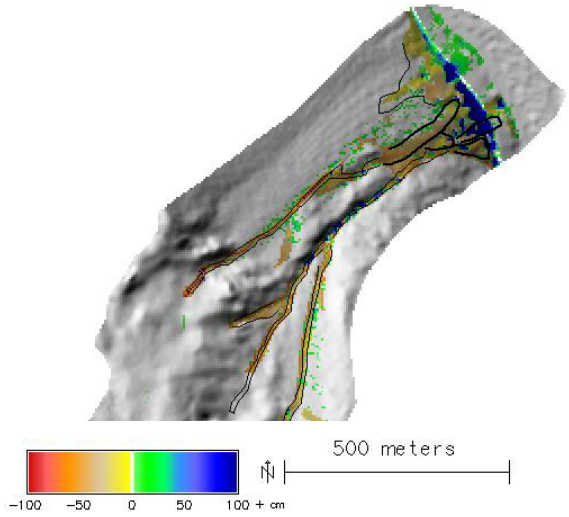

Figure 5.62: Sediment balance from debris flows.

4 Rainfall scenario: 40 mm in 140 minutes. Stretching the rainfall duration while maintaining the sum resulted in enhanced infiltration and reduced runoff, similar to the scenarios with 100 mm rainfall. The runoff coefficient on soil was zero, the wetting front reached depths between 15 cm and 1.20 m (Figures 5.63 and 5.64). All runoff occurring on soil was a consequence of inflow from upward rock slopes.

Figure 5.64 illustrates the effects of surface runoff coming down from bedrock outcrops. As soon as moving over a soil-covered slope, the water infiltrates until nothing is left at the surface. Therefore, the depth of the wetting front beneath the flow channels decreases downslope and then drops to the minimum (15 cm; only effective rainfall contributes to soil water). Away from the flow channels, where no inflow from upward occurs, the simulated wetting front is located at a depth of 15 cm over the entire soil-covered portion of the catchment. These patterns are true for all scenarios and all the *Guido* study areas. Of course, the values change with changing rainfall characteristics. With Scenario 3, for instance, the phenomenon described was also visible, but due to the higher values of runoff depth and velocity and the limited infiltration capacity of the soil, water from bedrock upslope moved farther downwards and infiltration was more levelled (compare Figure 5.61). The maximum depth of the wetting front was lower particularly due to the shorter duration of Scenario 3.

Due to the deeper wetting front in the critical areas, more material was simulated to be mobilized as debris flows, compared to Scenario 3 (34,100 m³; 36,200 m³ were identified as potentially unstable). Debris flow processes entrained 300 m³ of soil, leading to a total deposit of 34,300 m³. 2,800 m³ of debris ended up on the international road, according to the model (Figure 5.65).

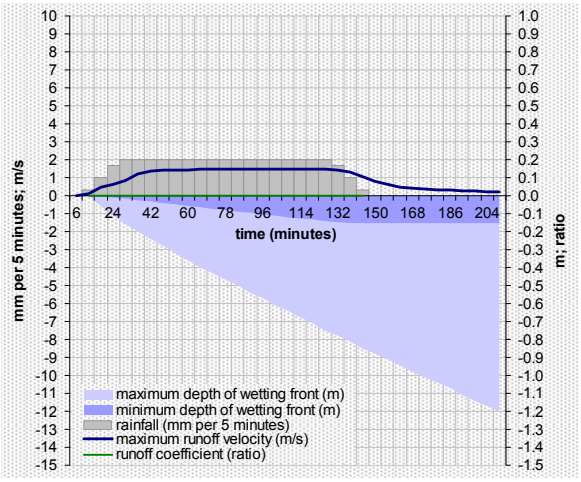

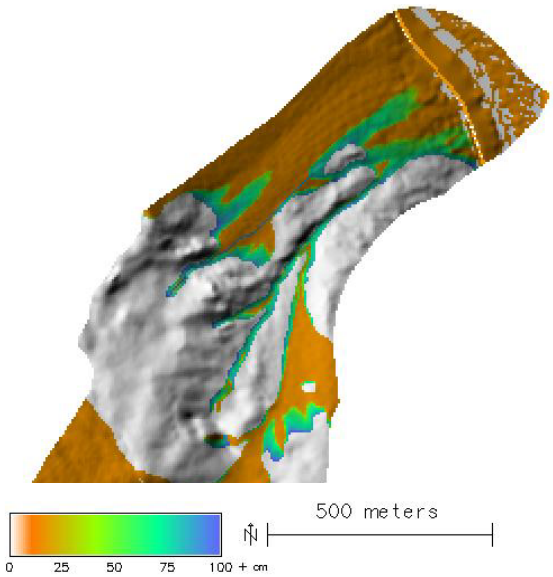

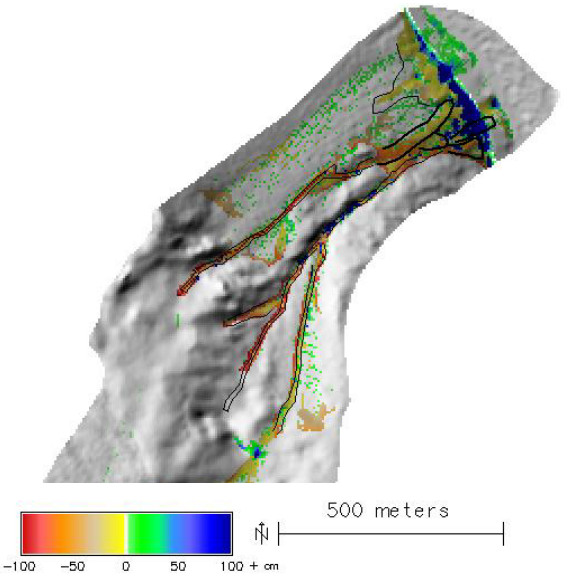

Figure 5.63 (top): System variables.
Figure 5.64 (middle): Depth of wetting front beneath flow channels at the end of the scenario.
Figure 5.65 (bottom): Sediment balance from debris flows.

5 Rainfall scenario: 40 mm in 40 minutes. Shortening the period of rainfall while maintaining the sum resulted in almost the same range in the depth of the wetting front as for the duration of 80 minutes (Figure 5.66). However, since the higher rainfall intensity resulted in higher flow velocities, peaking at 2.8 m s^{-1}, water from upslope bedrock outcrops could move farther downwards (Figure 5.67; compare Figures 5.61 and 5.64). No runoff was modelled to develop on the soil itself.

According to the shallower wetting front in the critical areas, less soil was simulated to be involved in debris flow processes than for the other scenarios with 40 mm rainfall: 21,700 m^3 of soil were identified as potentially unstable, 20,700 of which were considered as starting material of debris flows. Together with 200 m^3 of entrained soil, 21,000 m^3 of sediment were deposited. 1,600 m^3 ended up on the international road, according to the model (Figure 5.68).

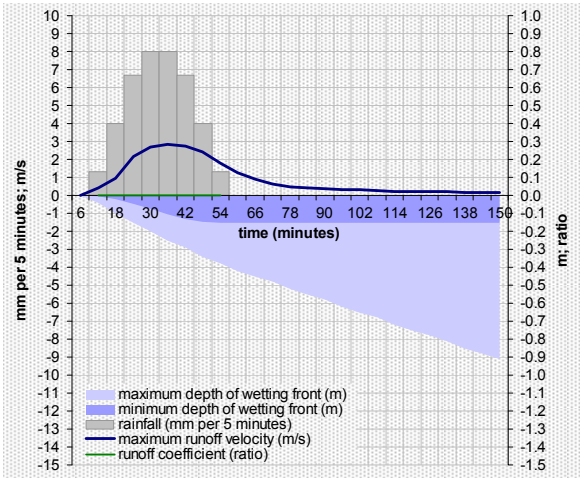

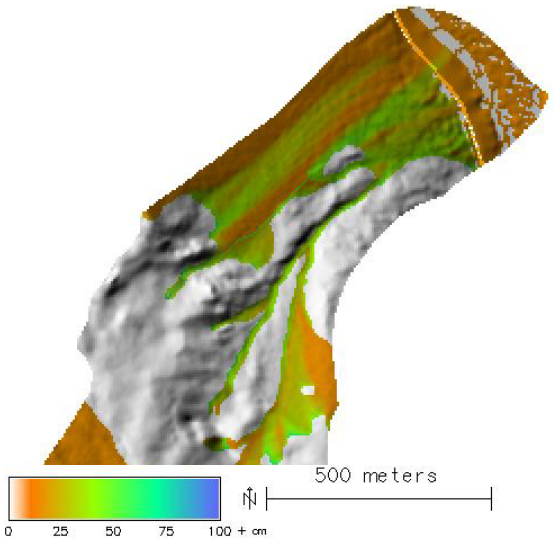

Figure 5.66 (top): Hydrological system variables for Scenario 5.
Figure 5.67 (bottom): Depth of wetting front below flow channels at the end of the scenario.

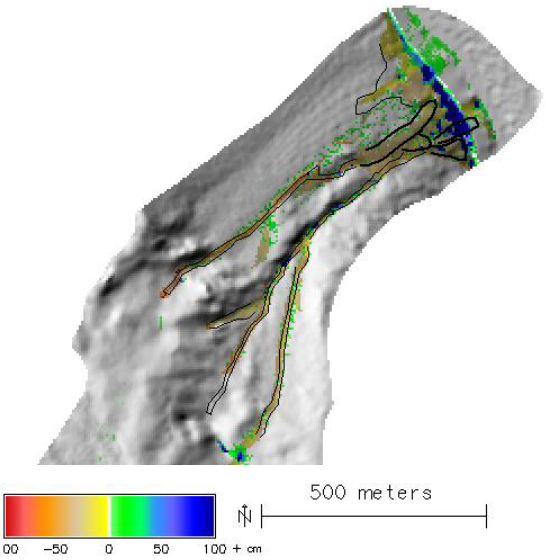

Figure 5.68: Sediment balance from debris flows.

6 Rainfall scenario: 10 mm in 80 minutes. Figure 5.69 shows the system variables for a scenario of 10 mm of rainfall in 80 minutes. No runoff developed on soil, and, at the end of the scenario, the wetting front was located at soil depths between 4 cm and 84 cm. Whilst the minimum was very shallow (what is not surprising, considering the low amount of rainfall), the maximum was not so much shallower than after the other scenarios with much more rainfall. When looking at Figure 5.70, however, it becomes obvious that the high values were concentrated to a very narrow belt directly at the base of rocky slopes, where relatively slow (maximum 0.9 m s^{-1}) runoff moved onto soil.

8,600 m^3 of soil were identified as potentially unstable, 8,200 m^3 of which were mobilized as debris flow, according to the model. 100 m^3 were entrained. 300 m^3 of sediment were deposited on the road (total deposit: 8,200 m^3). Figure 5.71 shows the corresponding sediment balance.

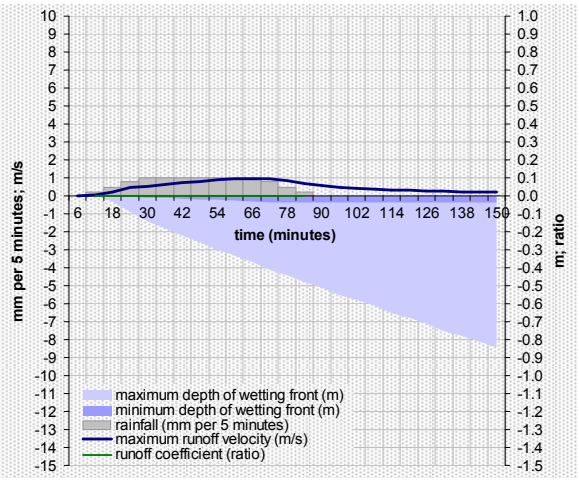

Figure 5.69: System variables.

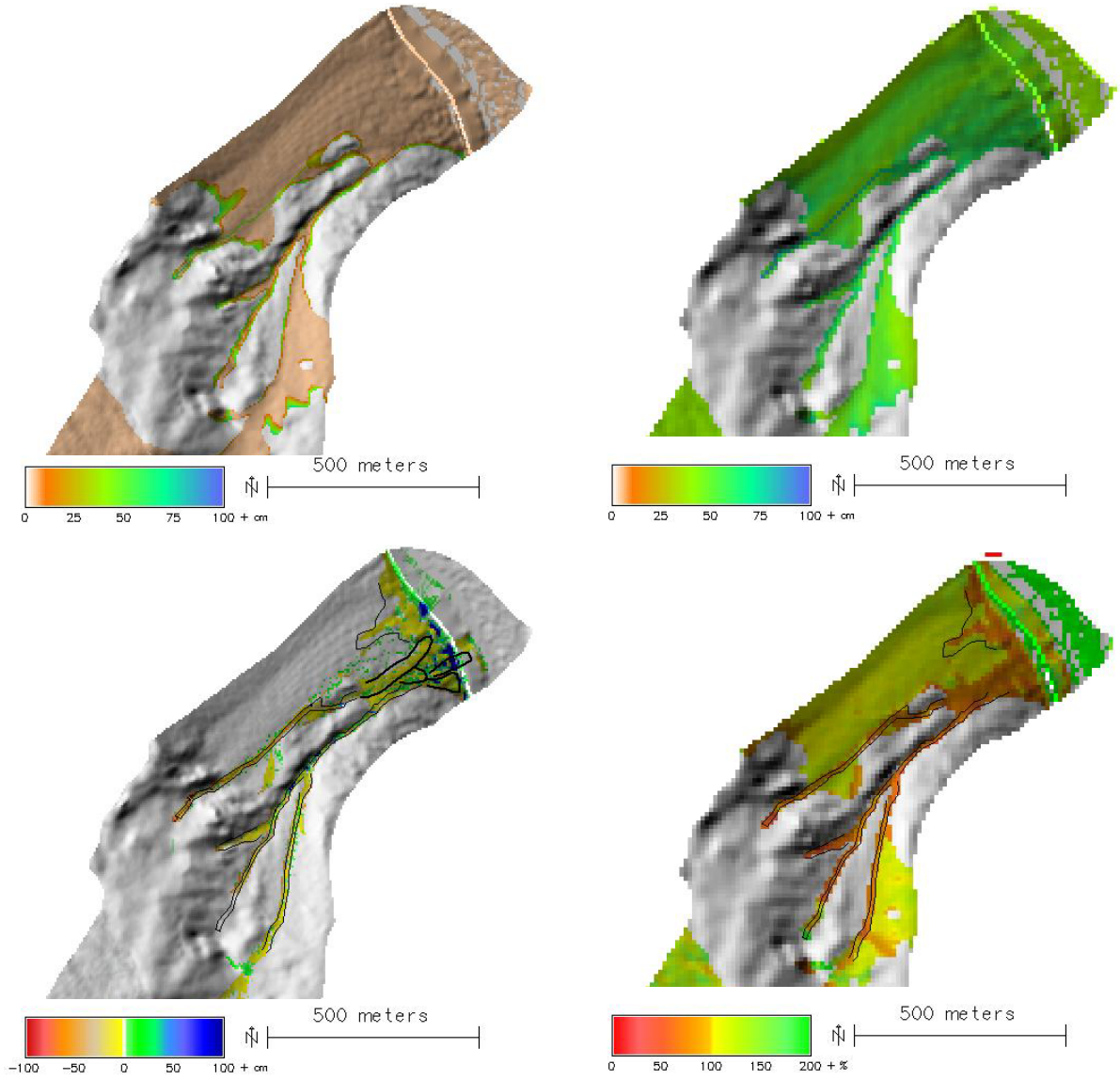

Figure 5.70 (top): Depth of wetting front at the end of the scenario.
Figure 5.71 (bottom): Sediment balance from debris flows connected to a rainfall scenario of 10 mm in 80 minutes.

5.3.3 Analysis of sensitivity

All parameter studies for the study area Castillo de Rocas were computed for a 100 mm rainfall scenario with a duration of 80 minutes.

7 Spatial resolution: 10 m. Doubling the cell size did not result in significant impacts on the model output, compared to 5 m resolution. The wetting front at the end of the event was located at depths between 0.38 m and 0.92 m (Figure 5.72; compare Figure 5.44), whilst the runoff coefficient on soil-covered slopes was 0.02 and runoff velocity reached a maximum of about 3.6 m s^{-1}.

Also the spatial distribution of potentially unstable soil (Figure 5.73) corresponded quite well to that computed at the standard resolution of 5 m (compare Figure 5.45).

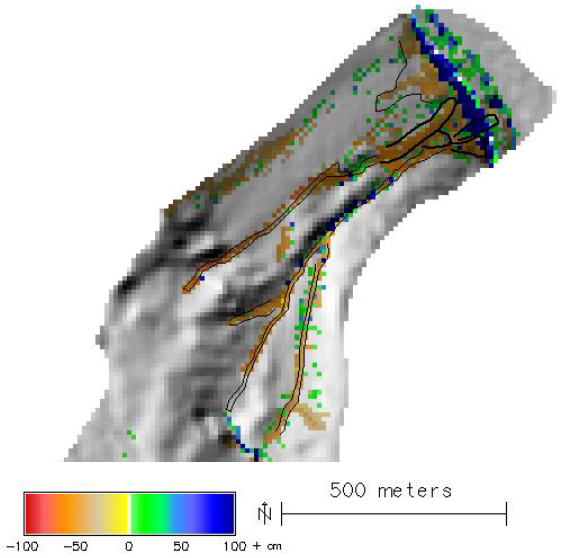

Figure 5.72 (top): Depth of wetting front beneath flow channels at the end of the scenario (10 m resolution).
Figure 5.73 (middle): Factor of safety.
Figure 5.74 (bottom): Sediment balance form debris flows.

42,400 m³ of potentially unstable soil were detected in total (at 5 m resolution: 44,700), 40,600 m³ of which were considered to be mobilized as debris flow (40,600 m³), entraining further 2,100 m³ (1,800 m³) of soil. 2,300 m³ (3,600 m³) out of the resulting deposit of 42,700 m³ (42,300 m³) were simulated to end up on the international road. The lower value denoted for deposition on the road is supposed to be mainly an effect of local raster resolution (the road is not much wider than one cell). The spatial distribution of moved soil volumes is more or less similar to that computed at 5 m resolution (Figure 5.74; compare Figure 5.55).

8 Angle of internal friction. A rather high value for the angle of internal friction φ (43.0°) has been chosen for the rainfall scenarios in order to compensate for setting soil cohesion to zero. When testing the model with lower values of φ, also measured with samples from the same soil class (compare Table A1.1), the influence of this parameter on the model output became obvious. The Figures 5.75 to 5.79 represent the factor of safety and the starting material of debris flows for φ = 40.0° and φ = 36.2°.

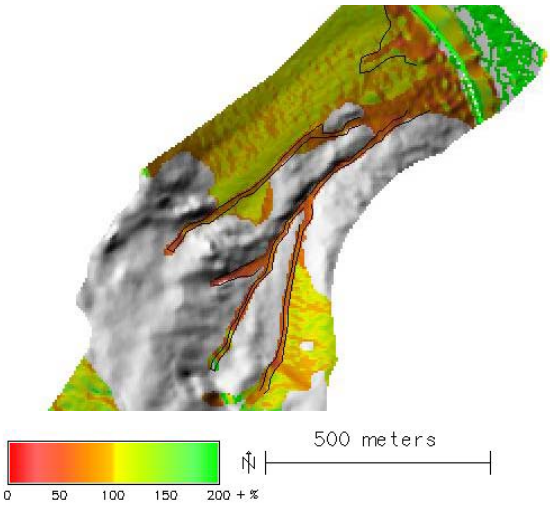

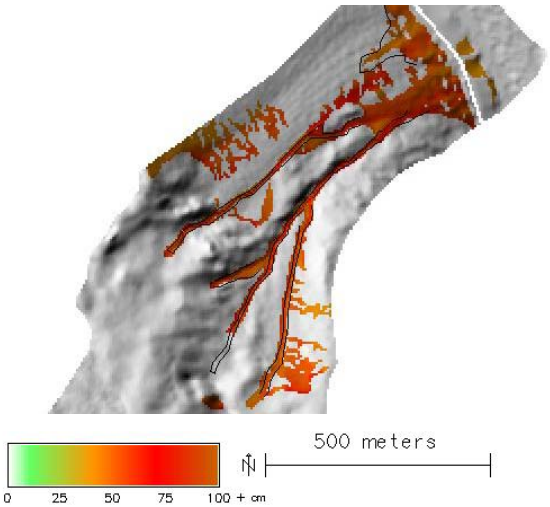

Figure 5.75 (top): Factor of safety for φ = 40.0°.
Figure 5.76 (bottom): Depth of starting material of debris flows for φ = 40.0°.

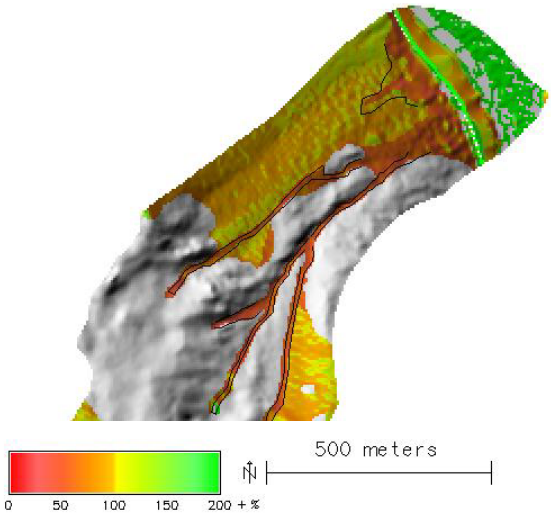

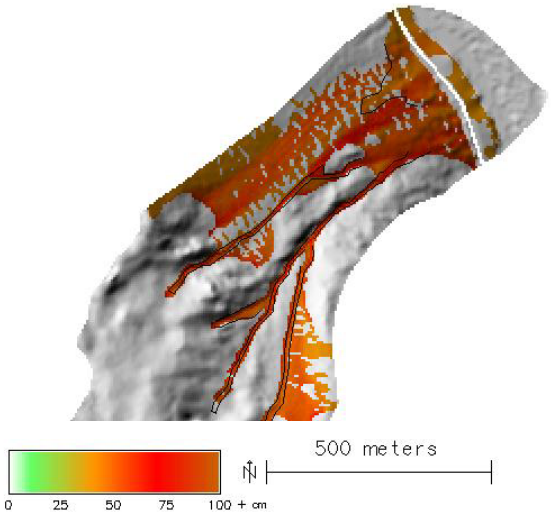

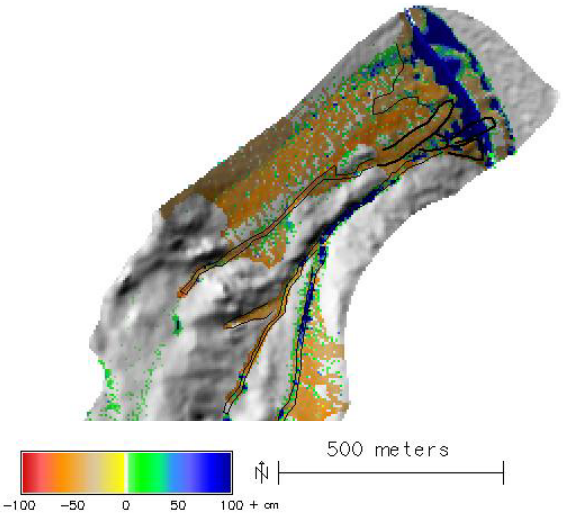

Figure 5.77 (top): Factor of safety for φ =36.2°.
Figure 5.78 (middle): Depth of starting material of debris flows for φ = 36.2°.
Figure 5.79 (bottom): Sediment balance from debris flows for φ = 36.2°.

With φ = 40.0°, 65,300 m³ of potentially unstable soil were detected by the model, 56,800 m³ of which were identified as starting material of debris flows. 1200 m³

of soil were entrained, leading to a deposit of 58,000 m³ (4,600 m³ on the international road).

With $\varphi = 36.2°$, 97,800 m³ of potentially unstable soil were modelled, 94,100 m³ of which were identified as starting material of debris flows. Including 300 m³ of entrained soil, 94,400 m³ were deposited, 6,900 m³ on the international road (Figure 5.77).

9 Soil cohesion. When assuming a soil cohesion of 4000 N m^{-2} together with $\varphi = 40.0°$ (a combination measured in the laboratory), 300 m³ of slope failures, but no starting areas for debris flows were detected by the model.

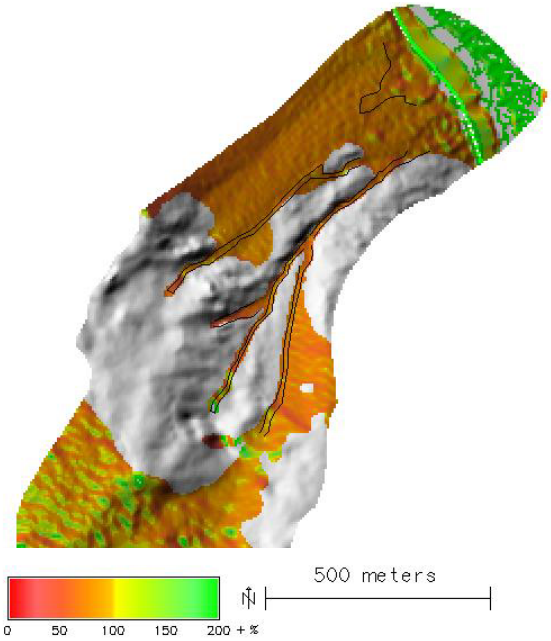

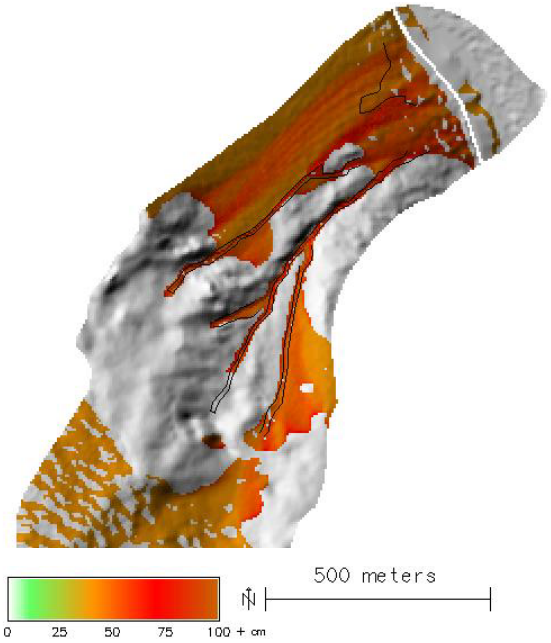

Figure 5.80 (top): Factor of safety, neglecting root cohesion.
Figure 5.81 (bottom): Starting material of debris flows.

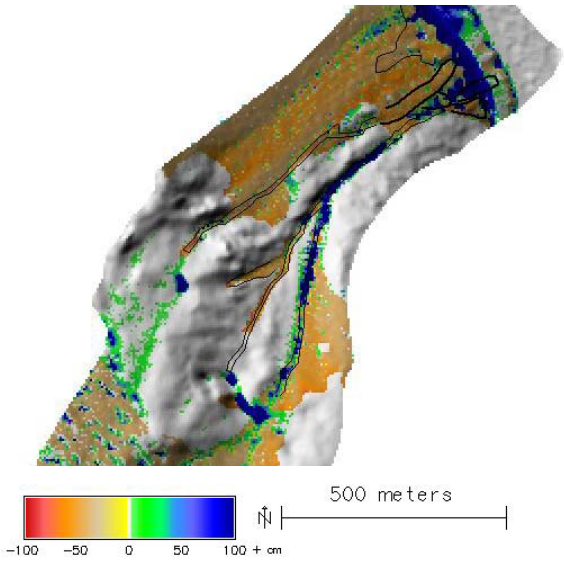

Figure 5.82: Sediment balance from debris flows.

10 Root cohesion. Neglecting root cohesion when executing the infinite slope stability model resulted in much larger soil volumes simulated as unstable, compared to Scenario 1: 144,500 m³, 142,800 m³ of which were identified as starting material of debris flow processes. Together with 100 m³ of scoured soil, 142,900 m³ of sediment were deposited, according to the model, 8,700 m³ on the international road (Figures 5.80 to 5.82).

11 Dry soil. Excluding soil water from the slope stability calculations led to the identification of only some isolated unstable patches (2,900 m³), none of which was identified as starting area for a debris flow.

5.3.4 debris flow runout based on the SH model (r.avalanche)

Three simulations with *r.avalanche* were performed for *Castillo de Rocas*, using defined starting areas with $h_i = 1$ m and varying the bed friction angle δ as well as the spatial resolution. The angle of internal friction, not being supposed to exert a major influence on the model results, was kept constant for all calculations ($\varphi = 43.0°$).

12 Defined starting areas, $\delta = 28°$, spatial resolution = 5 m. The debris flows reached a maximum velocity of 48 m s^{-1}, according to the model (Figure 5.83). Runout length was severely overestimated, compared to the debris flow deposits observed in the field. Though one patch remained around its starting area (probably due to deficiencies of the elevation model used), most of the simulated debris flows even crossed the valley bottom and left the study area on the other side. There are no indicators in the field that this has occurred in the near past. The debris flow deposit on the road reached a maximum volume of 190 m³, but then decreased to almost zero at the end of the simulation (Figure 5.84). Compare Figure 5.89 for a temporal series of debris flow depth.

13 Defined starting areas, $\delta = 33°$, spatial resolution = 5 m. When increasing bed friction angle, the simulated maximum flow velocity decreased to 28 m s^{-1} (Figure 5.85) Runout length decreased too, corresponding well to the runout length observed in the field. Figure 5.86 shows that about 350 mm of debris were deposited on the international road at the end of the simulation (maximum: slightly more than 430 mm). Lateral spreading of the flow appeared too pronounced, compared to field evidence. For flow depth at different time steps compare Figure 5.90.

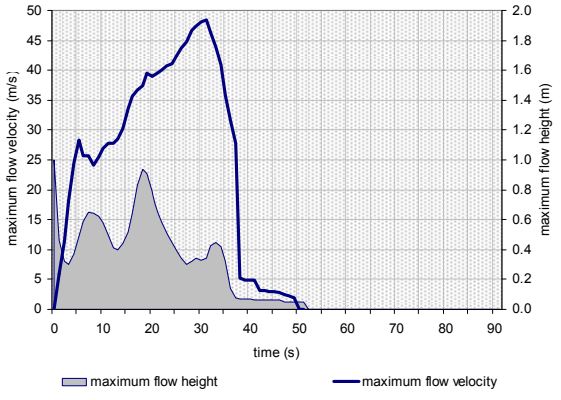

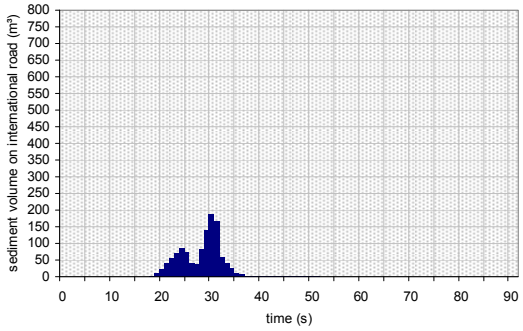

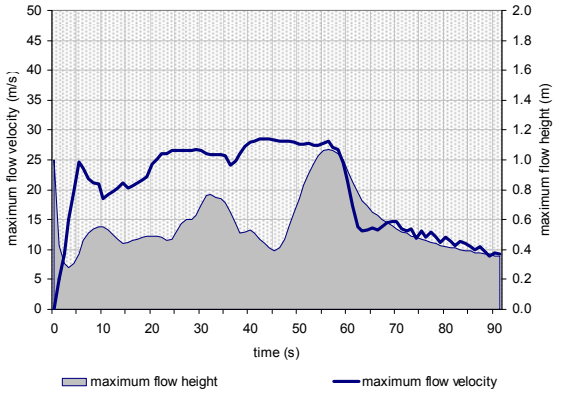

Figure 5.83 (top): Maximum flow depth and velocity (defined starting areas; $\delta = 28°$).
Figure 5.84 (middle): Debris flow volume on international road (defined starting areas; $\delta = 28°$).
Figure 5.85 (bottom): Maximum flow depth and velocity (defined starting areas; $\delta = 33°$).

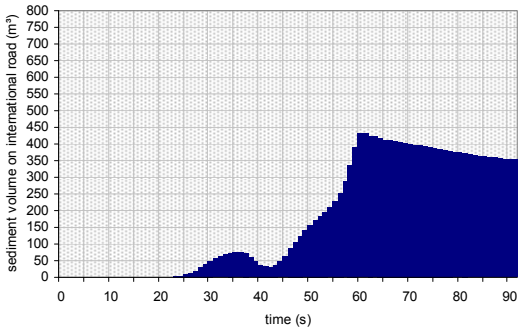

Figure 5.86: Debris flow volume on international road (defined starting areas; $\delta = 33°$).

14 Predefined starting areas, bed friction angle $\delta = 33°$, spatial resolution = 10 m. The runout length and the maximum flow velocity were pretty the same as for 5 m spatial resolution. The flow depth and the volume deposited on the road (maximum 410 mm; 220 mm at the end; Figure 5.88) were smaller. Figure 5.91 shows that these patterns were connected to an extensive spreading of the simulated flow, much more pronounced than at 5 m resolution.

The Figures 5.89 to 5.91 illustrate the temporal development of flow depth for all three simulations.

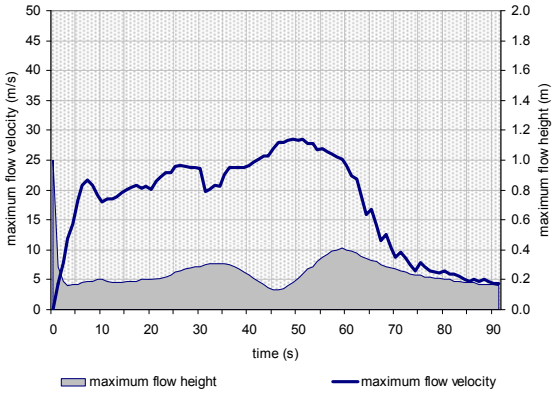

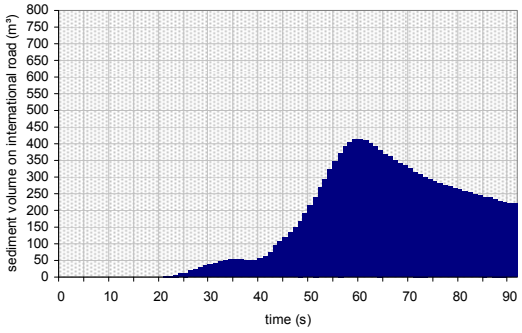

Figure 5.87 (top): Maximum flow depth and velocity (defined starting areas; $\delta = 33°$; spatial resolution = 10 m).
Figure 5.88 (bottom): Debris flow volume on international road (defined starting areas; $\delta = 33°$; spatial resolution = 10 m).

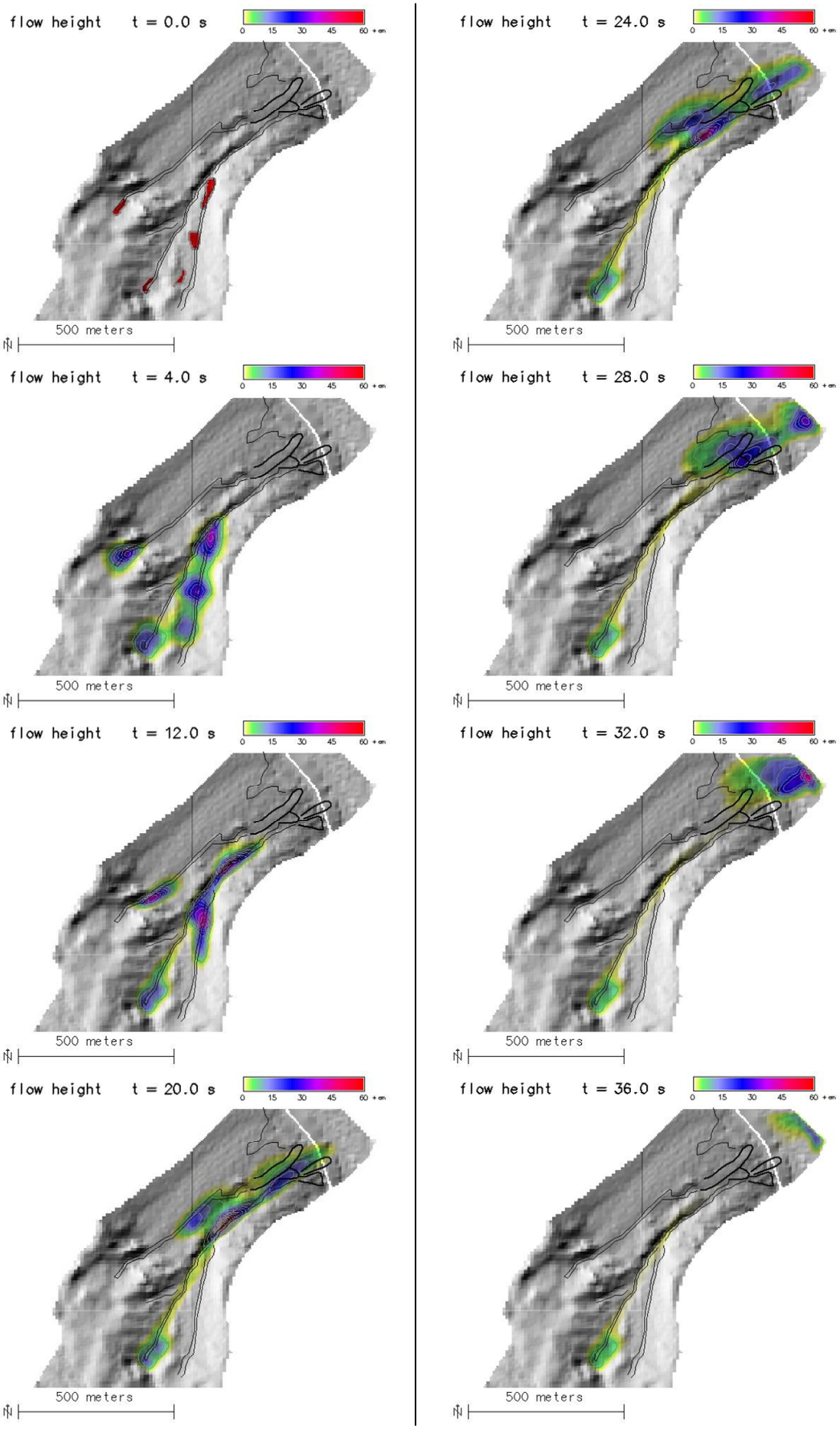

Figure 5.89: Depth of debris flow at different time steps (defined starting areas; δ = 28°; resolution = 5 m).

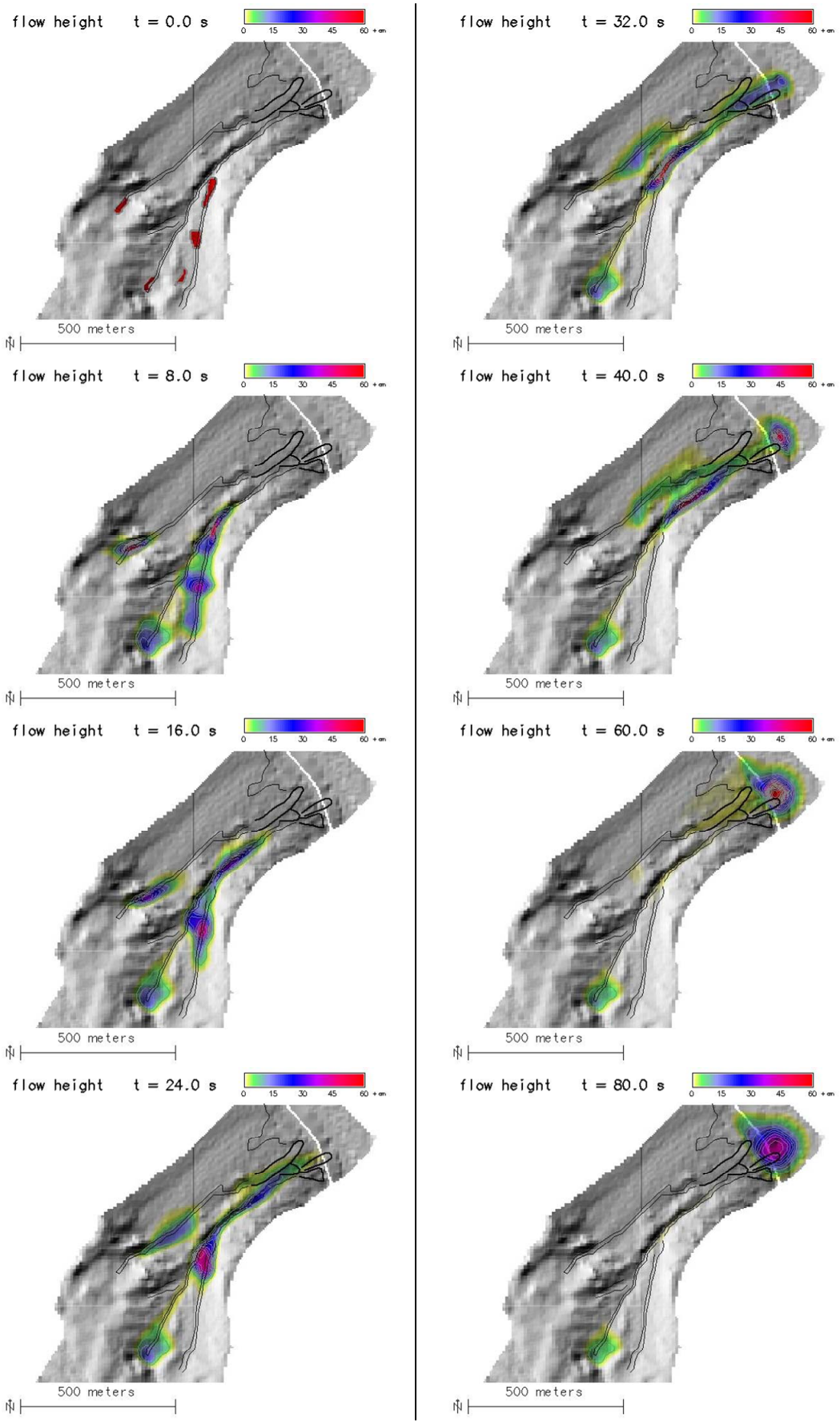

Figure 5.90: Depth of debris flow at different time steps (defined starting areas; δ = 33°; resolution = 5 m).

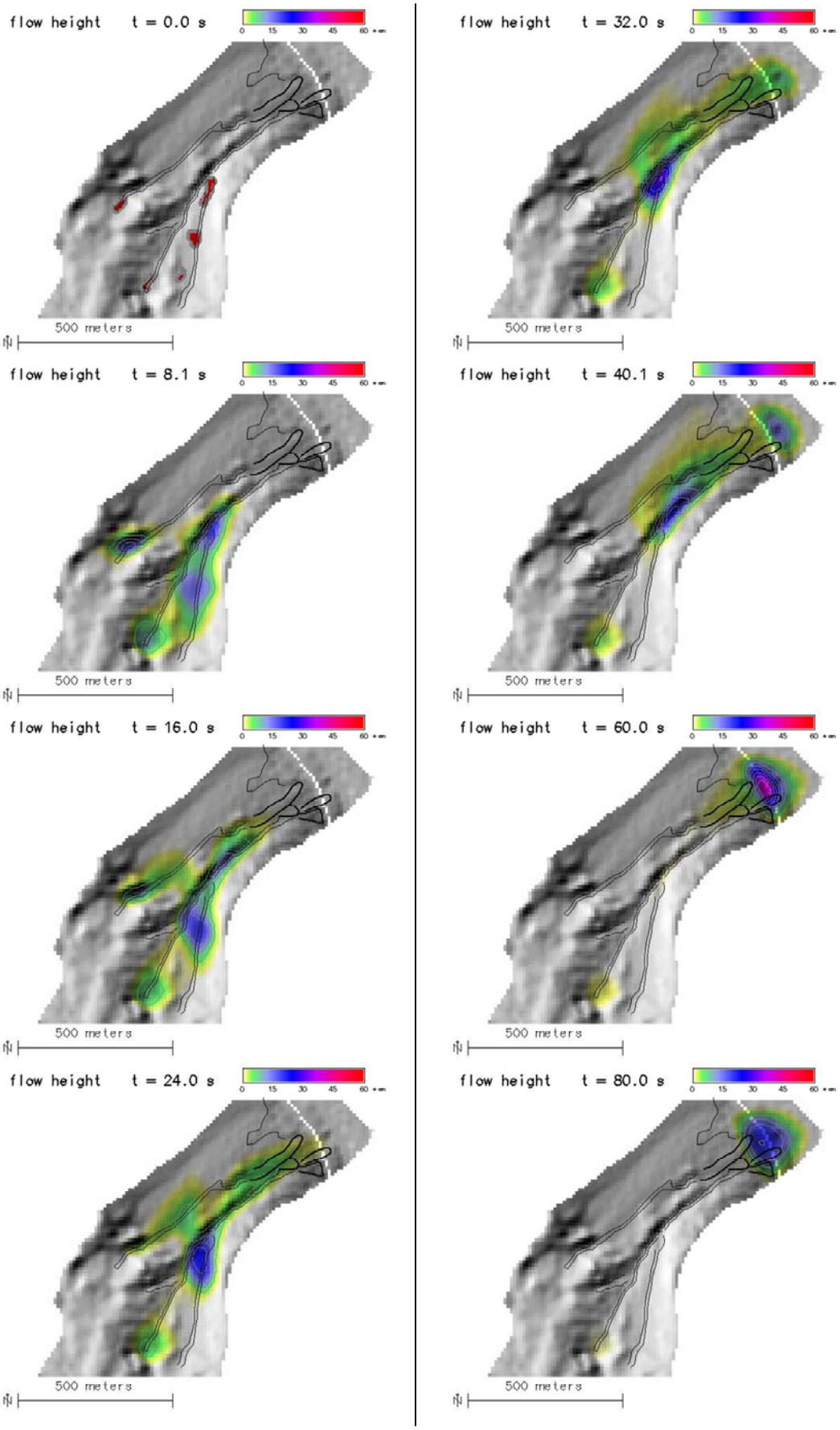

Figure 5.91: Depth of debris flow at different time steps (defined starting areas; δ = 33°; resolution = 10 m).

5.3.5 Summary

Figure 5.92 shows the volumes of potentially unstable soil for different scenarios of rainfall sum and duration. Not surprisingly, the volumes increased with increasing rainfall sum, but also with increasing rainfall duration. For the 100 mm scenarios, this was at least partly a result of the larger amount of infiltrating water since surface runoff only developed in connection to Scenario 1. The increase in potentially failed volume with increasing rainfall duration observed with the 40 mm scenarios can also be explained with the limited infiltration capacity: a larger portion of the water moving down from bedrock outcrops can infiltrate immediately – usually on steep slopes with low *FOS* – with smaller runoff depth. With increasing runoff depth, a larger portion moves farther downwards and infiltrates in areas with *FOS* > 1, where the depth of the wetting front does not matter.

The inflow of water from upwards was also responsible for the fact that the volumes of potentially unstable soil were not at all proportional to rainfall sum (Table 5.6). Directly at the base of rocky slopes, where the terrain is steepest and therefore most susceptible to instabilities, plenty of water is available for infiltration also with low rainfall sums.

According to the simulations, between 300 m³ and 5,400 m³ of debris were deposited on the international road (excluding the analyses of sensitivity; compare Table 5.6). The fact that, under dry conditions, the system seemed to be near to equilibrium (only some few unstable patches) indicated a suitable choice of the major parameters. A comparison with the other study areas and with reference data will be provided in Section 6.1.

r.avalanche worked quite well for simulating runout length when the parameters were calibrated. However, the patterns of deposition were not modelled successfully.

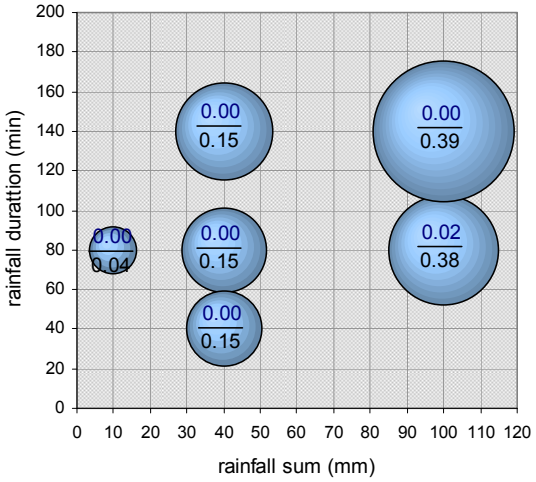

Figure 5.92: Volumes of potential slope failure as calculated for different rainfall scenarios (dimensionless). The blue numbers represent the runoff coefficients connected to the corresponding scenarios, the black numbers the minimum depth of wetting front (away from flow channels).

Table 5.6: Summary of some of the major system variables and moved soil volumes for all of the scenarios and analyses with the study area *Castillo de Rocas*; rcoef = runoff coefficient over the entire event; dwfront = depth of wetting front at the end of the simulation; (1) = away from flow channels; (2) = maximum.

scenario	pot. failure (m³)	start (m³)	entrainment (m³)	deposit (m³)	on road (m³)	rcoef	dwfront (1)	dwfront (2)
1: 100/80	44,709	40,552	1,775	42,327	3,552	0.02	-0.38	-0.92
2: 100/140	72,165	67,168	1,252	68,420	5,421	0.00	-0.39	-1.22
3: 40/80	27,433	25,925	200	26,125	1,911	0.00	-0.15	-0.90
4: 40/140	36,230	34,093	250	34,343	2,766	0.00	-0.15	-1.20
5: 40/40	21,741	20,740	219	20,959	1,588	0.00	-0.15	-0.91
6: 10/80	8,580	8,154	89	8,243	307	0.00	-0.04	-0.84
7: res. 10 m	42,420	40,581	2,146	42,727	2,266	0.02	-0.38	-0.92
8a: φ= 40.0°	65,331	56,779	1,223	58,002	4,642			
8b: φ= 36.2°	97,842	94,078	293	94,371	6,915			
9: φ= 40.0°; c = 4.0 kN m^{-2}	310	0	0	0	0			
10: c_{root} = 0	144,516	142,812	116	142,928	8,724			
11 dry soil	2,872	0	0	0	0			

5.4 Quebrada Escondida

The study area *Quebrada Escondida* (Figure 5.93) is not only located closely adjacent to Castillo de Rocas (less than half a kilometre), but shows also some similarities (compare Section 3.7). The same scenarios were tested for both of the areas in order to explore differences and similarities in their potential reactions to heavy rainfall events. The model was tested for its sensitivity to variations of some hydraulic parameters, vegetation characteristics, and spatial resolution. Table 5.7 provides a summary of all the scenarios and tests that were computed for the study area *Quebrada Escondida*.

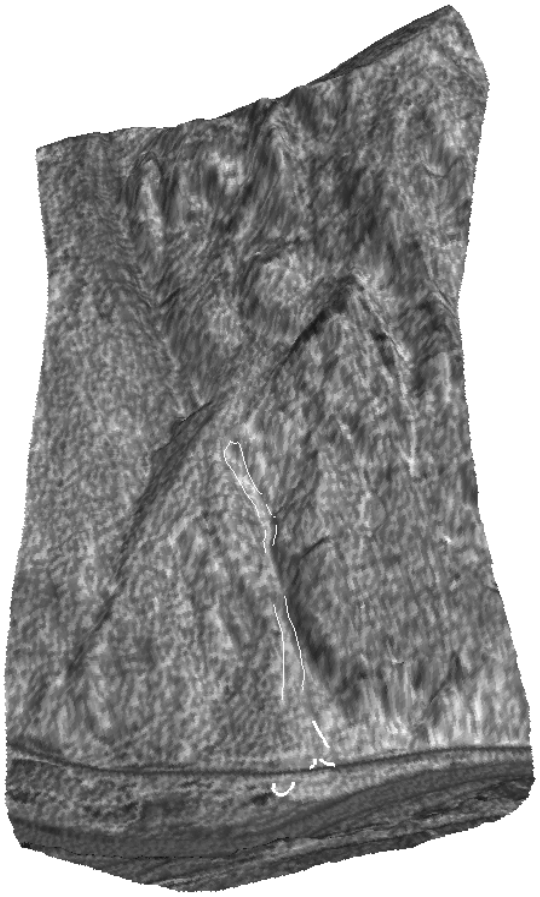

5.4.1 Tests of plausibility

1a Runoff and infiltration. The Figures 5.94 and 5.95 illustrate the runoff depth and the depth of the wetting front below the flow channels, representing the hydrological status of the catchment during and after Scenario 1. Figure 5.96 shows the temporal patterns of some of the hydrological system variables. Whilst runoff depth and velocity are lower than in the study area *Castillo de Rocas* (which is much larger) for the same scenario, the depth of the wetting front is very similar, and even equal away from the flow channels.

Figure 5.93: The study area *Quebrada Escondida* (compare Section 3.7). The thin white lines represent potential starting areas of debris flows according to field evidence, the bold white lines delineate debris flow deposits. Elevation model derived from aerial and SPOT5 imagery, draped orthophoto from SPOT5. Design: Martin Mergili, 04/2008.

Table 5.7: Parameter settings and scenarios for *Quebrada Escondida*. soil = soil parameters, lcov = land cover parameters, n/sed = Manning's n and parameters for sediment transport, pflow = preferential flow (per cent of total seepage), runout = parameters for runout model, res = spatial resolution, A = hydraulic model, B = sediment transport model, C = slope stability model, D = debris flow runout model; std = standard parameters (compare Section 4.1), cal = calibrated parameters, test = changed parameters for analysis of sensitivity, h_i = defined starting depth.

		Parameter settings						Used modules			
		soil	lcov	n/sed	pflow	runout	res (m)	A	B	C	D
Test of plausibility (with precipitation = 100 mm in 80 minutes; all as rainfall)											
1a	Infiltration and runoff model	std	std	std	0		5	x			
1b	Slope stability model	std	std				5			x	
1c	Sediment transport model	std	std	std	0		5		x		
1d	Debris flow runout model					std, cal	5				x
Scenarios											
1	Scenario 1: p.=100 mm in 80 min.	std	std	std	0	cal	5	x		x	x
2	Scenario 2: p.=100 mm in 140 min.	std	std	std	0	cal	5	x		x	x
3	Scenario 3: p.=40 mm in 80 min.	std	std	std	0	cal	5	x		x	x
4	Scenario 4: p.=40 mm in 140 min.	std	std	std	0	cal	5	x		x	x
5	Scenario 5: p.=40 mm in 40 min.	std	std	std	0	cal	5	x		x	x
6	Scenario 6: p.=10 mm in 80 min.	std	std	std	0	cal	5	x		x	x
Analysis of sensitivity (with precipitation = 100 mm in 80 minutes; all as rainfall)											
7	Spatial resolution	std	std	std	0	cal	10	x		x	x
8	Percolation through rock	test	std	std	0	cal	5	x		x	x
9	No vegetation	std	test	std	0	cal	5	x		x	x
10	Dry soil	std	std	std	0	cal	5			x	x
Runout model based on the SH model (r.avalanche)											
11	Defined starting areas (h_i = 1 m)	φ = 43.0°	δ = 33°				5				

The runoff coefficient over the entire scenario was 0.02, the depth of the wetting front at the end of the scenario ranged between 0.38 and 0.79 m, with maxima below the main flow channel and at the base of steep bedrock outcrops.

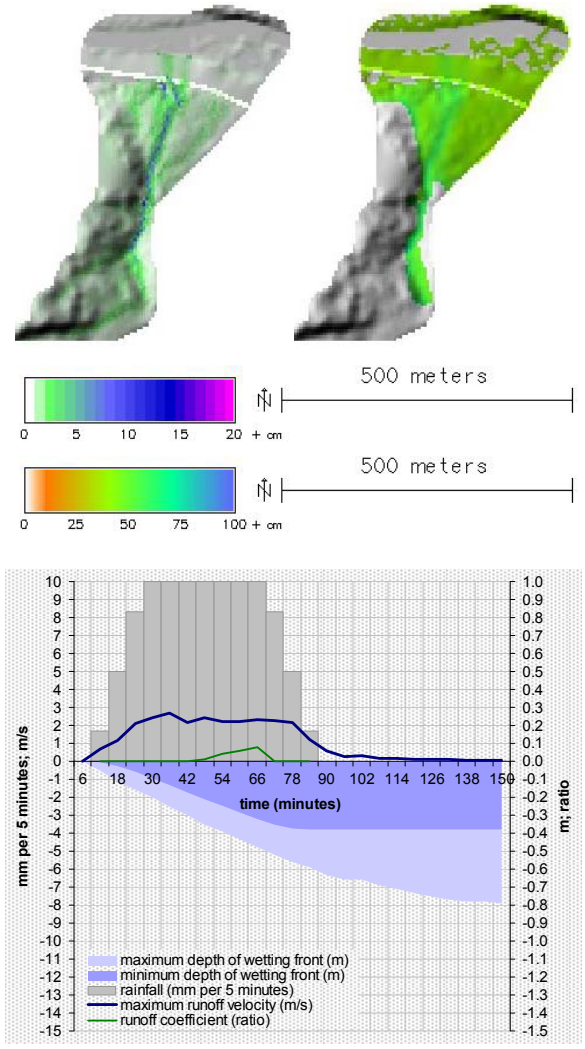

Figure 5.94 (top left): Runoff depth (t = 60 min).
Figure 5.95 (top right): Depth of wetting front below flow channels at the end of Scenario 1.
Figure 5.96 (bottom): System variables (Scenario 1).

1b Slope stability model. In general, the areas identified as potentially unstable corresponded quite well to the patterns observed in the field except in the lowermost part of the area, where a certain overestimation of instabilities seemed to occur (Figure 5.97). The modelled distribution of starting material of debris flows is shown in Figure 5.98. 8,600 m³ out of 9,100 m³ of potentially unstable soil were mobilized as debris flows, according to the simulation.

1c Sediment transport model. As discussed for the study area *Castillo de Rocas*, the reliability of the sediment transport model is not satisfactory because some parameters had to be calibrated in order to yield plausible results, but due to lacking field data this calibration could not be justified. Similar to *Castillo de Rocas*, stream power was used to get an idea about areas prone to detachment-driven debris flows (Figure 5.99). Also for Quebrada Escondida, the majority of the areas with high values of stream power coincided with mechanically unstable areas or areas subjected to entrainment (Figure 5.100), so that it could be justified to omit the sediment transport model from the simulations.

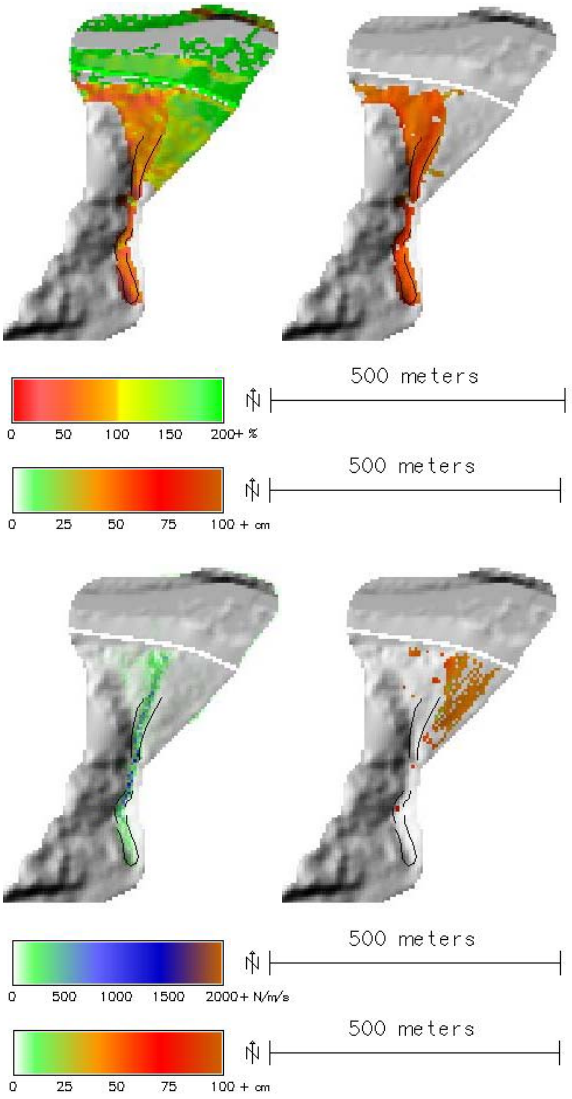

Figure 5.97 (top left): Factor of safety.
Figure 5.98 (top right): Depth of debris flow initiation.
Figure 5.99 (bottom left): Stream power (t = 60 min).
Figure 5.100 (bottom right): Depth of entrainment of soil by debris flows.

1d Debris flow runout model. Similar to *Castillo de Rocas*, the standard parameters for the runout model were not suitable – although the location of the runout zone was simulated correctly, the deposit appeared quite squeezed, not corresponding to the patterns of debris flow deposits observed in the field (Figure 5.101).

The correspondence was better when using a plain value of $\mu = 0.25$ while keeping M/D at 75 m and also leaving the remaining parameters unchanged (slope threshold 15°, velocity threshold 10 m s^{-1}, and

maximum depth of deposit 5 m). The location of the deposit downslope of the international road was not modelled correctly, but with a lateral offset – probably as a consequence of inaccuracies of the DEM used. Part of the material reached the bottom of the main valley, a behaviour that was not confirmed by field evidence (Figure 5.102).

However, the debris flow index illustrates that the majority of the material was deposited in areas corresponding to observations (Figure 5.103). Using the calibrated parameters, the model yielded an entrained soil volume of 1,500 m³ and a deposit of 10,100 m³. 1,900 m³ of the debris flow material were predicted to end up on the international road (Figure 5.104).

The modelled maximum velocity of debris flows exceeded 20 m s^{-1} with either the standard or the calibrated parameters (Figures 5.105 and 5.106). These values were only reached in some portions of the steepest part of the channel. Over the majority of their path, debris flows moved at velocities between 10 m s^{-1} and 15 m s^{-1}, decelerating considerably when passing the international road.

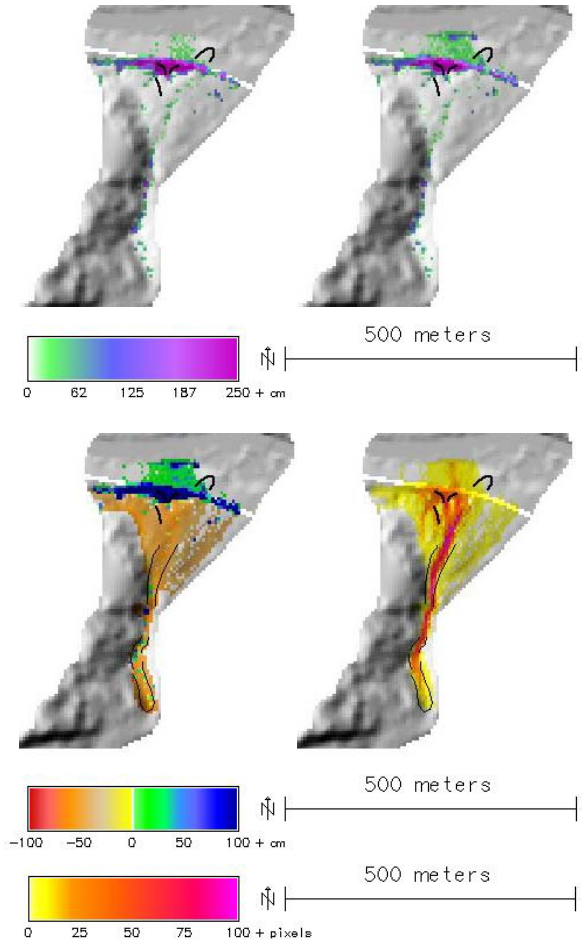

Figure 5.101 (top left): Deposition from debris flows with standard parameters.
Figure 5.102 (top right): Deposition from debris flows with calibrated parameters.
Figure 5.103 (bottom left): Sediment balance from debris flows (runout with calibrated parameters).
Figure 5.104 (bottom right): Debris flow index.

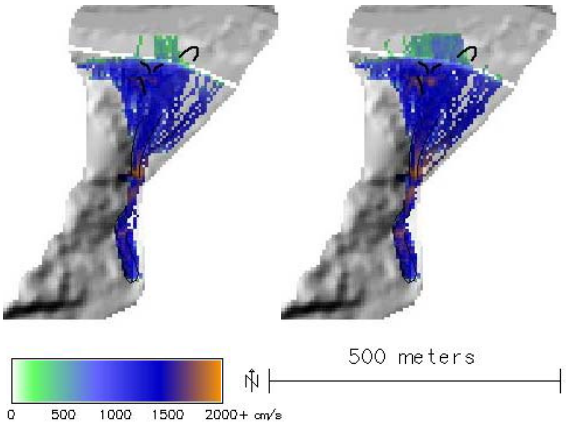

Figure 5.105 (left): Maximum velocity of debris flows with standard parameters.
Figure 5.106 (right): Maximum velocity of debris flows with calibrated parameters.

5.4.2 Scenarios

2 Rainfall scenario: 100 mm in 140 minutes. When extending rainfall duration while leaving the sum unchanged, there was a tendency towards increased infiltration and decreased runoff – the runoff coefficient dropped to zero. The wetting front at the end of the event ranged between 39 cm (away from flow channels) and 1.16 m. The system variables are illustrated in the Figures 5.107 to 5.109.

The spatial patterns of the factor of safety did not change, compared to Scenario 1. However, the deeper wetting front led to a larger volume of potential slope failures and subsequent debris flows: 14,600 m² of potentially unstable soil were detected by the simulation (14,500 m³ were identified as starting material for debris flows), 2,100 m³ of soil were entrained. 2,900 m³ out of the resulting 16,600 m³ were deposited on the international road, according to the model. Deposition and sediment balance from debris flows are illustrated in the Figures 5.110 and 5.111.

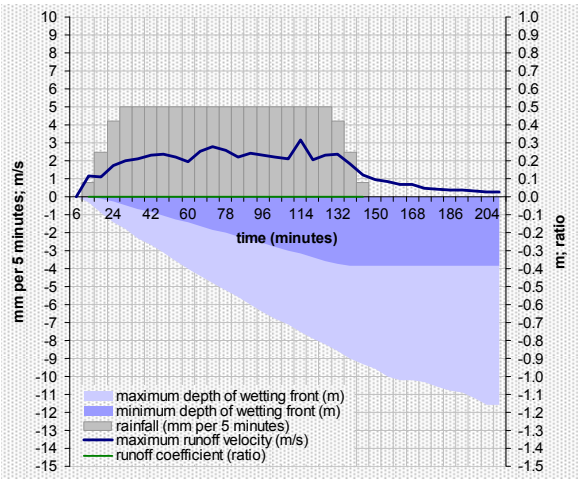

Figure 5.107: System variables (Scenario 2).

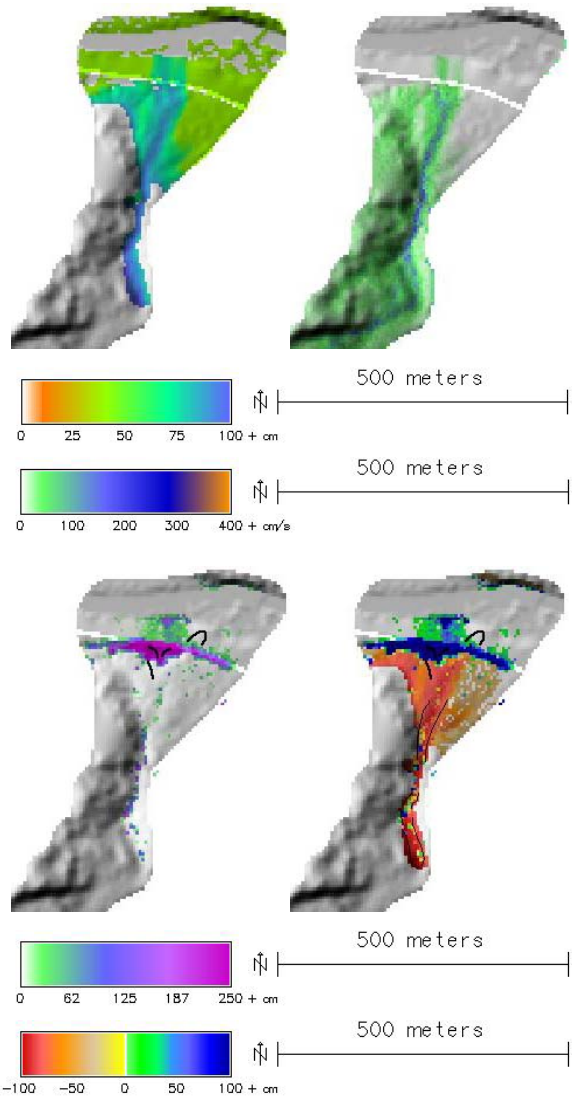

Figure 5.108 (top left): Depth of wetting front (below flow channels).
Figure 5.109 (top right): Runoff velocity (t = 120 min).
Figure 5.110: (bottom left) Deposition from debris flows.
Figure 5.111: (bottom right) Sediment balance from debris flows.

3 Rainfall scenario: 40 mm in 80 minutes. No runoff developed on soil-covered slopes, according to the model, while the depth of the wetting front ranged between 15 cm and 83 cm at the end of the scenario (Figure 5.112). Figure 5.113 illustrates the influence of runoff from rocky slopes on the depth of the wetting front. Runoff velocity reached maxima of about 2.3 m s^{-1}.

The following volumes were modelled: 7,600 m^3 of soil were detected as potentially unstable, 7,500 m^3 of which were identified as starting material for debris flows. 800 m^3 were entrained and 8,300 m^3 were deposited. 1,500 m^3 of sediment ended up on the international road. Figure 5.114 shows the corresponding sediment balance.

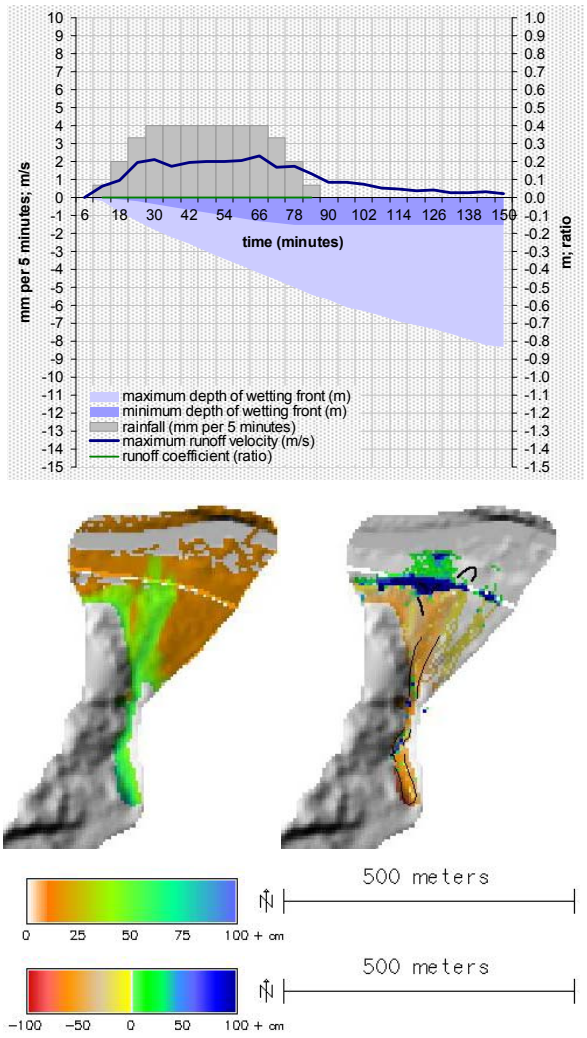

Figure 5.112 (top): System variables (Scenario 3).
Figure 5.113 (bottom left): Depth of wetting front below flow channels.
Figure 5.114 (bottom right): Sediment balance from debris flows.

4 Rainfall scenario: 40 mm in 140 minutes. When distributing the 40 mm of rainfall over 140 instead of 80 minutes, the maximum depth of wetting front increased to 1.13 m. Minimum depth remained at 15 cm since neither during the one nor during the other event any runoff developing on soil was predicted by the simulation. The much deeper maximum can be explained by the longer rainfall duration (Figures 5.115 and 5.116).

As a consequence of the deeper wetting front in critical areas, more soil material was identified as potentially unstable: 10,100 m^2 (more than connected to Scenario 1), 10,000 m^3 of which were identified as starting material of debris flows. 700 m^3 of soil were modelled to be entrained, resulting in a total deposit of 10,700 m^3, 1,800 m^3 of which ended up on the international road (runout computed with calibrated parameters; Figure 5.117).

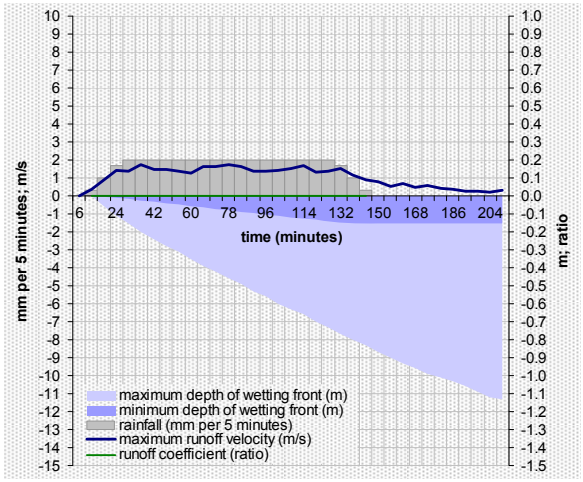

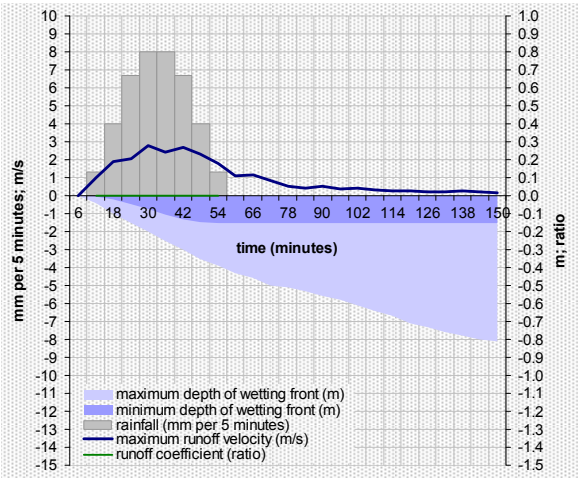

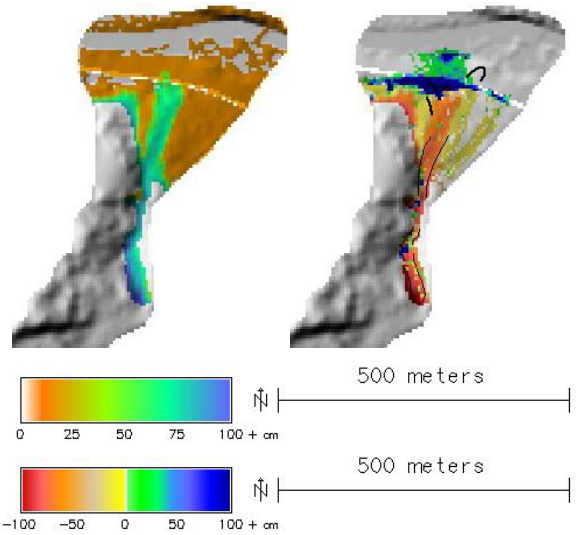

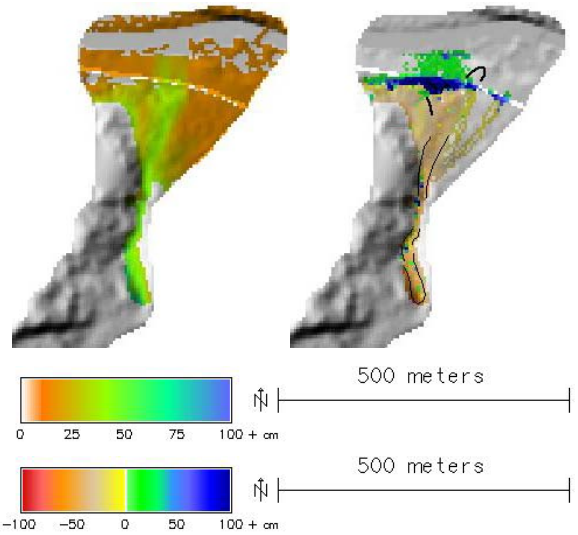

Figure 5.115 (top): System variables (Scenario 4).
Figure 5.116 (bottom left): Depth of wetting front below flow channels.
Figure 5.117 (bottom right): Sediment balance from debris flows.

5 Rainfall scenario: 40 mm in 40 minutes. Squeezing the 40 mm rainfall into a period of 40 minutes resulted in a shift from infiltration to runoff. Though no runoff developed on soil-covered slopes, the high rainfall intensity of 80 mm per hour led to vigorous runoff from the rocky upper slopes of the catchment, allowing a smaller portion of the water to infiltrate in the upper zones of the soil-covered slopes, compared to Scenario 4. The simulated maximum depth of the wetting front, with 81 cm, was not much less than for Scenario 3, but the maximum values were restricted to a small area directly at the base of a rock wall (Figures 5.118 and 5.119).

As a consequence of the relatively shallow wetting front, only 5,900 m³ of soil were identified as potentially unstable by the model, 5,800 m³ of which were considered as starting material for debris flow processes. Together with the entrained soil (700 m³), the deposit included 6,400 m³ of sediment. From this material, 1,200 m³ were predicted to end up on the international road (Figure 5.120).

Figure 5.118 (top): System variables (Scenario 5).
Figure 5.119 (bottom left): Depth of wetting front below flow channels at the end of the scenario.
Figure 5.120 (bottom right): Sediment balance from debris flows.

6 Rainfall scenario: 10 mm in 80 minutes. Scenario 6 did not lead to the development of runoff on soil-covered slopes, according to the model. Instead, the entire effective rainfall infiltrated. The wetting front at the end of the scenario was located between 4 and 78 cm below the soil surface, with the maxima only reached in a small area below a rock wall (similar to Scenario 5; Figures 5.121 and 5.122). The velocity of surface runoff reached maxima of about 1.2 m s^{-1}.

The modelled soil volume potentially subjected to slope failures was therefore relatively small, compared to the other scenarios: 2,900 m³, 2,800 m³ of which were identified as starting material for debris flows, entraining further 200 m³. The total deposit included 3,000 m³ (international road: 400 m³), according to the model. Figure 5.123 shows the corresponding sediment balance.

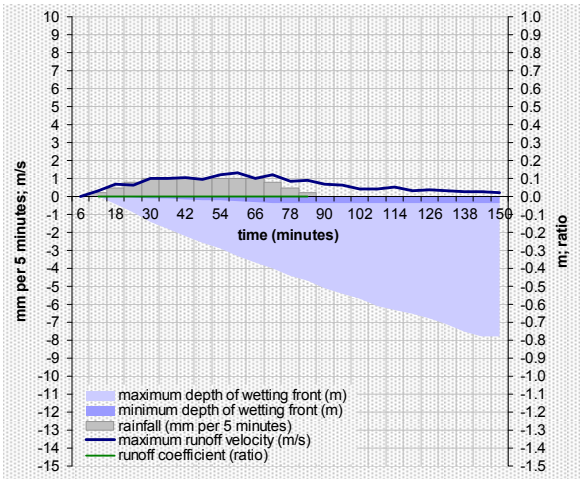

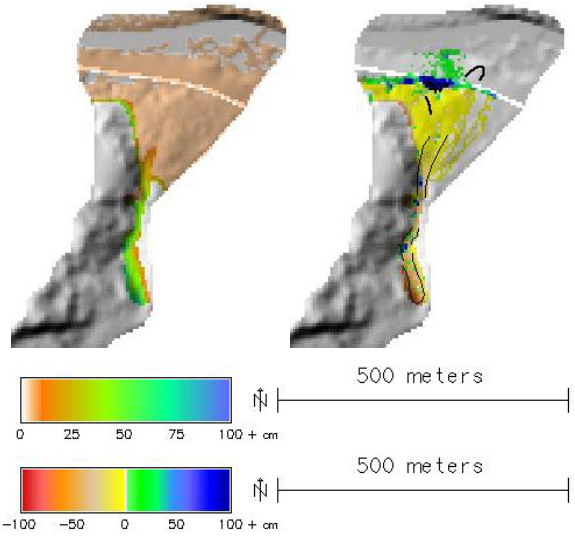

Figure 5.121 (top): System variables of Scenario 6.
Figure 5.122 (bottom left): Depth of wetting front below flow channels at the end of the scenario.
Figure 5.123 (bottom right): Sediment balance from debris flows.

5.4.3 Analysis of sensitivity

All studies of sensitivity were computed for a 100 mm rainfall event with a duration of 80 minutes (Scenario 1) in order to maintain comparability.

Spatial resolution: 10 m. When reducing the spatial resolution of the calculation, the maximum depth of the wetting front increased slightly from 79 cm to 80 cm, compared to the simulation at 5 m resolution. The maximum runoff velocity was subjected to some unphysical numerical oscillations (Figure 5.124).

The simulated volume of potentially failed soil increased slightly (9,700 m³; Figure 5.125 shows the factor of safety), the entrained volume (1,500 m³) remained unchanged. From the total deposit (10,800 m³, compared to 10,100 m³ for 5 m resolution, Figure 5.126), 1,500 m³ ended up on the international road (slightly less than with 10 m resolution). It can be concluded that even for such a pronounced terrain as present in the study area *Quebrada Escondida*, a spatial resolution of 10 m would be acceptable for simulations.

8 Percolation through rock. Assuming that 50 % of the water precipitating onto rock would percolate through cracks and fissures led to astonishingly small changes regarding the system variables and the simulated debris flows volumes. Maximum runoff velocity was reduced, but it appears that there was still sufficient water to infiltrate – regarding depth of the wetting front below flow channels, even a slight increase could be observed compared to the original Scenario 1. The mobilized and deposited volumes of soil and sediment all increased slightly, so that 1,900 m³ of debris were finally deposited on the international road, according to the model.

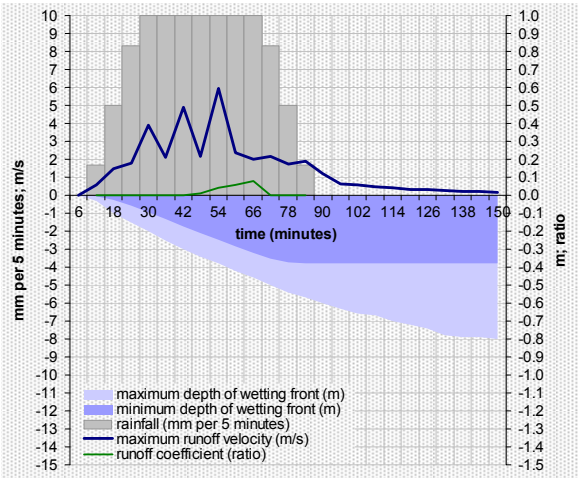

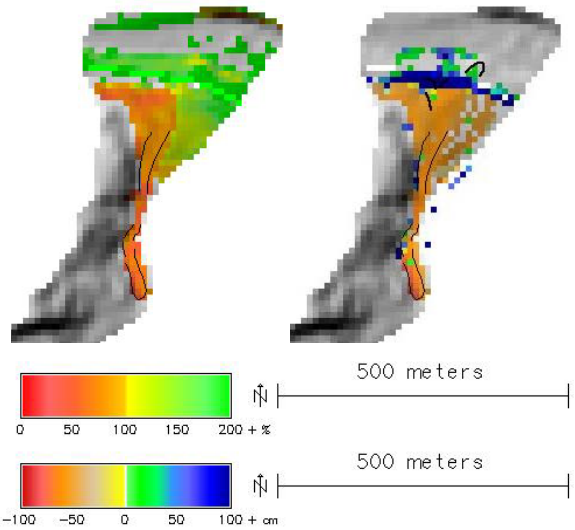

Figure 5.124 (top): System variables (resolution: 10 m).
Figure 5.125 (bottom left): Factor of safety with 10 m resolution.
Figure 5.126 (bottom right): Sediment balance from debris flows.

9 No vegetation. Assuming the entire area completely void of vegetation did not lead to substantial changes of the output of the hydraulic model components (small interception capacity). Changes in the

runoff regime had no significant direct influence on debris flow issues with the parameters used. However, the missing root cohesion led to an increased amount of potentially unstable zones, particularly on the cone in the lower part of the study area (Figure 5.127). 13,600 m³ of soil were simulated as potentially unstable, all of which developed into debris flows, entraining further 1,300 m³ of soil. Out of the deposit of 14,900 m³, 2,900 m³ were modelled to end up on the international road (Figure 5.128).

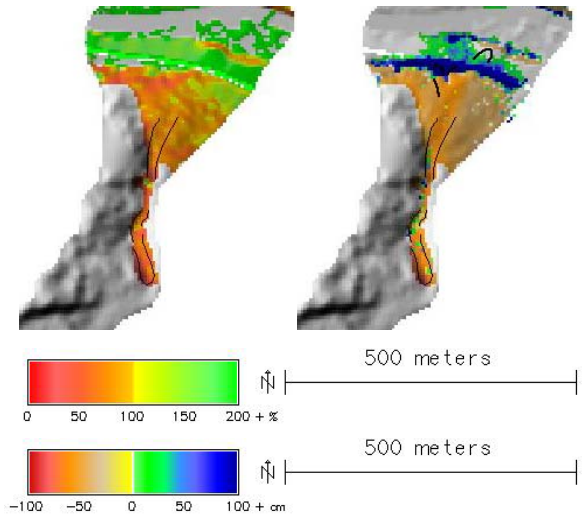

Figure 5.127 (left): Factor of safety, assuming a complete lack of vegetation.
Figure 5.128 (right): Sediment balance from debris flows.

10 Dry soil. A reduction from 9,100 m³ to 2,500 m³ of potential slope failures was observed when excluding the influence of soil water from the infinite slope stability model. 1,500 m³ of starting material of debris flows were detected, 5,300 m³ of soil were modelled to be entrained. 1,100 m³ out of the total deposit of 6,800 m³ ended up on the international road, according to the model (Figures 5.129 and 5.130).

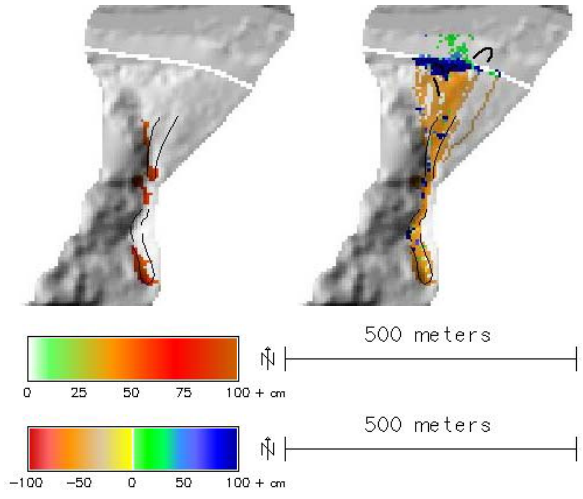

Figure 5.129 (left): Depth of starting material of debris flows, assuming dry soil.
Figure 5.130 (right): Sediment balance from debris flows.

5.4.4 Debris flow runout according to the Savage-Hutter model (r.avalanche)

One simulation with *r.avalanche* was carried out for the study area *Quebrada Escondida*. Major purpose of this was to test whether the pronounced horizontal curve in the upper part of the flow channel would be a problem for the use of *r.avalanche*.

11 Defined starting areas; h_i = 1 m; φ = 33°. The simulated flow velocity reached a maximum of about 30 m s^{-1} (Figure 5.131). Runout length was realistic, but rather overestimated, coinciding with the lowest observed deposit (Figure 5.132). Finally, about 130 m³ of sediment were simulated to be deposited on the international road (maximum: 190 m³).

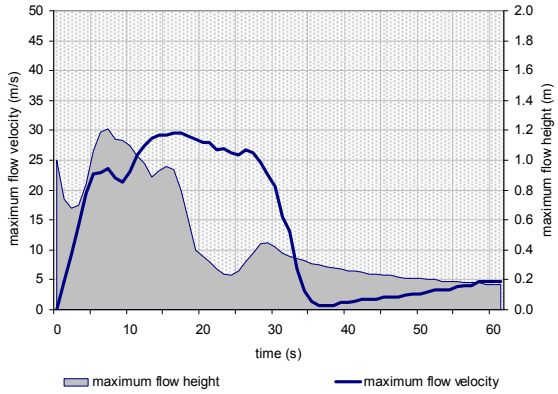

Figure 5.131: Maximum flow depth and flow velocity.

However, as expected, the validity of the simulation is limited as the used solution of the SH model is not really applicable to the conditions prevailing in this study area: in the upper part of the area, where the flow channel shows a pronounced horizontal curvature, the debris flow did not run around the corner properly, but demonstrated a rather unphysical behaviour with a clear tendency to move in the predefined x direction (compare Section 4.3) instead of down the channel. Part of the material even left the channel and took another way down, in contrast to field evidence (compare Figure 5.132).

5.4.5 Summary

The moved sediment volumes increased with rainfall sum and duration, driven by an increased depth of the wetting front. However, this relationship is not proportional – increasing the rainfall sum from 10 mm to 100 mm (factor 10) led to an increase in the volume of potential slope failure of a factor of 3.2 (Figure 5.133 and Table 5.8). Though surface runoff on soil only developed in connection to Scenario 1, water from the rocky slopes in the upper portion of the catchment provided plenty of water for infiltration. With higher rainfall sums, surface runoff reached the bottom of the main valley, with lower sums, the entire water infiltrated further upslope (compare Figures 5.108 and 5.122).

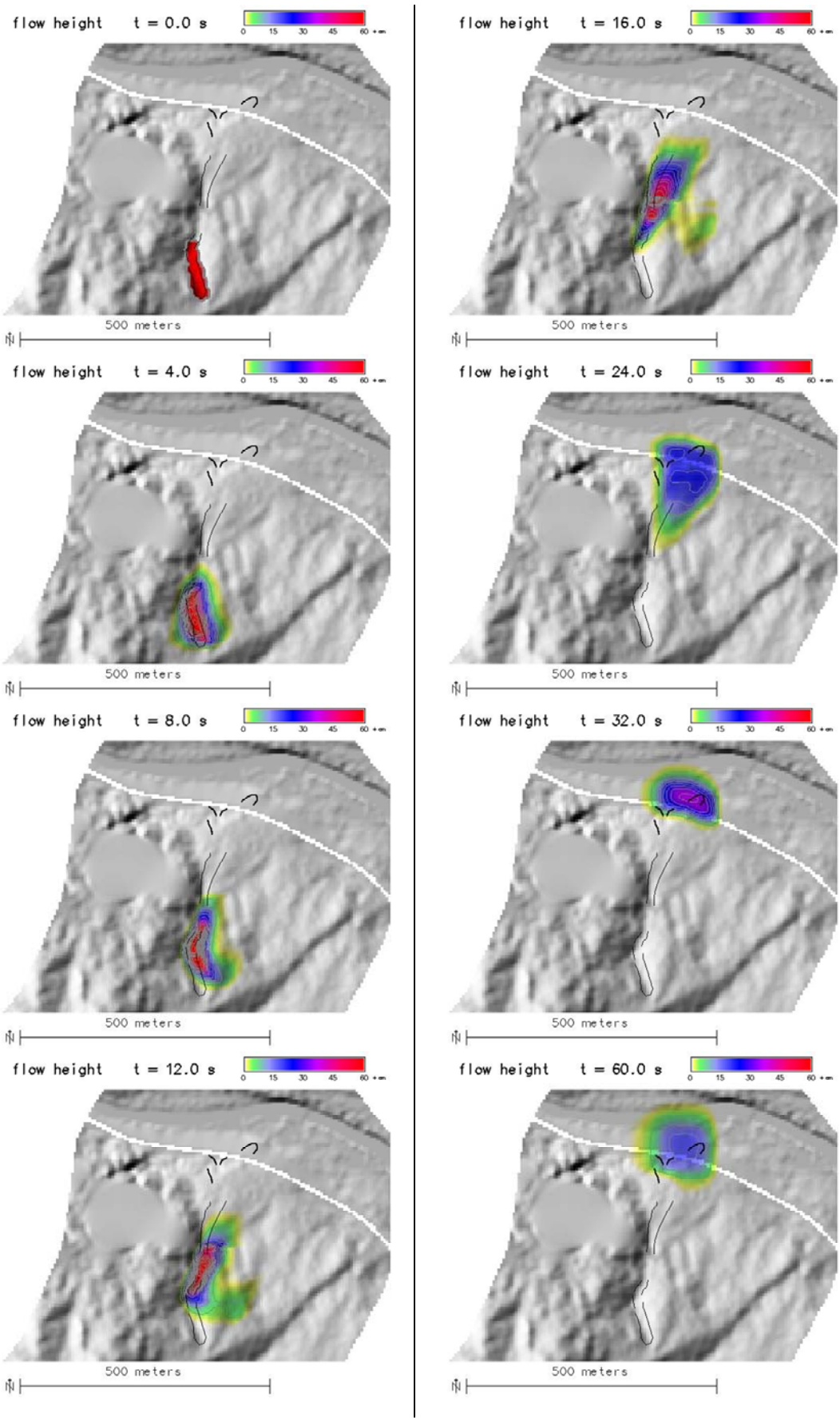

Figure 5.132: Depth of debris flow at different time steps, computed with *r.avalanche*.

The patterns shown in Figure 5.133 are very similar to those for the study area *Castillo de Rocas* (compare Figure 5.92) what is not surprising due to the quite similar soil properties governing infiltration and run-off coefficient.

The current implementation of ***r.avalanche*** seems not to be fit for an application with curved channels as present in the study area *Quebrada Escondida*.

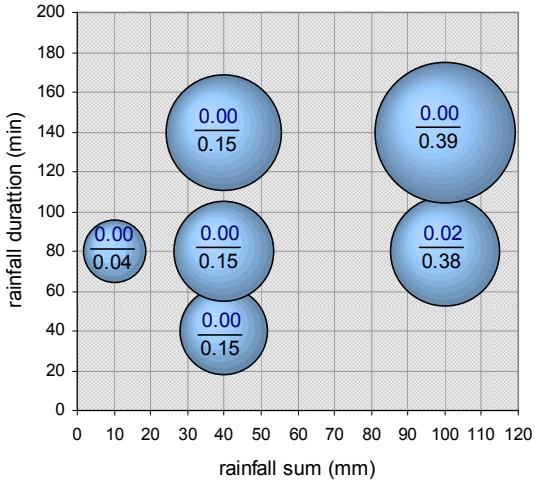

Figure 5.133: Volumes of potential slope failure as calculated for different rainfall scenarios (dimensionless). Blue numbers represent the runoff coefficients connected to the corresponding scenarios, black numbers the minimum depth of wetting front.

Table 5.8: Summary of some of the major system variables and moved soil volumes for all of the scenarios and analyses with the study area *Quebrada Escondida*; rcoef = runoff coefficient over the entire event; dwfront = depth of wetting front at the end of the simulation; (1) = away from flow channels; (2) = maximum.

scenario	pot. failure (m³)	start (m³)	entrainment (m³)	deposit (m³)	on road (m³)	rcoef	dwfront (1)	dwfront (2)
1: 100/80	9,103	8,572	1,499	10,072	1,948	0.02	0.38	0.79
2: 100/140	14,635	14,491	2,120	16,611	2,891	0.00	0.39	1.16
3: 40/80	7,592	7,497	783	8,280	1,509	0.00	0.15	0.83
4: 40/140	10,090	10,001	722	10,723	1,774	0.00	0.15	1.13
5: 40/40	5,876	5,751	678	6,430	1,159	0.00	0.15	0.81
6: 10/80	2,860	2,832	150	2,982	427	0.00	0.04	0.78
7: res. 10 m	9,692	9,366	1,468	10,835	1,500	0.02	0.38	0.80
8: perc. rock	9,221	9,056	1,468	10,523	1,889	0.02	0.38	0.83
9: no veg.	13,573	13,573	1,306	14,879	2,861	0.02	0.38	0.86
10: dry soil	2,477	1,512	5,274	6,785	1,063			

5.5 La Ampolleta

With an area of about 2.3 km², *La Ampolleta* is the largest of the Argentine study areas (Figure 5.134). It has short common divides with *Quebrada Escondida* and *Castillo de Rocas* and consists of the same granitic rocks and soils. The catchment ends up in a large cone with plenty of debris flow deposits most of which, however, appear inactive and do not reach the international road crossing the lower portion of the cone. However, some deposits indicate recent debris flow activity interfering with the road. Since the study area shows a somewhat smoother topography than those discussed before, the model was run with a spatial resolution of 10 m instead of 5 m (Table 5.9).

5.5.1 Tests of plausibility

1a Infiltration and runoff. Compared to the previously discussed study areas, a much more vigorous runoff developed in the *La Ampolleta* area, mainly due to the larger catchment. For Scenario 1, runoff velocity peaked at about 3.3 m s^{-1}, and runoff depth exceeded 20 cm in some sections of the major flow channel. Whilst the wetting front was located at the same depth as in the other areas at the end of a similar rainfall event away from the flow channels (38 cm), it reached 90 cm in some places below flow channels due to the larger infiltrable amount of water. The Figures 5.135 to 5.138 illustrate the temporal and spatial patterns of the hydrological system variables. Only the lower portion of the catchment is represented in the maps since the large upper part is flat and of no direct importance for debris flows.

Figure 5.134: The study area *La Ampolleta* (compare Section 3.7). The thin white lines represent potential starting areas of debris flows according to field evidence, the bold white lines delineate debris flow deposits. Elevation model derived from aerial and SPOT5 imagery, draped orthophoto from SPOT5. Design: Martin Mergili, 04/2008.

Table 5.9: Parameter settings and scenarios for the study area *La Ampolleta*. soil = soil parameters, lcov = land cover parameters, n/sed = Manning's n and parameters for sediment transport, pflow = preferential flow (per cent of total seepage), runout = parameters for runout model, res = spatial resolution, A = hydraulic model, B = sediment transport model, C = slope stability model, D = debris flow runout model; std = standard parameters (compare Section 4.1), cal = calibrated parameters, test = changed param. for analysis of sensitivity, h_i = defined starting depth.

		Parameter settings						Used modules			
		soil	lcov	n/sed	pflow	runout	res (m)	A	B	C	D
Test of plausibility (with precipitation = 100 mm in 80 minutes; all as rainfall)											
1a	Infiltration and runoff model	std	std	std	0		10	x			
1b	Slope stability model	std	std				10			x	
1c	Sediment transport model	std	std	std, cal	0		10	x	x		
1d	Debris flow runout model					std, cal	10				x
Scenarios											
1	Scenario 1: p.=100 mm in 80 min.	std	std	std	0	cal	10	x		x	x
2	Scenario 2: p.=100 mm in 140 min.	std	std	std	0	cal	10	x		x	x
3	Scenario 3: p.=40 mm in 80 min.	std	std	std	0	cal	10	x		x	x
4	Scenario 4: p.=40 mm in 140 min.	std	std	std	0	cal	10	x		x	x
5	Scenario 5: p.=40 mm in 40 min.	std	std	std	0	cal	10	x		x	x
6	Scenario 6: p.=10 mm in 80 min.	std	std	std	0	cal	10	x		x	x
Analysis of sensitivity (with p = 100 mm in 80 minutes; all as rainfall)											
7	Preferential flow	std	std	std	75	cal	10	x		x	x
8	Soil hydraulic conductivity	test	std	std	0	cal	10	x		x	x
9	No vegetation	std	test	std	0	cal	10	x		x	x
10	Pre-wetting of the soil	test	std	std	0	cal	10	x		x	x
10	Dry soil	std	std	std	0	cal	10			x	x
Runout model based on the SH model (r.avalanche)											
11	Defined starting areas (h_i = 1 m)	φ = 43.0°	δ = 33°				5				
12	Defined starting areas (h_i = 1 m)	φ = 43.0°	δ = 27°				5				
13	Defined starting areas (h_i = 5 m)	φ = 43.0°	δ = 27°				5				
14	Starting areas from Scenario 1	φ = 43.0°	δ = 27°				5				
15	Starting areas from Scenario 1	φ = 32.0°	δ = 27°				5				

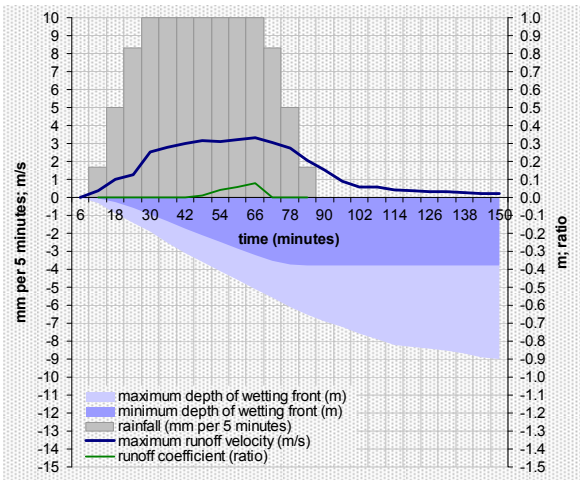

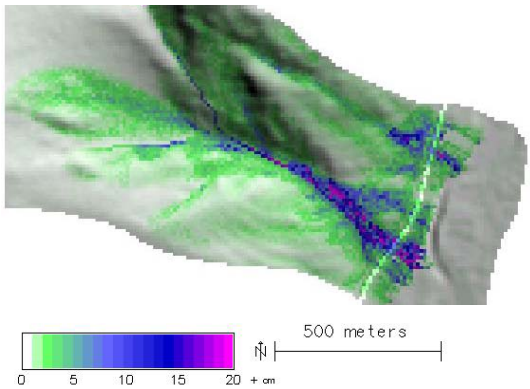

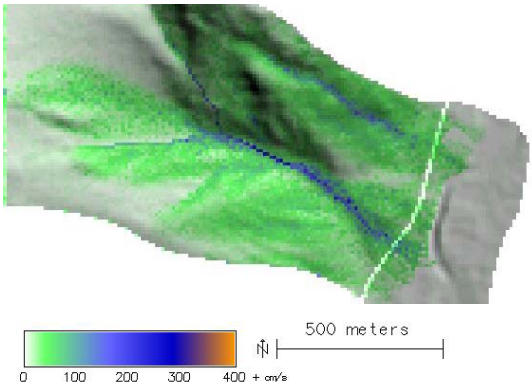

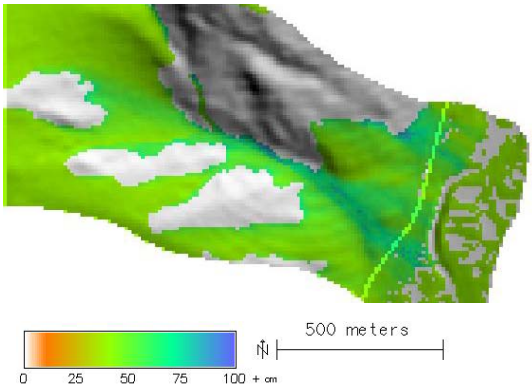

Figure 5.135 (top): System variables.
Figure 5.136 (top middle): Runoff depth (t = 60 min)
Figure 5.147 (bottom middle): Runoff velocity (t = 60 min).
Figure 5.138 (bottom): Depth of the wetting front below flow channels at the end of the scenario.

1b Slope stability model. The factor of safety is represented in Figure 5.139. Compared to field evidence, the areas susceptible to slope failure appear to be overestimated. In fact, many slopes not identified as unstable in the field are steep and with evidence of active slope dynamics, but without a clear indication of starting areas of debris flows. There is frequently a sparse vegetation cover which may hold back masses of initially moving soil.

On the other hand, all areas identified as unstable in the field are connected to low values of the factor of safety in the model output. Figure 5.140 shows the simulated starting areas of debris flows.

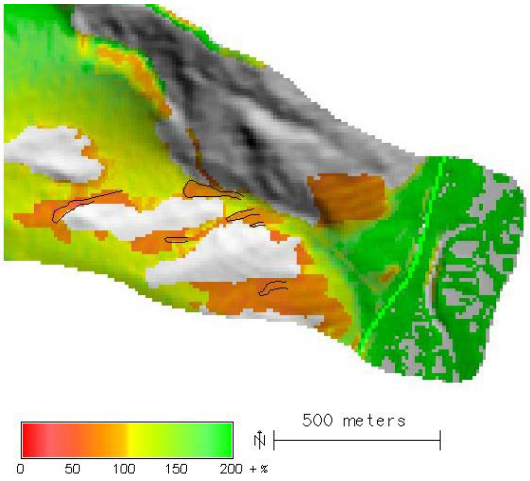

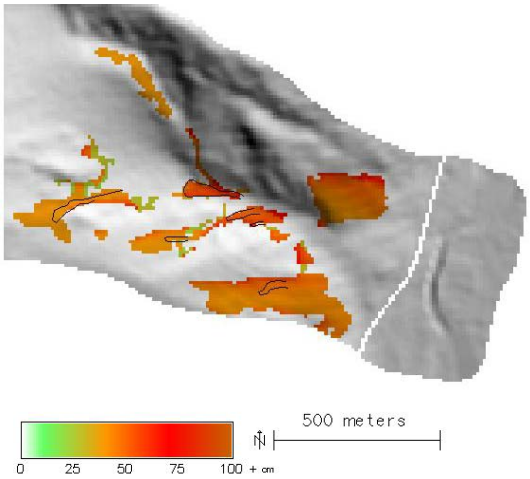

Figure 5.139 (top):Factor of safety.
Figure 5.140 (bottom): Depth of mobilization of debris flows.

1c Sediment transport model. Similar to the previously discussed study areas, the sediment transport model did not yield plausible results without calibrating the parameters. Stream power (Figure 5.141) as an indicator for the tendency of surface runoff to develop into a debris flow reached high values in areas also identified as starting areas for debris flows from slope instabilities, and in areas subjected to entrainment (compare Figure 5.144). The sediment transport model was excluded from the simulations for the *La Ampolleta* area.

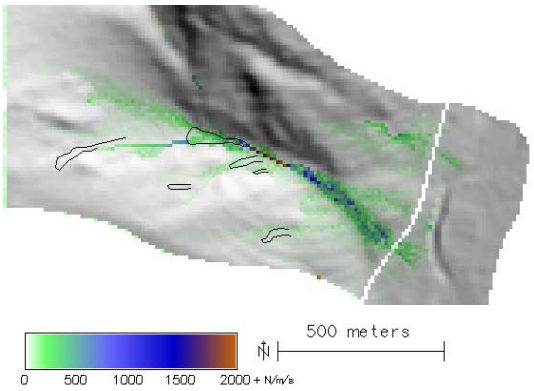

Figure 5.141: Stream power (t = 60 min).

1d Debris flow runout model. Figure 5.142 was generated using the standard parameters for debris flow runout, with μ computed according to GAMMA (2000) for channelized debris flows, and with entrainment/deposition thresholds of 15° local slope and a velocity of 10 m s^{-1}. M/D was set to 75, and the depth of the deposit was limited to 5 m. Using these parameters, the correspondence to the maximum runout length observed in the field was not bad, but part of the debris flow material was deposited too far upwards, compared to field evidence.

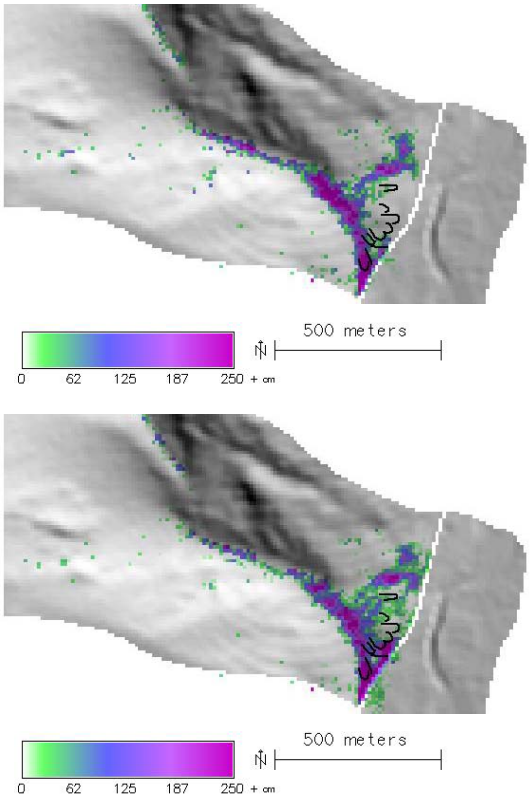

Figure 5.142 (top): Depth of deposition from debris flow with standard parameters.
Figure 5.143 (bottom): Depth of deposition from debris flow with calibrated parameters.

Setting μ to a constant value of 0.25 while leaving all the other parameters unchanged led to a better correspondence since the flow could accelerate more intensely in the upper part of the area. However, the actual deposits mapped in the field were not met satisfactorily by the model results – one major reason for this deficiency seems to be that the actual deposits in the field appear as small hills in the elevation model, so that debris flows take another way – as they would do in nature. The simulated runout length corresponds well to the observations and also the remaining deposits on the upper part of the fan appear realistic (Figure 5.143).

Figure 5.144 represents the depth of entrainment of soil by debris flows, based on the runout model with calibrated parameters. Figure 5.145 illustrates the sediment balance from debris flows, and Figure 5.146 shows the debris flow index.

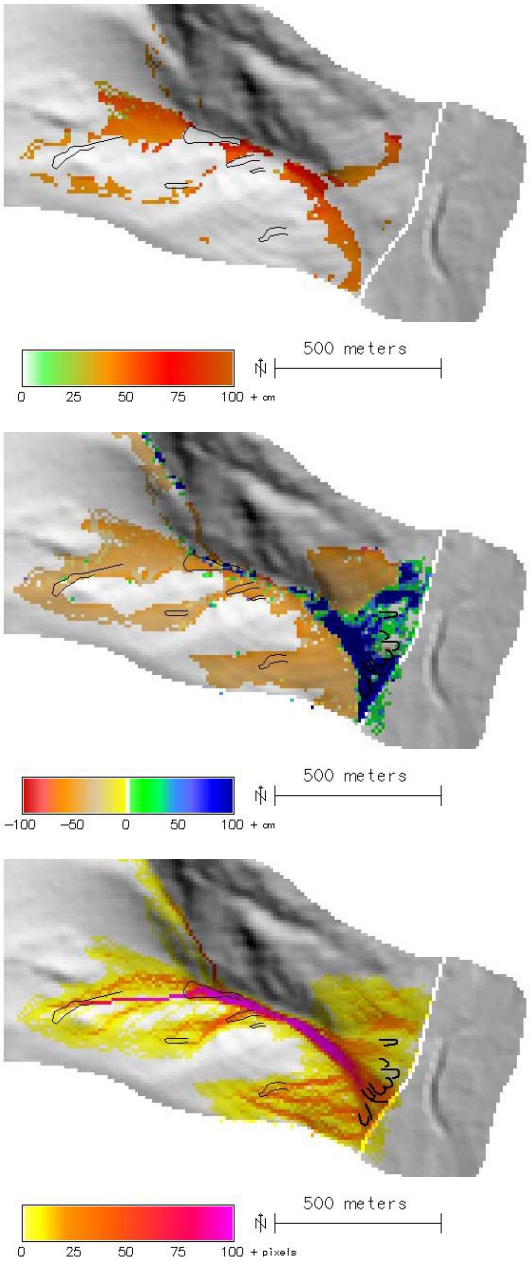

Figure 5.144 (top): Entrainment of soil by debris flows.
Figure 5.145 (middle): Sediment balance from debris flows.
Figure 5.146 (bottom): Debris flow index.

All in all, 65,800 m³ of soil were identified as potentially unstable by the model, 63,900 of which were considered as material developing into debris flows, entraining further 22,600 m³ of soil. Out of the total deposit of 86,500 m³, 4,700 m³ of sediment ended up on the international road, according to the model.

Figure 5.147 shows the maximum velocity of debris flow runout with the parameters calibrated as explained. 20 m s^{-1} were exceeded in the steepest portions. A steady deceleration from around 15 m s^{-1} to zero was modelled on the cone.

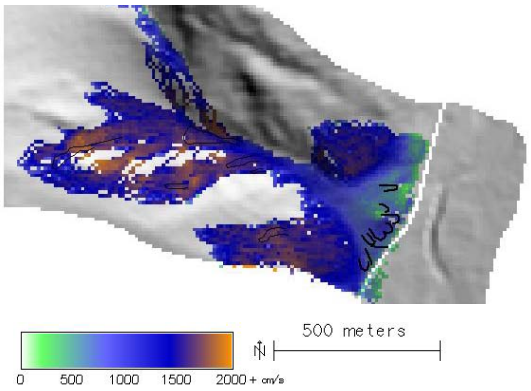

Figure 5.147: Maximum velocity of debris flows.

5.5.2 Rainfall scenarios

2 Rainfall scenario: 100 mm in 140 minutes. Identically to the other study areas, extending the rainfall period while maintaining the sum led to a shift from runoff towards infiltration (Figure 5.148). The runoff coefficient for soil-covered slopes over the entire scenario decreased to zero, whilst the wetting front at the end of the scenario was located at depths between 39 cm and 1.20 m (Figure 5.149). The highest values occurred in the major flow channel and directly below rocky slopes.

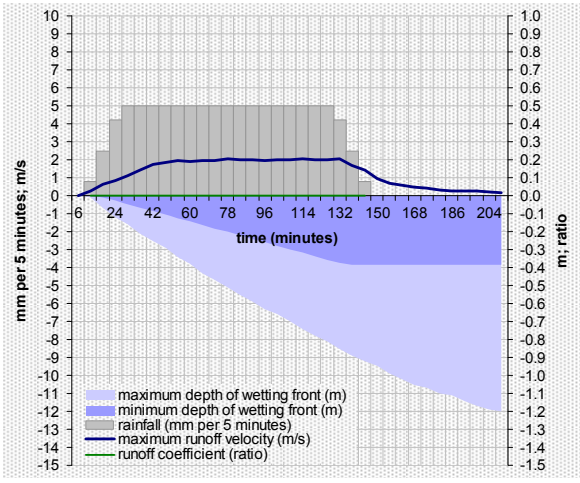

Figure 5.148: System variables (Scenario 2).

As a consequence of the deeper wetting front, an increased volume of potentially unstable material (93,000 m³) was simulated, compared to Scenario 1. 90,100 m³ of soil developing into debris flows and 25,000 m³ of entrained soil were modelled. From a total of 115,000 m³, 5,700 m³ were predicted to be deposited on the international road. Figure 5.150 shows the sediment balance from debris flows for this scenario.

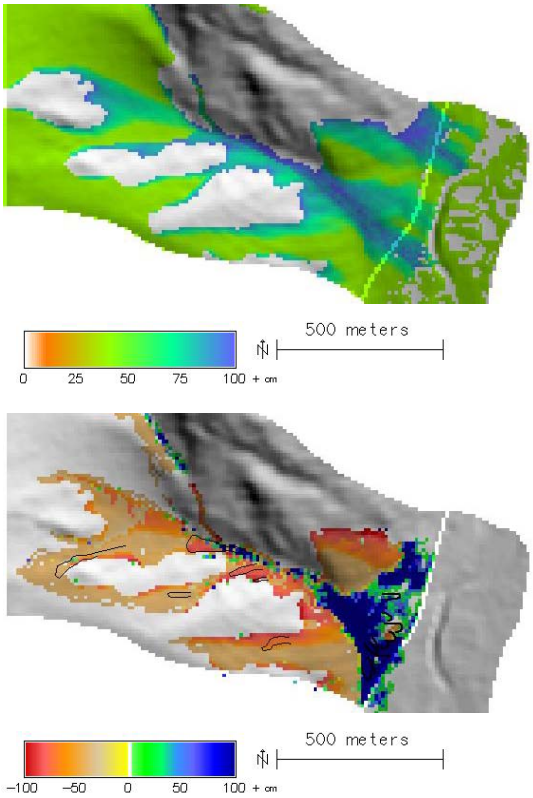

Figure 5.149 (top): Depth of wetting front below flow channels at the end of Scenario 2.
Figure 5.150 (bottom): Sediment balance from debris flows.

3 Rainfall scenario: 40 mm in 80 minutes. At the end of the scenario, the wetting front was located at a soil depth between 15 cm and 81 cm, according to the model (Figures 5.151 and 5.152). The entire rainfall was simulated to infiltrate into the soil, so that runoff on soil-covered slopes was only fed by inflow from upslope bedrock outcrops.

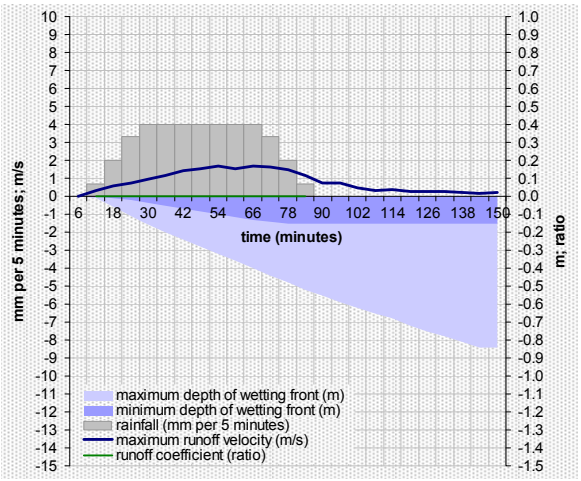

Figure 5.151: Temporal patterns of system variables.

The shallower wetting front led to less soil material susceptible to slope failure: 35,800 m³ of unstable soil were detected by the model. Out of this volume, 34,900 m³ were identified to develop into debris flows, entraining further 13,300 m³ of soil. Out of the deposit of 48,200 m³, 2,400 m³ ended up on the international road, according to the simulation (Figure 5.153).

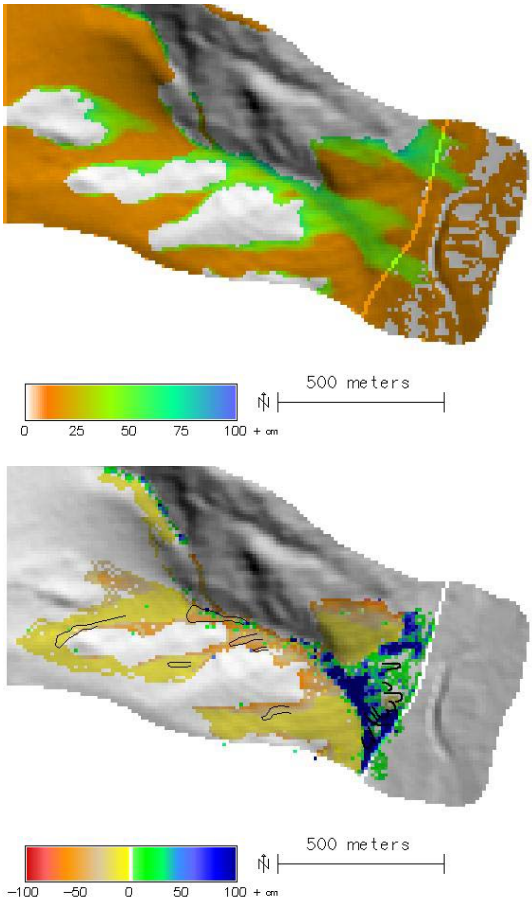

Figure 5.152 (top): Depth of wetting front below flow channels at the end of the scenario.
Figure 5.153 (bottom): Sediment balance from debris flows.

4 Rainfall event: 40 mm in 140 minutes. When decreasing rainfall intensity whilst maintaining sum, the effects were basically the same as for the 100 mm scenarios. The processes shifted towards infiltration (the runoff coefficient remained zero, whilst the depth of the wetting front at the end of the event increased to a range of 15 cm to 1.12 m (Figures 5.154 and 5.155).

The volume of potential slope failure was quantified with 43,200 m², 41,500 m³ of which were identified as starting material of debris flows. Including 12,300 m³ of entrained soil, 53,700 m³ of sediment were deposited, according to the model. 2,600 m³ ended up on the international road. The sediment balance from debris flows is shown in Figure 5.156.

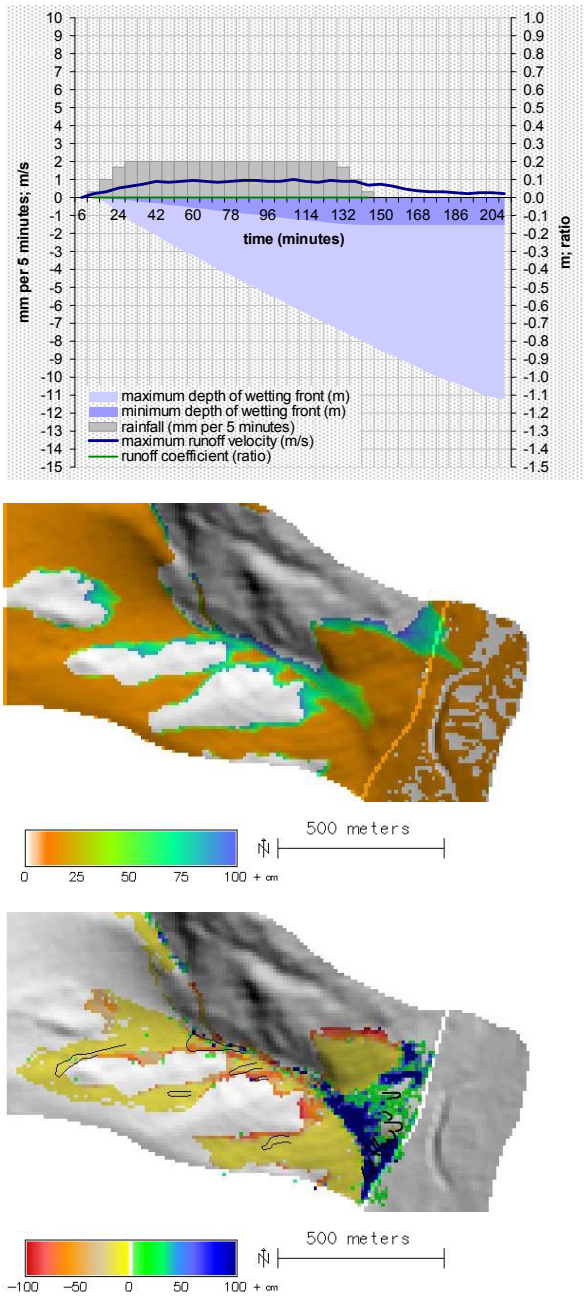

Figure 5.154 (top): System variables (Scenario 4).
Figure 5.155 (middle): Depth of wetting front below flow channels at the end of the scenario.
Figure 5.156 (bottom): Sediment balance from debris flows.

5 Rainfall scenario: 40 mm in 40 minutes. Similar to the study areas discussed above, increasing the rainfall intensity whilst maintaining the sum caused a shift from infiltration towards runoff. Though no runoff developed on soil (runoff coefficient of zero), a smaller portion of the water moving down from bedrock outcrops could infiltrate immediately. Whilst the depth of the wetting front peaked at 0.81 m, the maximum velocity of surface runoff reached about 2.5 m s^{-1}, compared to 1 m s^{-1} for Scenario 4 (Figure 5.157). The maximum depth of the wetting front was reached along a small belt at the bottom of bedrock slopes (Figure 5.158).

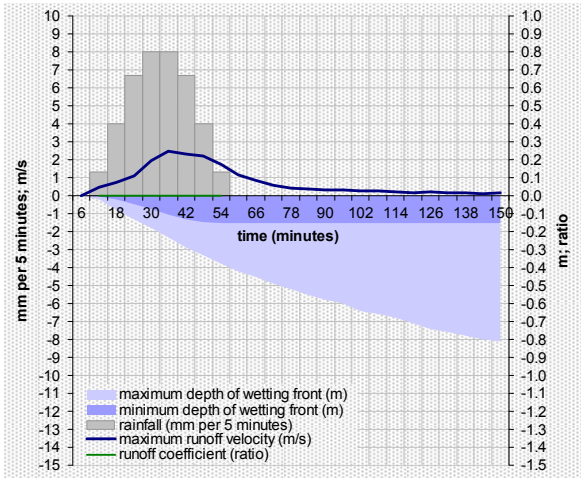

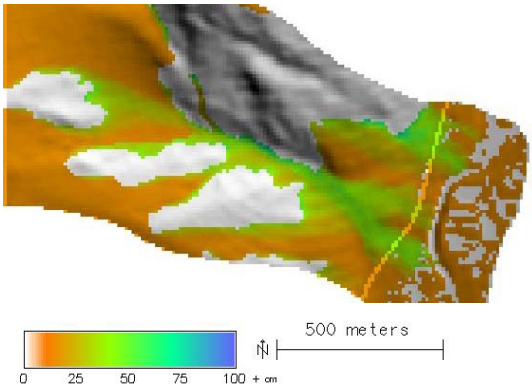

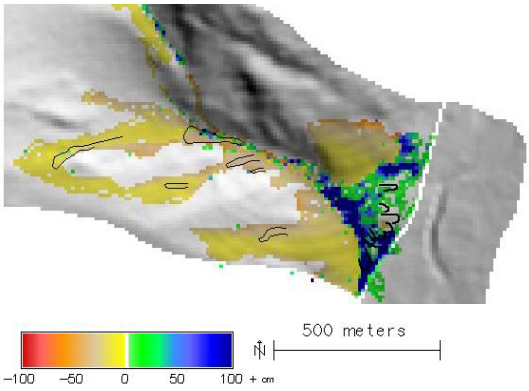

Figure 5.157 (top): System variables (Scenario 5).
Figure 5.158 (middle): Depth of wetting front below flow channels at the end of the scenario.
Figure 5.159 (bottom): Sediment balance from debris flows.

The shallower wetting front led to smaller volumes involved into debris flow processes: 31,000 m³ and 30,200 m³, respectively, were identified as potentially unstable and as starting material for debris flows. 11,800 m³ were entrained, leading to a deposit of 42,100 m³. 2,100 m³ of sediment ended up on the international road, according to the model (Figure 5.159).

Rainfall scenario: 10 mm in 80 minutes. 10 mm of rainfall did not lead to the development of runoff on soil, according to the model. Whilst the simulated wetting front away from the flow channels was very shallow (about 4 cm), it reached a maximum of 75 cm at the base of rocky slopes, not so much less than for the scenarios with much more rainfall. However, this zone was restricted to a very narrow belt, where all the water from upwards infiltrated. Farther downwards, no runoff was simulated at all. The maximum runoff velocity remained below 1 m s^{-1} (Figures 5.160 and 5.161).

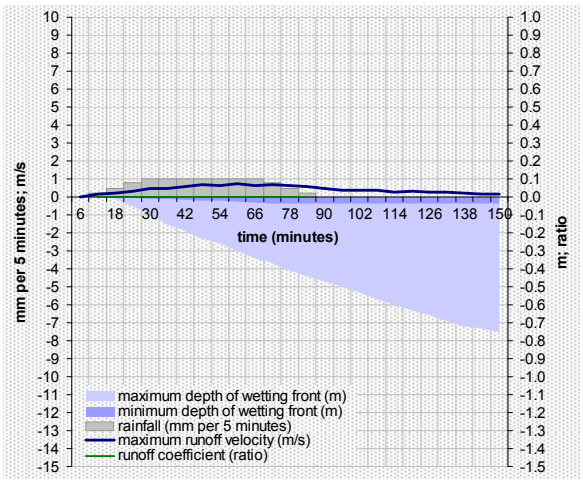

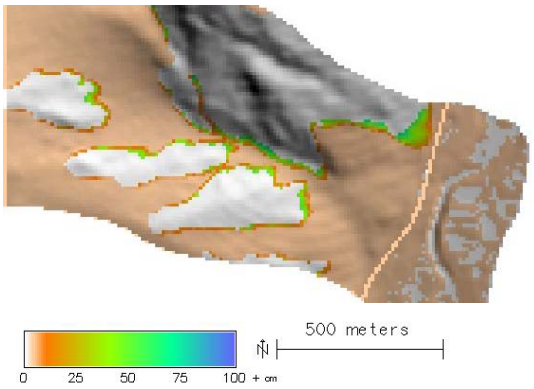

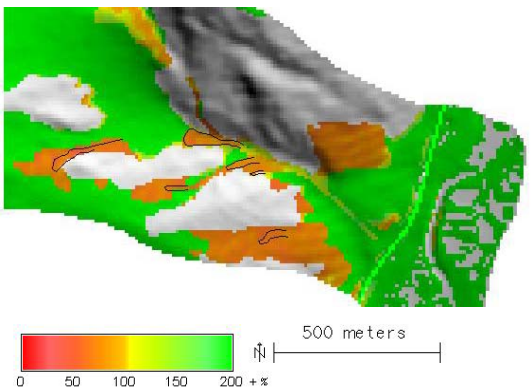

Figure 5.160 (top): System variables.
Figure 5.161 (middle): Depth of wetting front (below flow channels) at the end of the scenario.
Figure 5.162 (bottom): Factor of safety.

The factor of safety for vegetated soils (Figure 5.162) was different from that modelled for Scenario 1 (compare Figure 5.139): For deeper potential failure planes, the stabilizing role of cohesion (in this case root cohesion) decreases. However, this phenomenon was not pronounced enough in this case to exert a substantial influence on slope stability.

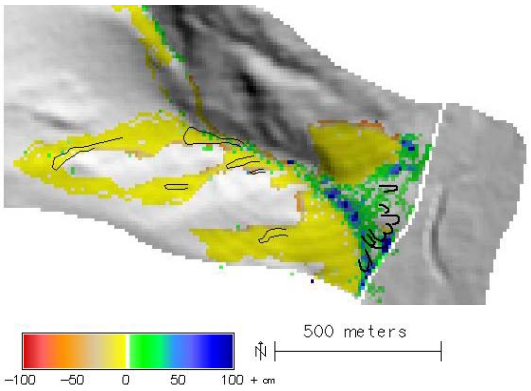

Figure 5.163: Sediment balance from debris flows.

10,300 m³ of potentially unstable soil were detected, 9,900 m³ of which were identified as starting material of debris flows, entraining further 2,900 m³ of soil. 600 m³ out of the total deposit of 12,900 m³ were simulated to end up on the international road (Figure 5.163).

5.5.3 Analysis of sensitivity

All studies of sensitivity for the study area *La Ampolleta* were carried out for a 100 mm rainfall event with a duration of 80 minutes (Scenario 1).

7 Preferential flow. Seepage through macropores is difficult to determine. The assumption that the entire seepage would occur through micropores yielded plausible results for the study areas under investigation. However, the effects on preferential flow through macropores have to be explored. Partly following SUKHIJA et al. (2003), it was assumed that 75 % of total seepage would occur through macropores. The Figures 5.164 and 5.165 illustrate the influence on the hydrological state of the system. The modelled wetting front away from flow channels was identical to that after Scenario 2, as there was just not more water present to infiltrate. But where runoff entered soil-covered slopes from upward bedrock outcrops, the wetting front proceeded as deep as 2.76 m, according to the simulation. Due to the extensive infiltration, runoff velocity was much lower than for the original Scenario 1, culminating at 2.2 m s^{-1}.

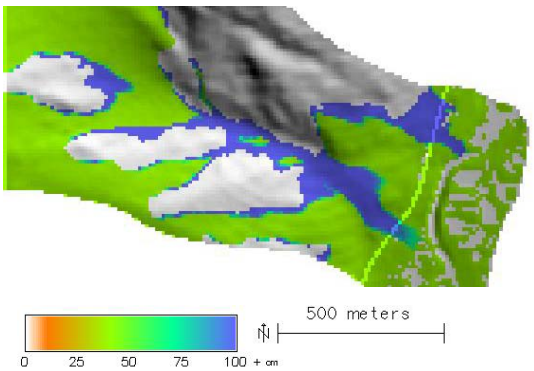

Figure 5.164: Depth of wetting front beneath flow channels (with preferential flow).

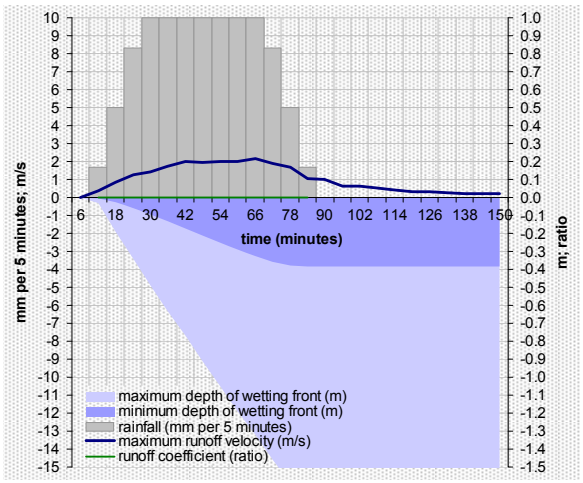

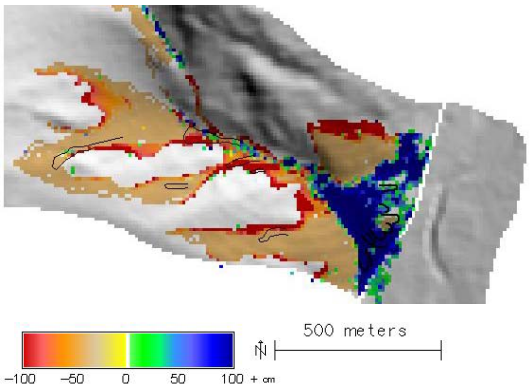

Figure 5.165 (top): System variables (with preferential flow).
Figure 5.166 (bottom): Sediment balance from debris flows.

116,000 m³ of soil were identified as potentially unstable by the model, 112,700 of which were considered as starting material of debris flows, entraining further 25,200 m³. Out of the final deposit of 137,900 m³, 6,500 m³ ended up on the international road, according to the model (Figure 5.166).

8 Hydraulic conductivity. The values of soil hydraulic conductivity for the Green-Ampt model provided by RAWLS et al. (1983) are rather low when compared with the values of saturated hydraulic conductivity provided by CARSEL & PARRISH (1988; compare Table 4.3). The effect of applying the latter ones is quite similar to that shown above for the introduction of preferential flow. The wetting front reaches a maximum depth of 1.90 m, with a similar spatial distribution as shown in Figure 5.164.

104,500 m³ of soil were simulated as potentially unstable, 101,600 m³ as starting material of debris flows. Including the entrained soil volume of 24,000 m³, 125,600 m³ of debris were deposited, according to the model. 6,200 m³ ended up on the international road.

9 Vegetation-free catchment. Assuming a catchment completely void of vegetation did not result in major changes of the hydrological system status, compared to the original Scenario 1. The maximum runoff velocity remained around 3.3 m s^{-1} whilst the

maximum depth of the wetting front decreased slightly, probably as a consequence of the less concentrated flow assumed for unvegetated slopes.

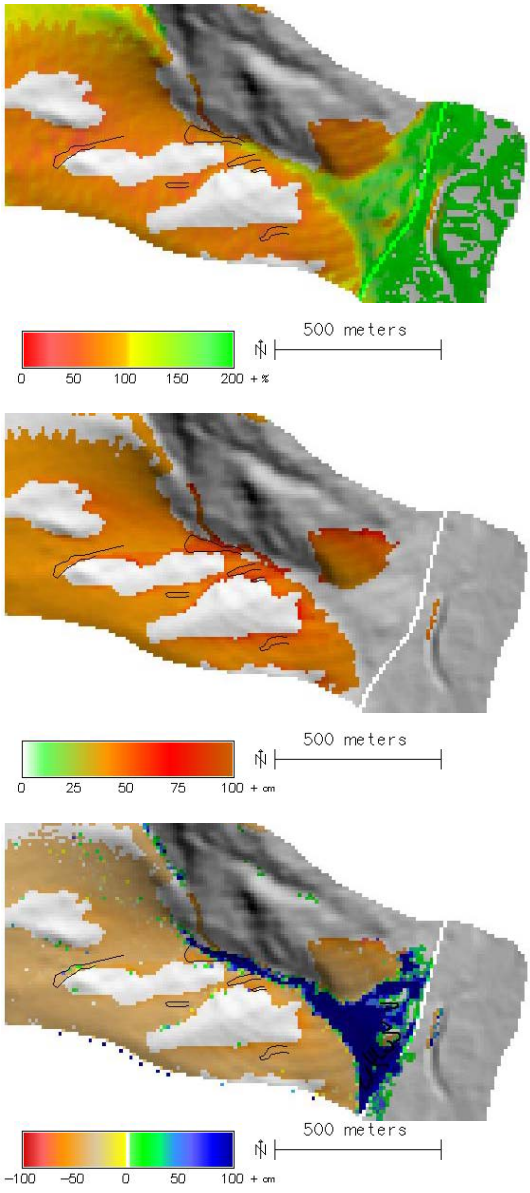

Figure 5.167 (top): Factor of safety.
Figure 5.168 (middle): Starting material of debris flows.
Figure 5.169 (bottom): Sediment balance from debris flows.

Due to the missing root cohesion, several otherwise stable areas were detected as potentially unstable (Figure 5.167). The simulation predicted 156,200 m³ of unstable soil, 154,500 m³ of which were identified as starting material for debris flows (Figure 5.168). 9,300 m³ were entrained, resulting in a total deposit of 163,800 m³. 7,000 m³ of sediment were predicted to end up on the international road (Figure 5.169).

10 Dry soil. Excluding soil water effects from the slope stability model led to the detection of some few potentially unstable patches (900 m³), including 500 m³ of starting material of debris flows. Together with 5,400 m³ of entrained soil, 5,900 m³ of sediment were deposited, nothing on the international road (Figures 5.170 and 5.171). These findings indicate a good choice of parameters since the catchment largely appears to be in equilibrium.

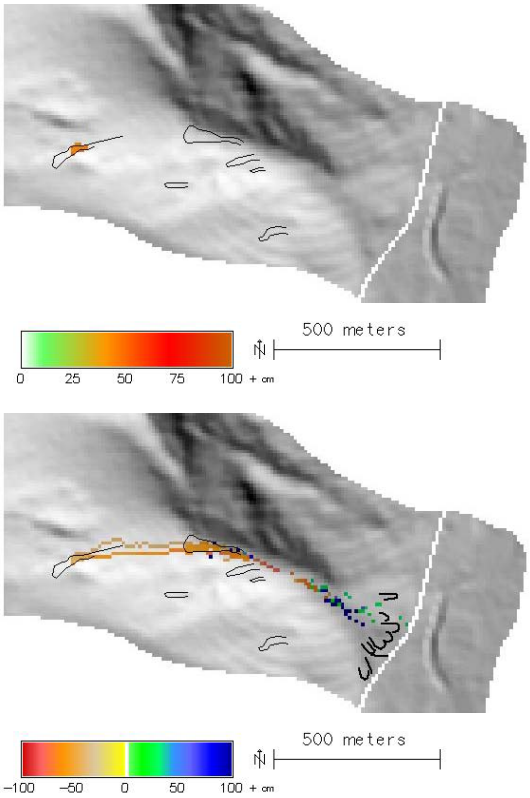

Figure 5.170 (top): Starting material of debris flows assuming dry soil.
Figure 5.171 (bottom): Sediment balance from debris flows.

5.5.4 Runout model based on the SH model (r.avalanche)

For the study area *La Ampolleta*, five simulations were run with *r.avalanche*.

11 Defined starting areas, $\delta = 33°$, $h_i = 1$ m. Flow velocity peaked at about 29 m s^{-1} (Figure 5.172). The debris flows stopped in the major flow channel above the cone. No sediment was deposited on the road, according to the model (compare Figure 5.178). These findings indicate that, in contrast to the other study areas around Guido, a bed friction angle of 33° is too high for the conditions in the *La Ampolleta* area.

12 Defined starting areas, $\delta = 27°$, $h_i = 1$ m. The runout, now reaching maximum flow velocities of 45 m s^{-1} (Figure 5.173), stopped in the central part of the cone, where certain debris flow deposits can be observed in the field. The lowermost part of the simulated deposit reached the international road, where 280 m³ of material ended up, according to the simulation (Figure 5.174). In principle, all this corresponds very well to field observations: most of the deposits only interfere with the road in their foremost parts (compare Figure 5.179).

However, spreading of the flow in the upper parts, but particularly on the cone, was far too pronounced, compared to field evidence, where deposits have a much more elongated shape. This may be caused (1) by a too coarse grid resolution, and (2) by an insufficient representation of the channels and ridges on the cone in the elevation model.

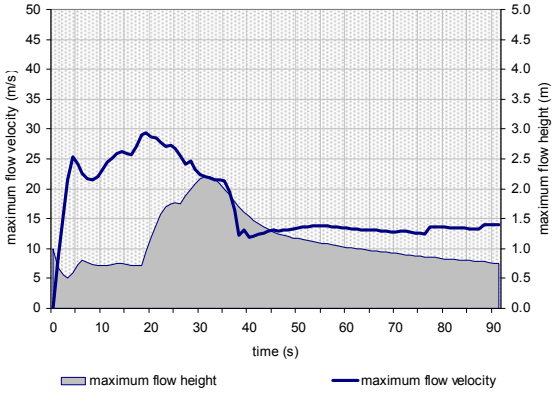

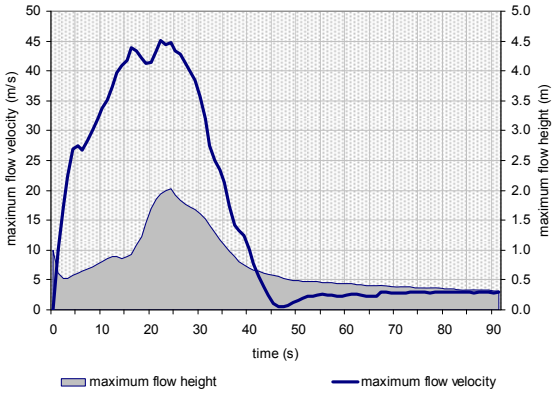

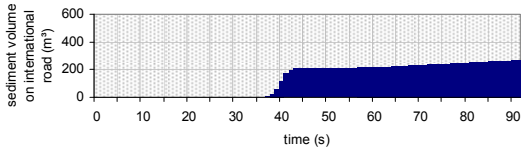

Figure 5.172 (top): Flow depth and velocity (defined starting areas; δ = 33°; h_i = 1 m).
Figure 5.173 (middle): Flow depth and velocity (defined starting areas; δ = 27°; h_i = 1 m).
Figure 5.174 (bottom): Debris flow volume on the international road.

13 Defined starting areas, δ = 27°, h_i = 5 m. A drastical increase in the depth of the starting material, but unchanged spatial patterns did not result in a notable increase of the maximum simulated flow velocity, which reached about 48 m s^{-1} (Figure 5.175). Also the increase in maximum flow depth was underproportional, meaning that spreading of the flow was more pronounced than with a starting depth of 1 m. The spatio-temporal patterns shown in Figure 5.180 are quite similar to those illustrated in Figure 5.179. Deposition on the road (1,800 m³) was slightly more than 5-fold, compared to 1 m starting depth.

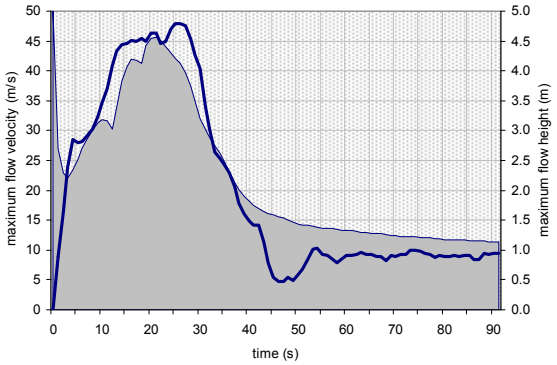

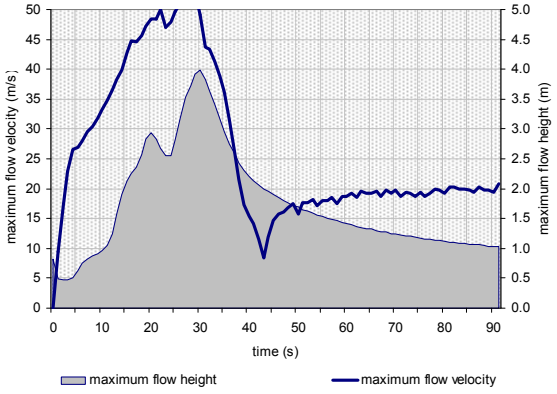

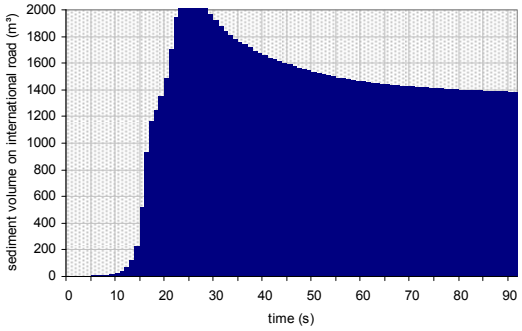

Figure 5.175 (top): Flow depth and velocity (defined starting areas; δ = 27°; h_i = 5 m).
Figure 5.176 (middle): Flow depth and velocity (starting areas from Scenario 1; δ = 27°).
Figure 5.177 (bottom): Debris flow volume on the international road (rainfall scenario: 100 mm in 80 min.; δ = 27°).

14 Starting areas from Scenario 1, δ = 27°. Using the modelled starting areas and depths led to a longer runout, mainly caused by debris flow material from the outer part of the catchment which did not first have to pass the narrower channel before reaching the road. Maximum flow velocity was 53 m s^{-1} (Figure 5.176), and 1,370 m³ of debris were deposited on the international road, according to the simulation (Figure 5.177). The extensive spreading discussed above was also observed with this analysis (compare Figure 5.181).

15 Starting areas from Scen. 1, δ = 27°, φ = 32°. Reducing the angle of internal friction did not result in any significant changes, compared to the same simulation with the standard value of φ (43.0°).

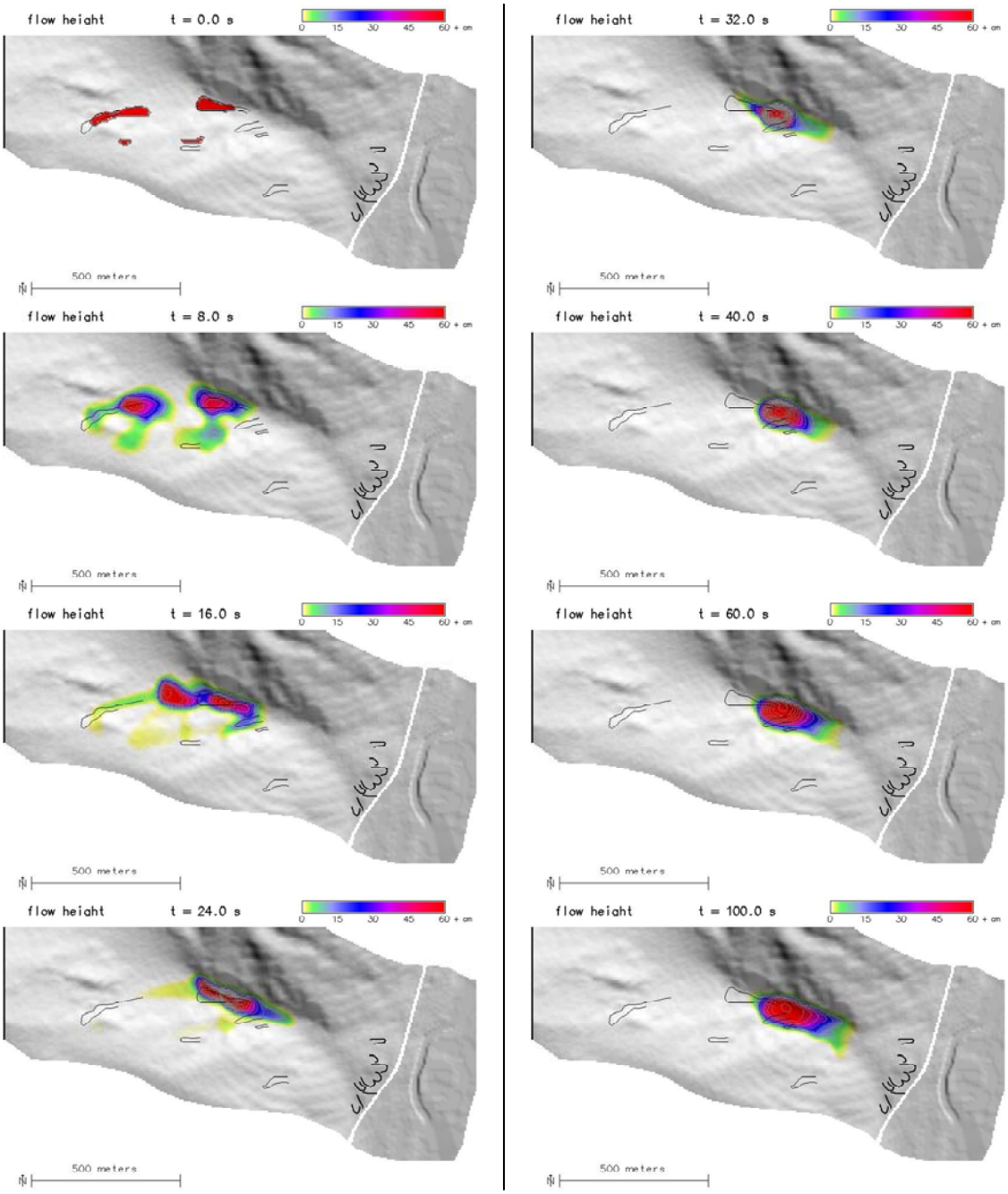

Figure 5.178: Simulation with *r.avalanche* with defined starting areas, δ = 33°, and h_i = 1 m.

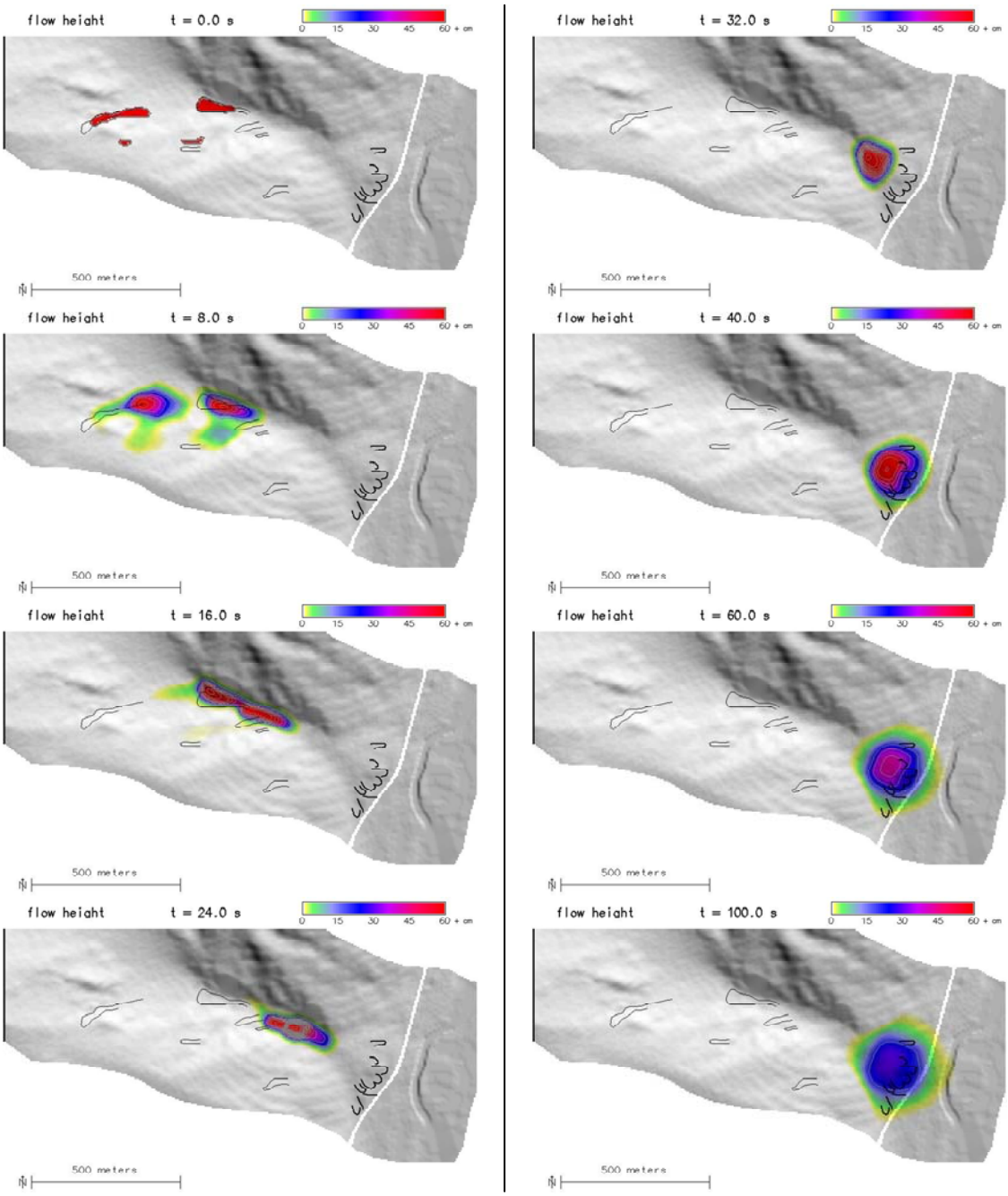

Figure 5.179: Simulation with *r.avalanche* with defined starting areas, δ = 27°, and h_i = 1 m.

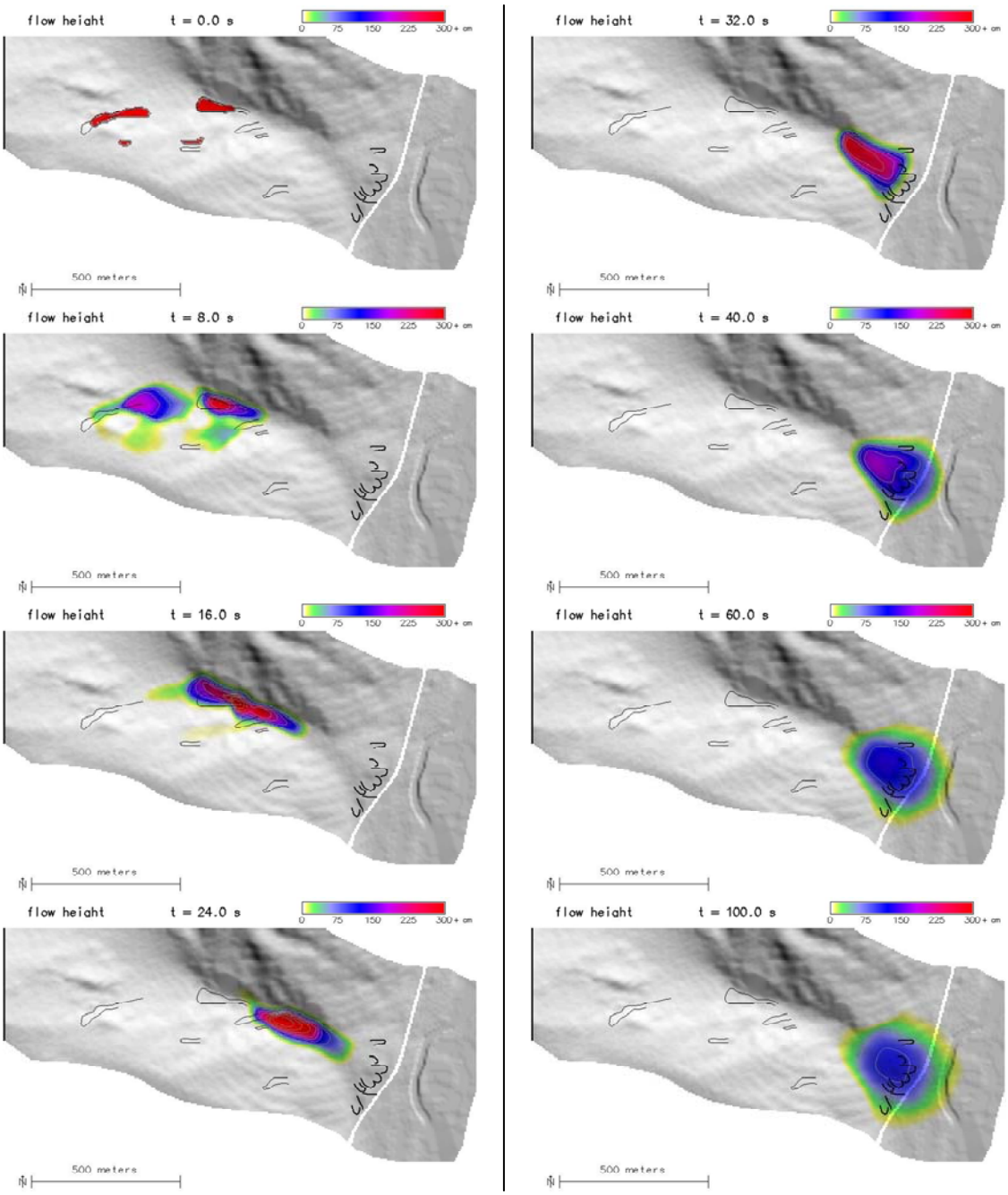

Figure 5.180: Simulation with *r.avalanche* with defined starting areas, δ = 27°, and h_i = 5 m.

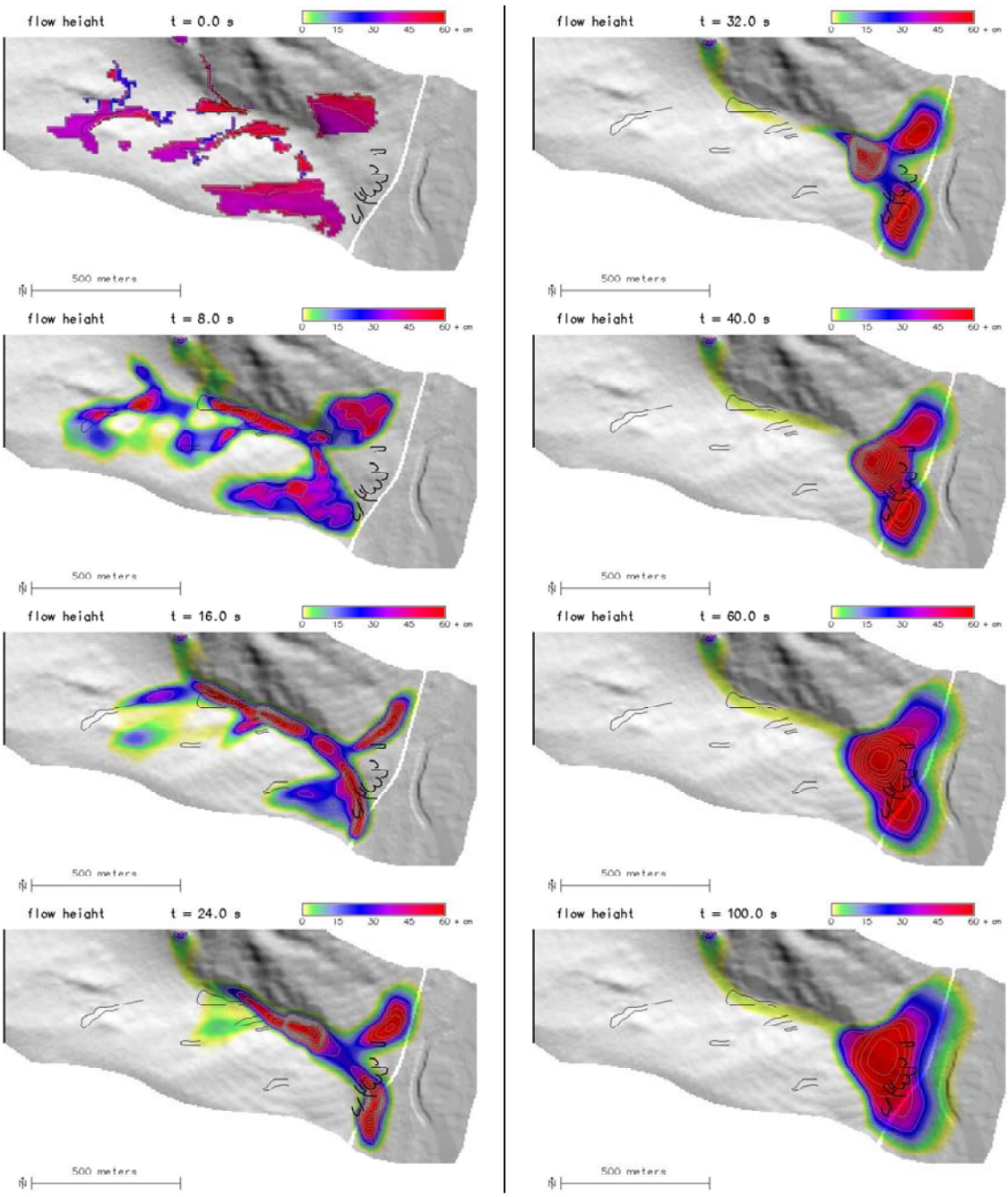

Figure 5.181: Simulation with *r.avalanche* with starting areas from Scenario 1 and δ = 27°.

5.5.5 Summary

The volumes of slope failures illustrated in Figure 5.182 follow the same patterns as to those investigated for the study areas *Castillo de Rocas* and *Quebrada Escondida*. Between 600 m³ and 5,700 m³ of sediment were deposited on the international road, depending on the scenario (Table 5.10). A comparison to the other study areas and to reference data will follow in Section 6.1.

Similar to its application to *Castillo de Rocas*, ***r.avalanche*** proved useful for computing runout length – at least for the simulations with defined starting areas – but not for simulating the spatial patterns of the debris flow deposit.

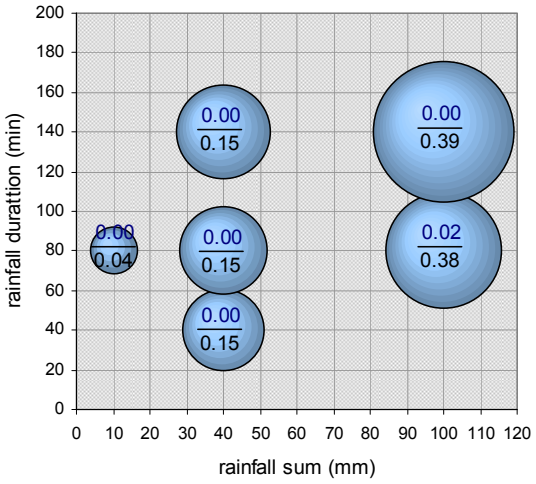

Figure 5.182: Volumes of potential slope failure as calculated for different rainfall scenarios (dimensionless). The blue numbers represent the runoff coefficients connected to the corresponding scenarios, the black numbers the minimum depth of the wetting front (away from flow channels).

Figure 5.183 shows the potential infiltration rate and the runoff coefficient for the soils of the study areas *Castillo de Rocas*, *Quebrada Escondida*, and *La Ampolleta* as a function of infiltrated depth (compare Eq. 4.6). The influence of a surface water table is excluded. While infiltration rates are high in the beginning – as long as the distance between soil surface and wetting front is small – it drops rapidly with proceeding wetting front, asymptotically approaching the hydraulic conductivity *K*. At a rainfall intensity of 100 mm h^{-1} (corresponding to the Scenario 1), surface runoff starts with a depth of the wetting front of less than 20 cm, increasing to a maximum of 0.17. For rainfall intensities of 80 mm h^{-1} or lower – concerning all scenarios except Scenario 1 – no runoff develops on soil.

Figure 5.184 shows the same variables based on the assumption that a 10 cm surface water table is present. Due to the increased hydrostatic pressure, infiltration rate is higher and runoff starts later. However, the consequence of this is not necessarily that the entire water table infiltrates into soils with a shallow wetting front: in the case that there is inflow flow upslope, it only means that outflow from the cell is less than inflow.

In relation to other soil classes (compare Figures 5.186 to 5.188) infiltration is relatively high and runoff coefficients are low.

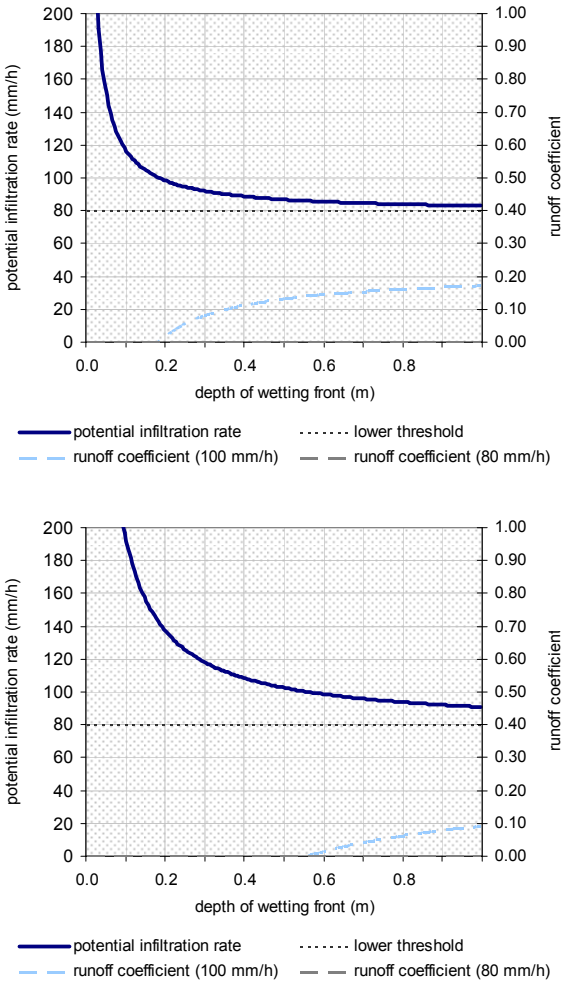

Figure 5.183 (top): Potential infiltration rate and runoff coefficients as a function of depth of the wetting front in the absence of a surface water table.
Figure 5.184 (bottom): Potential infiltration rate and runoff coefficients as a function of depth of the wetting front assuming a surface water table of 10 cm.

Table 5.10: Summary of some of the major system variables and moved soil volumes for all of the scenarios and analyses with the study area *La Ampolleta*; rcoef = runoff coefficient over the entire event; dwfront = depth of wetting front at the end of the simulation; (1) = away from flow channels; (2) = maximum.

scenario	pot. failure (m^3)	start (m^3)	entrainment (m^3)	deposit (m^3)	on road (m^3)	rcoef	dwfront (1)	dwfront (2)
1: 100/80	65,804	63,916	22,591	86,507	4,742	0.02	-0.38	-0.90
2: 100/140	93,017	90,072	24,959	115,031	5,724	0.00	-0.39	-1.20
3: 40/80	35,840	34,943	13,258	48,201	2,361	0.00	-0.15	-0.84
4: 40/140	43,206	41,460	12,257	53,717	2,564	0.00	-0.15	-1.12
5: 40/40	30,965	30,248	11,837	42,086	2,100	0.00	-0.15	-0.81
6: 10/80	10,293	9,929	2,922	12,850	589	0.00	-0.04	-0.75
7: pref. flow	116,020	112,687	25,196	137,883	6,523	0.00	-0.39	-2.76
8: *k* increase	104,508	101,613	24,004	125,617	6,183	0.00	-0.39	-1.90
9: no veg.	156,210	154,519	9,282	163,801	7,045	0.02	-0.38	-0.85
10: dry soil	851	520	5,363	5,883	0			

5.6 Las Murallas

The study area *Las Murallas* (compare Section 3.7) is located upstream of the three study areas discussed above. Situated at the very edge of the granitic intrusion, it represents a mosaic of granitic and volcanic rocks and soils. While some steep sediment walls are present in the lower portion of the area (Figure 5.185), The upper portion appears to be more stable. Some deposits may not be recognizable in the field as they coincide with the international road and are therefore removed after each event. Table 5.11 shows the scenarios and tests applied to *Las Murallas*.

Figure 5.185: The study area *Las Murallas* (compare Section 3.7). The thin white lines represent potential zones of debris flow initiation according to field evidence, the bold white lines delineate debris flow deposits. Elevation model derived from aerial and SPOT5 imagery, draped orthophoto from SPOT5. Design: Martin Mergili, 07/2008.

5.6.1 Tests of plausibility: rainfall event 100 mm in 80 minutes

1a Hydraulic model. The soil classes identified in the study area *Las Murallas* differ from those present in the other study areas around *Guido*, particularly those derived from the volcanic soils of the Choiyoi group (compare Section 3.2), containing more loam. They show much lower values of hydraulic conductivity *K* and therefore a lower infiltration capacity and a tendency to produce surface runoff also at low rainfall intensities and a shallow wetting front.

These patterns are illustrated in the Figures 5.186 to 5.188 (compare Figures 5.183 and 5.184 for sandy soils). The runoff coefficient of granitic soils in the area (texture class LS) quickly increases to 0.80 for Scenario 1, for volcanic soils (texture class SL) even to 0.90 and more. These patterns change only slightly when assuming a surface water table with a depth of 10 cm.

When reducing rainfall intensity to 20 mm h^{-1}, the maximum runoff coefficient drops to zero for the granitic soils whilst it remains as high as 0.66 for the volcanic soils (assumption: no surface water table).

Table 5.11: Parameter settings and scenarios for the study area *Las Murallas*. soil = soil parameters, lcov = land cover parameters, n/sed = Manning's n and parameters for sediment transport, pflow = preferential flow (per cent of total seepage), runout = parameters for runout model, res = spatial resolution, A = hydraulic model, B = sediment transport model, C = slope stability model, D = debris flow runout model; std = standard parameters (compare Section 4.1), cal = calibrated parameters, test = changed param. for analysis of sensitivity.

		Parameter settings						Used modules			
		soil	lcov	n/sed	pflow	runout	res (m)	A	B	C	D
Test of plausibility (with precipitation = 100 mm in 80 minutes; all as rainfall)											
1a	Hydraulic model	std	std	std	0		5	x			
1b	Slope stability model	std,cal	std				5	x		x	
1c	Debris flow runout model					std	5				x
Scenarios											
1	Scenario 1: p=100 mm in 80 min.	cal	std	std	0	std	5	x		x	x
2	Scenario 2: p=100 mm in 140 min.	cal	std	std	0	std	5	x		x	x
3	Scenario 3: p=40 mm in 80 minut.	cal	std	std	0	std	5	x		x	x
4	Scenario 4: p=40 mm in 140 min.	cal	std	std	0	std	5	x		x	x
Analysis of sensitivity (with precipitation = 100 mm in 80 minutes; all as rainfall)											
5	Spatial resolution	test	std	std	0	std	10	x		x	x
6	Dry soil	test	std	std	0	std	5			x	x
7	Soil cohesion	test	std	std	0	std	5			x	x
8	Soil hydraulic conductivity	test	std	std	0	std	5	x		x	x

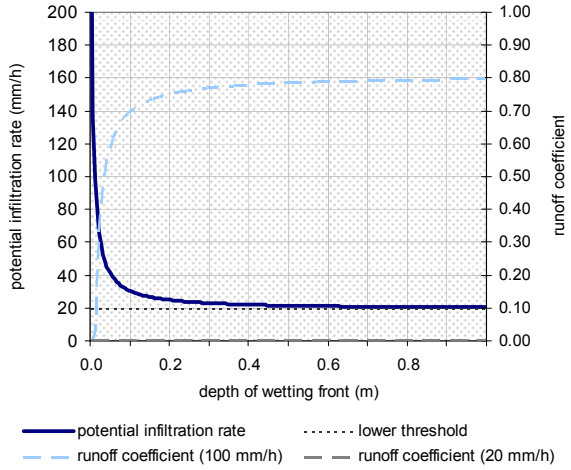

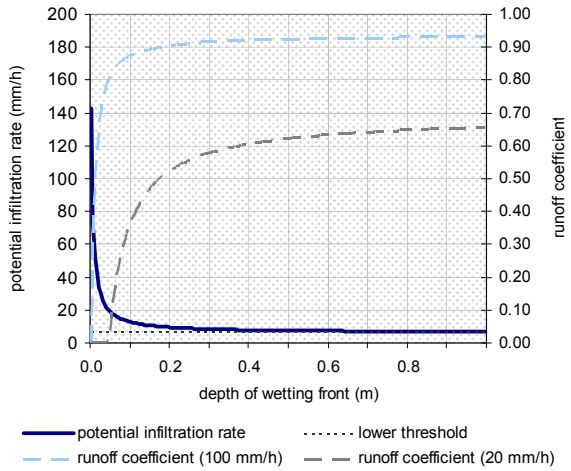

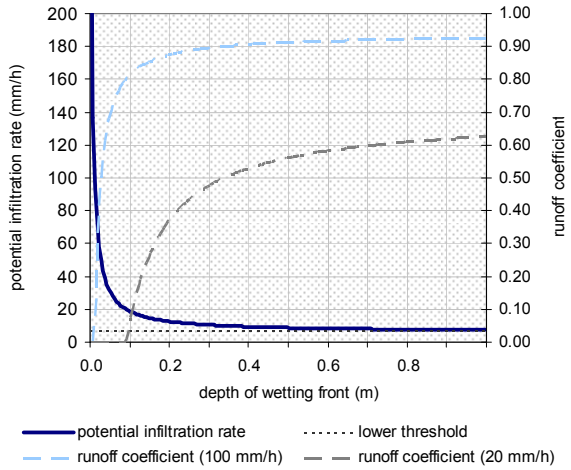

Figure 5.186 (top): Potential infiltration rate and runoff coefficients for the granitic soils of the study area *Las Murallas* as a function of depth of the wetting front in the absence of a surface water table.
Figure 5.187 (middle): Potential infiltration rate and runoff coefficients for the volcanic soils as a function of depth of the wetting front in the absence of a surface water table.
Figure 5.188 (bottom): Potential infiltration rate and runoff coefficients for the volcanic soils as a function of depth of the wetting front assuming a surface water table of 10 cm.

For Scenario 1, the simulated runoff velocities (maximum: 4.7 m s^{-1}) and depths of infiltration (maximum: 0.37 m) appeared plausible (Figures 5.189 to 5.192). However, like for the other study areas, a direct validation was not possible. The runoff coefficients over the entire event were 0.59 for the more sandy (LS) granitic soil and 0.77 for the more loamy volcanic soil (SL), mirroring the higher hydraulic conductivity of the former soil class. These values appear very high, compared to those for the three other study areas around *Guido* (compare Figures 5.183, 5.184 and 5.186 to 5.188).

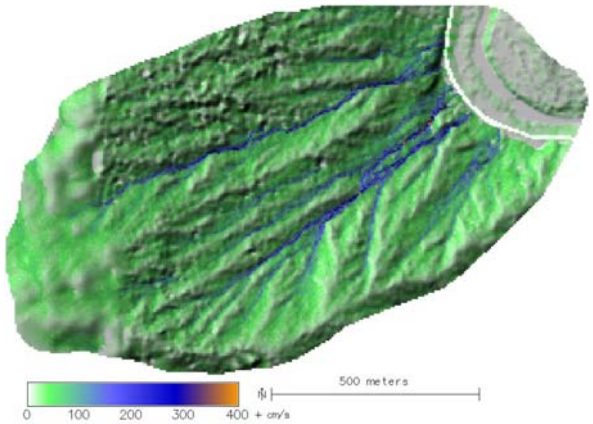

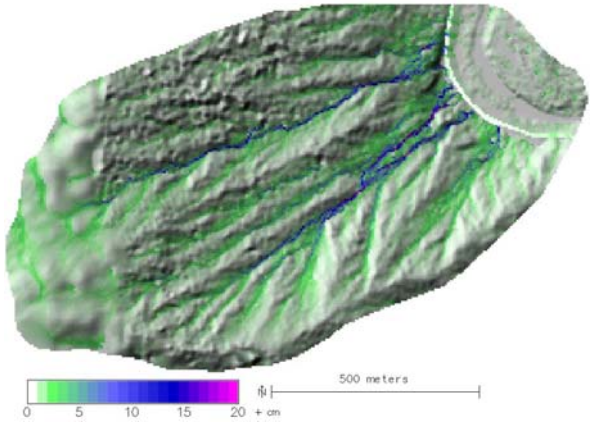

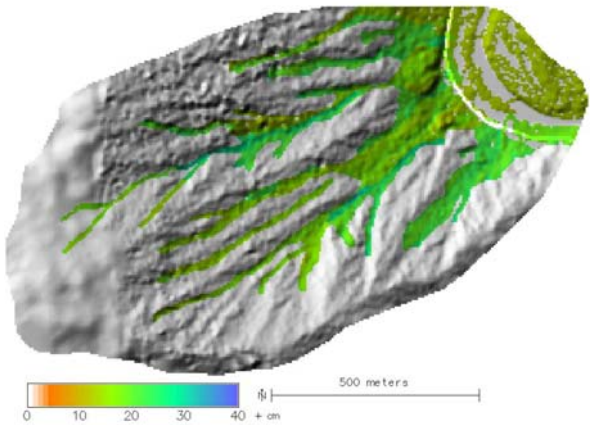

Figure 5.189 (top): Velocity of surface runoff (t = 60 min).
Figure 5.190 (middle): Depth of surface runoff (t = 60 min).
Figure 5.191 (bottom): Depth of wetting front below flow channels at the end of the scenario.

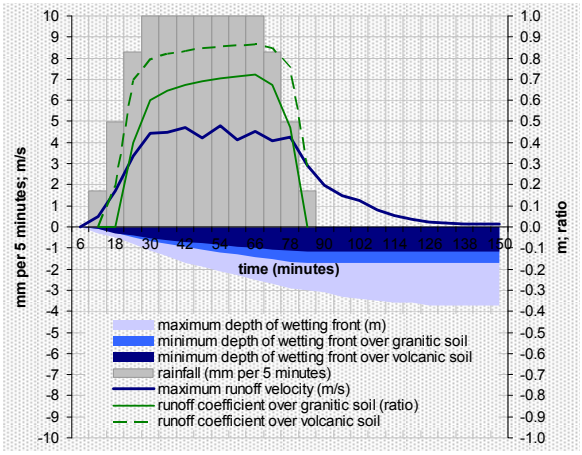

Figure 5.192: State of the hydrological system.

1b Slope stability model. Following the field evidence, debris flows in the area were assumed to be initiated by slope failures only. Due to the two substantially different soil classes in the study area, the slope stability conditions are relatively complex. The granitic soils, with only one sample where c and φ were determined, show a cohesion of 10 kN m^{-2}. However, when using this value in the slope stability model, large areas of failure observed in the field remained undetected (Figures 5.193 and 5.194).

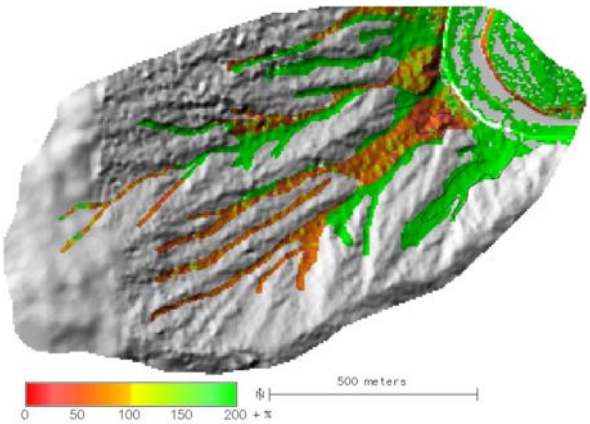

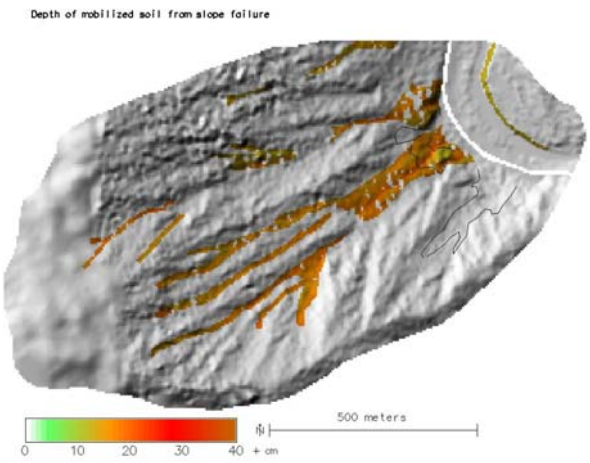

Figure 5.193 (top): Factor of safety with cohesive granitic soil.
Figure 5.194 (bottom): Depth of debris flow initiation with cohesive granitic soil.

It was therefore assumed – in accordance with the measurements and results from the study areas discussed above – that the measured cohesion only acts in some places but, in general, the slope is cohesionless. Based on this assumption (setting $c = 0$ and leaving φ unchanged), the simulated patterns of slope stability corresponded much better to the observed patterns for the granitic soils (Figures 5.195 and 5.196).

27,400 m³ of potentially unstable soil were detected, 27,000 m³ of which were identified as starting material for debris flows. The correlation with field observations showed an overestimation of starting material for the granitic, but particularly for the volcanic soils: apparently stable portions of the upper slopes were identified as potentially unstable by the model.

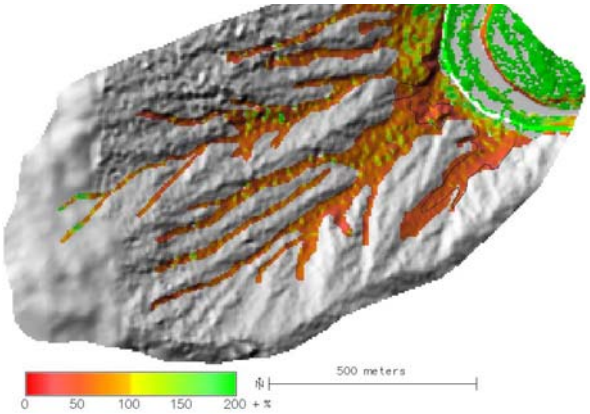

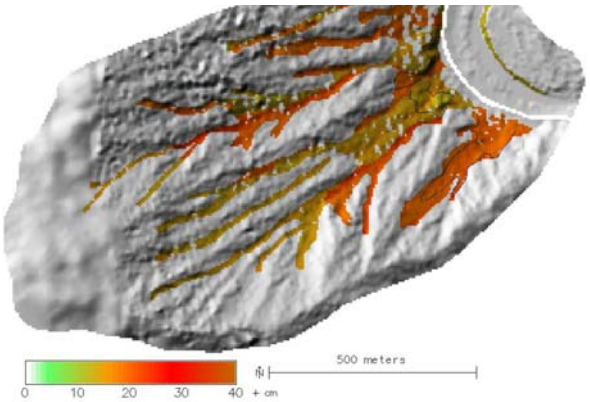

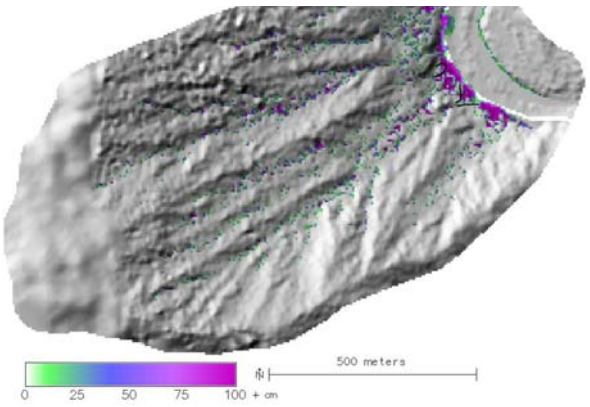

Figure 5.195 (top): Factor of safety with cohesionless granitic soil.
Figure 5.196 (middle): Starting material of debris flows.
Figure 5.197 (bottom): Deposition from debris flows.

1c Debris flow runout model. The standard parameters for runout length μ and M/D according to GAMMA (2000) and WICHMANN (2006) yielded plausible results for runout length (the minimum of μ was set to 0.045). The slope and velocity thresholds, however, had to be calibrated. A combination of 20° and 15 m s^{-1} yielded a good correlation with the patterns of deposition observed in the field (Figures 5.197 and 5.198). Only 4 m³ of soil were entrained by debris flows, according to the model, leading to a deposit of 27,000 m³. 1,000 m³ of sediment ended up on the international road, according to the model.

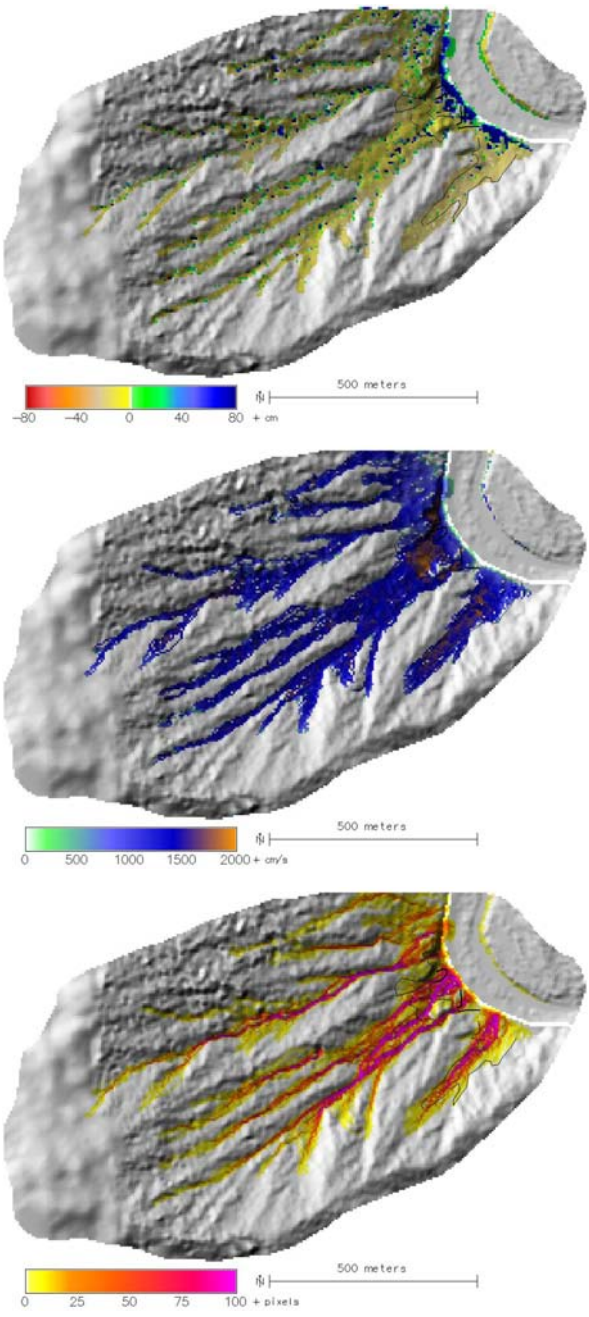

Figure 5.198 (top): Sediment balance from debris flows.
Figure 5.199 (middle): Maximum runout velocity.
Figure 5.200 (bottom): Debris flow index.

The maximum velocity of debris flows in the area was around 15 m s^{-1} over most of the steeper slopes, according to the model, reaching maxima exceeding 20 m s^{-1} in the steepest sections and decelerating rapidly when reaching the road (Figure 5.199). Figure 5.200 shows the debris flow index (the number of times each cell is hit by a debris flow cell during the random walk process).

5.6.2 Rainfall scenarios

2 Rainfall scenario: 100 mm in 140 minutes. Like for the other study areas, extending the rainfall duration when maintaining sum led to increased infiltration and decreased runoff, with maximum runoff velocities of 3.8 m s^{-1}, and runoff coefficients of 0.67 on volcanic soil and 0.37 on granitic soil (Figures 5.201 and 5.202). The maximum depth of the wetting front increased from 37 cm to 46 cm, compared to Scenario 1. The modelled areas of potential slope failure remained unchanged, but – due to the deeper wetting front – the volume increased to 39,100 m³.

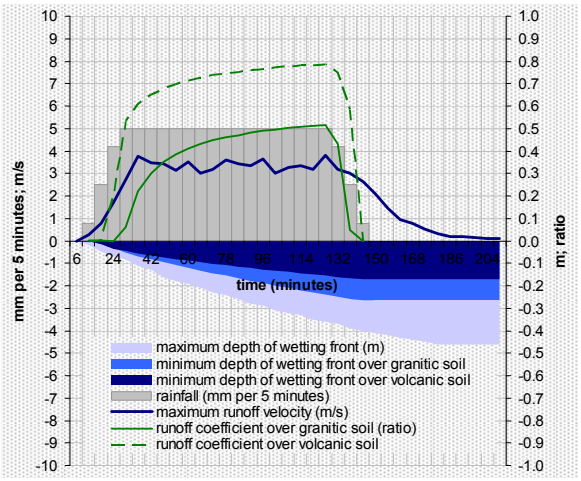

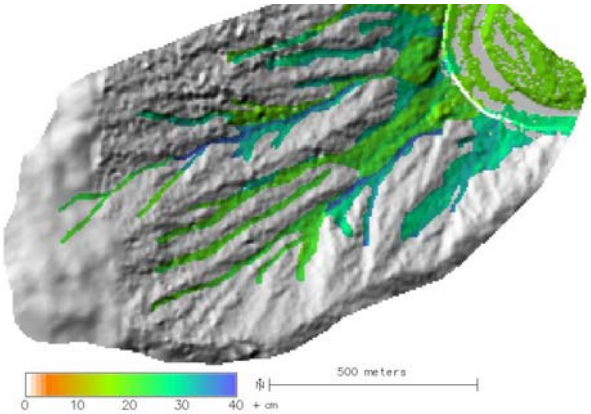

Figure 5.201 (top): State of the hydrological system.
Figure 5.202 (bottom): Depth of wetting front below flow channels at the end of the scenario.

38,400 m³ of starting material were detected by the model and 5 m³ of soil were entrained, leading to a total deposit of 38,400 m³. 1,600 m³ were simulated to end up on the international road (Figure 5.203).

The patterns of maximum debris flow runout velocity did not undergo substantial changes, compared to Scenario 1.

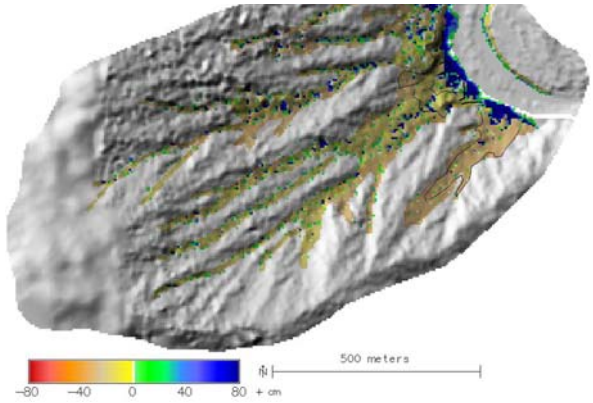

Figure 5.203: Sediment balance from debris flows.

3 Rainfall scenario: 40 mm in 80 minutes. The runoff coefficients were 0.46 (volcanic soil) and 0.11 (granitic soil), respectively. The wetting front proceeded down to a maximum of 31 cm, whilst the maximum runoff velocity reached 3.3 m s^{-1} (Figure 5.204). The depth of the wetting front below the flow channels and the depth of starting material of debris flows were less than for the Scenarios 1 and 2, but the spatial patterns were identical and are therefore not represented separately.

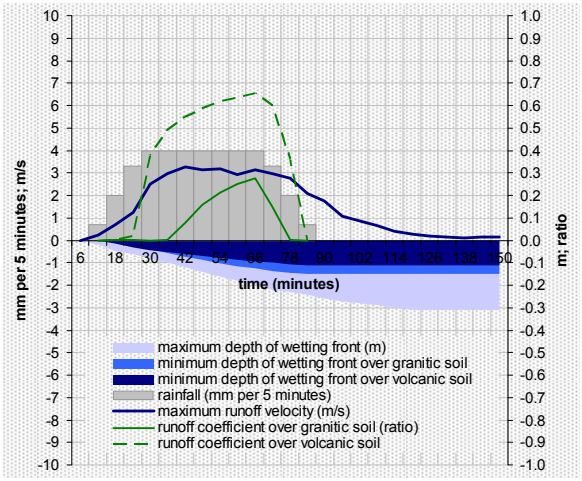

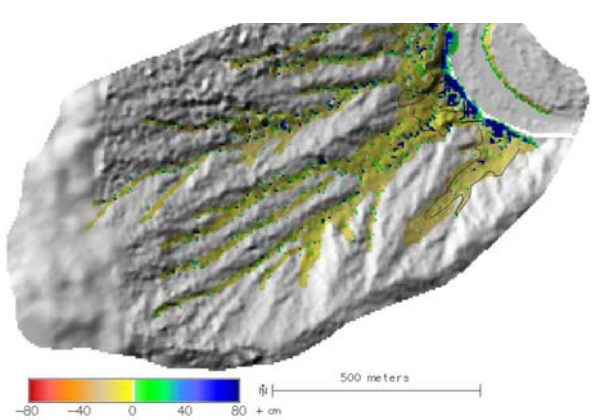

Figure 5.204 (top): State of the hydrological system.
Figure 5.205 (bottom): Sediment balance from debris flows.

24,800 m³ of soil were identified as potentially unstable at the end of the simulation, 24,400 m³ as starting material for debris flows. 3 m³ of soil were entrained, 24,400 m³ were deposited in total. According to the model, the international road would have been covered by about 800 m³ of debris (Figure 5.205). The runout velocities remained more or less unchanged, compared to the scenarios shown above.

4 Rainfall scenario: 40 mm in 140 minutes. Similar to the scenarios with 100 mm of rainfall, the hydrological system shifted from runoff towards infiltration when increasing the duration of the assumed 40 mm rainfall event. Whilst the runoff coefficient was still relatively high over volcanic soil (0.24), it decreased to zero over granitic soil. The maximum depth of the wetting front reached 40 cm at the end of the simulation. The velocity of the surface runoff peaked at 2.3 m s^{-1} (Figure 5.206).

32,800 m³ of soil were identified as potentially unstable by the model, leading to a starting volume of debris flows of 32,300 m³. 7 m³ of soil were entrained by debris flow processes, resulting in a total deposit of 32,300 m³. 1,300 m³ of sediment ended up on the international road, according to the model (Figure 5.207). The maximum runout velocities of the simulated debris flows were similar to those computed for the other scenarios.

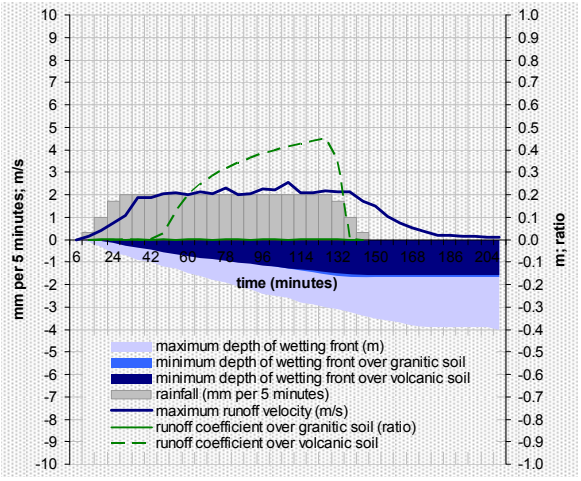

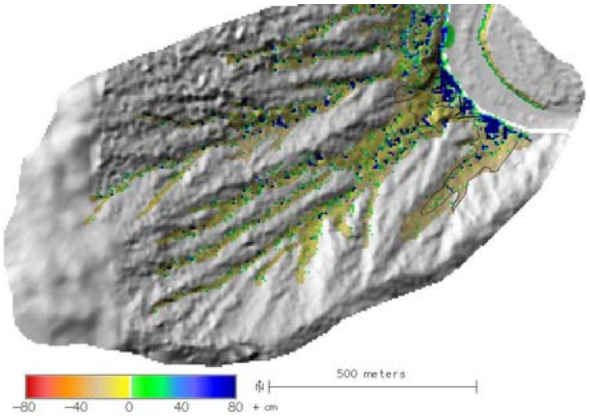

Figure 5.206 (top): State of the hydrological system.
Figure 5.207 (bottom): Sediment balance from debris flows.

5.6.3 Analysis of sensitivity

All tests of sensitivity for *Las Murallas* were based on Scenario 1.

5 Spatial resolution. Decreasing the spatial resolution for the simulation from 5 m to 10 m cell size did lead to some, but not to substantial changes in the model output. Whilst the runoff coefficients remained constant, the maximum depth of the wetting front decreased from 0.37 m to 0.33 m. The maximum runoff velocity was 4.9 m s^{-1} (Figure 5.208).

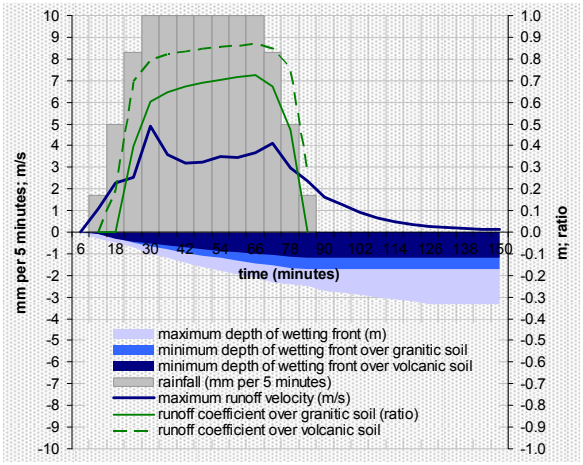

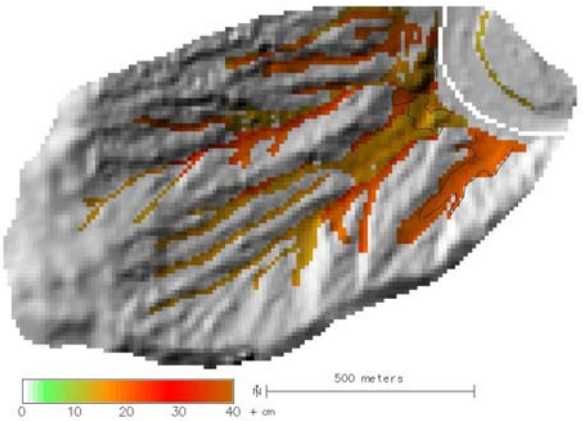

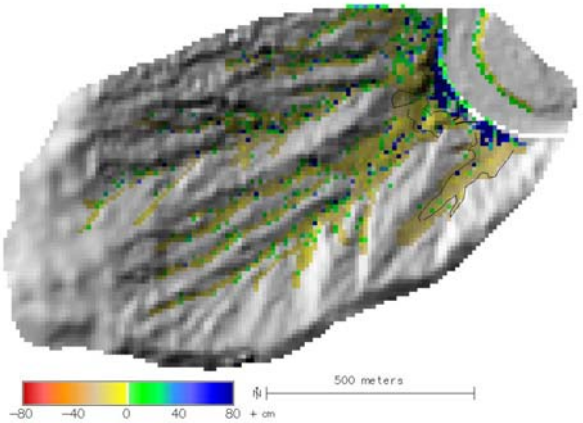

Figure 5.208 (top): System status (10 m resolution).
Figure 5.209 (middle) Starting material of debris flows.
Figure 5.210 (bottom): Sediment balance from debris flows.

29,100 m³ of potentially unstable soil were detected by the model (at 5 m resolution: 27,400 m³), 28,900 m³ (27,000 m³) were identified as starting volume of debris flows (Figure 5.209). Nothing (7 m³) was entrained, leading to a total deposit of 28,900 m³ (27,000 m³). 800 m³ (1,000 m³) were calculated to end up on the international road (Figure 5.210).

6 Dry soil. Assuming dry soil (or vertical instead of slope-parallel seepage) resulted in increased stability. Particularly the upper portions of the catchment otherwise identified as unstable were modelled as stable (Figure 5.211). The model detected a total of 11,400 m³ of potentially unstable soil and 5,700 m³ of starting material of debris flows (Figure 5.212).

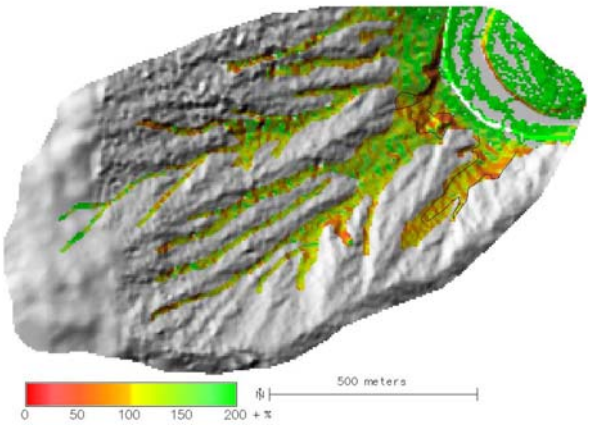

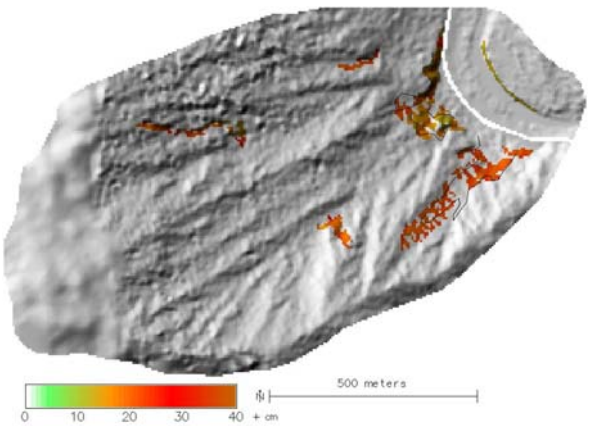

Figure 5.211 (top) Factor of safety with dry soil or vertical seepage.
Figure 5.212 (bottom) Starting material of debris flows.

The starting areas shown in Figure 5.212 constitute an underestimate, compared to field observations. This means that the characteristic soil water movement is probably intermediate between vertical and slope-parallel.

7 Soil cohesion. Introducing a soil cohesion of 1 kN m^{-2} over the entire soil-covered portion of the study area led to the detection of 9,600 m³ of potentially unstable soil, but no debris flows, whilst 2.5 kN m^{-2} resulted in the disappearance of all potential instabilities in the study area – it appears that for such shallow wetting fronts, also small values of cohesion do stabilize relatively steep slopes.

8 Soil hydraulic conductivity. The values of soil hydraulic conductivity for the Green-Ampt model taken from RAWLS et al. (1983) are relatively low, compared to the values of saturated hydraulic conductivity listed by CARSEL & PARRISH (1988; compare Table 4.3). Testing the model for *Las Murallas* using the latter values therefore resulted in a deeper wetting front (between 28 cm and 1.07 m) and lower runoff coefficients (0.46 for volcanic soil and zero for granitic soil; Figures 5.213 and 5.214).

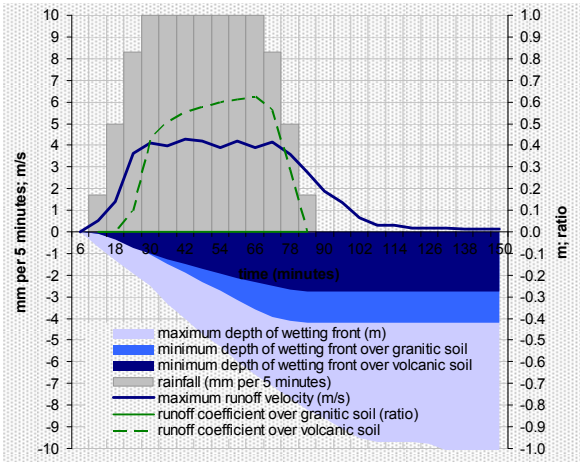

Figure 5.213: State of the hydrological system.

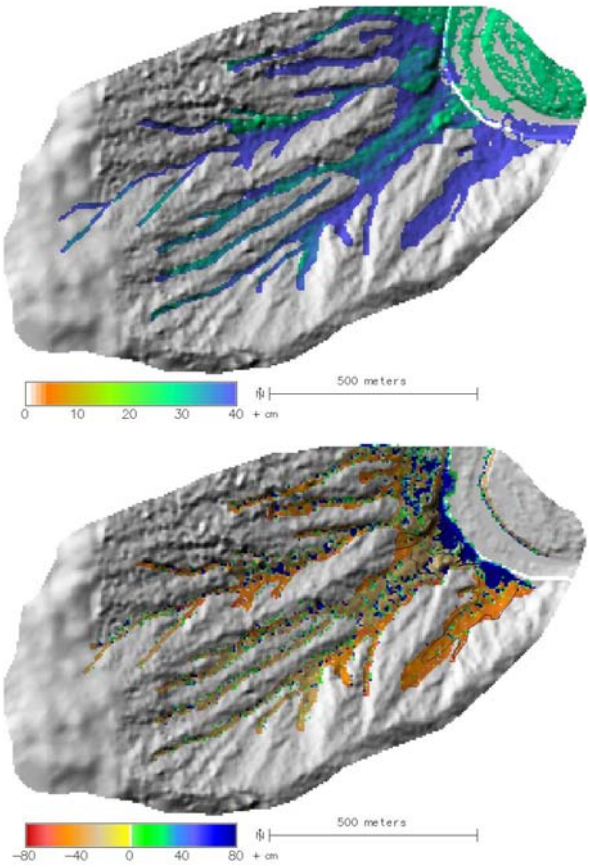

Figure 5.214 (top): Depth of wetting front below flow channels at the end of the simulation.
Figure 5.215 (bottom): Sediment balance from debris flows.

Modelled areas of potential slope failure did not change substantially, compared to the basic scenario, but the deeper wetting front led to larger volumes involved: the model detected 69,000 m³ of potentially unstable soil, 67,900 m³ of which were identified as starting material of debris flows. Including 20 m³ of entrained soil, 67,900 m³ of debris were deposited. 3,800 m³ ended up on the international road, according to the model (Figure 5.215).

5.6.4 Summary

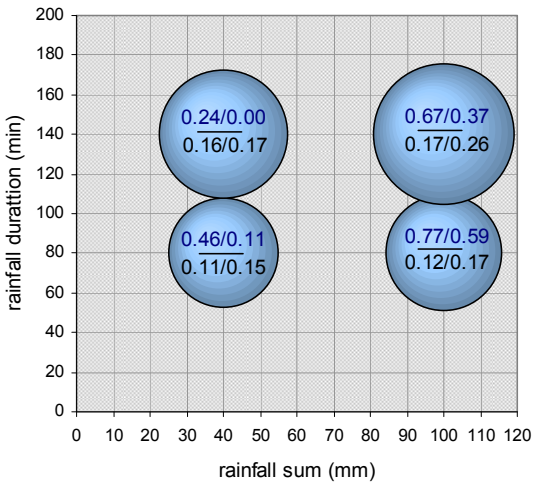

Figure 5.216: Volumes of potential slope failures as calculated for the different rainfall scenarios (dimensionless). The blue numbers represent the runoff coefficients connected to the corresponding scenarios, the black numbers the minimum depth of wetting front (away from the flow channels); left numbers stand for volcanic soil, right numbers for granitic soil.

Similar to the previously discussed study areas, the moved volumes increased under-proportionally compared to rainfall sum since a higher portion of rainfall infiltrated at lower intensities, contributing to a deeper wetting front (Figure 5.216).

Volumes of 800 m³ to 1,600 m³, of debris were simulated to be deposited on the international road, with higher hydraulic conductivity up to 3,800 m³ (Table 5.12). A direct comparison with reported volumes deposited on the road was not possible due to lacking information. Particularly concerning the failed material from the walls in the lower portion of the catchment, the processes are probably no real debris flows, but rather transitional to other mass movement processes (fall, slide).

Table 5.12: Simulated volumes and moved by debris flows and system states in the *Las Murallas* area for different scenarios and tests; rcoef = runoff coefficient; dwfront = depth of wetting front; (a) = for volcanic soil; (b) = for granitic soil; (1) = away from flow channels; (2) = maximum.

scenario	pot. failure (m^3)	start (m^3)	entrainment (m^3)	deposit (m^3)	on road (m^3)	rcoef (a)	rcoef (b)	dwfront (m; a1)	dwfront (m; b1)	dwfront (m; 2)
1: 100/80	27,419	26,972	4	26,976	950	0.77	0.59	-0.12	-0.17	-0.37
2: 100/140	39,066	38,418	5	38,423	1,598	0.67	0.37	-0.17	-0.26	-0.46
3: 40/80	24,828	24,424	3	24,427	818	0.46	0.11	-0.11	-0.15	-0.31
4: 40/140	32,789	32,265	7	32,272	1,282	0.24	0.00	-0.16	-0.17	-0.40
5: res. 10 m	29,137	28,883	0	28,883	822	0.77	0.59	-0.12	-0.17	-0.33
6: dry soil	11,414	5,690	482	6,171	277					
7: c_s = 1 kN m^{-2}	9,570	0	0	0	0					
8: *k* incease	68,985	67,900	18	67,918	3,799	0.46	0.00	-0.28	-0.42	-1.07

6 Discussion

6.1 Model results and observations

6.1.1 r.debrisflow

Table 6.1 shows the modelled and the reported volumes of debris deposited on the international road (compare Table 4.5 and Chapter 5). Except for the study area *Guardia Vieja*, the modelled and the reported values are of the same magnitude.

These results have to be evaluated with caution. First of all, one has to be careful to avoid circular reasoning: the runout model was calibrated in order to provide patterns matching with the observed deposits (compare Section 6.2) so that a good correlation is not surprising. However, the spatial patterns of deposition simulated by the two-parameter friction model are not influenced by the moved volume (unless the user-defined maximum depth of deposition comes into action), meaning that the locations and the depths of the starting areas of debris flows are likely to be modelled in a realistic way. This statement is supported by the generally good correspondence between simulated and observed starting areas (with the exception of *Guardia Vieja* and, partly, *Las Murallas*);

For some of the study areas, runout lengths and volumes were modelled correctly, but the modelled deposit was shifted laterally, compared to the observed deposit. This phenomenon is most likely a consequence of deficiencies in the elevation model used. Since the DEMs were derived from different types of imagery, partly without calibration protocol, using reference datasets at 15 m and 30 m resolution (compare Section 4.1), they do not constitute high-accuracy datasets. Though providing a good representation of the topographic features, incorrect representation of the details of a rather smooth topography are likely, for example the steepest flow path on a cone. Furthermore, existing debris flow deposits represented in the DEM may lead to a different runout behaviour for new debris flows.

The modelled soil volumes involved into debris flows increase with increasing rainfall duration and decreasing intensity: the more water infiltrates, the more soil is potentially susceptible to fail, according to the model used. Particularly for the *Guido* study areas, this logical phenomenon was difficult to validate: the rain gauge is only few kilometres away from the study areas, but the episodic rainstorms are of a very local nature and the values measured at the station do not necessarily correspond to those in the catchment. This may be one reason for the fact that the official reports about sediment volumes deposited on the international road from debris flows do not at all correlate with rainfall sums measured at the nearby meteorological station (compare Table 4.5). It appears impossible to give reliable information about the volumes deposited as a response to a defined rainfall event – too many factors not included in the simulation due to lacking data play a role (for example prewetting of the soil or depth of soil). Regarding *Guido*, another possible explanation for the missing correspondence of rainfall sums and debris flow volumes regarding the 1996 events could be that the first event, connected to a smaller measured rainfall sum, had removed a lot of unstable material which was not available during the second event a few weeks later.

Table 6.1: Modelled and reported volumes of debris flow deposits on the international road Mendoza - Central Chile for the considered rainfall scenarios in selected study areas. Numbers in brackets indicate maxima including tests of parameters sensitivity. For the study area *Quebrada del Ferrocarril*, predefined starting areas and volumes of debris flows were used, for all other study areas, the starting areas and volumes were computed.

study area	starting volume (m^3)	modelled deposit on road (m^3)	reported volume on road (m^3)	remarks
La Ampolleta	10,000 – 90,000	600 – 5,700 (7,000)	together 600 – 15,000	reports include some material from rock fall; no more differentiated data available
Quebrada Escondida	3,000 – 14,000	400 – 2,900 (2,900)		
Castillo de Rocas	8,000 – 67,000	300 – 5,400 (8,700)		
Las Murallas	24,000 – 38,000	800 – 1,600 (3,800)		
Quebrada del Ferrocarril	36,000	9,800 (12,000)	8,000 – 14,000	defined starting volume (snow melt-triggered debris flows)
Guardia Vieja	2,641,000	106,000 (133,000)	45,000	infiltration of entire effective rainfall assumed

Not all of the mass movements occurring in the area are necessarily debris flows – for *Las Murallas*, for example, failures from the steep sediment walls were identified as debris flows in the simulations due to lacking criteria for exclusion, but since the deposits are not any more present, there is doubt regarding the truth of this. Also in the lower portions of the other study areas, mobilized soil does not necessarily develop into real debris flows as it quickly moves onto flat terrain. The reports about volumes deposited on the road – particularly for the *Guido* area (ESPEJO 1996) – do not necessarily exclusively refer to debris flows – the volumes may also contain some quantities of material from rock fall and from sediment-laden surface runoff.

Direct reference data – volumes of debris deposited on the road – was only available regarding the final model results and, for the *Guido* area, only as aggregated values for a number of study areas. A direct validation of the intermediary results – particularly those yielded by the hydraulic model components – was not possible due to lacking reference information.

6.1.2 r.avalanche

The bed friction angle δ had to be calibrated in order to match the simulated runout lengths with field evidence. The calibrated values partly exceeded the values used by WANG et al. 2004 by far and also varied considerably among the study areas (33° appeared suitable for *Castillo de Rocas* and *Quebrada Escondida*, 27° for *La Ampolleta*, and 23° for *Guardia Vieja*).

Compared to field observations, spreading of the debris flow mass – particularly in the runout zone – was too pronounced. A too coarse spatial resolution chosen for the simulations was identified as the main reason for this deficiency. Decreasing the spatial resolution from 5 m to 10 m resulted in even more lateral spreading. However, with the current version of *r.avalanche* and the hardware used, a further increase of the spatial resolution would result in unacceptably long computing times (some days or even weeks). The large amount of spreading of the simulated flow expressed itself in smaller volumes of debris deposited on the road: for Scenario 1 in the study area *La Ampolleta*, where runout was computed comparatively with *r.debrisflow* and *r.avalanche*, the simulated values differed considerably (4,700 m³ and 1,370 m³, respectively).

A rather unphysical behaviour of the flow was observed in curved channels. This phenomenon is a logical consequence of the way the Savage-Hutter model was implemented (WANG et al. 2004; compare Section 4.3).

6.2 Capabilities and limitations of the models

r.debrisflow and *r.avalanche*, which were developed, applied, and tested in the course of the present thesis, are still under development. – they show some capabilities, but also a number of limitations. Some of them have been denoted in Section 6.1. However, a more detailed account is required.

6.2.1 Capabilities

Both simulation models are freely available for everyone to be applied, tested, and modified, enabling an independent quality control and a potential for further model enhancement not only by the developer himself (compare App. 3.1 and 3.2). This can be considered as a first major capability connected to both of the models. Further capabilities are that

- *r.debrisflow* has proved successful for integrated modelling of debris flows potentially triggered by rainfall of high intensity and short duration, from the triggering event to the deposition of the flow (given the availability of the required input information);
- due to its predominantly physically-based character, it needs relatively limited calibration for new study areas to be applied to (except for the sediment transport model and the runout model);
- the component of *r.debrisflow* which is not fully deterministic, the runout model, is complemented by *r.avalanche*, which adds some value to the entire framework. *r.avalanche* is based on one of the leading theories for modelling granular flows, the Savage-Hutter (SH) model (compare Section 4.3), meaning that it is able to simulate the flow without requiring prior assumptions regarding flow path or runout length;
- *r.debrisflow* can be applied over a certain range of raster cell sizes: applying it with 5 m and 10 m spatial resolution did not result in major differences of the results – the runout model is expected to work best between 5 m and 25 m resolution (WICHMANN et al. in press).

However, regarding future development, the limitations of the model versions developed and used for the present thesis are of particular interest. Debris flows are without any doubt complex phenomena which incorporate several interdependent subprocesses involving atmosphere, biosphere, hydrosphere, eventually cryosphere, and of course the pedo- and the lithosphere, not to forget the anthroposphere which may play a crucial role in some cases.

Investigations on such complex processes always involve several uncertainties limiting the accuracy or the

correctness of the results and defining the extent to which they can are applicable to purposes of risk management. To a large degree, such limitations are a consequence of insufficient data regarding some or all of the components involved in the process. Another source of limitations, of course, is the model itself, adding value to the input information.

6.2.2 Limitations regarding input data

General limitations

Many of the parameters to be used in debris flow models are relatively easy to measure or to derive for specific sites defined by a set of coordinates. The spatial distribution or differentiation of these parameters, however, has to be estimated by statistical or heuristic methods. This issue particularly concerns two components of the system:

- meteorological input – particularly precipitation and evapotranspiration – can be measured at specific sites, but their spatial patterns are highly complex;
- regarding soil properties, these problems are even more severe, as there is one dimension more included. Pronounced differences of the soil profile may occur over short distances. Furthermore, important soil characteristics like hydraulic conductivity are uncertain, and preferential flow through macropores still remains an unsolved problem. The entire issue becomes even more complicated as soon as the influence of plants on the soil system is included, regarding water budget and slope stability.

  A disputed topic is the stone content of the soil. In the pre-sent thesis it has been excluded from the water storing capacity, following the assumption that the water transport through the soil is supported by the matric whilst the stone content would neither contribute to the water storing capacity nor significantly alter hydraulic conductivity, at least when averaged over a certain soil volume. Only with a stone content from about 60 per cent upwards, water transport through macropores between the stones would become dominant (LEHMANN et al. in press; GEITNER pers. comm.).

  This concept, of course, constitutes a rough approximation, since water transport does not occur through the soil particles, but through the pores. Many geotechnical engineers, for instance, reject the concept of stone content, always considering the mixture of finer and coarser particles as one entity (FELLIN pers. comm.). In the international literature dealing with infiltration and seepage, it is hardly referred to stone content at all, also when using grain size classification systems only referring to grains smaller than 2 mm (e.g. XIE et al. 2004a; CHEN & YOUNG 2006).

Looking at debris flows themselves, the starting areas are sometimes easy to detect (e.g. clearly distinguishable slope failures), but in most cases – particularly regarding debris flows starting in channels – it is very difficult to clearly identify areas of mobilization. An additional level of complexity is added to this issue when considering that the transition between hyperconcentrated surface runoff and debris flow is not a sharp one, but rather transitional. Identification of depth of entrainment – or even distinguishing between initiation and entrainment – are difficult tasks, too. High accuracy remote sensing methods like airborne or terrestrial laser scanning may help if applied before and after a debris flow event, but they can not assist in the decision whether a change in the elevation of a cell is caused by runoff or hyperconcentrated flow (detachment/deposition), by a slope failure, or by a debris flow (entrainment/deposition). Summarized, the temporal and spatially distributed knowledge regarding specific debris flow events, which would not be required for model application, but the more for model validation, is still very limited. The velocity of debris flows can be measured (COSTA 1984), but such measurements are only available for very few events. Patterns of deposition are in general more easily identifiable than the patterns of mobilization, velocity, and entrainment, at least as long as clearly defined lobes are present.

Also the bed friction angle δ used for *r.avalanche* is quite uncertain. It was assumed constant over each study area under investigation, but in fact, unaccounted variations over short distances may be responsible for some of the inaccuracies or errors in the model output.

Specific limitations in the study areas

Though a lot of general investigations on landslides and debris flows do exist in the Aconcagua and Mendoza valleys (e.g. MOREIRAS 2004a; 2004b; 2005), the detailed knowledge about historical debris flow events is rather limited, some official reports excluded (ESPEJO 1996; HAUSER (2000b; 2005). During the field work for the present thesis it was possible to collect a lot of information on the system components included in the debris flow processes, but they underlie the limitations mentioned above regarding accuracy, representativeness and spatial distribution.

Concerning the debris flow events themselves, the sparse information available from official sources had to be used, and traces of previous debris flows in the field had to be found for facilitating model evaluation. Regarding the debris flows ending up on and close to the international road, there was no field reference available as the deposits had been removed in order to reestablish the traffic.

The official reports on volumes of debris deposited on the international road are very useful for the Chilean study areas *Quebrada del Ferrocarril* and *Guardia*

Vieja – for the *Guido* study areas, they can only give a rough estimation as they are not split up according to each catchment, but are specified for the entire area and may also contain material of different origin (rock fall, deposition from runoff).

No runoff gauges do exist in the study areas. The existing rain gauges nearby are valuable, but the they only provide daily sums which have to be broken down to shorter durations artificially.

6.2.3 Model limitations: r.debrisflow

In contrast to the limitations with data and parameters, being immanent to all research, the limitations with the model can be overcome more easily – however, the best model will not provide reliable results without the appropriate, correct, and accurate input. The version of ***r.debrisflow*** used for the present thesis was designed in order to work as far as possible with the available data for the study areas and to account for the conditions prevailing there – this results in the following limitations:

- infiltration and seepage: due to the use of the Green-Ampt infiltration model, the model is only appropriate for simulating debris flows from slope failures triggered by short-term rainfall events where the approximation with a sharp wetting front moving downwards is acceptable and evapotranspiration is negligible. Seepage becomes more complex with longer rainfall duration or with the occurrence of snow melt. Debris flows from slope failures triggered by upwelling groundwater can not be simulated at all;
- the sediment transport model as implemented in the present model version requires a large amount of calibration with field data. Since reference data for the justification of the calibration parameters was not available in the study areas, it was not possible to use the sediment transport model properly. The model was developed for less steep channels than those in the study areas, so that its applicability may be limited. Also the generalizations required for the application of the model for the purpose of the present thesis (compare Section 4.2) may constitute a severe problem;

  The modelled starting volumes of debris flows (from slope failures) increased with increasing rainfall duration and constant rainfall sum, since a higher portion of water from rainfall infiltrated and a deeper soil column was susceptible to fail. It would be interesting to explore if this effect is outbalanced by higher of surface runoff velocities and the connected detachment – however, a sediment transport model requiring less or no calibration would be needed for this purpose;
- infinite slope stability models as used in ***r.debrisflow*** are designed for shallow translational slope failures whilst they are inappropriate for deep-seated rotational failures. The results for the study area *Guardia Vieja* shall therefore be seen with caution (compare Section 5.2).

  Slope-parallel seepage is assumed when executing the infinite slope stability model. This is only true in a strict sense when an impermeable layer is present impeding further percolation. In reality, the spatial distribution of the depth of such impermeable layers is largely unknown. At least for the study areas used for the present thesis it can be assumed that, despite the lacking of classical impermeable layers, there are large boulders in the soil leading at least partly to slope-parallel seepage so that this worst-case assumption can be justified;
- the debris flow runout model, like all conceptual models, has to be calibrated for each study area, limiting its suitability for making class A predictions of future debris flows. Table 6.2 summarizes the parameters used for all of the study areas. WICHMANN (2006) stated that the two-parameter friction model which was also used for the present study could first be calibrated for maximum flow velocity using M/D and then for runout length using μ, in order to avoid calibrating the model for one target parameter using two predictors (different combinations could result in the same outcome). However, things are more complex in reality because μ is actually a combination of four parameters when computed according to GAMMA (2000), and the slope and velocity thresholds for particle entrainment and deposition have to be calibrated, too;

  Furthermore, the runout model does not serve for simulating more particular conditions, for example if shrubs or stems of trees block the channel.

6.2.4 Model limitations: r.avalanche

r.avalanche needs a much more limited set of input data and parameters than ***r.debrisflow***. In contrast, its mathematical-technical background is much more sophisticated. The version used for the present thesis shows the following limitations:

- it is only applicable to flow channels without major horizontal curvature – the results for *Quebrada Escondida*, for example, show clearly that corners in the flow channel lead to a completely unphysical behaviour of the flow – the same phenomenon was observed with *Quebrada del Ferrocarril* (the results are not shown in Chapter 5);

Table 6.2: Parameter settings for the runout model found to be suitable for the study areas.

study area	*M/D* (m)	μ	μ_{min}	μ_{max}	slope threshold (°)	velocity threshold (m s^{-1})
Guardia Vieja	75	0.1	-	-	15	10
Quebrada del Ferrocarril	75	0.045	-	-	8	10
Las Murallas	75	$0.13a^{-0.25}$	0.045	0.3	20	15
Castillo de Rocas	75	$0.13a^{-0.25}$	0.15	0.3	20 (27.5)	15 (17.5)
Quebrada Escondida	75	0.25	-	-	15	10
La Ampolleta	75	0.25	-	-	15	10

- entrainment of soil during the flow is not included – it is therefore difficult to calibrate the model with the study areas used as entrainment may play a major role for runout distance and also flow path (MCDOUGALL & HUNGR 2005);
- the role of pore water for runout behaviour is neglected, but in reality debris flows are a mixture of solid and fluid components and should be considered as such;
- in the SH model and also in *r.avalanche*, the bed friction angle δ is considered as independent from earth pressure – a more realistic account of this relationship could improve the quality of the model;

6.3 Comparison with other studies

It was not possible to directly relate the results of the present study to those of comparable studies as such do not exist in the research area. The investigations of MOREIRAS (2004a; 2004b; 2005) were of statistical nature, considering a completely different spatial scale (a large portion of the Mendoza valley). However, the findings of MOREIRAS (2005) that also small rainfall events may trigger debris flows are in line with the findings from the present thesis.

Regarding the choice of empirically derived parameters for the runout model, the values of bed friction coefficient μ and mass-to-drag ratio M/D proposed by GAMMA (2000) worked fine for the study areas *Las Murallas* and *Castillo de Rocas* (Table 6.2), but different upper and lower thresholds were used for the two areas. For the other study areas, constant values of μ appeared to suit better to the local conditions. A high content of water (*Guardia Vieja*) or even snow (*Quebrada del Ferrocarril*) is most probably the reason that, for these study areas, the model proved successful with comparatively low values of μ (compare Table 6.2). The slope and velocity thresholds for entrainment and deposition had to be calibrated for each study area – values of 15° and 10 m s^{-1} appear reasonable for most of the areas, lower values lead to better correlation with the reported patterns of deposition in the *Quebrada del Ferrocarril* area. In contrast, for the study area *Castillo de Rocas*, the thresholds (particularly slope threshold) had to be increased considerably in order to attain a reasonable correlation with field observations. The standard value of the M/D ratio (75 m) led to plausible flow velocities in all of the study areas.

For the first tests of *r.debrisflow*, where the approach according to VANDRE (1985) was used, much higher values than the proposed ones had to be chosen for the slope thresholds (compare App. 2.3). Together with the high bed friction angle to be used for *r.avalanche*, this indicates that the behaviour of debris flows in the granitic residuals around *Guido* (and particularly in the study area *Castillo de Rocas*) differs from those in many other areas of the world. Particularly the onset of deposition occurs much earlier (at steeper slopes) than the general values from the literature indicate.

6.4 Implications for hazard and risk management

The focus of the present thesis is rather a methodical one, concentrating on the development, testing and implementation of simulation models for debris flows. The models developed, at their present stage, are usable for purposes of risk management only with a lot of care and a very thorough validation. More testing with a larger number of study areas as well as a number of improvements are required for making the models mature for a reliable application for hazard prediction. One step of particular importance towards enabling class A predictions would be to replace the model components needing calibration by fully deterministic components. Further model development shall go in this direction (compare Section 6.5).

6.5 Preview

The development of both of the models, *r.debrisflow* and *r.avalanche*, is prospected to be continued in order to reduce the limitations discussed above. Further development shall also include an evaluation using a larger number of study areas with more input data and parameters available, and where comparable models have been applied.

Data management currently works with shell scripts. For the future, it is prospected to create graphical user Interfaces (GUIs) for both of the models in order to enhance their ease of use.

6.5.1 Improvement of r.debrisflow

The following improvements are prospected:

(1) Regarding seepage, an alternative approach capable to cope with more complex conditions like partial saturation and flow directions different from vertically downwards shall be implemented as a prerequisite for the detection of slope failures triggered by rainfall events of longer duration;

(2) a more complex slope stability model with the capability to deal with rotational failures usually occurring in cohesive soils shall be implemented alternatively to the infinite slope stability approach (compare XIE et al. 2003; 2006);

(3) the sediment transport model has to be reworked in order to be applicable, as far as possible, without calibration;

(4) a more sophisticated scheme for distinguishing between initiation of debris flows and other types of mass movements (particularly slides) shall be eleborated;

(5) the analyses of sensitivity for the hydraulic model components and the slope stability model showed a large influence of assumptions and uncertain parameters on the simulation results. Since such uncertainties are data-immanent, some model components shall be equipped with probabilistic elements, comparable to *SINMAP* (PACK et al 1998) or XIE et al. (2004b).

6.5.2 Improvement of r.avalanche

One particular focus shall be put on the extension of *r.avalanche* to a full-capability model for simulating debris flow runout. This is of high priority for risk management since at present, no user-friendly Open Source software is available for performing this task. Empirical-statistical or semi-empirical models (like those implemented in *r.debrisflow*) do exist, but they are difficult to use for the purpose of hazard prediction since they do not fully incorporate the physical processes behind the flow and have to be calibrated. In contrast, models like *SAMOS* (developed for snow avalanches, but also available for debris flows; SAMPL & ZWINGER 2004) or *DAN* (HUNGR 1995), are expensive or difficult to use and therefore not widely applied. A GIS-based approach (as extension to a proprietary software product) has been developed by CHAU & LO (2004), based on the TAKAHASHI (1992) model. However, this model does not fully include particle entrainment.

The current version of *r.avalanche* constitutes a first try to implement a fully deterministic model for the motion of granular flows into Open Source GIS. Therefore, it has been kept relatively simple and shows some limitations summarized in Section 6.2. Prospected improvements are:

(1) to select and adapt a sound method for modelling rapid granular flows over arbitrary topography, in order to overcome the severe limitation that the model can only be applied for relatively simple topographies. The method shall be extended by incorporating particle entrainment, which can lead to important implications for the runout behaviour of granular flows, and the role of pore fluid. The differential formulation of the model shall be derived analytically, using and extending the existing theories;

(2) to devise an appropriate numerical scheme (including shock capturing) for solving the equations derived in (1). Numerical solutions of the analytical model for arbitrary topography will be elaborated, using the BOUCHUT & WESTDICKENBERG (2004) approach, and implemented into *GRASS GIS*, analogous to the present version of *r.avalanche*;

(3) to evaluate the quality of the developed approach by comparing it to existing methods and models (*DAN*, *SAMOS*) and to validate the results with data from past snow avalanches and debris flows.

The fact that the bed friction angle δ has to be calibrated separately for each study area is not acceptable if the tool should be used for class A-predictions. Therefore it has to be looked for generally valid bed friction angles for various types of channels and slopes.

An additional improvement would be to find a more efficient way of data management during the computation in order to decrease computing time and to facilitate simulations at a higher spatial resolution.

6.6 Conclusions

The model frameworks *r.debrisflow* and *r.avalanche*, based on the Open Source GIS software *GRASS*, were created for the simulation of triggering, mobilization, and runout of debris flows. The application of the models to some selected study areas along the Trans-Andean road corridor from Mendoza (Argentina) to central Chile showed the potential of the two models, but also their limitations:

r.debrisflow was applied to all of the study areas: in general, the model output corresponded well to reports and field observations, but it was not possible to model the response to specific smaller rainfall events or to establish rainfall thresholds for the occurrence of debris flows. The simulation results were very sensitive to changes in the soil parameters. The sediment transport model and the runout model required calibration with reference data. It can therefore be concluded that *r.debrisflow* is a suitable tool for modelling worst case debris flow scenarios, but that more work is required to improve its predictive force.

r.avalanche, designed for simulating debris flow runout, requires less data, but is mathematically more sophisticated. The version and the results presented here shall be considered as a first step towards an Open Source GIS-based, fully deterministic debris flow runout model. It yielded good results for debris flows over simple topographies. A solution for arbitrary topography as well as some more extensions are required for making the model fully usable.

References

ABELE, G. 1984: Derrumbes de montaña y morrenas en los Andes chilenos.. Revista de Geografía Norte Grande 11: 17-30. In Spanish.

ABRAHAMS, A.D., LI, G., KRISHNAN, C. & ATKINSON, J.F. 2001: A sediment transport equation for interrill overland flow on rough surfaces. *Earth Surface Processes and Landforms* 26: 1443-1459.

ADAMS, J. 1995: Risk. Routledge, London. 228 pp.

AHRENDT, A. & ZUQUETTE, L.V. 2003: Triggering factors of landslides in Campos do Jordão city, Brazil. *Bulletin of Engineering Geology and the Environment* 62: 231-244.

AL-HOMOUD, A.S. & MASANAT, Y. 1998: A classification system for the assessment of slope stability of terrains along highway routes in Jordan. *Environmental Geology* 34: 59-69.

AL-HOUMOUD, A.S. & AL-MASRI, G.A. 1999: CSEES: An expert system for analysis and design of cut slopes and embankments. *Environmental Geology* 39: 75-89.

ANDRONOPOULOS, B. 1982: The geological structure and the tectonic evolution as factors of instability in the Pindos zone area (Greece). *Rock Mechanics and Rock Engineering* 15: 41-54.

ARCEMENT, G.J. & SCHNEIDER, V.R. 2000: Guide for Selecting Manning's Roughness Coefficients for Natural Channels and Flood Plains. *USGS Water-supply Paper* 2339. 67 pp.

ATKINSON, P., JISKOOT, H., MASSARI, R. & MURRAY, T. 1998: Generalized linear modelling in geomorphology. *Earth Surface Processes and Landforms* 23: 1185-1195.

AYALEW, L. 1999: The effect of seasonal rainfall on landslides in the highlands of Ethiopia. *Bulletin of Engineering Geology and the Environment* 58: 9-19.

AYALEW, L., YAMAGISHI, H. & UGAWA, N. 2004: Landslide susceptibility mapping using GIS-based weighted linear combination, the case in Tsugwa area of Agano River, Niigata Prefecture, Japan. *Landslides* 1: 73-81.

BAEZA, C. & COROMINAS, J. 2001: Assessment of shallow landslide susceptibility by means of multivariate statistical techniques. *Earth Surface Processes and Landforms* 26: 1251-1263.

BAGNOLD, R.A. 1980: An empirical correlation of bedload transport rates in flumes and natural rivers. *Proceedings of the Royal Society of London, Series A, Containing Papers of a Mathematical and Physical Character* 372: 453-473.

BAKER, R. 1980: Determination of the critical slip surface in slope stability computations. *International Journal for Numerical and Analytical Methods in Geomechanics* 4: 333-359.

BATHURST, J. 2002: DAMOCLES. Debrisfall Assessment in Mountain Catchments for Local End-Users. Detailed Report of Contractor for Fifth Progress Meeting. University of Newcastle upon Tyne, UK. 22 pp.

BELL, F.G. & MAUD, R.R. 2000: Landslides associated with colluvial soils overlying the Natal Group in the greater Durban area of Natal, South Africa. *Environmental Geology* 39: 1029-1038.

BISTACCHI, B., DAL PIAZ, G.V., MARTINOTTI, G., MASSIRONI, M., MONOPOLI, B. & SCHIAVO, A. 2000: Structural setting and large landslides in upper Isarco Valley (Alto Adige) [abstract].

BOGAARD, D.A. & VAN ASCH, T.W.J. 2002: The role of the soil moisture balance in the unsaturated zone on movement and stability of the Beline landslide, France. *Earth Surface Processes and Landforms* 27: 1177-1188.

BORGA, M., DALLA FONTANA, G., DA ROS, D. & MARCHI, L. 1998: Shallow landslide hazard assessment using a physically based model and digital elevation data. *Environmental Geology* 35: 81-88.

BORGA, M., DALLA FONTANA, G., GREGORETTI, C. & MARCHI, L. 2002: Assessment of shallow landsliding by using a physically based model of hillslope stability. *Hydrological Processes* 16: 2833-2851.

BOUCHUT, F. & WESTDICKENBERG, M. 2004: Gravity driven shallow water models for arbitrary

topography. *Communications in Mathematical Sciences* 2: 359-389.

BRARDINONI, F. & CHURCH, M. 2004: Representing the Landslide Magnitude-Frequency Relation: Capilano River Basin, British Columbia. *Earth Surface Processes and Landforms* 29: 115-124.

BRAUD, I., VICH, A.I.J., ZULUAGA, J., FORNERO, L. & PEDRANI, A. 2001: Vegetation influence on runoff and sediment yield in the Andes region: Observation and modelling. *Journal of Hydrology* 254: 124-144.

BRECKLE, S.-W. 2002: Walter's Vegetation of the Earth. Fourth edition. Springer, Berlin, Heidelberg, New York. 547 pp.

BRIMICOMBE, A.J. & Tsui, P.H.Y. 2000: A variable resolution, geocomputational approach to the analysis of point patterns. *Hydrological Processes* 14: 2143-2155.

BROOKS, S.M., CROZIER, M.J., GLADE, T.W. & ANDERSON, M.G. 2004: Towards Establishing Climatic Thresholds for Slope Instability: Use of a Physically-based Combined Soil Hydrology-slope Stability Model. *Pure and Applied Geophysics* 161: 881-905.

BUMA, J. & DEHN, M. 1998: A method for predicting the impact of climate change on slope stability. *Environmental Geology* 35: 190-196.

BUMA, J. 2000: Finding the most suitable slope stability model for the assessment of the impact of Climate Change on a landslide in Southeast France. *Earth Surface Processes and Landforms* 25: 565-582.

BURTON, A. & BATHURST, J.C. 1998: Physically based modelling of shallow landslide sediment yield at a catchment scale. *Environmental Geology* 35: 89-99.

BURTON, A., ARKELL, T.J. & BATHURST, J.C. 1998: Field variability of landslide model parameters. *Environmental Geology* 35: 100-114.

CARDINALI, M., ARDIZZONE, F., GALLI, M., GUZZETTI, F. & REICHENBACH, P. w.j: Landslides triggered by rapid snow melting: The December 1996-January 1997 event in Central Italy [abstract].

CARRARA, A. 1983: Multivariate models for landslide hazard evaluation. *Mathematical Geology* 15: 403-426.

CARRARA, A., GUZZETTI, F., CARDINALI, M. & REICHENBACH, P. 1999: Use of GIS Technology in the Prediction and Monitoring of Landslide Hazard. *Natural Hazards* 20: 117-135.

CARSEL, R. F. & PARRISH, R. S. 1988: Developing joint probability distributions of soil water retention characteristics. *Water Resources Research* 24: 755-769.

CASADEI, M., DIETRICH, W.E. & MILLER, N.L. 2003: Testing a model for predicting the timing and location of shallow landslide initiation in soil-mantled landscapes. *Earth Surface Processes and Landforms* 28: 925-950.

CAVIEDES, C. 1972: Geomorfología del Cuartenario del valle del Aconcagua, Chile Central. Freiburger Geographische Hefte 11, 153 pp. In Spanish.

ÇEVIK, E. & TOPAL, T. 2003: GIS-based landslide susceptibility mapping for a problematic segment of the natural gas pipeline, Hendek (Turkey). *Environmental Geology* 44: 949-962.

CHAU, K.T. & LO, K.H. 2004: Hazard assessment of debris flows for Leung King Estate of Hong Kong by incorporating GIS with numerical simulations. *Natural Hazards and Earth System Sciences* 4: 103-116.

CHEN, L. & YOUNG, M.H. 2006: Green-Ampt infiltration model for sloping surfaces. *Water Resources Research* 42. 9 pp.

CHIEN-YUAN, C., TIEN-CHIEN, C., FAN-CHIEH, Y., WEN-HUI, Y. & CHUN-CHIEH, T. 2005: Rainfall duration and debris-flow initiated studies for real-time monitoring. *Environmental Geology* 47: 715-724.

CHIGIRA, M., DUAN, F., YAGI, H. & FURUYA, T. 2004: Using an airborne laser scanner for the identification of shallow landslides and susceptibility assessment in an area of ignimbrite overlain by permeable pyroclastics. *Landslides* 1: 203-209.

CIAT (INTERNATIONAL CENTRE FOR TROPICAL AGRICULTURE) 2004: Void-filled seamless SRTM data V1, available from the CGIAR-CSI SRTM 90 m Database. http://srtm.csi.cgiar.org

CLAESSENS, L., HEUVELINK, G.B.M., SCHOORL, J.M. & VELDKAMP, A. 2005: DEM resolution effects on shallow landslide hazard and soil redistribution modelling. *Earth Surface Processes and Landforms* 30: 461-477.

COLLISON, A.J.C. & ANDERSON, M.G. 1996: Using a combined slope hydrology/stability Model to identify suitable conditions for landslide prevention by vegetation in the humid tropics. *Earth Surface Processes and Landforms* 21: 737–747.

COROMINAS, J. & SANTACANA, N. 2003: Stability analysis of the Vallcebre translational slide (Eastern Pyrenees, Spain) by means of a GIS. *Natural Hazards* 30: 473-485.

COROMINAS, J., COPONS, R., VILAPLANA, J.M., ALTAMIR, J. & AMIGÓ, J. 2003: Integrated Land-

slide Susceptibility Analysis and Hazard Assessment in the Principality of Andorra. *Natural Hazards* 30: 421-435.

CORTE, A.E. & ESPIZÚA, L.E. 1981: Inventario de glaciares de la cuenca del río Mendoza. CONICET-IANIGLA, Mendoza. 64 pp + 20 maps. In Spanish.

COSTA, J.E. 1984: Physical geomorphology of debris flows. In: COSTA, J.E. & FLEISCHER, P.J. (eds.): Developments and applications of geomorphology, 269-317.

CROZIER, M.J. 1999: Prediction of rainfall-triggered landslides: a test of the antecedent water status model. *Earth Surface Processes and Landforms* 24: 825-833.

DAI, F.C., LEE, C.F., LI, J. & XU. Z.W. 2001: Assessment of landslide susceptibility on the natural terrain of Lantau Island, Hong Kong. *Environmental Geology* 40: 381-391.

DAI, F.C. & LEE, C.F. 2003: A spatiotemporal probabilistic modelling of storm-induced shallow landsliding using aerial photographs and logistic regression. *Earth Surface Processes and Landforms* 28: 527-545.

DAI, F.C., LEE, C.F., THAM, L.G., NG, K.C. & SHUM, W.L. 2004: Logistic regression modelling of storm-induced shallow landsliding in time and space on natural terrain of Lantau Island, Hong Kong. *Bulletin of Engineering Geology and the Environment* 63: 315-327.

DALLMAN, P.R. 1998: Plant life in the world's mediterranean climates: California, Chile, South Africa, Australia, and the Mediterranean Basin. University of California Press, Berkeley, Los Angeles. 257 pp.

D'AMBROSIO, D., DI GREGORIO, S. & IOVINE, G. 2003: Simulating debris flows through a hexagonal cellular automata model: SCIDDICA $S_{3\text{-hex}}$. *Natural Hazards and Earth System Sciences* 3: 545-559.

DAPPORTO, S., RINALDI, M., CASAGLI, N. & VANNOCCI, P. 2003: Mechanisms of riverbank failure along the Arno River, Central Italy. *Earth Surface Processes and Landforms* 28: 1303-1323.

DEL CAMPO TELLO, P., SUCKEL, H. & JORGE RAZETO, M. (eds.) 2001: Patrimonio Natural del Aconcagua. Ediciones del Centro ALMENDRAL. Collección Cuadernos Patrimoniales. 99 pp. In Spanish.

DHAKAL, A.S. & SIDLE, R.C. 2004: Distributed simulations of landslides for different rainfall conditions. *Hydrological Processes* 18: 757-776.

DIAZ, H.F. & MARKGRAF, V. 2000: El Niño and the Southern Oscillation. Multiscale Variability and Global and Regional Impacts. Cambridge University Press. 496 pp.

DUMAN, P.Y., CAN, T., GOKCEOGLU, C. & NEFESLIOGLU, H.A. 2005: Landslide susceptibility mapping of Cekmece area (Istanbul, Turkey) by conditional probability. *Hydrology and Earth System Sciences Discussions* 2: 155-208.

DUTTON, A.L., LOAGUE, K. & WEMPLE, B.C. 2005: Simulated effect of a forest road on near-surface hydrologic response and slope stability. *Earth Surface Processes and Landforms* 30: 325-338.

ERCANOGLU, M. & GOKCEOGLU, C. 2002: Assessment of landslide susceptibility for a landslide-prone area (north of Yenice, NW Turkey) by fuzzy approach. *Environmental Geology* 41: 720-730.

ERICKSON, T. & STEFAN, H.G. 2007: Groundwater Recharge from a Changing Landscape. Project Report No. 490, St. Anthony Falls Laboratory, University of Minnesota.

ESPEJO, J. 1996: Unpublished reports about mass movements interfering with the international road from Mendoza to Central Chile. In Spanish.

ESPIZÚA, L.E. & BENGOCHEA, J.D. 1991: A Pleistocene landslide in the Río Mendoza Valley [abstract]. In: LIU TUNGSHENG (ed.): Highlights of Quaternary geology in China. International Union for Quaternary Research, XIII International Congress, Beijing, Hefei, People's Republic of China: Press of the University of Science and Technology of China.

ESPIZUA, L.E. & BENGOCHEA, J.D. 2002: Landslide Hazard and Risk Zonation Mapping in the Río Grande Basin, Central Andes of Mendoza, Argentina. *Mountain Research and Development* 22: 177-185.

ESPIZÚA, L.E. 1993: Quaternary glaciations in the Rio Mendoza Valley, Argentine Andes. *Quaternary Research* 40: 150-162.

ESPIZÚA, L.E., BENGOCHEA, J.D. & AGUADO, C. 1993: Mapa de riesgo de remoción en masa en el valle del Río Mendoza. XII Congreso Geológico Argentino y II Congreso de Exploración de Hidrocarburos. Actas T° VI: 323-332. In Spanish.

FABBRI, A.G., CHUNG, C.-J. F., CENDRERO, A. & REMONDO, J. 2003: Is Prediction of Future Landslides Possible with a GIS? *Natural Hazards* 30: 487-499.

FAUQUÉ, L., ROSAS, M. & BAUMANN, V. 2004: Natural Hazards in the Puente del Inca Region of Mendoza, Argentina. Multinational Andean Project: Geoscience for Andean Communities 4(4). www.pma-map.com

FERNÁNDEZ, T., IRIGARAY, C., EL HAMDOUNI, R. & CHACÓN, J. 2003: Methodology for Landslide Susceptibility Mapping by Means of a GIS. Application to the Contraviesa Area (Granada, Spain). *Natural Hazards* 30: 297-308.

FERNÁNDEZ-GARCÍA, F. & MIKKAN, R. 2003: Evaluación Global del Medio Geográfico, como base de un ordeniamento racional en el principal corredor Bioceánico del Plan Mercosur: Valles de Río Mendoza (Argentina) y Aconcagua (Chile). Editorial de la Facultad de Filosofía y Letras de la Universidad Nacional de Cuyo, Mendoza. 104 pp. In Spanish.

FLORIS, M., MARI, M., ROMEO, R.W. & GORI, U. 2004: Modelling of Landslide-Triggering Factors - A Case Study in the Northern Apennines, Italy. *Lecture Notes in Earth Sciences* 104: 745-753.

FUKUOKA, H., WANG, G., SASSA, K., WANG, F. & MATSUMOTO, T. 2004: Earthquake-induced rapid long-travelling flow phenomenon: May 2003 Tsukidate landslide in Japan. *Landslides* 1: 151-155.

GAMMA, P. 2000: *dfwalk* – Ein Murgang-Simulationsprogramm zur Gefahrenzonierung. *Geographica Bernensia* G66, 144 pp. In German.

GIANNECHINI, R. 2005: Rainfall triggering soil slips in the southern Apuan Alps (Tuscany, Italy): *Advances in Geosciences* 2: 21-24.

GLADE, T. 1998: Establishing the frequency and magnitude of landslide-triggering rainstorm events in New Zealand. *Environmental Geology* 35: 160-174.

GLADE, T., CROZIER, M. & SMITH, P. 2000: Applying Probability Determination to Refine Landslide-triggering Rainfall Thresholds Using an Empirical "Antecedent Daily Rainfall Model". *Pure and Applied Geophysics* 157: 1059-1079.

GORSEVSKI, P.V., GESSLER, P.E. & JANKOWSKI, P. 2003: Integrating a fuzzy k-means classification and a Bayesian approach for spatial prediction of landslide hazard. *Journal of Geographical Systems* 5: 223-251.

GOVERS, G. 1990. Empirical relationships for transport capacity of overland flow. *IAHS Publication* 189: 45-63.

GREEN, W.H. & AMPT, G.A. 1911: Studies on soil physics. *Journal of Agricultural Sciences* 4: 1-24.

GRIFFITHS, D.V. & LU, N. 2005: Unsaturated slope stability analysis with steady infiltration or evaporation using elasto-plastic finite elements. International *Journal for Numerical and Analytical Methods in Geomechanics* 29: 249-267.

GUZZETTI, F., REICHENBACH, P. & GHIGI, S. 2004: Rockfall Hazard and Risk Assessment Along a Transportation Corridor in the Nera Valley, Central Italy. *Environmental Management* 34: 191-208.

GYSSELS, G. & POESEN, J. 2003: The importance of plant root growth characteristics in controlling concentrated flow erosion rates. *Earth Surface Processes and Landforms* 28: 371-384.

HAIRSINE, P.B. & ROSE, C.W. 1992: Modeling water erosion due to overland flow using physical principles, 2. Rill Flow. *Water Resources Research* 28: 245-250.

HANTZ, D., VENGEON, J.M. & DUSSAUGE-PEISSER, C. 2003: An historical, geomechanic and probabilistic approach to rockfall-hazard assessment. *Natural Hazards and Earth System Sciences* 3: 693-701.

HARBITZ, C.B. 1998: Snow avalanche modelling, Mapping and Warning in Europe (SAME), Report of the Fourth European Framework Programme: Environment and Climate, NGI, Norway.

HAUSER, A. 2000a: Remociones en masa en Chile (versión actualizada). Servicio Nacional de Geología y Minería, Subdirección Nacional de Geología, Boletín No. 59, Santiago de Chile. 89 pp. In Spanish.

HAUSER, A. 2000b: Flujos detríticos en segmento del Camino Internacional a Argentina, sector Juncal – Paso Los Libertadores: Causas, efectos, medidas de control. Report of the Servicio Nacional de Geología y Minería, Subdirección Nacional de Geología, Santiago de Chile. 14 pp. In Spanish.

HAUSER, A. 2005: Evaluación de vulnerabilidad y propuesta de procedimientos para el control de flujos detríticos o aluvionales en segmento Juncal-Portillo, del Camino Internacional a la República Argentina. Report of the Servicio Nacional de Geología y Minería, Subdirección Nacional de Geología, Santiago de Chile. 12 pp. In Spanish.

HENNRICH, K. & CROZIER, M.J. 2004: A hillslope hydrology approach for catchment-scale slope stability analysis. *Earth Surface Processes and Landforms* 29: 599-610.

HERMANNS, R. 2004: Field work on Bioceanic Corridor, Mendoza Province, Argentina. Multinational Andean Project: Geoscience for Andean Communities 4(3). www.pma-map.com

HESSEL, R. & JETTEN, V. 2007: Suitability of transport equations in modelling soil erosion for a small Loess Plateau catchment. *Engineering Geology* 91: 56-71.

HONG, Y., HIURA, H., SHINO, K., SASSA, K. & FUKUOKA, H. 2005: Quantitative assessment on the influence of heavy rainfall on the crystalline schist

landslide by monitoring system-case study on Zentoku landslide, Japan. *Landslides* 2: 31-41.

HUGHES, B.D. 1995: Random walks and random environments. Oxford University Press. 654 pp.

HUNGR, O. 1995: A model for the runout analysis of rapid flow slides, debris flows, and avalanches. *Canadian Geotechnical Journal* 32: 610–623.

IBSEN, M.L. & CASAGLI, N. 2004: Rainfall patterns and related landslide incidence in the Porretta-Vergato-Region, Italy. *Landslides* 1: 143-150.

IIDA, T. 2004: Theoretical research on the relationship between return period of rainfall and shallow landslides. *Hydrological Processes* 18: 739-756.

IIRITANO, G., VERSACE, P. & SIRANGELO, B. 1998: Real-time estimation of hazard for landslides triggered by rainfall. *Environmental Geology* 3: 175-183.

IRIGARAY, C., LAMAS, F., El HAMDOUNI, R., FERNÁNDEZ, T. & CHACÓN, J. 2000: The Importance of the Precipitation and the Susceptibility of the Slopes for the Triggering of Landslides Along the Road. *Natural Hazards* 21: 65-81.

IVERSON, R. M. 1997: The physics of debris flows. *Reviews of Geophysics* 35: 245-296.

JUANG, C.H., LEE, D.H. & SHEU, C. 1992: Mapping slope failure potential using fuzzy sets. *ASCE Journal of Geotechnical and Geoenvironmental Engineering* 118: 312–325.

KEEVER, D.K. 2002: Investigating landslides caused by earthquakes - a historical review. *Surveys in Geophysics* 23: 473-510.

KNAPEN, A., POESEN, J., GOVERS, C., GYSSELS, G. & NACHTERGAELE, J. 2007: Resistance of soils to concentrated flow erosion: A review. *Earth-Science Reviews* 80: 75-109.

KO KO, C., FLENTJE, P. & CHOWDHURY, R. 2004: Interpretation of probability of landsliding triggered by rainfall. *Landslides* 1: 263-275.

LAN, H.X., LEE, C.F., ZHOU, C.H. & MARTIN, C.D. 2005: Dynamic characteristics analysis of shallow landslides in response to rainfall event using GIS. *Environmental Geology* 47: 254-267.

LAZZARI, M. & SALVANESCHI, P. 1999: Embedding a Geographic Information System in a Decision Support System for Landslide Hazard Monitoring. *Natural Hazards* 20: 185-195.

LEBOURG, D., FABRE, R., CLEMENT, B. & FRAPPA, M. 2003: High-mountain landslides in the Atlantic Pyrenees: their relationship with the geology and geomorphology. *Bulletin of Engineering Geology and the Environment* 62: 221-229.

LEE, S. & MIN, K. 2001: Statistical analysis of landslide susceptibility at Yongin, Korea. *Environmental Geology* 40: 1095-1113.

LEE, S., CHOI, J. & MIN, K. 2002: Landslide susceptibility analysis and verification using the Bayesian probability model. *Environmental Geology* 43: 120-131.

LEE, S., RYU, J.H., LEE, M.J. & WON, J.S. 2003a: Use of an artificial neural network for analysis of the susceptibility to landslides at Boun, Korea. *Environmental Geology* 44: 820-833.

LEE, S., RYU, J.H., MIN, K., WON, J.S. 2003b: Landslide susceptibility Mapping Using GIS and Artificial Neural Network. *Earth Surface Processes and Landforms* 28: 1361-1376.

LEE, S. 2004a: Application of Likelihood Ratio and Logistic Regression Models to Landslide Susceptibility Mapping Using GIS. *Environmental Management* 34: 223-232.

LEE, S. 2004b: Soil erosion assessment and its verification using the Universal Soil Loss Equation and Geographic Information System: a case study at Boun, Korea. *Environmental Geology* 45: 457-465.

LEE, S. & DAN, N.T. 2005: Probabilistic landslide susceptibility mapping in the Lai Chau province of Vietnam: focus on the relationship between tectonic fractures and landslides. *Environmental Geology* 48: 778-787.

LEE, S. & TALIB, J.A. 2005: Probabilistic landslide susceptibility and factor effect mapping. *Environmental Geology* 47: 982-990.

LEHMANN, A., DAVID, S. & STAHR, K. in press: TUSEC (Technique of Urban Soil Evaluation in City Regions). Eine Methode zur Bewertung natürlicher und anthropogen überformter Böden. *Hohenheimer Bodenkundliche Hefte*. In German.

LIU, X., WANG, S. & ZHANG, X. 1992: Influence of geologic factors on landslides in Zhaotong, Yunnan province, China. *Environmental Geology* 19: 17-20.

LOW, H.S. 1989: Effect of sediment density on bed-load transport. *Journal of Hydraulic Engineering* 115: 124-138.

MALAMUD, B.D., TURCOTTE, D.L., GUZZETTI, F. & REICHENBACH, P. 2004: Landslide inventories and their statistical properties. *Earth Surface Processes and Landforms* 29: 687-711.

MALKAWI, A.I.H. & TAQIEDDIN, S.A. 1996: Geotechnical study of landslides resulting from a highway construction in Jordan. *Natural Hazards* 13: 1-15.

MANNING, R. 1890: On the Flow of Water in Open Channels and Pipes. Institution of Civil Engineers of Ireland.

MAURER, T. 1997: Physikalisch begründete, zeitkontinuierliche Modellierung des Wassertransports in kleinen ländlichen Einzugsgebieten. Dissertation at the University of Karlsruhe, Germany. 252 pp. In German.

MCDOUGALL, S. & HUNGR, O. 2004: A Model for the Analysis of Rapid Landslide Motion across Three-Dimensional Terrain. *Canadian Geotechnical Journal* 41:1084-1097.

MCDOUGALL, S. & HUNGR, O. 2005: Dynamic modeling of entrainment in rapid landslides. *Canadian Geotechnical Journal* 42: 1437-1448.

MEIßL, G. 1998: Modellierung der Reichweite von Felsstürzen. *Innsbrucker Geographische Studien* 28, 249 pp. In German.

MIKKAN, R. 1997: Geomorfología y dinamica de vertientes del valle del río Mendoza entre las estaciones Guido y Uspallata, provincia de Mendoza - Rep. Argentina. *Revista de Estudios Regionales* (Centro Interdisciplinario de Estudios Regionales CEIDER) 17: 81-135.

MILLER, D.J. & SIAS, J. 1998: Deciphering large landslides: linking hydrological, groundwater and slope stability through GIS. *Hydrological Processes* 12: 923-941.

MONTGOMERY, D.R., SULLIVAN, K. & GREENBERG, H.M. 1998: Regional test of a model for shallow landsliding. *Hydrological Processes* 12: 943-955.

MOREIRAS, S.M. 2004a: Landslide incidence zonation in the Rio Mendoza Valley, Mendoza Province, Argentina. *Earth Surface Processes and Landforms* 29: 255-266.

MOREIRAS, S.M. 2004b: Landslide susceptibility zonation in the Rio Mendoza Valley, Argentina. *Geomorphology* 66: 345-357.

MOREIRAS, S.M. 2005: Climatic effect of ENSO associated with landslide occurrence in the Central Andes, Mendoza Province, Argentina. *Landslides* 2: 53-59.

MSILIMBA, G.G. & HOLMES, P.J. 2005: A Landslide Hazard Assessment and Vulnerability Appraisal Procedure: Vunguvungu/Banga Catchment, Northern Malawi. *Natural Hazards* 34: 199-216.

NAGARAJAN, R., ROY, A., VINOD-KUMAR, R., MUKHERJEE, A. & KHIRE, M.V. 2000: Landslide hazard susceptibility mapping based on terrain and climatic factors for tropical monsoon regions. *Bulletin of Engineering Geology and the Environment* 58: 275-287

NAGARAJAN, R. 2002: Rapid assessment procedure to demarcate areas susceptible to earthquake-induced ground failures for environment management - a case study from parts of northeast India. *Bulletin of Engineering Geology and the Environment* 61: 99-119..

NASA LANDSAT PROGRAM 2001: Landsat 7 scenes, USGS, Sioux Falls. Data source: Global Land Cover Facility. www.landcover.org

NEMČOK, A., PAŠEK, J. & RYBÁŘ, J. 1972: Classification of landslides and other mass movements. *Rock Mechanics and Rock Engineering* 4: 71-78.

NICHOL, J. & WONG, M.S. 2005: Detection and interpretation of landslides using satellite images. *Land Degradation and Development* 16: 243-255.

NOVÁK, V., PERFILIEVA, I. & MOČKOŘ, J. 1999: Mathematical principles of fuzzy logic. Kluwer Academic, Dordrecht. 336 pp.

O'BRIEN, J.S. 2003: FLO-2D Users' Manual Version 2003.06, July 2003. FLO-2D Software Inc., Nutrioso, Arizona, USA. 232 pp.

OHL, C. & BUSSMANN, R. 2004: Recolonization of natural landslides in tropical mountain forests of Southern Ecuador. *Feddes Repertorium* 115: 248-264.

ONDA, Y., TSUJIMURA, M. & TABUCHI, H. 2004: The role of subsurface waterflow paths on hillslope hydrological processes, landslides and landform development in steep mountains of Japan. *Hydrological Processes* 18: 637-650.

PACK, R.T., TARBOTON, D.G. & GOODWIN, C.N. 1998: The SINMAP Approach to Terrain Stability Mapping, Paper Submitted to 8th Congress of the International Association of Engineering Geology, Vancouver, British Columbia.

PARISE, M. & WASOWSKI, J. 1999: Landslide Activity Maps for Landslide Hazard Evaluation: Three Case Studies from Southern Italy. *Natural Hazards* 20: 159-183.

PARUELO, J.M., JOBBAGY, E.G. & SALA, O.E. 2001: Current distribution of ecosystem functional types in temperate South America. *Ecosystems* 4: 683-698.

PERLA, R., CHENG, T.T. & MCCLUNG, D.M. 1980: A Two-Parameter Model of Snow Avalanche Motion. *Journal of Glaciology* 26: 197-207.

PETLEY, D.N. & ALLISON, R.J. 1997: The mechanics of deep-seated landslides. *Earth Surface Processes and Landforms* 22: 747-758.

PISTOCCHI, A., LUZI, L. & NAPOLITANO, P. 2002: The use of predictive modeling techniques for optimal exploitation of spatial databases: a case study in landslide hazard mapping with expert

system-like methods. *Environmental Geology* 41: 765-775.

PRESS, F., SIEVER, R., GROTZINGER, J. & JORDAN, T. 2003: Understanding Earth. Fourth edition. W.H Freeman and Company, New York. 568 pp.

PRESTON, N.J. & CROZIER, M.J. 1999: Resistance to shallow landslide failure through root-derived cohesion in east coast hill country soils, North Island, New Zealand. *Earth Surface Processes and Landforms* 24, 665-675.

PUDASAINI, S.P. 2003: Dynamics of Flow Avalanches Over Curved and Twisted Channels. Theory, Numerics and Experimental Validation. Dissertation at the Technical University of Darmstadt, Germany. 200 pp.

PUDASAINI, S.P. & HUTTER, K. 2007: Avalanche Dynamics: Dynamics of rapid flows of dense granular avalanches. Springer, Berlin Heidelberg New York. 626 pp.

QIN, S.Q., JIAO, J.J. & WANG, S.J. 2001: The predictable time scale of landslides. *Bulletin of Engineering Geology and the Environment* 59: 307-312.

RAHARDJO, H., LI, X.W., TOLL, D.G., LEONG, E.C. 2001: The effect of antecedent rainfall on slope stability. *Geotechnical and Geological Engineering* 19: 371-399.

RAMOS, V.A. 1996: Geología de la Región del Aconcagua. Provincias de San Juan y Mendoza, República Argentina. *Anales de la Dirección Nacional del Servicio Geológico, Subsecretaría de Minería de la Nación* 24: 510 pp. + 2 maps. In Spanish.

RAWLS, W.J., BRAKENSIEK, D. L. & MILLER, N. 1983: Green-Ampt infiltration parameters from soil data. *Journal of Hydraulic Engineering* 109: 62-70.

REICHENBACH, P., CARDINALI, M., DE VITA, P. & GUZZETTI, F. 1998: Regional hydrological thresholds for landslides and floods in the Tiber River Basin (central Italy). *Environmental Geology* 35: 146-159.

REMONDO, J., GONZÁLEZ, A., DÍAZ DE TERÁN, J.R., CENDRERO, A., FABBRI, A. & CHUNG, C.-J. F. 2003: Validation of Landslide Susceptibility Maps: Examples and Applications from a Case Study in Northern Spain. *Natural Hazards* 30: 437-449.

RICKENMANN, D. 1990: Bedload transport capacity of slurry flows at steep slopes. *Mitteilungen der Versuchsanstalt für Wasserbau, Hydrologie und Glaziologie, ETH Zürich* 103: 249 pp.

RICKENMANN, D. 1999: Empirical Relationships for Debris Flows. *Natural Hazards* 19: 47-77.

ROESSNER, S., WETZEL, H.U., KAUFMANN, H. & SARNAGOEV, A. 2005: Potential of Satellite Remote Sensing and GIS for Landslide Hazard Assessment in Southern Kyrgyzstan (Central Asia). *Natural Hazards* 35: 395-416.

SAHA, A.K., GUPTA, R.P., SARKAR, I., ARORA, M.K. & CSAPLOVICS, E. 2005: An approach for GIS-based landslide susceptibility zonation - with a case study in the Himalayas. *Landslides* 2: 61-69.

SAMPL, P. & ZWINGER, T. 2004: Avalanche Simulation with *SAMOS*. *Annals of Glaciology* 38: 393-398.

SANTACANA, N., BAEZA, B., COROMINAS, J., DE PAZ, A. & MARTURIÁ, J. 2003: A GIS-based Multivariate Statistical Analysis for Shallow Landslide Susceptibility Mapping in La Pobla de Lillet Area (Eastern Pyrenees, Spain). *Natural Hazards* 30: 281-295.

SATTLER, K., KEILER, M., ZISCHG, A. & SCHROTT, L. 2007: Development of Debris Flow Activity influenced by Climate Change in Periglacial High Mountain Areas: Schnalstal, Italy. In: KELLERER-PIRKLBAUER, A., KEILER, M., EMBLETON-HAMANN, C. & STÖTTER, J. (eds.): Proceedings of the Conference 'Geomorphology for the Future', Obergurgl: 169-176.

SAVAGE, S.B. & HUTTER, K. 1989: The motion of a finite mass of granular material down a rough incline. *Journal of Fluid Mechanics* 199: 177–215.

SCHEIDEGGER, A.E. 1973: On the prediction of the reach and velocity of catastrophic landslides. *Rock Mechanics and Rock Engineering* 5: 231-236.

SCHMIDT, K.M., ROERING, J.J., STOCK, J.D., DIETRICH, W.E., MONTGOMERY, D.R. & SCHAUB, T. 2001: The variability of root cohesion as an influence on shallow landslide susceptibility in the Oregon Coast Range. *Canadian Geotechnical Journal* 38: 995-1024.

SCHNEIDER-MUNTAU, B. & FELLIN, W. 2005: Fallstudie Mure Nals – Untersuchung des Muranbruchs mittels Standsicherheitsberechnung . *Österreichische Ingenieur- und Architektenzeitschrift* 150: 42-45. In German.

SCHOKLITSCH, A. 1962: Handbuch des Wasserbaues. Third edition. Springer, Vienna. 722 pp. In German.

SCHÖNWIESE, C.-D. 1994: Klimatologie. Ulmer, Stuttgart. 436 pp. In German.

SCHOORL, J.M., SONNEVELD, M.P.W. & VELDKAMP, A. 2000: Three-dimensional landscape process modelling: the effect of DEM resolution. *Earth Surface Processes and Landforms* 25: 1025-1034.

SEKIGUCHI, T. & SATO, H.P. 2004: Mapping of micro topography using airborne laser scanning. *Landslides* 1: 195-202.

SENDIR, H. & YILMAZ, I. 2002: Structural, geomorphological and geomechanical aspects of the Koyulhisar landslides in the North Anatolian Fault Zone (Sivas, Turkey). *Environmental Geology* 42: 52-60.

SIRANGELO, B. & VERSACE, P. 1996: A real time forecasting model for landslides triggered by rainfall. *Meccanica* 31: 73-85.

SOUSA, J. & VOIGHT, P. 1995: Multiple-pulsed debris avalanche emplacement at Mount St. Helens in 1980: evidence from numerical continuum flow simulations. *Journal of Volcanology and Geothermal Research* 66: 227-250.

STRICKLER, A. 1923: Beiträge zur Frage der Geschwindigkeitsformel und der Rauhigkeitszahl für Ströme, Kanäle und geschlossene Leitungen. *Mitteilungen des Eidgenössischen Amtes für Wasserwirtschaft*, Bern. In German.

SUKHIJA, B.S., REDDY, D.V., NAGABHUSHANAM, P. & HUSSAIN, S. 2003: Recharge processes: piston flow vs preferential flow in semi-arid aquifers of India. *Hydrogeology Journal* 11: 387-395.

SÜZEN, M.L. & DOYURAN, V. 2004: A comparison of the GIS based landslide susceptibility assessment methods: multivariate versus bivariate. *Environmental Geology* 45: 665-679.

TAKAHASHI, T., NAKAGAWA, H., HARADA, T. & YAMASHIKI, Y. 1992: Routing debris flows with particle segregation, *Journal of Hydraulic Research* 118: 1490-1507.

TEOMAN, M.B., TOPAL, T. & IŞIK, N.S. 2004: Assessment of slope stability in Ankara clay: a case study along E90 highway. *Environmental Geology* 45: 963-977.

TERLIEN, M.T.J. 1998: The determination of statistical and deterministic hydrological landslide-triggering thresholds. *Environmental Geology* 35: 124-130.

THIEBES, B., BELL, R. & GLADE, T. 2007: Deterministic Landslide Analysis using *SINMAP*. A Case Study in the Swabian Alb, Germany. In: KELLERER-PIRKLBAUER, A., KEILER, M., EMBLETON-HAMANN, C. & STÖTTER, J. (eds.): Proceedings of the Conference 'Geomorphology for the Future', Obergurgl: 177-184. In German.

THYWISSEN, K. 2006: Components of risk. A comparative glossary. In: SOURCE, 'Studies of the University: Research, Counsel, Education'. Publication Series of UNU-EHS 2/2006. Bonn.

TROMBOTTO, D. 1991: Untersuchungen zum periglazialen Formenschatz und zu periglazialen Sedimenten in der "Lagunita del Plata", Mendoza, Argentinien. *Heidelberger Geographische Arbeiten* 90. 151 pp. In German.

TROPEANO, D. & TURCONI, L. 2004: Using Historical Documents for Landslide, Debris Flow and Stream Flood Prevention. Applications in Northern Italy. *Natural Hazards* 31: 663-679.

UCHIDA, T. 2004: Clarifying the role of pipe flow on shallow landslide initiation. *Hydrological Processes* 18: 375-378.

UROMEIHY, A. & MAHDAVIFAR, M.R. 2000: Landslide hazard zonation of the Khorshrostam area, Iran. *Bulletin of Engineering Geology and the Environment* 58: 207-213.

VAN ASCH, TH.W.J. & BUMA, J.T. 1997: Modelling groundwater fluctuations and the frequency of movement of a landslide in the Terres Noires region of Barcelonnette (France). *Earth Surface Processes and Landforms* 22: 131-141.

VAN WESTEN, C.J. & TERLIEN, M.J.T. 1996: An approach towards deterministic landslide hazard analysis in GIS. A case study from Manizales (Colombia). *Earth Surface Processes and Landforms* 21: 853-868.

VAN WESTEN, C.J., SEIJMONSBERGEN, A.C. & MANTOVANI, F. 1999: Comparing Landslide Hazard Maps. *Natural Hazards* 20: 137-158.

VAN WESTEN, C.J. 2000: The Modelling of landslide hazards using GIS. *Surveys in Geophysics* 21: 241-255.

VAN WESTEN, C.J., RENGERS, N. & SOETERS, R. 2003: Use of Geomorphological Information in Indirect Landslide Susceptibility Assessment. *Natural Hazards* 30: 399-419.

VANDRE, B.C. 1985: Rudd Creek debris flow. In: BOWLES, D.S. (ed.): Delineation of landslide, flashflood, and debris flow hazards in Utah. Utah Water Research Laboratory, Utah State University, Logan, Utah, 117-131.

VARNES, D.J. 1978: Slope movement types and processes: In: Landslide Analysis and Control: In SCHUSTER R. & KRIZAK, L. (eds.): Transportation Research Board Special Report 176, National Academy of Sciences, Washington, D.C., 11-33.

VIEIRA, B.C. & FERNANDES, N.F. 2004: Landslides in Rio de Janeiro: The role played by variations in soil hydraulic conductivity. *Hydrological Processes* 18: 791-805.

VILÍMEK, V., LUYO ZAPATA, M., KLIMEŠ, J., PATZELT, Z. & SANTILLÁN, N. 2005: Influence of glacial retreat on natural hazards of the Palcacocha Lake area, Peru. *Landslides* 2: 107-115.

VOELLMY, A. 1955: Über die Zerstörungskraft von Lawinen. *Schweizerische Bauzeitung* 73, 159–162, 212–217, 246–249, 280–285. In German.

WACHAL, D.J. & HUDAK, P.F. 2000: Mapping landslide susceptibility in Travis County, Texas, USA. *GeoJournal* 51: 245-253.

WALTER, H. & BRECKLE, S.W. 1984: Ökologie der Erde Band 2: Spezielle Ökologie der Tropischen und Subtropischen Zonen. 461 pp. In German.

WANG, G., SUEMINE, A., FURUYA, G., KAIBORI, M. & SASSA, K. 2005: Rainstorm-induced landslides at Kisawa village, Tokushima Prefecture, Japan, August 2004. *Landslides* 2: 235-242.

WANG, H.B & SASSA, K. 2005: Comparative evaluation of landslides susceptibility in Minamata area, Japan. *Environmental Geology* 47: 956-966.

WANG, Y.; HUTTER, K.; PUDASAINI, S.P. 2004: The Savage-Hutter theory: A system of partial differential equations for avalanche flows of snow, debris, and mud. *ZAMM - Journal of Applied Mathematics and Mechanics / Zeitschrift für Angewandte Mathematik und Mechanik* 84:507-527

WASOWSKI, J. 1998: Understanding rainfall-landslide relationships in man-modified environments: a case-history from Caramanico Terme, Italy. *Environmental Geology* 35: 197-209.

WEIDINGER, J.T. 2007: Petrologic and Structural Control on the Geomorphology of Large Rockslides in the Himalayas. In: KELLERER-PIRKLBAUER, A., KEILER, M., EMBLETON-HAMANN, C. & STÖTTER, J. (eds.): Proceedings of the Conference 'Geomorphology for the Future', Obergurgl: 185-192.

WICHMANN, V. 2006: Modellierung geomorphologischer Prozesse in einem alpinen Einzugsgebiet. Abgrenzung und Klassifizierung der Wirkungsräume von Sturzprozessen und Muren mit einem GIS. *Eichstätter Geographische Arbeiten* 15. 231 pp. In German.

WICHMANN, V., RUTZINGER, M. & VETTER, M. in press: Digital terrain model generation from airborne laser scanning point data and the effect of grid-cell size on the simulation results of a debris flow model. In: Hamburger Beiträge zur Physischen Geographie und Landschaftsökologie.

WILKINSON, P.L., BROOKS, S.M. & ANDERSON, M.G. 2000: Design and application of an automated non-circular slip surface search within a combined hydrology and stability model (CHASM). *Hydrological Processes* 14: 2003-2017.

WILKINSON, P.L., ANDERSON, M.G. & LLOYD, D.M. 2002: An integrated hydrological model for rain-induced landslide prediction. *Earth Surface Processes and Landforms* 27: 1285-1297.

WISNER, B., BLAIKIE, P., CANNON, T. & DAVIS, I. 2004: At Risk: Natural hazards, people's vulnerability and disasters. Second edition. Routledge, London. 471 pp.

XIE, M., ESAKI, T., ZHOU, G. & MITANI, Y. 2003: Three-dimensional stability evaluation of landslides and a sliding process simulation using a new geographic information systems component. *Environmental Geology* 43: 503-512.

XIE, M., ESAKI, T. & CAI, M. 2004a: A time-space based approach for mapping rainfall-induced shallow landslide hazard. *Environmental Geology* 46: 840-850.

XIE, M., ESAKI, T. & ZHOU, G. 2004b: GIS-Based Probabilistic Mapping of Landslide Hazard Using a Three-Dimensional Deterministic Model. *Natural Hazards* 33: 265-282.

XIE, M., ESAKI, T., QIU, C. & WANG, C. 2006: Geographical information system-based computational implementation and application of spatial three-dimensional slope stability analysis. *Computers and Geotechnics* 33: 260-274.

YALIN, M.S. 1963: An expression for bedload transportation. *Journal of the Hydraulics Division. Proceedings of the American Society of Civil Engineers* 89: 221-250.

YANG, C.T. 1973: Incipient motion and sediment transport. *Journal of the Hydraulics Division. Proceedings of the American Society of Civil Engineers* 99: 1679-1703.

ZÊZERE, J.L., REIS, E., GARCIA, R., OLIVEIRA, S., RODRIGUES, M.L., VIEIRA, G. & FERREIRA, A.B. 2004: Integration of spatial and temporal data for the definition of different landslide hazard scenarios in the area north of Lisbon (Portugal). *Natural Hazards and Earth System Sciences* 4: 133-146.

Appendix 1: Maps and tables

This section contains maps and tables not included in the main text due to their size, or because they only contain additional information not directly required for the understanding of the study.

The following maps are included:

- Figure A1.1: Study area *Guardia Vieja*
- Figure A1.2: Study area *Quiebrada del Ferrocarril*
- Figure A1.3: Study area *Las Murallas*
- Figure A1.4: Study area *Castillo de Rocas*
- Figure A1.5: Study area *Quebrada Escondida*
- Figure A1.6: Study area *La Ampolleta*

For the locations of the study areas please consult the Figures 3.1 and 3.2. The soil and land cover classes referred to in the legends of the maps are compiled in the Tables 4.2 and 4.4, the soil samples shown in the map are compiled in Table A1.1.

The following Tables are included:

- Table A1.1: Soil parameters investigated in the laboratory
- Table A1.2: Average grain sizes and Van Genuchten parameters for the classes of the USDA soil taxonomy
- Table A1.3: Scheme for approximating Manning's n

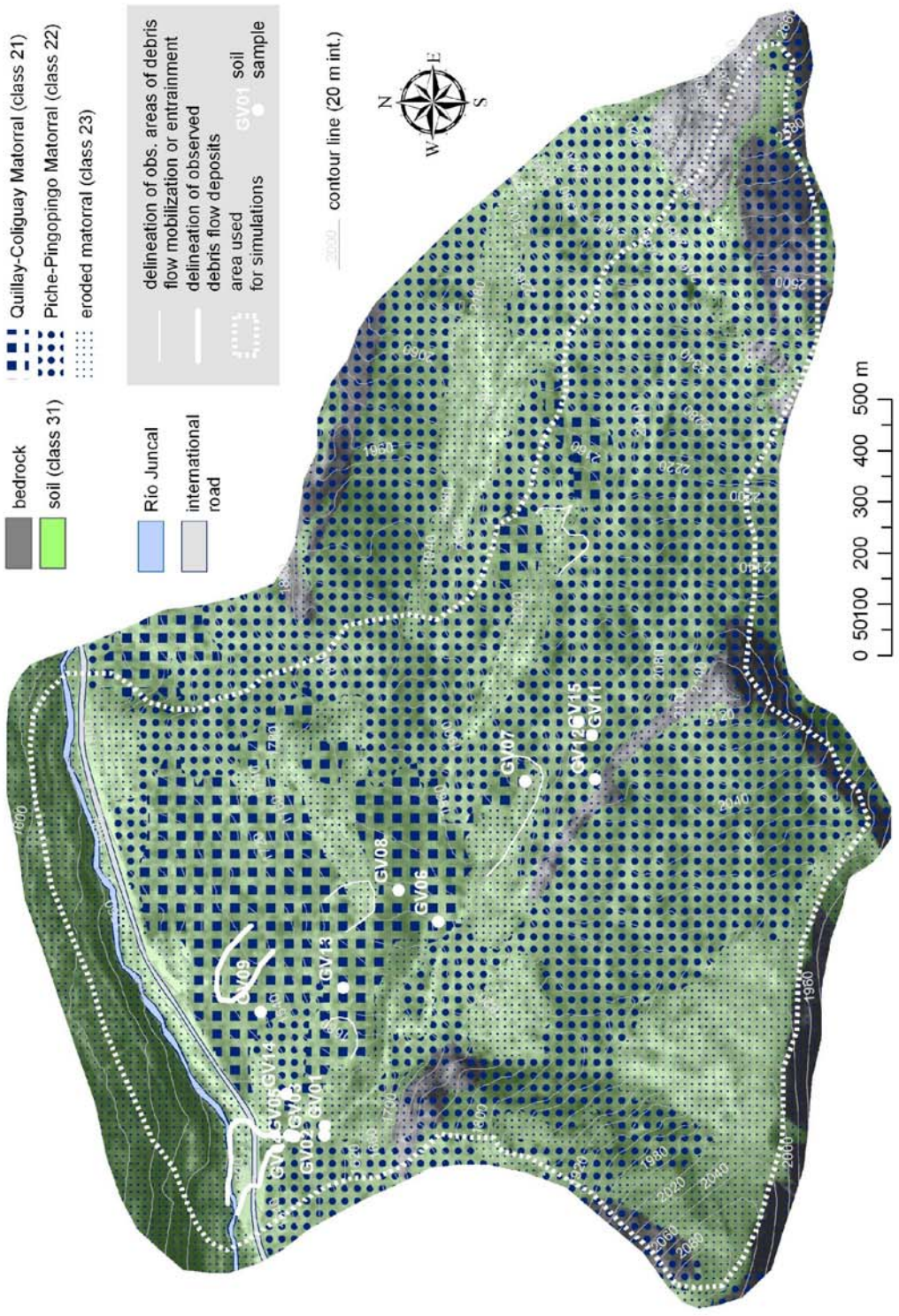

Figure A1.1: Map of the study area *Guardia Vieja*.

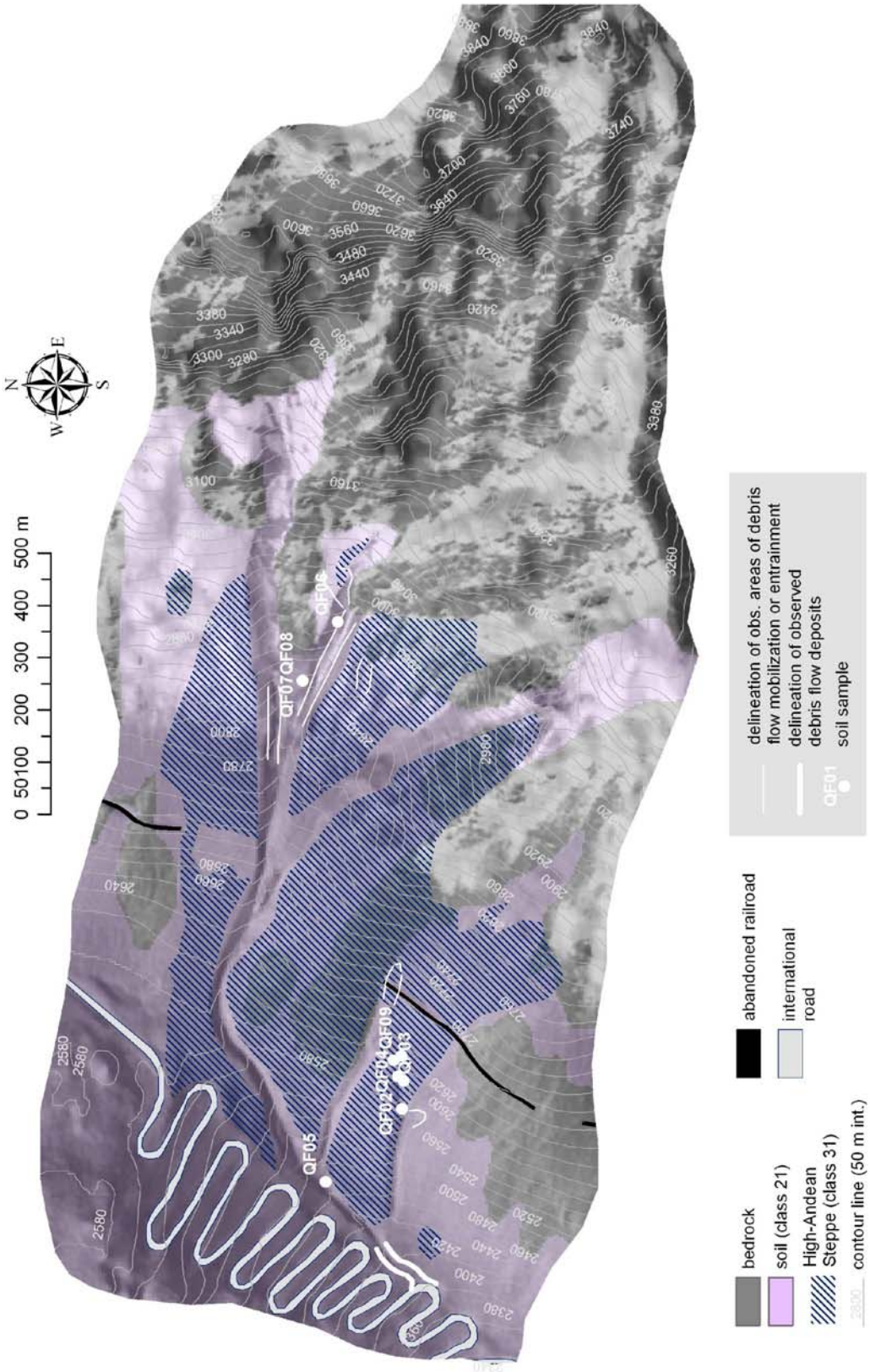

Figure A1.2: Map of the study area *Quebrada del Ferrocarril*.

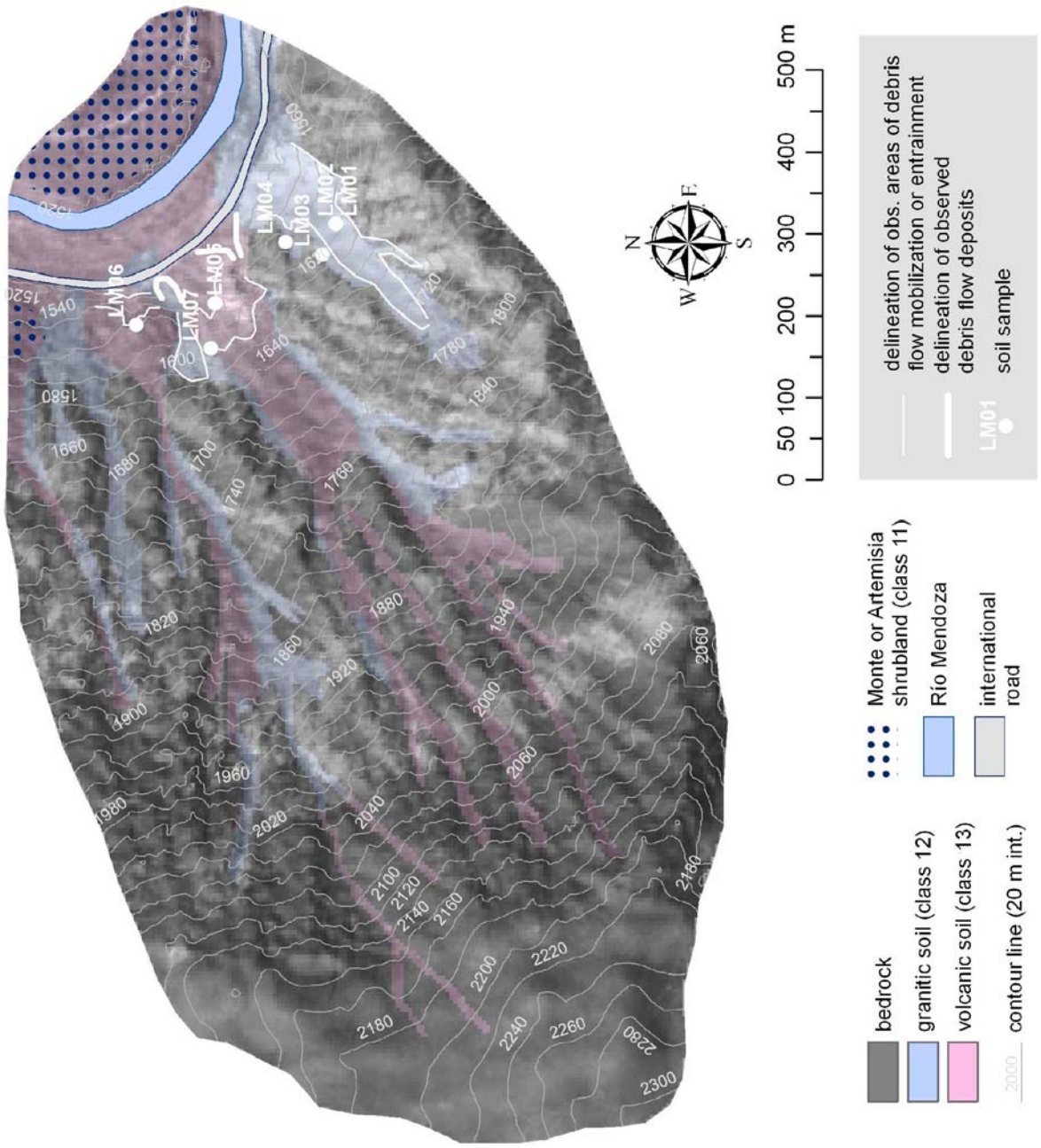

Figure A1.3: Map of the study area *Las Murallas*.

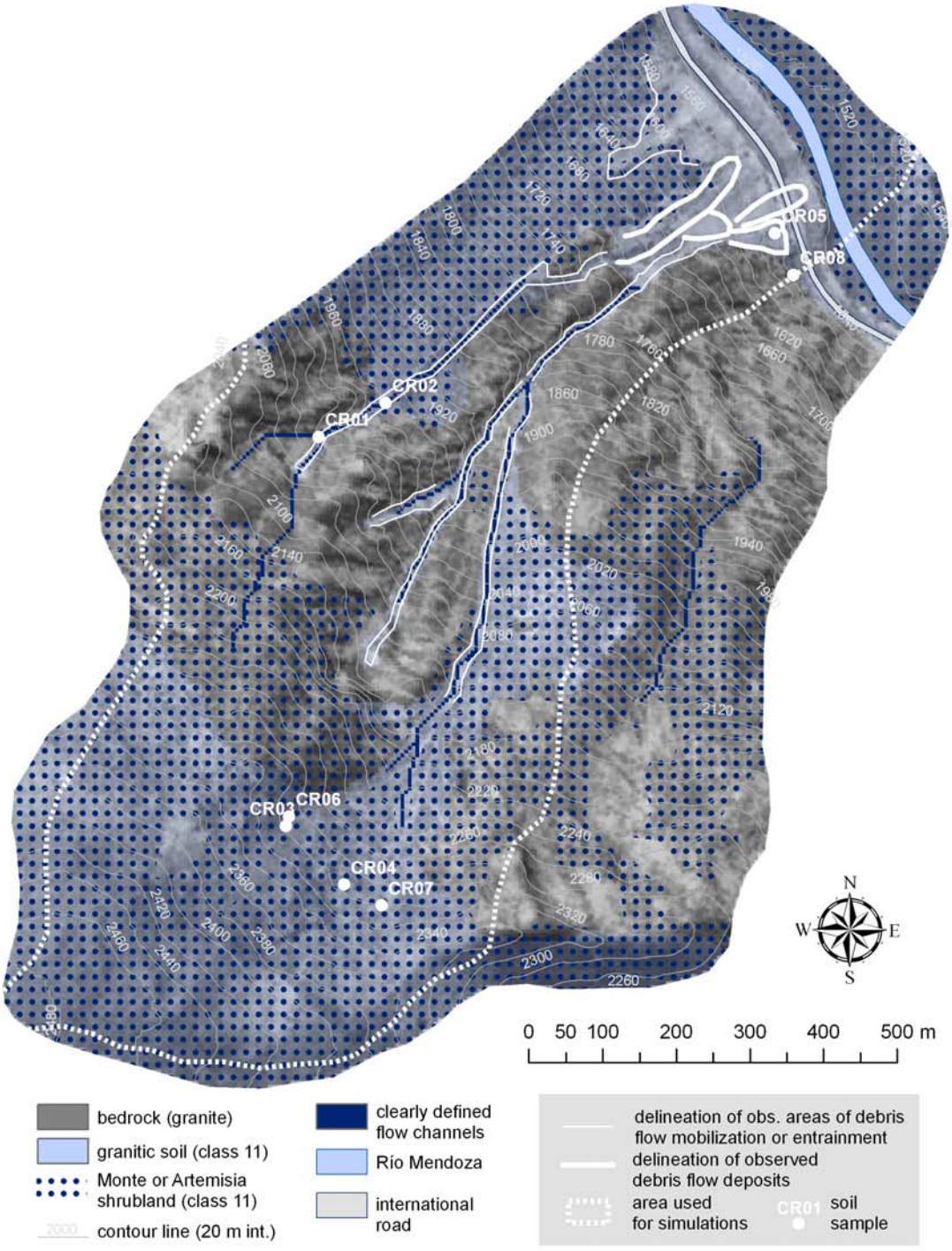

Figure A1.4: Map of the study area *Castillo de Rocas*.

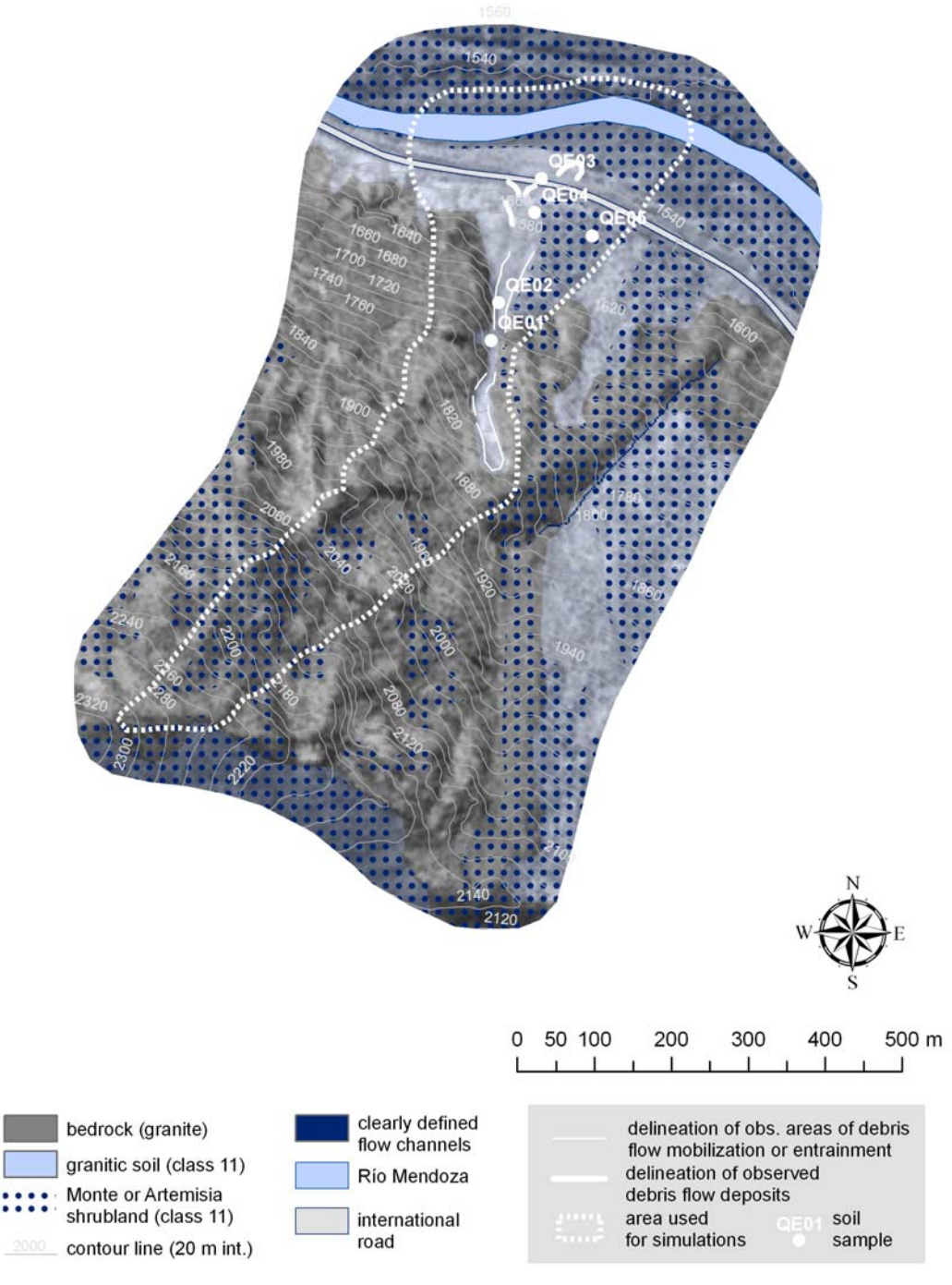

Figure A1.5: Map of the study area *Quebrada Escondida*.

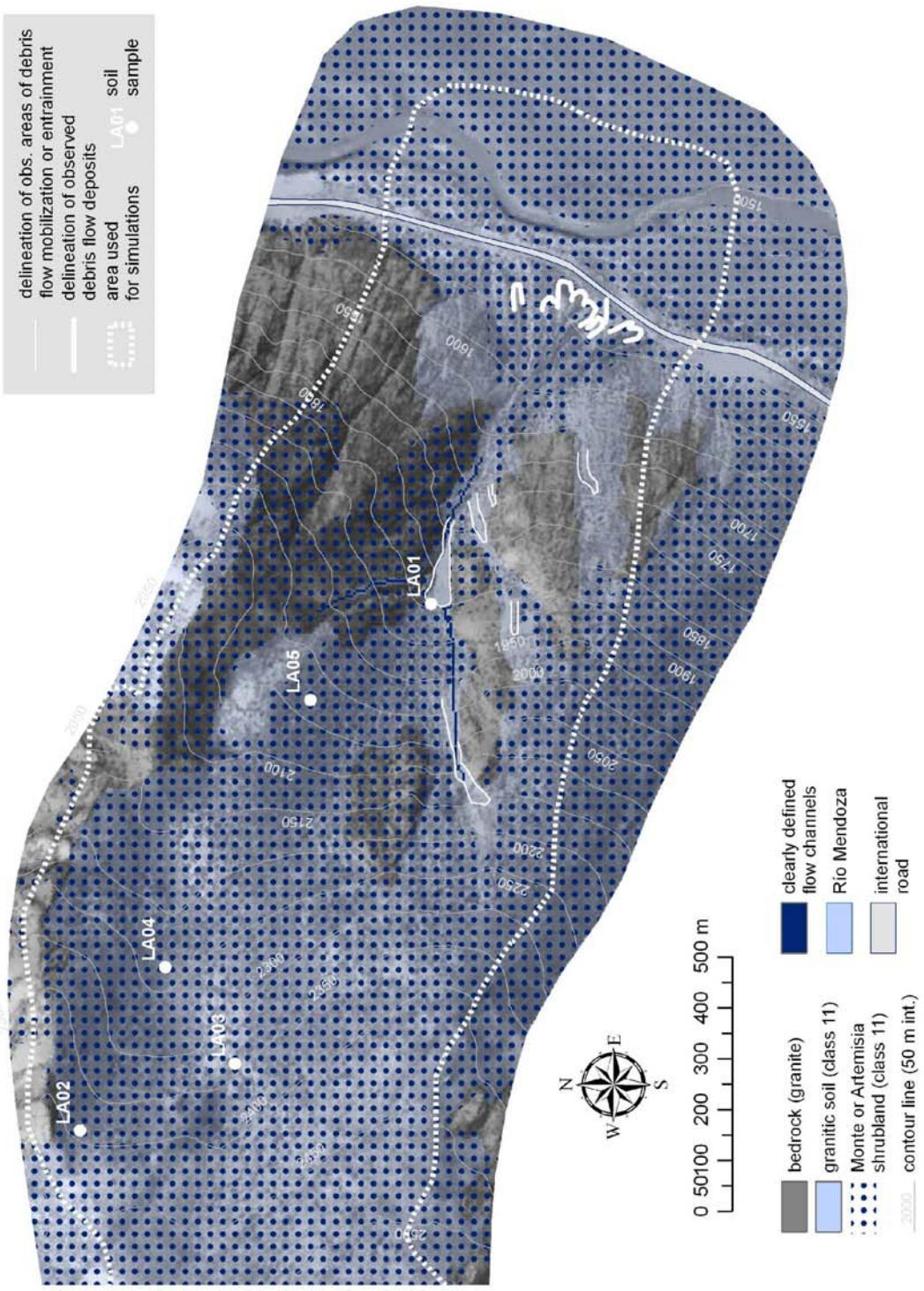

Figure A1.6: Map of the study area *La Ampolleta*.

Table A1.1: Soil parameters investigated in the laboratory (compare Figures A1.1 – A1.6 for the sampling sites). γ_d = dry density (measured from disturbed samples); c_{soil} = soil cohesion; φ = angle of internal friction.

sample number	soil class	stones	gravel	sand	silt	clay	D30	D50	D90	texture class	stone cont.	γ_d	c_{soil}	φ
		m-%	m-%	m-%	m-%	m-%	mm	mm	mm		m-%	N m^{-3}	N m^{-2}	degree
LA01	11	0.0	50.8	43.9	4.5	0.8	0.75	2.0	10	S	51	19,600	0	43.0
LA02	11	0.0	24.4	71.1	4.1	0.3	0.50	0.9	5	S	24			
LA03	11	0.0	46.6	50.5	2.5	0.4	0.75	2.0	7	S	47			
LA04	11	0.0	32.3	60.6	6.3	0.8	0.30	0.8	7	S	32			
LA05	11	0.0	55.8	41.9	2.1	0.2	0.80	3.0	15	S	56			
QE01	11	0.0	36.2	59.7	3.5	0.6	0.65	1.5	10	S	36	17,800	23,000	36.2
QE02	11	0.0	24.9	66.4	7.4	1.3	0.30	0.7	7	S	25			
QE03	11	0.0	45.4	47.6	6.1	0.9	0.65	1.5	15	LS	45			
QE04	11	0.0	48.3	45.7	5.2	0.7	0.75	2.0	10	S	48			
QE05	11	0.0	53.5	40.0	5.6	1.0	0.75	2.5	30	LS	54			
CR01	11	0.0	47.6	47.6	4.3	0.4	0.80	2.0	8	S	48	18,100	4,000	40.0
CR02	11	0.0	55.4	41.1	3.0	0.4	1.00	2.5	10	S	55			
CR03	11	0.0	36.2	59.0	4.0	0.8	0.35	1.0	10	S	36			
CR04	11	0.0	67.7	29.9	2.0	0.4	2.00	4.5	15	S	68			
CR05	11	0.0	66.8	29.7	3.3	0.3	2.00	4.0	15	S	67			
CR06	11	0.0	32.2	65.6	1.7	0.5	0.35	0.8	7	S	32			
CR07	11	0.0	30.5	62.7	6.0	0.8	0.35	0.9	6	S	31			
CR08	11	0.0	77.5	20.5	1.8	0.2	2.50	4.5	10	S	78			
LM01	12	0.0	41.8	46.8	10.9	0.6	0.40	1.5	8	LS	42			
LM02	12	0.0	64.6	29.0	5.8	0.7	1.50	4.0	15	LS	65			
LM03	12	0.0	52.8	37.2	9.9	0.1	0.75	25.0	15	LS	53	19,700	10,000	39.5
LM04	12	0.0	39.4	47.9	12.4	0.3	0.40	1.5	15	LS	39			
LM05	13	0.0	55.6	28.9	15.1	0.5	0.60	2.5	15	SL	56			
LM06	13	0.0	51.6	29.7	15.5	3.2	0.30	2.0	25	SL	52	21,800	0	41.3
LM07	13	0.0	61.6	26.6	9.8	2.0	1.00	3.5	20	SL	62			
QF01	21	0.0	27.9	46.4	17.7	8.0	0.10	0.7	6	SL	28			
QF02	21	0.0	49.3	33.9	14.0	2.8	0.40	2.0	15	SL	49			
QF03	21	0.0	50.8	31.1	11.8	6.4	0.45	2.0	20	SL	51	20,800	35,000	36.9
QF04	21	0.0	52.5	33.8	10.3	3.4	0.65	2.5	15	SL	53			
QF05	21	0.0	52.7	26.9	18.8	1.6	0.30	2.5	15	SL	53			
QF06	21	0.0	29.4	52.6	14.3	3.8	0.30	1.0	8	LS	29			
QF07	21	0.0	49.2	28.7	17.5	4.6	0.20	2.0	20	SL	49			
QF08	21	0.0	50.5	29.9	14.7	4.9	0.40	2.0	25	SL	51	21,100	0	40.5
QF09	21	31.4	65.4	2.5	0.0	0.0	10.00	20.0	70	S	97			
GV01	31	0.0	37.5	41.0	19.2	2.4	0.20	1.0	15	SL	38			
GV02	31	0.0	39.8	30.2	23.6	6.4	0.06	0.8	15	L	40			
GV03	31	0.0	36.3	43.8	15.4	4.5	0.25	1.0	10	SL	36	20,100	0	37.1
GV04	31	0.0	32.6	47.5	17.5	2.4	0.20	0.8	8	SL	33			
GV05	31	0.0	45.5	40.4	12.8	1.5	0.50	1.5	15	LS	46			
GV06	31	0.0	53.9	33.3	10.1	2.7	0.60	2.5	20	SL	54			
GV07	31	0.0	41.5	48.5	8.7	1.4	0.55	1.5	7	LS	42			
GV08	31	0.0	40.2	39.1	16.5	4.2	0.20	1.0	10	SL	40			
GV09	31	0.0	39.4	30.8	23.7	6.1	0.06	0.8	15	L	39			
GV10	31	0.0	24.2	41.8	27.0	6.9	0.04	0.3	6	SL	24	18,900	0	39.2
GV11	31	0.0	26.4	47.1	24.1	2.4	0.08	0.4	7	SL	26			
GV12	31	0.0	37.1	49.9	11.8	1.2	0.30	1.0	15	LS	37			
GV13	31	0.0	35.6	41.4	20.8	2.1	0.15	0.9	15	SL	36			
GV14	31	0.0	37.9	35.4	24.3	2.4	0.09	1.0	7	SL	38			
GV15	31	98.8	0.6	0.4	0.0	0.0	65.00	70.0	80	S	99			

Table A1.2: Avg. grain sizes, Van Genuchten param. for the classes of the USDA soil taxonomy (MAURER 1997; data from CARSEL & PARRISH 1988). Θ_r = residual water content; Θ_s = saturated water content; α = reciprocal of point of air admittance; n = indicator for smoothness of pore distribution; K = saturated hydraulic conductivity.

class	S	Sl	C	θ_r (vol-%)				θ_s (vol-%)				α (m^{-1})				n				K (cm h^{-1})			
				μ	σ	lb	ub	μ	σ	lb	ub	μ	σ	lb	ub	μ	σ	lb	ub	μ	σ	lb	ub
S	93	4	3	4,5	1,0	3,5	5,5	43	6	37	49	14,5	2,9	11,6	17,4	2,68	0,29	2,39	2,97	8,250E-5	4,333E-5	3,917E-5	1,258E-4
LS	81	13	6	5,7	1,5	4,2	7,2	43	9	34	52	12,4	4,3	8,1	16,7	2,28	0,27	2,01	2,55	4,053E-5	3,155E-5	8,983E-6	7,208E-5
SL	63	26	11	6,5	1,7	4,8	8,2	41	9	32	50	7,5	3,7	3,8	11,2	1,89	0,17	1,72	2,06	1,228E-5	1,564E-5	-3,356E-6	2,792E-5
SCL	54	19	27	10,0	0,6	9,4	10,6	39	7	32	46	5,9	3,8	2,1	9,7	1,48	0,13	1,35	1,61	3,633E-6	7,606E-6	-3,972E-6	1,124E-5
SC	48	11	41	10,0	1,3	8,7	11,3	38	5	33	43	2,7	1,7	1,0	4,4	1,23	0,10	1,13	1,33	3,361E-7	7,750E-7	-4,389E-7	1,111E-6
L	40	40	20	7,8	1,3	6,5	9,1	43	10	33	53	3,6	2,1	1,5	5,7	1,56	0,11	1,45	1,67	2,894E-6	5,058E-6	-2,164E-6	7,953E-6
CL	30	37	33	9,5	1,0	8,5	10,5	41	9	32	50	1,9	1,5	0,4	3,4	1,31	0,09	1,22	1,40	7,167E-7	1,944E-6	-1,228E-6	2,661E-6
SIL	17	65	18	6,7	1,5	5,2	8,2	45	8	37	53	2,0	1,2	0,8	3,2	1,41	0,12	1,29	1,53	1,250E-6	3,414E-6	-2,164E-6	4,664E-6
C	15	30	55	6,8	3,4	3,4	10,2	38	9	29	47	0,8	1,2	-0,4	2,0	1,09	0,09	1,00	1,18	5,556E-7	1,169E-6	-6,139E-7	1,725E-6
SICL	8	59	33	8,9	0,6	8,3	9,5	43	7	36	50	1,0	0,6	0,4	1,6	1,23	0,06	1,17	1,29	1,972E-7	5,333E-7	-3,361E-7	7,306E-7
SI	6	85	9	3,4	1,0	2,4	4,4	46	11	35	57	1,6	0,7	0,9	2,3	1,37	0,05	1,32	1,42	6,944E-7	9,139E-7	-2,194E-7	1,608E-6
SIC	6	48	46	7,0	2,3	4,7	9,3	36	7	29	43	0,5	0,5	0,0	1,0	1,09	0,06	1,03	1,15	5,833E-8	3,000E-7	-2,417E-7	3,583E-7

Table A1.3: Scheme for approximating Manning's n. Modified from COWAN (1956; after ARCEMENT & SCHNEIDER 2000).

variable	class	description	value
basic n_{bas}	earth	-	0.020
	rock	-	0.025
	fine gravel	-	0.024
	coarse gravel	-	0.028
irregularity n_1	smooth	surface comparable to the best attainable for the materials involved	0.000
	minor	... good dredged channels; slightly eroded or scoured side slopes of canals or drainage channels	0.005
	moderate	... fair to poor dredged channels; moderately sloughed or eroded side slopes of canals or drainage channels	0.010
	severe	... badly sloughed banks of natural streams; badly eroded or sloughed sides of canals or drainage channels; unshaped, jagged, and irregular surfaces of channels excavated in rock	0.020
cross section n_2	gradual	change in size or shape occurring gradually	0.000
	occasional	large and small sections alternating occasionally or shape changes causing occasional shifting of main flow from side to side	0.005
	alternating	large and small sections alternating frequently or shape changes causing frequent shifting of main flow from side to side	0.010 – 0.015
obstructions n_3	negligible	no further specification	0.000
	minor	no further specification	0.010 – 0.015
	appreciable	no further specification	0.020 – 0.030
	severe	no further specification	0.040 – 0.060
vegetation n_4	low	conditions comparable to dense growths of flexible turf grasses or weeds, of which Bermuda grass and bluegrass are examples, where the average depth of flow is two or more times the height of vegetation ... supple seedling tree switches, such as willow, cottonwood, or salt cedar, where the avg. depth of flow is three or more times the height of the veg.	0.005 – 0.010
	medium	... turf grasses where the average depth of flow is one to two times the height of the vegetation ... stemmy grasses, weeds, or tree seedlings with moderate cover, where the average depth of flow is two to three times the height of the vegetation ... bushy growths, moderately dense, similar to willows one to two years old, dormant season, along side slopes with no significant vegetation along bottom, where the hydraulic radius is greater than 60 cm	0.010 – 0.020
	high	... turf grasses where avg. depth of flow is about equal to height of veg. ... willow or cottonwood trees 8 to 10 years old intergrown with some weeds and brush, dormant season, where the hydraulic radius is 60 to 120 cm ... bushy willows about 1 year old intergrown with some weeds in full foliage along side slopes, no significant vegetation along channel bottom where hydraulic radius is 60 to 120 cm	0.025 – 0.050
	very high	... turf grasses where the average depth of flow is less than one-half the height of the vegetation ... bushy willows about 1 year old intergrown with weeds along side slopes, dense growth of cattails along channel bottom, all vegetation in full foliage, any value of hydraulic radius up to 3.0 or 3.6 m ... trees intergrown with weeds and brush, all vegetation in full foliage, any value of hydraulic radius up to 3.0 or 3.6 m	0.050 – 0.100
meandering m	minor	ratio of meander length to straight length 1.0 – 1.2	1.00
	appreciable	... 1.2 – 1.5	0.15
	severe	... 1.5 and greater	0.30

Appendix 2: Scientific publications

The following articles and abstracts were published or accepted for publication. They are collected on the following pages:

A2.1 MERGILI, M. 2007: Stereo matching of terrestrial digital photographs - an alternative for the generation of high-resolution DEMs in situations of poor data availability? In: CAR, A., GRIESEBNER, G. & STROBL, J. (eds.): Geospatial Crossroads @ GI_Forum - Proceedings of the First Geoinformatics Forum Salzburg: 110-119.

A2.2 MERGILI, M., MOREIRAS, S.M., FELLIN, W. & STÖTTER, J. 2007: Preliminary results of slope stability simulations for the prediction of debris flows in the Central Andes (Mendoza, Argentina). In: KELLERER-PIRKLBAUER, A., KEILER, M., EMBLETON-HAMANN, C. & STÖTTER, J. (eds.): Proceedings of the Conference 'Geomorphology for the Future', Obergurgl: 145-152.

A2.3 MERGILI, M. & FELLIN, W. 2007: GRASS GIS and modelling of natural hazards: an integrated approach for debris flow simulation. *OSGeo* 3 (FOSS4G 2007 Proceedings): 53-59.

A2.4 MERGILI, M., FELLIN, W., MOREIRAS, S.M. & STÖTTER, J. 2008: Integrated modelling of debris flows in the Central Andes based on Open Source GIS. *Geophysical Research Abstracts* 10.

A2.5 MERGILI, M., SCHRATZ, K., THALHAMMER, M., STÖTTER, J., OSTERMANN, A. & FELLIN, W. accepted: Simulation of debris flows based on OpenSource GIS. Abstract for the International Geological Congress, Oslo (Norway).

A2.6 MERGILI, M., SCHRATZ, K., THALHAMMER, M., FELLIN, W. & OSTERMANN, A. accepted: An Open Source model for the simulation of granular flows: First results with GRASS GIS and needs for further investigations. *OS Geo* (FOSS4G 2008 Proceedings).

Additionally, the following oral and poster presentations were given at or accepted for international or national conferences and workshops:

MERGILI, M. 2007: Stereo matching of terrestrial digital photographs - an alternative for the generation of high-resolution DEMs in situations of poor data availability? Oral presentation at the GI Forum, July 4th, 2007, Salzburg (Austria).

MERGILI, M. 2007: Die Modellierung von Murereignissen in den zentralen Anden: Der Versuch eines integrierten Ansatzes mit GRASS GIS. Oral presentation at the conference 'Geomprphology for the Future', Sept. 5th, 2007, Obergurgl, Austria. In German.

MERGILI, M. & FELLIN, W. 2007: GRASS GIS and modelling of natural hazards: an integrated approach for debris flow simulation. Poster presentation at the FOSS4G Meeting, Sept. 24 – 27th, 2007, Victoria (BC, Canada).

MERGILI, M., SCHRATZ, K., OSTERMANN, A. & FELLIN, W. 2008: Simulation von Lawinen und Muren mit Hilfe mathematischer Modelle. Poster presentation at the Day of Mathematics, January 27th, 2008, Innsbruck (Austria). In German.

MERGILI, M. & FELLIN, W. 2008: Simulation of debris flows in the Central Andes. A model approach based on Open Source GIS. Poster presentation at the Workshop of the Austrian Latin America Institute, Division Tirol: "Aktuelle Lateinamerika-Forschung in Innsbruck", January 18th, 2008, Innsbruck (Austria).

MERGILI, M., FELLIN, W., MOREIRAS, S.M. & STÖTTER, J. 2008: Integrated modelling of debris flows in the Central Andes based on Open Source GIS. Oral Presentation at the EGU General Assembly, April 18th, 2008, Vienna (Austria).

MERGILI, M., SCHRATZ, K., THALHAMMER, M., STÖTTER, J., OSTERMANN, A. & FELLIN, W. 2008: Simulation of debris flows based on OpenSource GIS. Oral presentation accepted for the International Geological Congress, August 13th, 2008, Oslo (Norway).

MERGILI, M., SCHRATZ, K., THALHAMMER, M., FELLIN, W. & OSTERMANN, A. 2008: An Open Source model for the simulation of granular flows: First results with GRASS GIS and needs for further research. Oral presentation accepted for the FOSS4G Meeting, Sept. 29th – Oct. 3rd, 2008, Cape Town (South Africa).

A2.1 Stereo matching of terrestrial digital photographs – an alternative for the generation of high-resolution DEMs in situations of poor data availability?

Martin Mergili

peer-reviewed article published in CAR, A., GRIESEBNER, G. & STROBL, J. (eds.): Geospatial Crossroads @ GI_Forum - Proceedings of the First Geoinformatics Forum Salzburg: 110-119, 2007

Abstract. The paper evaluates the applicability of terrestrial digital photographs for stereo matching in order to generate high-resolution DEMs in areas with extremely pronounced relief. Images of the study slopes, located along a transect between Mendoza (Argentina) and Valparaíso (Chile), were recorded from the opposite side of the valley using a digital SLR camera. Stereo matching was performed using standard remote sensing software. The reference plane had to be tilted in order to enable a proper rectification. The resulting raster maps were adjusted in order to enhance the consistency with the reference datasets. The method, though connected to some limitations concerning the accuracy of the results, proved successful and may be a valuable tool for small-scale studies in areas with limited data availability, particularly in developing countries.

Background

High-resolution digital elevation models (DEMs) constitute an essential tool for a large variety of applications. Therefore an array of methods for generating such datasets has been developed in the previous years and decades (compare Tab. 1). Some of the most common approaches are:

(1) Airborne laser scanning (Ackermann 1999; Pfeifer 2006) comes up with spatial resolutions well below 1 m. In highly developed countries airborne laser scanning data are available for an increasing portion of the land surface. Terrestrial laser scanning is used more and more for obtaining high resolution DEMs of small areas.

(2) A common way for generating high resolution DEMs of large areas is stereo matching of high resolution satellite imagery like IKONOS (Zhang et al. 2002).

(3) For small-scale studies, matching of stereo aerial photos has widely been applied, replacing the traditional stereoscopic viewing (Gruen & Baltsavias 1986; Fig. 1). The method, being the same as for satellite imagery, is supported by standard remote sensing software. It makes use of the parallax between two images recorded from different positions as well as of the texture of the images in order to compute the position of each pixel in a reference coordinate system, based on camera geometry, control points, and the exterior orientation of the camera (optional). Würländer et al. (2004) provide a comparison of this method with laser scanning techniques.

Use of the methods (1) and (2) usually implies considerable costs for data acquisition, largely constraining its application to projects with high budget. In addition, processing of data derived from laser scanning is still connected to specialized data processing tools that are now starting to be included into the standard GIS software tools like ArcGIS, GRASS (Rutzinger et al. 2006), or PCI Geomatica.

Tab. 1: Some common methods for the generation of high-resolution DEMs.

Method	Advantages	Disadvantages
Airborne laser scanning	high accuracy, identification of vertical structures	expensive; cost-efficiently only for large areas
Terrestrial laser scanning	high accuracy, identification of vertical structures	specialized equipment and personnel
Stereo matching of high-resolution satellite imagery	cover of large areas	high cost for data
Stereo matching of aerial imagery	low cost for data, good data availability for many areas	labour-extensive for large areas, limited by the image quality, moderate accuracy

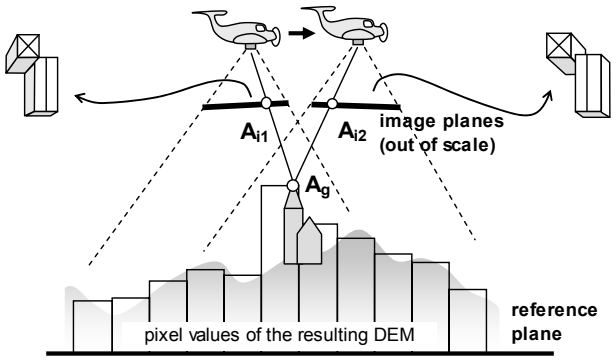

Fig. 1: Stereo matching of aerial images. Graphics modified from the PCI Geomatica Help. A_{i1} and A_{i2} represent the image coordinates of the clock tower's top, Ag its ground coordinates.

For small-scale projects, stereo-matching of aerial images works fine in many areas, but nevertheless bears some limitations as well. Particularly in peripheral regions of developing countries imagery is not always available. Images may be of poor quality, and not all land surface types are suitable for image matching. Particularly patches with poor texture and/or particularly high or low albedo, like snow or ice, may cause serious problems, leading to large holes in the DEM.

In contrast to aerial imagery, hardly any attempts to use terrestrial imagery for the extraction of high-resolution DEMs have become public up to now. This appears somewhat astonishing as

(1) the mathematical background and the methodology are almost the same as for aerial imagery,

(2) in areas with pronounced relief it may be easy to access spots with a good overview of the area of interest, particularly in the case of small-scale studies,

(3) the spatial resolution and the image quality may be much better than in the case of aerial imagery, and finally

(4) in other fields, similar methods have been successfully applied for representing the geometry of buildings, or even of human faces (Gruen & Baltsavias 1989).

The purpose of the present study is to attack this gap by evaluating the possibilities as well as the limitations connected to the generation of high-resolution DEMs by stereo-matching of terrestrial photographs.

The experiment is part of a project dealing with the prediction of debris flows based on a deterministic model, therefore requiring a DEM at an appropriate resolution (≤5 m). The study includes six slopes along a transect across the Andes between Mendoza (Argentina) and Valparaíso (Chile), following an important road corridor connecting the two countries (Fig. 2).

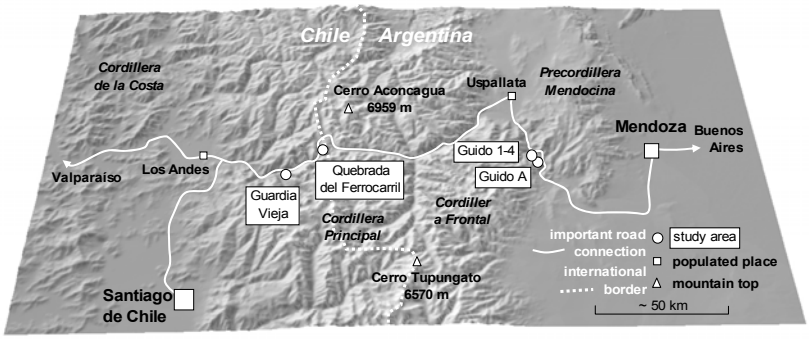

Fig. 2: Location of the study areas. Shaded relief map calculated from SRTM data.

Fig. 3: Example of a stereo pair of terrestrial images recorded from the slope opposite to the study area Guido 3. Source: Mergili, 10/2006.

Data

The stereo images were recorded using a standard digital SLR camera (Konica Minolta Dynax 5D) with a chip size of 23.5 x 15.7 mm. A focal length of 18 mm was chosen for all images, the distortion parameters of the lens were not known. The recording points were chosen in a way that the distances between the stereo images would be sufficient for ensuring a reasonable stereo effect, but not too much in order to prevent troubles with automatic pixel matching. The positions were approximated using a standard field GPS device with an accuracy of ≤10 m. The distance to the target slopes was of a magnitude of some 100s of meters. Figure 3 illustrates one of the stereo pairs used.

Orthophotos and a 30 m resolution DEM were used as ground references. The orthophotos were generated from aerial imagery provided by the provincial government of Mendoza (scale 1:20,000), and by the aero-photogrammetric service of Chile (1:60,000), respectively. The 30 m DEM was purchased as final product derived from ASTER satellite imagery. Additionally, GPS control points were recorded in the study areas. Due to their unbalanced patterns (caused by the inaccessibility of parts of the slopes) and their relatively low vertical accuracy it was decided not to use them as GCPs.

Methods

The workflow of the study, represented in Fig. 4, may be divided into the following steps:

(1) Collecting GCPs from orthophotos and from the ASTER DEM.

(2) Definition of an appropriate reference plane. In contrast to stereo matching based on aerial imagery it was not possible just to use a simple projected coordinate system like UTM, for the reason that the rectification algorithm applied in the OrthoEngine of PCI Geomatica, which was used for the DEM extraction, is not suitable for dealing with extreme variations of the z coordinate (elevation) compared to the image size, like appearing in the terrestrial photographs. Therefore a slope-parallel reference plane had to be introduced. It was defined by a rotation α and an inclination β, related to the UTM system (Fig. 5). α and β were determined individually for each study area by minimizing the root mean square (RMS) values of the z-coordinates of the respective GCPs.

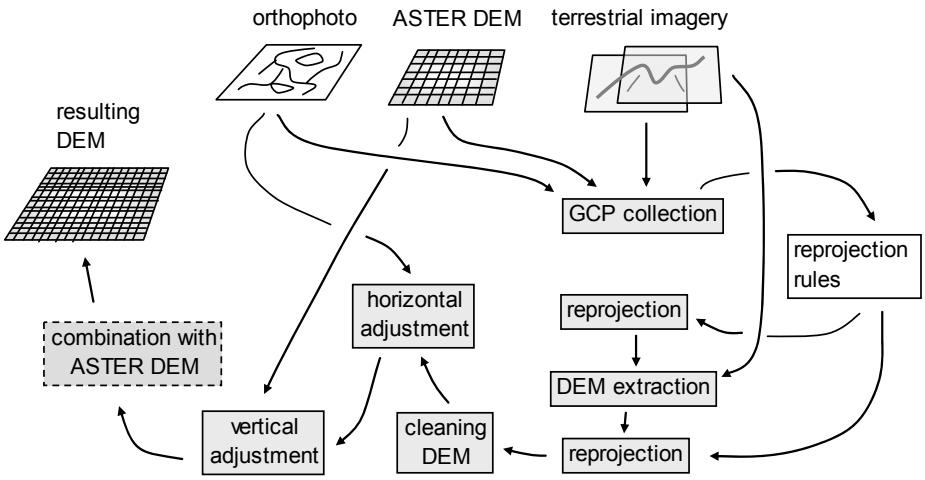

Fig. 4: Workflow of the study.

(3) Recalculating the GCPs to the new reference plane. The transformation was given by

$$x' = x\cos\alpha - y\sin\alpha \quad \text{Eq. (1)},$$

$$y' = \left(y\cos\alpha + x\sin\alpha\right)/\cos\beta + \Delta z\sin\beta \quad \text{Eq. (2), and}$$

$$z' = \Delta z\cos\beta \quad \text{Eq. (3)},$$

where x, y, and z are the coordinates in the UTM reference plane, but with P0 as origin (compare Fig. 5), x', y', and z' are the coordinates in the new reference system, a is the rotation angle, and β stands for the inclination angle (compare Fig. 5). Δz is the elevation difference between the new reference plane and the elevation of P_0 in the UTM system, given by

$$\Delta z = \left(y\cos\alpha + x\sin\alpha\right)\tan\beta \quad \text{Eq. (4)}.$$

(4) Image matching based on textural features and the parallax between the images, as mentioned above and illustrated in Fig. 1. This step is a standard functionality of PCI Geomatica and will therefore not be discussed in detail in this place.

(5) Recomputation of the DEM to the UTM reference system. This was done by converting the result of (4) into a lattice, and applying Eq. (1) to (4) to the coordinates, inverting α and β. The resulting irregularly spaced cluster of points was recalculated to a raster map, using a natural neighbours algorithm. Artificial tops and sinks within the DEM were then removed manually (referred to as "cleaning DEM" in Fig. 4).

(6) Horizontal adjustment. A geometrical correction was necessary in order to synchronize the new DEM datasets with the underlying orthophoto and the ASTER DEM. Distinct topographic features clearly recognizable in both the new DEM and the orthophoto were used as control points.

(7) Vertical adjustment. The raster was subtracted from the ASTER DEM in order to determine large-scale distortions in the stereo DEM. A correction raster, as an extremely smoothed representation of the difference between the datasets, was interpolated and applied for the adjustment of the stereo DEM. Thus the small-scale patterns were conserved while fitting the large-scale patterns to the ASTER DEM, removing distortions and allowing for a proper combination of the two datasets.

Results

Image correlation worked well for some of the study areas, for some others holes of considerable sizes – primarily caused by snow patches and cloudy conditions at the time of the recording – led to a lower quality level. The results will be discussed in more detail for the study areas Guido A and Guido 3 (compare Fig. 2). The stereo DEMs for these areas showed no holes in the central areas of the DEMs, and the matching scores were above 80 % over the majority of the surfaces. A spatial resolution of 2 m was chosen for Guido A, 1 m for Guido 3. A few artificial peaks and sinks (1 % of the surface of Guido A, 3.5 % of the surface of Guido 3) had to be removed in order to derive visually clean DEMs for both study areas (Fig. 6).

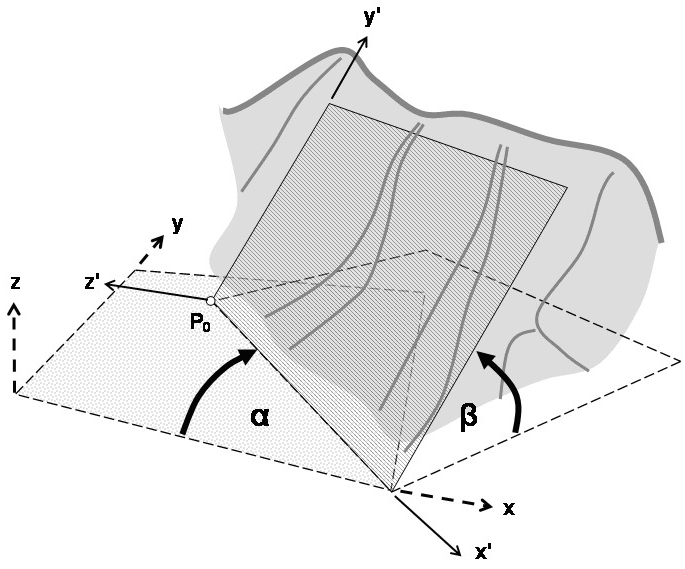

Fig. 5: Reference plane introduced for rectification and DEM generation.

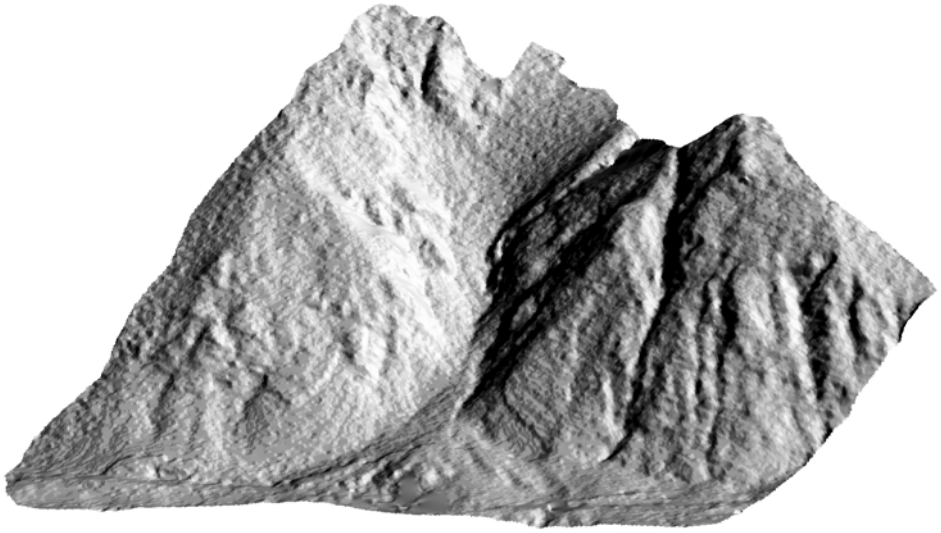

Fig. 6: DEM (resolution 2m) derived from stereo images for the study area Guido A, after removing peaks and holes. The international road is well recognizable at the lower edge of the DEM. Its length represented in the dataset is about 800 m, the elevation difference 700 m.

A horizontal adjustment was required for both stereo DEMs in order to bring them in cover with the orthophoto and the ASTER DEM. For Guido A, the overlay with the ASTER DEM showed considerable vertical deviations between the two datasets. More than 25 % of the pixels were more than 40 m off, only about 35 % less than 20 m (Fig. 7). For Guido 3, the datasets corresponded better, with more than 50 % of the pixels being less than 20 m off.

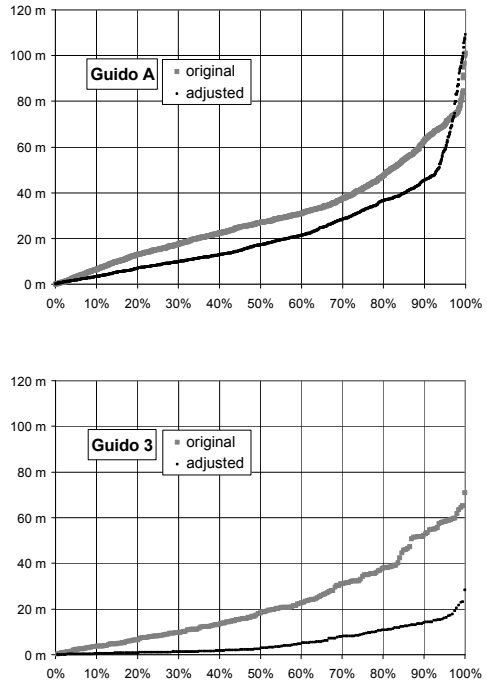

Fig. 7: Deviation between the stereo DEM and the ASTER DEM for the study areas Guido A (left) and Guido 3 (right), before and after the vertical adjustment. The absolute deviation between the two datasets, plotted along the ordinate, falls below the indicated value at the corresponding percentage of pixels (abscissa).

Vertical adjustment of the stereo DEMs was performed for both areas, decreasing the deviation from the ASTER DEM (compare Fig. 7). However, maintaining the topographical structures was given priority to a perfect fit, considering the relatively large inaccuracies to be expected in the ASTER DEM itself (10s of meters). The offset error was only moderately reduced for the Guido A DEM, leading to slightly less than 60 % of the pixels being less than 20 m off. In contrast, the adjustment of the Guido 3 DEM led to a considerable reduction of the deviation, with about 75 % of the pixels less than 10 m off and more than 95 % of the pixels less than 20 m off.

A lot of emphasis was put on the synchronization of the connection lines of the stereo DEM with the ASTER DEM, in order to allow for a hydrologically, geomorphologically, and visually consistent combination of the two datasets. Fig. 8 illustrates the combined DEMs for the study areas Guido A and Guido 3, enabling an estimation of the hydrological input to the areas of interest. The hydrological consistency of the composite DEMs was tested using the standard parameters flow direction and flow accumulation. It proved successful for both of the study areas.

Discussion

The method presented above does not lead to high-precision results – it rather provides a more or less distorted image of the reality. Therefore it is required to know about the uncertainties and limitations, but also about the potential of DEMs derived from terrestrial stereo images.

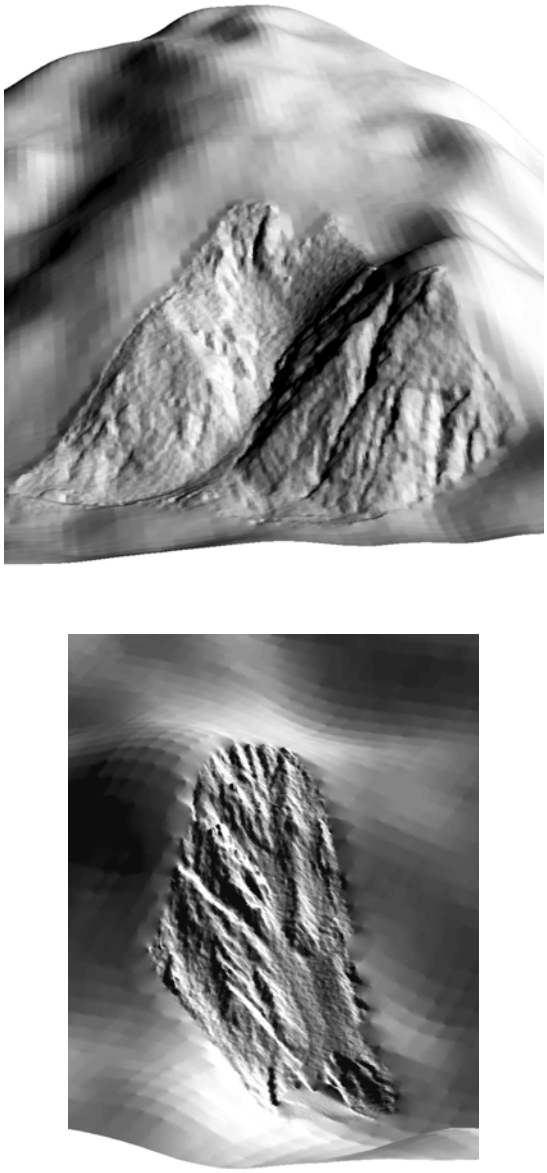

Fig. 8: Combined stereo and ASTER DEMs for the study areas Guido A (left side, resolution 5 m) and Guido 3 (right side, resolution 2 m, width of the stereo DEM about 200 m).

The absolute accuracy of the resulting DEM product is limited by the accuracy of the GCPs used for rectification. The orthophotos from which the GCPs were collected had a sufficient resolution and accuracy, and its features were clearly identifiable in the terrestrial imagery. However, the elevation of the GCPs was a major factor of uncertainty as only an ASTER DEM with a resolution of 30 m was available over the entire surface of the study areas. Unfortunately it was not possible to use GPS records as GCPs, as (1) they were only available for accessible areas and mixing them with other GCPs would have introduced inconsistencies, (2) their horizontal and vertical accuracy was limited, and (3) it was difficult in the field to recognize appropriate GCPs.

The situation would prove even more difficult in areas without orthophotos available. For such cases, panchromatic LANDSAT images (15 m resolution) or SPOT images would be an alternative. However, a low horizontal accuracy and potential problems with the identification of proper GCPs would be the consequence.

The accuracy of the resulting DEM products was not only limited by the accuracy of the GCPs, but also by the constraints of the rectification algorithm. All standard remote sensing software products, including the PCI Geomatica OrthoEngine, have been developed for the processing of satellite and aerial imagery, which both

(1) represent the earth surface more or less from straight above, with almost perpendicular x- and y- ground coordinates in the images, and an extremely short z-coordinate, and

(2) cover a horizontal surface exceeding the elevation by far over one scene.

Terrestrial digital photographs as used in the present study, in contrast, lack these geometric characteristics. The ground coordinates are arranged in an irregular pattern within the images, and the elevation variation over the image may be of the same magnitude as its horizontal extent. The definition of an appropriate, slope-parallel coordinate system can partly overcome this problem and make this method possible, but still, the $z/(x+y)$ - relationship is comparable to standard aerial imagery in extremely mountainous terrain, leading to a reduced level of accuracy in the resulting DEM. Thorough post-processing (horizontal and vertical adjustment) can remove part of the error, but inaccuracies additional to those caused by the reference data always remain.

Conclusions

The experiences from the experiment described in this paper allow for the following conclusions:

(1) Stereo-matching of terrestrial digital photographs constitutes a considerable potential for the generation of high-resolution DEMs and can be an extremely valuable tool, particularly for small-scale studies in areas where no data of higher accuracy is available, for example in peripheral areas of developing countries. However, the method is not universally applicable. The study area has to be visible from at least two accessible viewpoints for recording the images, and the images have to be recorded under clear weather conditions (no shadows of clouds).

(2) Due to the narrow field of view characterizing terrestrial images compared to aerial images, for many research purposes the DEM has to be combined with other high resolution DEMs, e.g. derived from aerial imagery, or with medium

resolution DEMs like ASTER-derived datasets. The combination has to be done with caution in order to ensure the consistency of the dataset.

(3) The expectable errors in derived products like slope, curvature, or hydrological characteristics are hard to quantify, but taking the quality of the DEMs for the study areas Guido A and Guido 3 as reference, it is to be expected that for many research purposes – particularly if the DEM is used for modeling processes like landslides or runoff – the impacts of errors and inaccuracies in other datasets (substrate parameters, vegetation patterns, precipitation input) usually exceed the impact of the inaccuracies in the DEM. In contrast, the method is hardly applicable if high-precision datasets are required, for instance for the detection of slow movements.

References

Ackermann, F. (1999): Airborne laser scanning - present status and future expectations. *ISPRS Journal of Photogrammetry & Remote Sensing* 54: 64-67.

Gruen, A. & Baltsavias, E. (1987): High-Precision Image Matching for Digital Terrain Model Generation. *Photogrammetria* 42: 97-112.

Gruen, A. & Baltsavias, E. (1989): Automatic 3-D Measurement of Human Faces with CCD-Cameras. Paper presented at the Biostereometrics '88, 14.-17. November, Basel. *Proc. of SPIE* 1030: 106-116.

Pfeifer, N. (2006): Airborne Laser Scanning - Examples for operational Application in Hydrology. *Geophysical Research Abstracts* 8, 10790.

Rutzinger, M., Höfle, B., Geist, T. & Stötter, J. (2006): Object-based building detection based on airborne laser scanning data within GRASS GIS environment. Proceedings UDMS: Urban data Management Symposium, Aalborg. CD-ROM.

Würländer, R., Eder, K. & Geist, T. (2004): High quality DEMs for glacier monitoring - image matching versus laser scanning. *International archives of Photogrammetry, Remote Sensing and spatial information science* 35, B7: 753 - 758.

Zhang, L., Paterski, M. & Baltsavias, E. (2002): Matching of Ikonos Stereo and Multitemporal GEO Images for DSM Generation. Proc. Map Asia 2002, Asian Conference on GIS, GPS, Aerial Photography and Remote Sensing, 7.-9. August, Bangkok. CD-ROM.

A2.2 Preliminary results of slope stability simulations for the prediction of debris flows in the Central Andes (Mendoza, Argentina)

Martin Mergili, Stella M. Moreiras, Wolfgang Fellin and Johann Stötter

peer-reviewed article published in KELLERER-PIRKLBAUER, A., KEILER, M., EMBLETON-HAMANN, C. & STÖTTER, J. (eds.): Proceedings of the Conference 'Geomorphology for the Future', Obergurgl: 145-152, 2007

Abstract. The preliminary results of debris flow simulations for some selected study areas along the international road corridor Mendoza (Argentina) – Valparaíso (Chile) are presented at the example of one small catchment. A deterministic coupled hydrological-slope stability model based on Open Source GIS products was designed for predicting the response of selected slopes and small catchments to rainfall events, including failures due to saturation of the soil as well as erosion due to the kinetic energy of overland flow. Samples were taken in the field and analyzed for their physical and mechanical characteristics in a geotechnical laboratory. Hydrological characteristics were derived using pedotransfer functions. The preliminary simulation results were promising, but more research is required for enabling a better evaluation and an optimization of the model.

Keywords. shallow slope failure, debris flow, numerical simulation, Mendoza Valley, Andes.

Introduction

Debris flows are rapid mass movements forming a mixture of rock fragments and water. They are intermediate between sediment-rich floods and landslides. Initiating as failures on slopes, in gullies or at gully walls, they are usually driven by seepage forces (saturation of the soil), or by the kinetic energy of overland flow, or by a combination of both. Debris flows are common phenomena in mountain regions all over the world, and they are strongly related to intensive or prolonged rainfall, often in association with intense snowmelt. As they often constitute a significant hazard for buildings and infrastructures, and therefore also for human lives, several qualitative, statistical and deterministic approaches have been developed in order to predict the occurrence of debris flows in space and time. However, up to now many models exist for modelling specific processes being involved into the initiation and movement of debris flows, but few approaches are known to simulate the entire process from rainfall impact to final accumulation. The model presented in this paper attempts to fill this gap. The hydrological modules and the identification of unstable cells are based on the Open Source GIS Software GRASS. With the identified regions of potential failure and starting mass, the motion and run-out of the debris flow should be calculated with a dynamic model. Such a model can be based e.g. on the Savage-Hutter model (Savage & Hutter 1989; Pudasaini & Hutter 2007). This final step, however, has not yet been implemented at the present stage of the project.

Study area

The research project includes selected study areas along the international road corridor from Mendoza/Argentina to Valparaíso/Chile between Potrerillos and Los Andes (Mendoza and Aconcagua valleys, Fig. 1), where some qualitative (Mikkan 1997) and statistical studies on debris flows (Moreiras 2004, 2005a and b) already exist. The study areas are seven small catchments (few km²) susceptible to debris flows and with a meteorological station in their vicinity. The paper discusses the first results for the study

area Guido A (Fig. 1), located about 50 km W of the city of Mendoza, between 1500 and 2750 m asl., covering 2.0 km². It constitutes a well-defined and rather homogeneous catchment, with granite outcrops and partly relocated residuals from weathering. Mean annual precipitation at the Guido Meteorological Station (5 km away) was 202 mm in the period 1970-2000. Excluding steep rocky slopes the catchment is covered in Monte shrubland, dominated by certain species of Larrea and further drought-resistant shrubs.

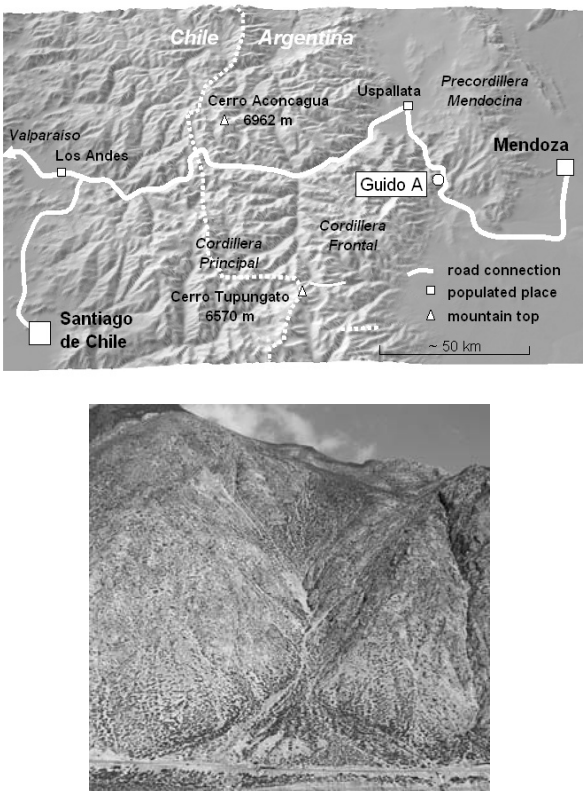

Fig. 1: The international road corridor Mendoza – Central Chile and the study area Guido A (left, hillshade from SRTM data); view of the study area Guido A from the opposite slope (right,, photo by M. Mergili). Note the international road crossing the distal part of the fan. The bottom of the photo represents a width of about 600 m.

Certain debris flows disrupting the international transit have been reported for the Guido area by the road maintenance agency, like during the afternoon and the evening of 08.04.1996 (later referred to as Event 1): A daily precipitation of 9.2 mm was recorded at the Guido meteorological station in the morning of the following day. 15,000 m³ of material had to be removed from the road over a total length of 4 km (including Guido A) in order to re-establish traffic. On 21.04.1996 (referred to as Event 2) the international traffic was disturbed by mass movements again. 40.0 mm daily precipitation were recorded at the Guido station, and 600 m³ of material had to be removed in several places at a length of 12 km, not directly including Guido A, according to the reports. This rather astonishing precipitation – disturbance relationship was possibly be caused either by removal of unstable material during the first event, or by local rainfall conditions different to those recorded at the gauge.

Materials and Methods

Soil samples were collected and analyzed for their physical and mechanical characteristics. Besides textural features and bulk density, cohesion c and angle of internal friction φ were determined in a laboratory using triaxial tests (Table 1). The major geomorphological and land cover classes in the study areas were mapped in the field and from orthophotos. A high resolution (5 m) digital elevation model (DEM) was derived from stereo pairs of aerial and terrestrial images. Meteorological records from stations close to the study areas were acquired on a daily basis from the Red Hidrológica Nacional (Argentina). Daily precipitation was broken down to short events of high intensity typical for the region. Finally, historical information on debris flow events in the previous years and decades was collected from existing records, newspapers, and official reports (Chapter 2).

Each land cover class was converted into an interception capacity (e.g. according to data published by Braud et al. 2001). Soil characteristics were assigned to each substrate class using the laboratory results. Hydrological parameters (Manning's roughness n and the Van Genuchten parameters) were extracted from the sediment characteristics using a pedotransfer table (Maurer 1997, Table 1).

Table 1: The major geotechnical and hydraulic characteristics of the granite residuals covering the study area Guido A as used in the model. ρ_d is dried bulk density, c is cohesion, φ is angle of internal friction, θ_s is saturation water content, and k_f is hydraulic conductivity. Lower threshold values for c and φ are the lowest values in the dataset for the granitic residuals of the Guido area, average values are the arithmetic mean within the same dataset (outliers excluded).

	grain size cl.	ρ_d kg m^{-3}	c N m^{-2}	φ deg.	θ_s vol-%	k_f cm h^{-1}
lower threshold	S (Sand)	1850	0	40.0	43	29.7
average	S (Sand)	1850	2000	41.5	43	29.7

A physically-based model combining hydrological processes and stability criteria was designed to distinguish between critical and non-critical constellations. Slope failures were considered to be initiated by seepage forces (saturation of the soil). Additionally, erosion by the kinetic energy of overland flow was computed. The slopes under investigation were considered as four-layered systems with vegetation, surface water table, soil, and bedrock. The model was implemented into the GRASS GIS environment as a raster module, using the C language.

The following simplifications were required for overcoming the complexity of nature and limitations with the input data: (1) soil was considered homogeneous over its entire vertical extent, without any stratification; (2) bedrock was considered impermeable and unconditionally stable; and (3) surface runoff was treated as unconcentrated overland flow without a predefined stream network.

The required parameters were fed into the model as raster maps, the meteorological data as text files. The model operates in four major steps. The steps (3) and (4) are based on a 3-dimensional matrix required to account for vertical variations of soil water status and failure conditions.

(1) Water input from precipitation is split up between vegetation and soil surface according to interception capacity. Surface water partly contributes to overland flow, and partly infiltrates into the soil. Infiltration is computed analogous to soil water movement (compare below), assuming a saturated top layer of the maximum grain size in the presence of a sufficient surface water table.

(2) Overland flow is simulated using the empirical Manning equation. The length of the time steps is dynamically determined depending upon flow velocity. Surface water table is updated for each pixel.

(3) Water flow between the cells of the soil is computed using the Richards equation for piston flow. Preferential flow is considered to occur only in the skeleton fraction of the soil, using relationships published by Sukhija et al. (2003). Water content, hydraulic conductivity, matric potential, and pressure head are updated for each time step.

(4) The dimensionless factor of safety *FS*, expressing the ratio between stabilizing and instabilizing forces, is the most widely used approach for is computed for modelling shallow slope failues. It can be expressed in certain ways, the following was chosen and applied to each cell (compare Fig. 2):

$$FS = \frac{1}{L}\left(\frac{c}{\gamma_w d \sin\alpha} + \frac{(L-m)\tan\varphi}{\tan\alpha}\right) \quad \text{Equation (1),}$$

where c (N m^{-2}) is soil cohesion, γ_w is the weight density of water (9810 N m^{-3}), d (m) is soil depth above the considered cell perpendicular to the soil surface, a is the local slope angle, m is the ratio of saturated soil depth to total soil depth (both above the considered cell), and φ is the angle of internal friction. The dimensionless factor L is computed as follows:

$$L = m\frac{\gamma_{sat}}{\gamma_w} + (1-m)\frac{\gamma_m}{\gamma_w} + \frac{R}{d} \quad \text{Equation (2),}$$

γ_{sat} (N m^{-3}) is the weight density of saturated soil, γ_m (N m^{-3}) the weight density of soil at field moisture content, and R (m) is the hydraulic radius. A detailed description of the approach and further literature are provided e.g. by Burton & Bathurst (1998). Cells with $FS > 1$ are considered stable, cells with $FS < 1$ are considered locally unstable. Strictly spoken $FS < 1$ predicts that an infinite slope will fail. In a first step it is assumed here that each cell will fail separately under such conditions, i.e. the volume of the cell down to the potential failure plane contributes to the total failed volume.

Erosion due to the kinetic energy of overland flow is less accessible to fully deterministic methods. Statistical relationships between stream power ω (kg s^{-3}) and detachment rate have been established for some soil texture classes. Stream power is computed as follows:

$$\omega = \gamma_w R v^2 \tan\alpha \quad \text{Equation (3),}$$

where R (m) is surface water table, and v (m s^{-1}) is flow velocity. The detachment rate (m s^{-1}) for sandy soil, as prevailing in the study area, was approached by combining relationships published by Zhang et al. (2003) and Salles et al. (2001).

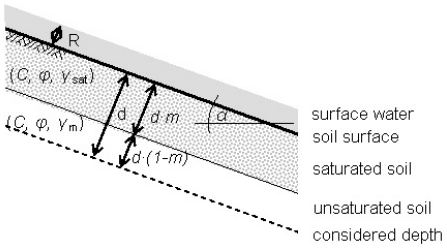

Fig. 2: Variables and arrangement of system elements for the computation of the factor of safety. In most cases the depth of the potential failure plane d is equal to the depth of saturated soil. For abbreviations refer to the text.

Results

The model was discretized with a horizontal resolution of 10 m and a vertical resolution of 25 cm. Two scenarios were computed, (1) for lower threshold strength parameter conditions, and (2) for average strength parameter conditions (Table 1). Fig. 3 illustrates the temporal variations of failed and eroded volume, flow velocity, and precipitation for the lower threshold strength parameter conditions. Slope failures peak as soon as the first layer becomes saturated, the second peak is connected to saturation of the second layer. About 60,000 m³ failed and 9,000 m³ eroded volume were predicted for Event 2. Erosion occurred mainly in the steeper sections of the valley bottom. Experiments with finer vertical resolutions indicated earlier onset of slope failures and smoother

graphs, whereas the total failed volume only changed slightly. For average strength parameter conditions, no slope failures were predicted and erosion by overland flow became the dominant process.

Event 1, at lower threshold strength parameter conditions, led to a total failed volume of about 2,800 m³ according to the model. 300 m³ were simulated to be eroded by overland flow. At average strength parameter conditions, the model predicted no slope failures.

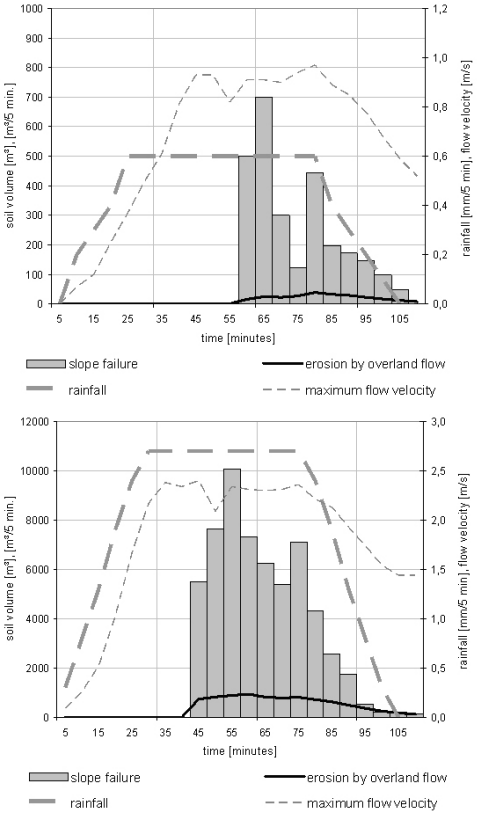

Fig. 3: Temporal development of failed and eroded volumes during Event 1 (left) and Event 2 (right), with precipitation and flow velocity as orientation, for lower threshold strength parameter conditions. Note the different scales of the ordinates.

The spatial distributions of failure depths for the two events at lower threshold strength parameter conditions are shown in Fig. 4.

Discussion

The model results for Event 1 show only some few unstable cells on steep, wet slopes. Thus the meteorological conditions were close to the threshold conditions for the potential initiation of debris flows. The 9.2 mm are within the range of thresholds for rainfall-triggered mass movements in the corresponding section of the Mendoza valley in general (6.6 to 12.9 mm per day) statistically determined by Moreiras (2005b) and therefore it is concluded that the preliminary simulation results are within a realistic magnitude.

As expected, the model reacts extremely sensitive to changes in input c and φ. Application of the lower threshold strength parameter conditions led to an overestimation of failures, compared to field observations, but is probably more realistic than the application of the average strength parameter conditions. However, more work is required on this issue, as well as on the investigation of global failure conditions (effects of slope geometry), and on the choice of suitable parameters for the simulation of erosion by overland flow.

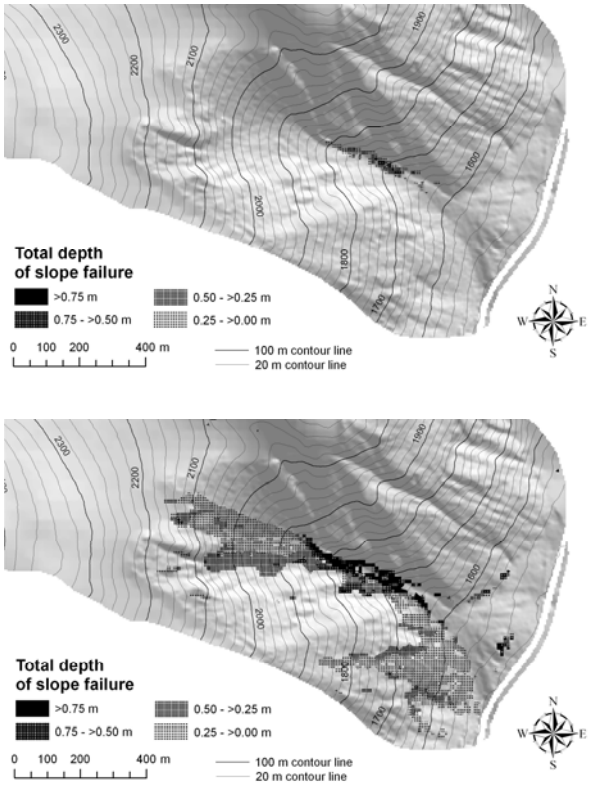

Fig. 4: Modelled potential failed depth during Event 1 (9.2 mm rainfall, top) and Event 2 (40.0 mm rainfall, bottom). The white band at the right repesents the international road.

More validation efforts are certainly required for model evaluation. For all of the areas under investigation, reports of historical debris flow events exist, specifying volumes of material deposited on the road, and being correlateable with certain precipitation (or, in one case, snow melt) events. In order to make the use of this data for validation purposes possible it will be required to simulate debris flow movement, a complex process. An established model will be used for this purpose (Pudasaini & Hutter 2007), and compared to a simple empirical approach.

With the required enhancements and careful validation and parameter sensitivity analysis (soil variables, but also rainfall duration and intensity), the model shall become a valuable tool for the prediction of debris flows on the small catchment scale.

Acknowledgements. The project is funded by the 'Doktoratsstipendium aus der Nachwuchsförderung der LFU', and by grants from the Office for International Relations and the Faculties for Natural Sciences, University of Innsbruck, as well as from the federal government of Upper Austria.

References

Braud, I., Vich, A.I.J., Zuluaga, J., Fornero, L. & Pedrani, A. (2001): Vegetation influence on runoff and sediment yield in the Andes region: Observation and modelling. *Journal of Hydrology* 254: 124-144.

Burton, A. & Bathurst, J.C. (1998): Physically based modelling of shallow landslide sediment yield at a catchment scale. *Environmental Geology* 35 (2-3): 89-99.

Maurer, T. (1997): Physikalisch begründete, zeitkontinuierliche Modellierung des Wassertransports in kleinen ländlichen Einzugsgebieten. Dissertation am Institut für Hydrologie und Wasserwirtschat der Universität Karlsruhe. 252 pp. In German.

Mikkan, R. (1997): Geomorfología y dinamica de vertientes del Valle del Río Mendoza entre las estaciones Guido y Uspallata, Provincia de Mendoza - Rep. Argentina. Revista de Estudios Regionales (Centro Interdisciplinario de Estudios Regionales CEIDER) 17: 81-135.

Moreiras, S.M. (2004): Landslide incidence zonation in the Rio Mendoza Valley, Mendoza Province, Argentina. *Earth Surface Processes and Landforms* 29: 255-266.

Moreiras, S.M. (2005a): Landslide susceptibility zonation in the Rio Mendoza Valley, Argentina. *Geomorphology* 66: 345-357.

Moreiras, S.M. (2005b): Climatic effect of ENSO associated with landslide occurrence in the Central Andes, Mendoza Province, Argentina. *Landslides* 2: 53-59.

Pudasaini, S.P. & Hutter, K. (2007): Avalanche Dynamics: Dynamics of rapid flows of dense granular avalanches. Springer, Berlin Heidelberg. 602 pp.

Salles, C., Poesen, J. & Govers, G. (2001): A Comparison of Rain Erosivity Parameters for Predicting Soil Detatchment on Interrills. In: Stott, D.E., Mohtar, R.H. & Steinhardt, G.C. (eds.): Sustaining the Global Farm. Selected papers from the 10th Int. Soil Conservation Organization Meeting: 834-837.

Savage, S.B. & Hutter, K. (1989): The motion of a finite mass of granular material down a rough incline. *Journal of Fluid Mechanics* 199: 177-215.

Sukhija, B.S., Reddy, D.V., Nagabhushanam, P. & Hussain, S. (2003): Recharge processes: piston flow vs preferential flow in semi-arid aquifers of India. *Hydrogeology Journal* 11: 387-395.

Zhang, G.-h., Liu, B.-y., Liu, G.-b., He, X.-w. & Nearing, M.A. (2003): Detachment of Undisturbed Soil by Shallow Flow. *Journal of the American Society of Soil Sciences* 67: 713-719.

A2.3 GRASS GIS and modelling of natural hazards: An integrated approach for debris flow simulation

First results of an application in the Central Andes

Martin Mergili and Wolfgang Fellin

article published in *OSGeo* 3 (FOSS4G 2007 Proceedings): 53-59, 2007

Background

Debris flows are rapid mass movements of water and debris, constituting a considerable hazard when interfering with people, buildings, or infrastructure. They are often triggered by heavy or prolonged rainfall or by extreme snow melt. Mobilization of the material occurs due to translational or rotational failure of saturated or undercut slopes, or by detatchment due to surface runoff or the debris flow itself. Various models do exist for simulating sub-processes included into debris flows, for example for detatchment (r.sim.sediment within the GRASS GIS environment), for soil hydrology (r.groundwater), for slope stability (Xie et al. , 2004), or for debris flow runout (Savage and Hutter , 1989; Pudasaini and Hutter , 2007). More integrated GIS-based approaches as attempted for example by Burton and Bathurst (1998) or Wichmann (2006) are scarce. Such approaches would be valuable for a quick assessment of hydrological thresholds for potential debris flow hazard regarding specified features at risk. This paper describes and discusses the development of such a model as GRASS GIS raster module. The model is designed for small catchments (few square kms) and is tested at the moment with seven study areas along the international road corridor from Mendoza (Western Argentina) to Central Chile, crossing the highest section of the Andes (figure 1). The preliminary results for the study area Guido A are presented.

Figure 1: Study areas. The preliminary results for Guido A are presented.

Model

Implementation and model design

The simulation model is implemented as a GRASS GIS raster module called r.debrisflow, based on the C programming language. Data management is facilitated using shell scripts. The model is in an intermediate stage of development right now, with major technical and methodical enhancements prospected for the near future. Additionally, a GUI for data management shall be created. By now, the latest development version can be downloaded from the homepage of the first author. r.debrisflow constitutes a framework of a number of sub-modules described in more detail below, the general model design is illustrated in figure 2. The sub-modules can be combined in two different ways, depending on the availability of input information:

Simulation mode 1: The entire hydrological, stability, detatchment and runout modelling is executed for a defined number of time steps during a rainfall or snowmelt event, requiring an extensive set of information as input, including meteorological data, an elevation model, soil mechanical and hydrological parameters and surface hydrological characteristics (including land cover).

Simulation mode 2: The zones of debris flow initiation are defined manually (e.g. from mapping in the field or from orthophotos), and only runout is computed. The advantage of this mode is that it requires much less input than the others, but, on the other hand, it is not suitable for predicting future events.

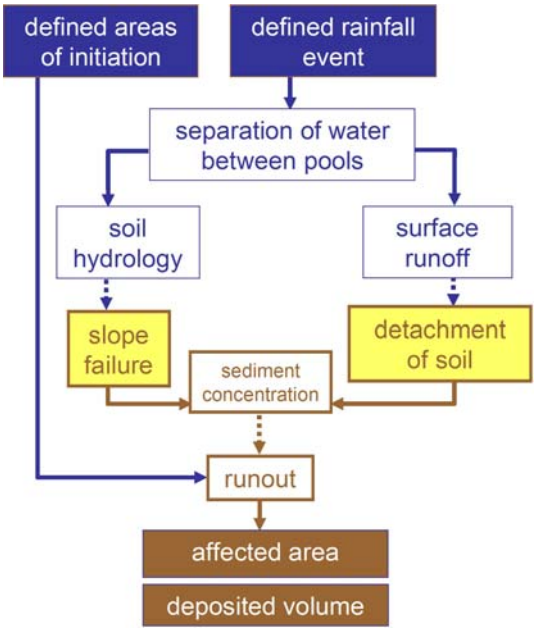

Figure 2: General model design.

Water input

Rainfall is read from the input file and added to the system by increasing the surface water table of each cell, reduced by interception. If a snow cover exists, snowmelt is computed for each cell with a user defined degree-day-factor and added to the surface water table.

Soil hydrology and slope stability

For this sub-module, a three-dimensional raster approach is used, down to the depth of bedrock (if known), or to a user-defined maximum soil depth. The soil is assumed to be homogeneous over its entire depth regarding its physical, hydrological and mechanical properties. Vertical flow between cells is computed with the Darcy-Equation. If the water content of a cell exceeds 90 per cent of the maximum content, groundwater flow is assumed to be parallel to the slope and it is tested whether the cell is stable or not, using an infinite slope stability approach (Xie et al. , 2004). For each pixel, the bottom of the deepest cell with a factor of safety lower than 1 is considered as failure plane (figure 3). It has to be pointed out that this approach constitutes a rough approximation to the reality with the character of a worstcase assumption: the stabilizing role of vertical water movement is neglected, and the destabilizing role of the assumed slope-parallel component is fully included in case of saturation. In the real world, both components are combined, resulting in more stable conditions than in the model.

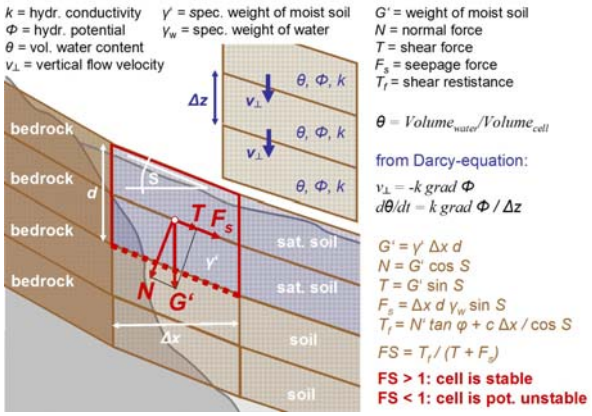

Figure 3: Subsurface hydrology and slope stability model.

Surface runoff and detatchment

All the water not infiltrated into the soil is added to the surface water table of the corresponding cell. Flow velocity from one cell to the other is computed using the Manning equation. If no flow channel is defined for any downward cell, flow takes place to all downward cells, weighted for slope angle. If a channel is defined, the entire flow moves there. Transport capacity is computed using the Yang (1973) equation, which it is supposed to suit best for the conditions in the study areas (O'Brien , 2003). Rates of detatchment are derived from the transport capacity. The model design is illustrated in figure 4.

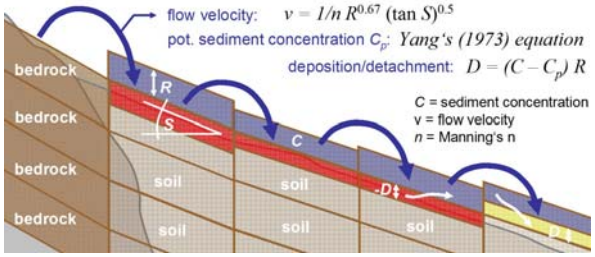

Figure 4: Surface runoff and detatchment model.

Debris flow runout and deposition

Debris flows are here understood in a strict sense, with a non-hydraulic flow regime and excluding heavily sediment-loaded water discharge. For this reason, the sediment concentration is computed for the mobilized soil volume of each cell:

(1) If the sediment concentration exceeds a threshold value (O'Brien , 2003), the entire mobilized volume is considered to develop into a debris flow. If mobilization occured due to slope failure, the cell is marked and runout of all the failed cells is computed at the end of the event. If mobilization occured due to detatchment, runout is calculated immediately at the end of the time step. This is a first approximation as the empirical runout models used (compare below) neglect the time required for runout.

(2) If the sediment concentration is too low for the development of a debris flow, the material is removed with surface runoff and either deposited downslope or removed from the system, following the Yang (1973) equation (compare figure 4). Though deposition from surface runoff does not fall into the concept of debris flow, it can provide valuable complementary information and is therefore regarded, too.

Debris flow runout itself can be simulated using physically-based models (Savage and Hutter , 1989; Pudasaini and Hutter , 2007), but they are complex and hard to be integrated into a GIS environment. Therefore it was decided to use a combination of empirical approaches first for estimating the runout distance and the distribution of the deposited volume (figure 5). Vandre (1985) developed an approach enabling the distinction between scouring and deposition areas, using threshold slope angles and the ratio between vertical distance of scouring and horizontal distance of deposition. Corominas et al. (2003) and Rickenmann (1999) used mobilized volume, angles, and runout distances for estimating the reach of the debris flow. These approaches, however, have the disadvantage that they dont allow distinguishing between areas of scouring and deposition, and therefore the distribution of the deposited material. The approach was included into the model as follows:

(1) The Vandre approach was applied with userdefined parameters for estimating distributed scoured and deposited volumes.

(2) The Corominas et al. and the Rickenmann approach were applied independently and then combined to an index.

The debris flow is routed downwards separately for each unstable cell, following a random walk (Hughes , 1995) weighted for slope angle and the existence of a defined channel, until the stop criteria for all of the three approaches is fulfilled. Though each cell is treated separately, the mobilized volume required for runout distance is calculated for each patch of debris flow initiation. In the area of scouring, the entire saturated soil column is considered to be removed, but never exceeding the depth of initiation. The initiated and scoured volumes are considered to distribute over the area of deposition as wedge shape rising towards the front.

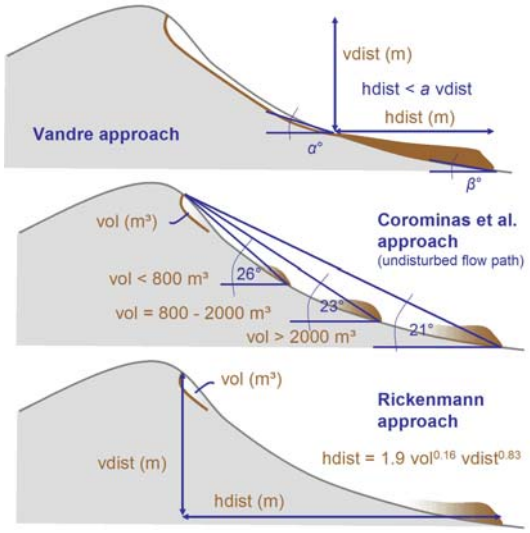

Figure 5: Runout models.

First results

The model was tested with the study area Guido A (compare figure 1). Mainly consisting of granite residuals, the soils of the catchment (area: 2 square kms) are relatively homogeneous. Therefore it was decided to use one single set of soil parameters for the entire area:

texture	ρ_d kg/m³	c_s N/m²	φ deg.	θ_s	k_f cm/h
Sand	1850	0	40.0	0.43	29.7

ρ_d is the dried bulk density of the soil, c_s is soil cohesion, φ stands for the angle of internal friction, θ_s is the maximum (saturated) water content, and k_f is the saturated hydraulic conductivity.

The figures 6 and 7 illustrate the mapped areas of debris flow initiation in the study area Guido A, and the patterns of surface change due to a debris flow event, based on the mapped areas of initiation and the computed patterns of scouring and deposition (simulation mode 2). The white line crossing the right part of the maps represents the international road, roughly coinciding with the distal part of the observed debris flow depositions.

The figures 8 to 11 show some of the simulation results for a hypothetical 100 mm rainfall event, corresponding to the maximum daily sum ever recorded at the nearby meteorological station, and therefore constituting a worst-case assumption (simulation mode 1). All maps show plausible patterns when compared to field observations. The areas of debris flow initiation and deposition are located correctly, but are overestimated compared to the patterns observed in the field (what is not surprising for a worstcase assumption).

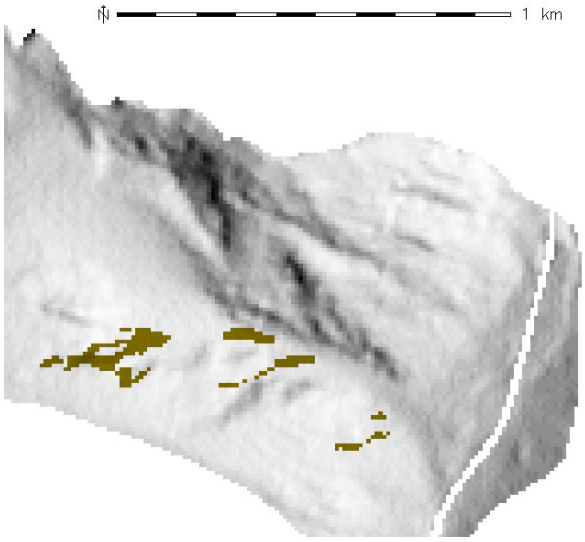

Figure 6: Mapped areas of clearly identifiable previous debris flow initiation, depth of initiation assumed as 0.75 m according to field evdence.

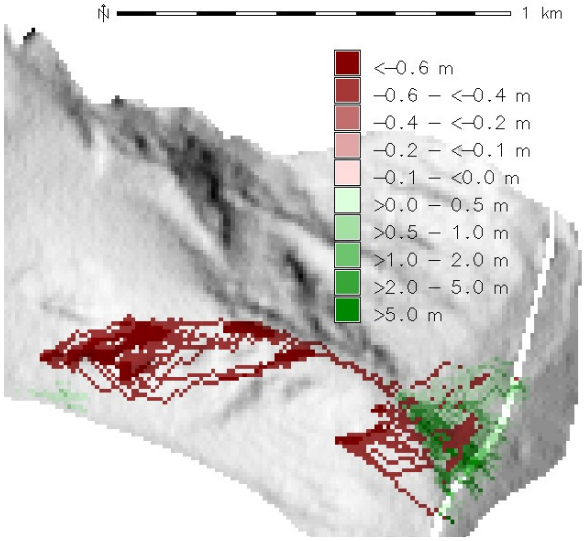

Figure 7: Simulated change of terrain height due to debris flow, using mapped areas of initiation.

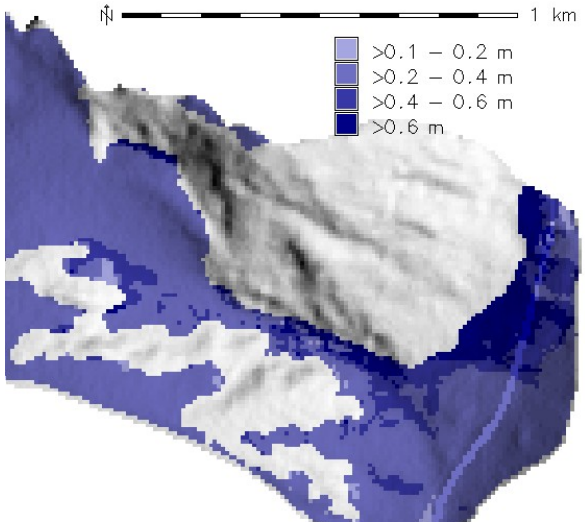

Figure 8: Maximum depth of saturation computed for 100 mm rainfall event.

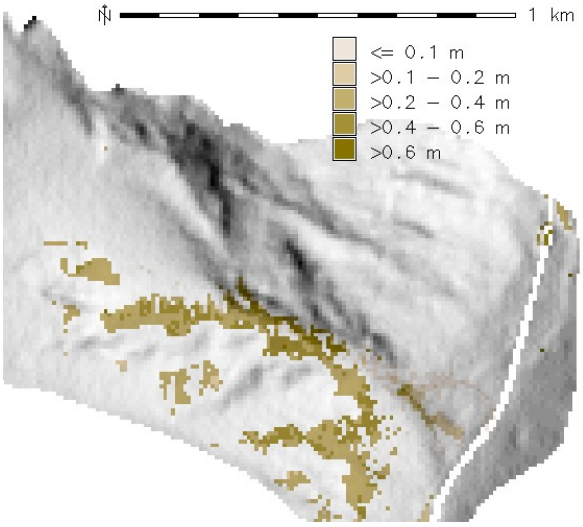

Figure 9: Simulated areas of potential debris flow initiation computed for 100 mm rainfall event.

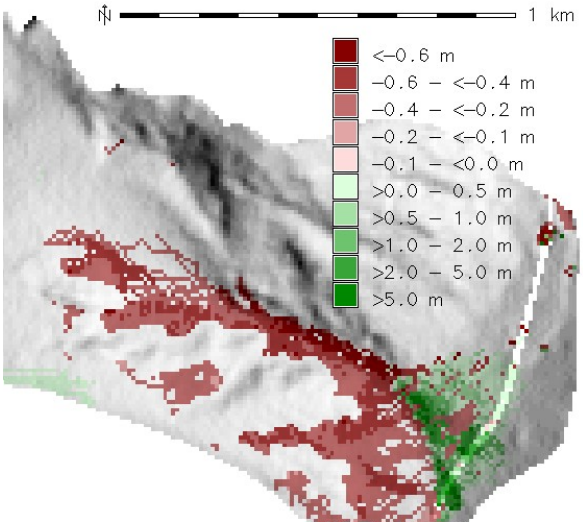

Figure 10: Simulated change of terrain height due to debris flow caused by 100 mm rainfall event.

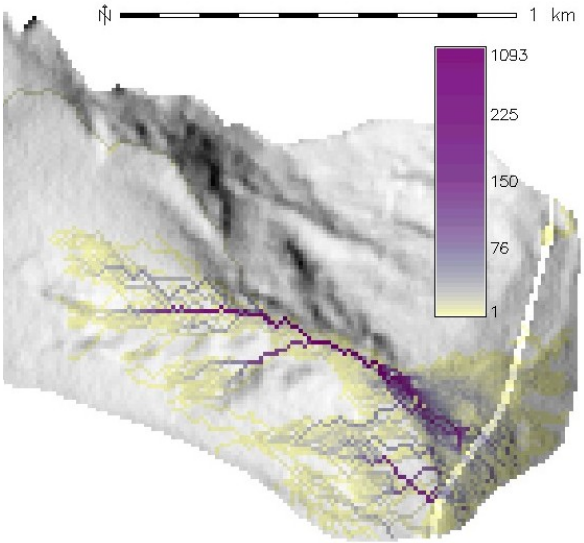

Figure 11: Debris flow index for 100 mm rainfall event, denoting number of cells the mobilized material of which hits the pixel.

The calculated sediment volumes deposited on the international road are within the same magnitude as those reported by the road authorities. When simulating the impacts of smaller rainfall events, the model results correspond well to the findings of Moreiras (2005) that debris flows in the Mendoza valley usually occur at daily rainfall sums exceeding 6.6 to 12.9 mm.

Discussion and Preview

Though the preliminary results for Guido A appear plausible, the simulation model still shows a number of shortcomings that have to be reworked.

(1) Infiltration of water into the soil is not yet modelled in a satisfactory way, so that the approach will have to be refined (Green-Ampt model). Slope-parallel groundwater flow will be included, too, for enabling a closer approximation to the reality of soil hydrology.

(2) The slope stability model as applied at the moment is only valid for plane, infinite, cohesionless slopes. For very shallow failures, this assumption is sufficiently close to reality, but for more deep-seated rotational failures, it is unsatisfactory and slope curvature has to be taken into account. Wilkinson et al. (2002) and Xie et al. (2003) could serve as examples for such an approach.

(3) The empirical approaches for debris flow runout shall be complemented by the implementation of a physiclly-based runout model according to Savage and Hutter (1989) and Pudasaini and Hutter (2007), or at least of an interface to a non GIS-based runout model.

(4) An interesting extension would be to introduce some probabilistic elements into the slope stability model (regarding the SINMAP model as an example) and into the distinction rules between debris flow and other types of movements.

(5) Finally, the model has to be applied to the remaining study areas (compare figure 1), and the results have to be tested carefully against the field observations and the validation data (reports about volumes of material deposited on the international road).

With the mentioned optimizations, r.debrisflow shall be a valuable tool for evaluating the potential magnitude of debris flows as a response to defined rainfall or snow melt events, including the possibility to determine meteorological thresholds for debris flow hazard. However, it has to be pointed out that all the results only denote potential ocurrences with the character of worst case scenarios or probabilities – it will probably never be possible to predict the actual response of a slope to a meteorological event in the real world, as nature is too complex to be fully understood in all details.

Acknowledgements: The project is funded by the 'Doktoratsstipendium aus der Nachwuchsförderung der LFU' and by grants from the Office for International Relations and the Faculties for Natural Sciences, University of Innsbruck, as well as from the Austrian Academy of Sciences and the Federal Government of Upper Austria. Thanks to Hans Stoetter, Axel Borsdorf, Clemens Geitner and Stella Moreiras for their support.

Bibliography

A. Burton, J.C. Bathurst (1998) Physically based modelling of shallow landslide sediment yield at a catchment scale. *Environmental Geology* 35,2-3: 89-99.

J. Corominas, R. Copons, J.M. Vilaplana, J. Altamir, J. Amigó (2003) Integrated Landslide Susceptibility Analysis and Hazard Assessment in the Principality of Andorra. *Natural Hazards* 30: 421-435.

B. D. Hughes (1995) Random walks and random environments: Volume 1: Random Walks. Oxford University Press. 652 pp.

X. Li (2007) Finite element analysis of slope stability using a nonlinear failure criterion. *Computers and Geotechnics* 34: 127-136.

S.M. Moreiras (2005) Climatic effect of ENSO associated with landslide occurrence in the Central Andes, Mendoza Province, Argentina. *Landslides* 2: 53-59.

J.S. O'Brien (2003) FLO-2D Users' Manual Version 2003.06, July 2003. FLO-2D Software Inc., Nutrioso, Arizona, USA. 232 pp. S.P. Pudasaini, K. Hutter (2007) Avalanche Dynamics: Dynamics

of rapid flows of dense granular avalanches. Springer, Berlin Heidelberg. 602 pp.

D. Rickenmann (1999) Empirical Relationships for Debris Flows. *Natural Hazards* 19: 47-77.

S.B. Savage, K. Hutter (1989) The motion of a finite mass of granular material down a rough incline. Journal of Fluid Mechanics 199: 177-215.

B.C. Vandre (1985) Rudd Creek debris flow. In: D.S. Bowles (ed): Delineation of landslide, flash flood, and debris flow hazards in Utah. Utah Water Research Laboratory, Utah State University, Logan, Utah, 117-131.

V. Wichmann (2006) Modellierung geomorphologischer Prozesse in einem alpinen Einzugsgebiet - Abgrenzung und Klassifizierung der Wirkungsräume von Sturzprozessen und Muren mit einem GIS. Eichstaeter geographische Arbeiten 15: 231 pp. In German.

P.L. Wilkinson, M.G. Anderson, D.M. Lloyd (2002) An integrated hydrological model for

rain-induced landslide prediction. *Earth Surface Processes and Landforms* 27: 1285-1297.

M. Xie, T. Esaki, G. Zhou, Y. Mitani (2003) Three-dimensional stability evaluation of landslides and a sliding process simulation using a new geographic information systems component. *Environmental Geology* 43: 503-512.

M. Xie, T. Esaki, M. Cai (2004) A time-space based approach for mapping rainfall-induced shallow landslide hazard. *Environmental Geology* 46: 840-850.

C.T. Yang (1973) Incipient motion and sediment transport. Journal of the Hydraulics Division. Proceedings of the American Society of Civil Engineers 99: 1679-1703.

A2.4 Integrated modelling of debris flows in the Central Andes based on Open Source GIS

Martin Mergili, Wolfgang Fellin, Stella M. Moreiras and Johann Stötter

abstract published in *Geophysical Research Abstracts* 10, 2008

An integrated model framework, designed as a module for the Open Source GIS software GRASS, was developed for simulating the occurrence of debris flows as a response to extreme rainfall events. The tool is suitable for study areas of few square kms and includes the following modules:

(1) Infiltration and surface runoff: water input from rainfall is distributed among vegetation, soil (Green-Ampt infiltration model), and surface runoff, which is calculated using the Manning-Strickler formula;

(2) Sediment transport: detachment of soil by surface runoff is computed using a sediment transport model, and locations where runoff may evolve into a debris flow are identified;

(3) Slope stability: an infinite slope stability approach is applied for identifying locations of potential slope failures which may contribute to debris flows;

(4) Runout and deposition: empirical rules and equations are applied for estimating runout distance of the identified debris flow material as well as the patterns of deposition.

For defined rainfall events, the model framework was applied to some selected study areas along the international road from Mendoza (Argentina) to Central Chile. All necessary parameters were investigated on a local scale: Soil samples were taken in the field and analyzed for their mechanical characteristics. Hydrological characteristics were derived using pedotransfer functions. High-resolution terrain models were generated from stereo imagery. The results of the scenarios were validated using historical archives and field observations.

Further development of the model framework will include particularly the implementation of a deterministic debris flow runout model, based on the Savage-Hutter concept.

A2.5 Simulation of debris flows based on Open Source GIS

Martin Mergili, Katharina Schratz, Stella M. Moreiras, Mechthild Thalhammer, Johann Stötter, Alexander Ostermann and Wolfgang Fellin

abstract accepted for the International Geological Congress, Oslo (Norway), 2008

A GIS-based model framework, designed as a raster module for the Open Source software GRASS, has been developed for simulating mobilization and movement of debris flows triggered by heavy rainfall. Designed for study areas of up to few square kilometers, the tool includes the following modules:

(1) Infiltration and surface runoff: water input from rainfall is distributed among the pools vegetation (interception), soil (Green-Ampt infiltration model), and surface runoff, which is calculated using the Manning-Strickler formula;

(2) Sediment transport: detachment of soil by surface runoff is estimated using a sediment transport model;

(3) Slope stability: an infinite slope stability approach is applied for detecting locations of potential slope failures which may contribute to debris flows;

(4) Debris flow mobilization: rules based on sediment concentration or water content and cohesion are applied to identify if detected areas of potential slope failure and erosion tend to produce a debris flow;

(5) Runout and deposition: a numerical model based on the Savage-Hutter theory for granular flow was implemented into GRASS and applied for estimating the runout distance of the identified debris flow material as well as the patterns of deposition. The results are compared to those yielded by empirical rules and equations.

The model framework was applied to some selected study areas along the international road from Mendoza (Argentina) to Central Chile. All necessary parameters were investigated on a local scale: Soil samples were taken in the field and analyzed for their mechanical characteristics. Hydrological characteristics were derived using pedotransfer functions. High-resolution terrain models were generated from stereo imagery.

The model was evaluated using field observations, historical archives, meteorological data, and the results of previous investigations in the area. Worst case scenarios and rainfall thresholds were worked out for the study areas as far as possible. The model output is quite sensitive to a number of parameters which are hard to capture (e.g. preferential flow through soil macropores, bed friction angle for debris flow runout), leading to uncertainties in the results which were quantified by an analysis of sensitivity.

The model framework as described above is mainly suitable for rainfall events of high intensity and short duration: the infinite slope stability model yields realistic results for shallow translational failures mainly connected to such events, but large uncertainties remain in the case of debris flows deriving from deep-seated rotational failures which are rather triggered by rainfall of long duration; therefore a better suited model approach for such failure mechanisms shall be added in the future; also more sophisticated approaches for soil water movement would be required for modelling the initiation of debris flows triggered by rainfall events of long duration.

A2.6 An Open Source model for the simulation of granular flows: First results with GRASS GIS and needs for further investigations

Martin Mergili, Katharina Schratz, Mechthild Thalhammer, Wolfgang Fellin and Alexander Ostermann

article accepted for *OS Geo* (FOSS4G 2008 Proceedings), 2008

Abstract

Granular flows like avalanches or debris flows pose a major threat to communities and infrastructures in mountain regions all around the globe. Besides the mobilization of snow or debris material, which is a complex issue on its own, the runout behaviour of granular flows is an important determinant for the degree of hazard connected to such processes. Empirical-statistical and semi-deterministic GIS-based Open Source models for the runout of avalanches, landslides, and debris flows do exist, for example in GRASS GIS or SAGA GIS. However, their general validity and their predictive capacity are limited as they do not fully account for the physical processes governing the flow. In contrast, some physically-based models do exist on the market, but they are either expensive or difficult to handle and therefore not widely used. Some of the models have a limited capability, too. No freely available, user-friendly full capability software for physically-based modelling of granular flows does yet exist.

The major goal of the study presented here is to fill this gap. It was decided to use the Savage-Hutter (SH) model, which is one of the most advanced concepts for describing the motion of granular flows. The SH model is based on a system of differential equations for the conservation of mass and momentum. Velocity is assumed to be constant over each vertical profile across the flow. Solutions have been found for relatively simple topographies or predefined channels by using shock-capturing numerical schemes.

For the beginning, a solution developed for debris flows following a talweg of a slope with rather smooth concave cross-section was implemented into GRASS GIS as a raster module named r.avalanche. The talweg in this solution is supposed to have a curvature in vertical direction only. The model output was tested against results from the literature for simple artificial topographies (plane and concave slopes running out into a horizontal plane), and against field data for real catchments in the Argentine Andes. The results were promising, but there is need for more research:

- The present implementation yields reasonable approximations for relatively simple topographies without pronounced horizontal curvature of the flow channels. It fails, however, for more complicated topographies. Therefore, an appropriate extension of the Savage-Hutter theory for arbitrary topography has to be worked out and implemented into GRASS;

- The entrainment of particles (snow or soil, respectively) may have a prominent role for runout length and volume deposited and shall therefore be included;

- It shall be taken into account that granular flows are often two-phase flows (solid and liquid fractions).

Additionally, a larger number of study areas with very good availability of parameters and data from past granular flows has to be used for model evaluation, including avalanches and debris flows of different types and sizes. At the moment, data management (including display of the results) for r.avalanche works relatively user-friendly via a shell script named r.avalanche.sh. For the future, it is planned to design a Graphical User Interface (GUI) for further facilitating the use of the program.

Background

GIS methods play a prominent role in mapping and prediction of landslide, debris flow, and avalanche hazard and risk. They enable an efficient management of spatial data at all scales, usually in raster or vector format. Whilst the GIS market was and still is dominated by proprietary and often expensive software products, the Open Source segment has recently gained a lot of popularity among scientists, national and regional authorities, and companies. A large array of Open Source GIS products, distributed under the GNU license, is available. GRASS – due to its modular design – allows the straightforward implementation of new modules using the C language and is widely used among natural scientists. Examples of applications of GRASS in the field of natural hazards are the RiskBox including two rock fall simulation algorithms (Cannata 2007) or r.debrisflow, a debris flow simulation program (Mergili & Fellin 2007; Mergili et al. submitted).

GIS methods are widely used with statistical or deterministic models for landslide initiation as well as with empirical-statistical approaches (Vandre, 1985; Rickenmann, 1999) or semi-deterministic models (Gamma, 2000; Wichmann, 2006) for runout of debris flows and snow avalanches. Such methods require a lot of parameter calibration for specific study areas and events, leading to a limited capacity for class A predictions.

Though fully deterministic models for simulating the runout of granular masses date back to the 1950s (Voellmy 1958), GIS implementations of such concepts are still rather scarce. Since the 1980s, various models for the motion of debris flows and flow avalanches have been developed by Savage & Hutter (1989), Takahashi et al (1992), Iverson (1997), or McDougall & Hungr (2004). Particularly the Savage-Hutter (SH) model has gained a lot of attention in the scientific community. The SH model assumes an incompressible fluid moving down an inclined plane, subject to Coulomb bed friction and internal friction. The SH model is based on a system of partial differential equations of mass and momentum balance (compare Eq. [1] to [3] in Chapter 2). The model is scale-invariant, meaning that validation is possible with small-scale experiments as well as with large-scale granular flows in nature.

Solutions for a set of idealized channel topographies have been elaborated (e.g. Pudasaini 2003). Some problems, however, remain unsolved. Among these is the question of entrainment or deposition of soild or fluid, which is a difficult issue due to the complex conditions at the upper and lower boundaries of the flow. Other models (e.g. Iverson 1997; McDougall & Hungr 2004) differ from the SH model in rheological assumptions, geometry, or the details of the numerial implementation (Harbitz 1998). Among all of them, the most detailed comparisons with experiments or field observations have been carried out for the SH model so far.

Chau & Lo (2004) modified the model of Takahashi et al. (1992) to model flow path and deposition of debris flows threatening the Leung King Estate (Hong Kong, China), based on a GIS.

Methods

The module *r.avalanche* provides a fully deterministic model for the motion of granular flows like debris flows, snow avalanches, or some types of industrial flows. It was developed as a raster module for GRASS GIS, using the C programming language. A shell script (*r.avalanche.sh*) facilitates data management (input and display). Raster maps and a set of parameters compiled in a text file serve as input. The program code as well as a documentation and a detailed manual can be downloaded from www.uibk.ac.at/geographie/personal/mergili/scripts.html.

The model builds on a solution of the SH model for simple concave topographies with an only vertically curved flow path ("talweg") running out into a horizontal plane, presented by Wang et al (2004) and illustrated in Figure 1. The current release of *r.avalanche* is therefore only suitable for a simple terrain with straight channels. Future development of the model is aimed at overcoming this problem (compare Chapter 4). The solution elaborated by Wang et al (2004) is based on a curvilinear coordinate system aligned with the "talweg".

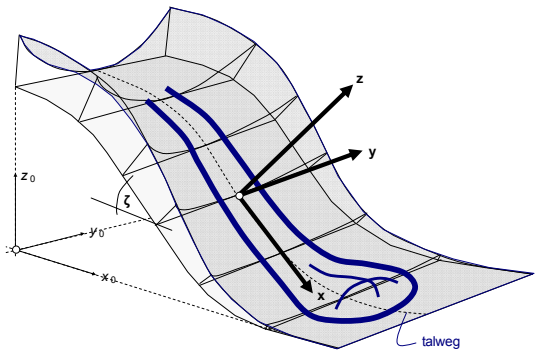

Figure 1: A typical topography suitable for *r.avalanche* (modified from Wang et al, 2004).

The SH theory is valid for a cohesionless, granular, incompressible material which can be considered as a fluid continuum. It has to be emphasized that all variables are dimensionless, meaning that the model is scale-invariant and can be used for simulating small-scale laboratory tests as well as large-scale flow phenomena in nature. The fundamental equations of the SH model are stated as follows:

$$\frac{\partial h}{\partial t} + \frac{\partial}{\partial x}(hu) + \frac{\partial}{\partial y}(hv) = 0 \qquad [1],$$

$$\frac{\partial}{\partial t}(hu)+\frac{\partial}{\partial x}(hu^2)+\frac{\partial}{\partial y}(huv)=hs_x-\frac{\partial}{\partial x}\left(\frac{\beta_x h^2}{2}\right) \quad [2],$$

$$\frac{\partial}{\partial t}(hv)+\frac{\partial}{\partial x}(huv)+\frac{\partial}{\partial y}(hv^2)=hs_y-\frac{\partial}{\partial y}\left(\frac{\beta_y h^2}{2}\right) \quad [3],$$

where $h = h(x,y)$ is the avalanche thickness, and u and v are the depth-averaged velocities in downslope and cross-slope direction, respectively. s_x and s_y are the net driving accelerations, the parameters β_x and β_y are determined by local slope and earth pressure. It is referred to Wang et al (2004) for a description of the geotechnical details of the model and the way how to solve the differential equations for the specific topographic situation illustrated in Figure 1. In particular, the differential equations Eq. [1] to [3] were solved using the NOC (Non-Oscillatory Central Differencing) scheme, which is a numerical scheme that prevents unphysical oscillations.

Furthermore, a slope limiter had to be used in order to restrict the size of the gradients of the flow. In the present study, the so-called minmod limiter, which is known to be the most diffusive one, reducing numerical oscillations, was chosen (compare Wang et al. 2004).

The resulting numerical scheme elaborated by Wang et al (2004), used for the implementation into GRASS, is complex and shall not be presented here. For understanding the GIS-specific aspects of *r.avalanche* it is sufficient to know that, for each time step, the avalanche thickness h and the depth-averaged velocities u and v are computed for each cell, based on the values of the surrounding 3x3 environment, the previous time step, the boundary conditions (topography, internal friction, bed friction), and additional variables. The simulation is repeated for a user-defined number of time steps. For stability reasons, time step length has to be kept sufficiently small to fulfill the CFL (Courant-Friedrichs-Levy) condition:

$$CFL_x = \max_{alli,j}\left(\frac{|u_{i,j}|+\sqrt{(\beta_x)_{i,j}\,h_{i,j}}}{\Delta x_{i,j}}\right) \quad [4],$$

$$CFL_y = \frac{\max_{alli,j}\left(|v_{i,j}|+\sqrt{(\beta_y)_{i,j}\,h_{i,j}}\right)}{\Delta y} \quad [5].$$

Here, Δx and Δy are cell sizes in x and y direction, and i and j are the cell numbers in x and y direction. The length of the time step Δt has to be smaller than half the minimum of CFL_x and CFL_y. In the model, the length of one time step Δt is determined dynamically, based on the CFL condition from the previous time step.

The SH model and its extension by Wang et al (2004) are not designed for GIS environments and therefore lead to difficulties when being implementated into GRASS. The model uses dimensionless formulations, whereas in GIS it is necessary to use dimensional values. Pudasaini (2003) provided a scaling procedure for solving this problem. The scaling is based on the variables L (typical avalanche length), and H (typical avalanche depth). A value of 1 m can be assumed for both of them. From now on, the dimensional variables are denoted by a cap.

$$\hat{x} = Lx \quad [6], \qquad \hat{y} = Ly \quad [7], \qquad \hat{h} = Lh \quad [8],$$

$$\hat{u} = u\sqrt{gL} \quad [9], \qquad \hat{v} = v\sqrt{gL} \quad [10],$$

$$\hat{t} = t\sqrt{L/g} \quad [11],$$

where g is gravity.

The major difficulty, however, is that the solution of Wang et al (2004) is based on a curvilinear coordinate system, aligned with a single, horizontally straight "talweg" (the predominant direction of the flow; compare Figure 1). Three steps are required for converting the original rectangular coordinate system in which the input raster maps are provided into the coordinate system to be used for the simulation:

(1) the coordinate system is rotated around the $\hat{z}$ axis, so that the expected predominant flow path – derived from two user-provided pairs of coordinates in the flow channel – is aligned with the new x direction;

(2) a reference surface is created, defined by the flow path and an inclination of zero in y (cross-slope) direction;

(3) based on this reference surface, the cell size Δx for each x parallel to the reference surface is computed. The elevation is defined as the height of the terrain perpendicular above the reference surface. This can not be done analytically: an iterative algorithm is required, increasing the shift based on the horizontal surface until tested height and terrain height converge.

Results

The module *r.avalanche* was first tested for a simple incline running out in a horizontal plane (Figure 2).

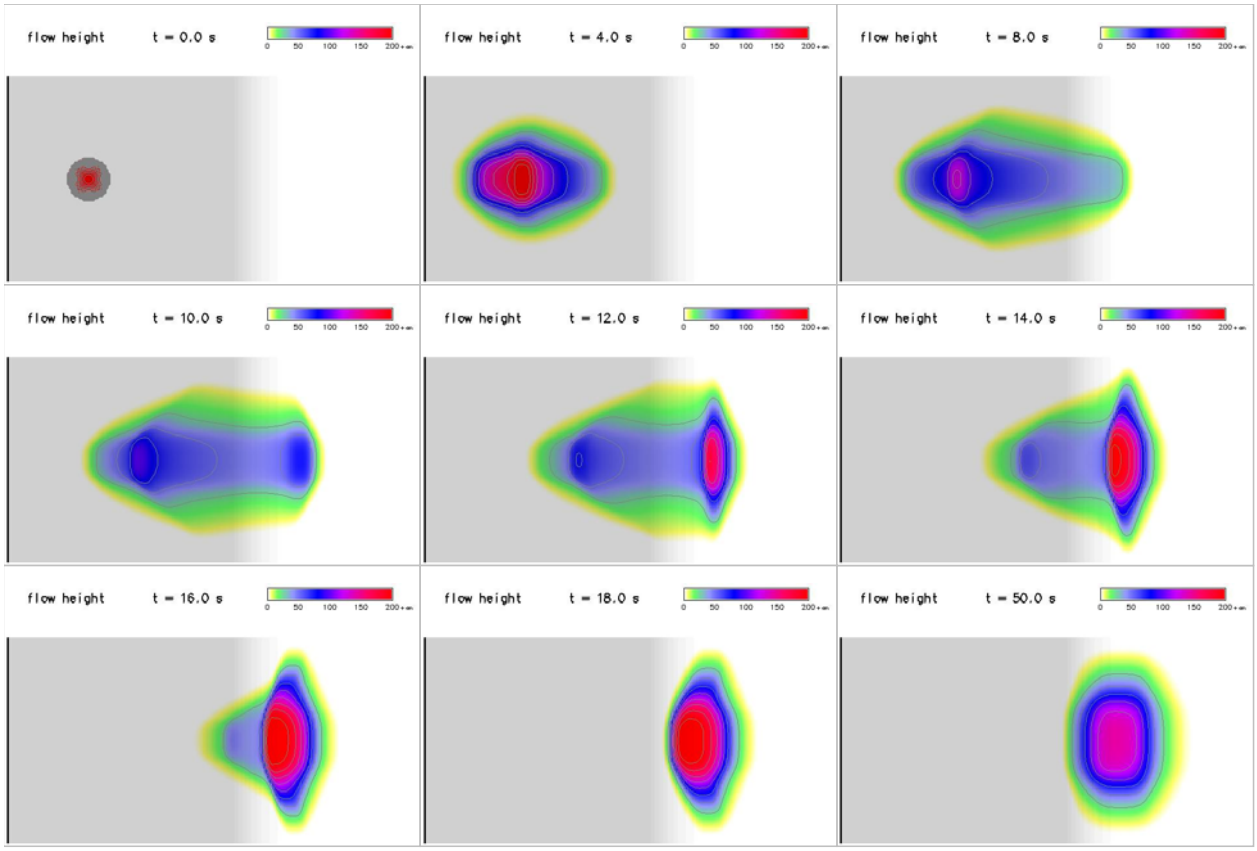

Figure 2: Debris flow runout over a simple topography with a bed friction angle δ = 28°

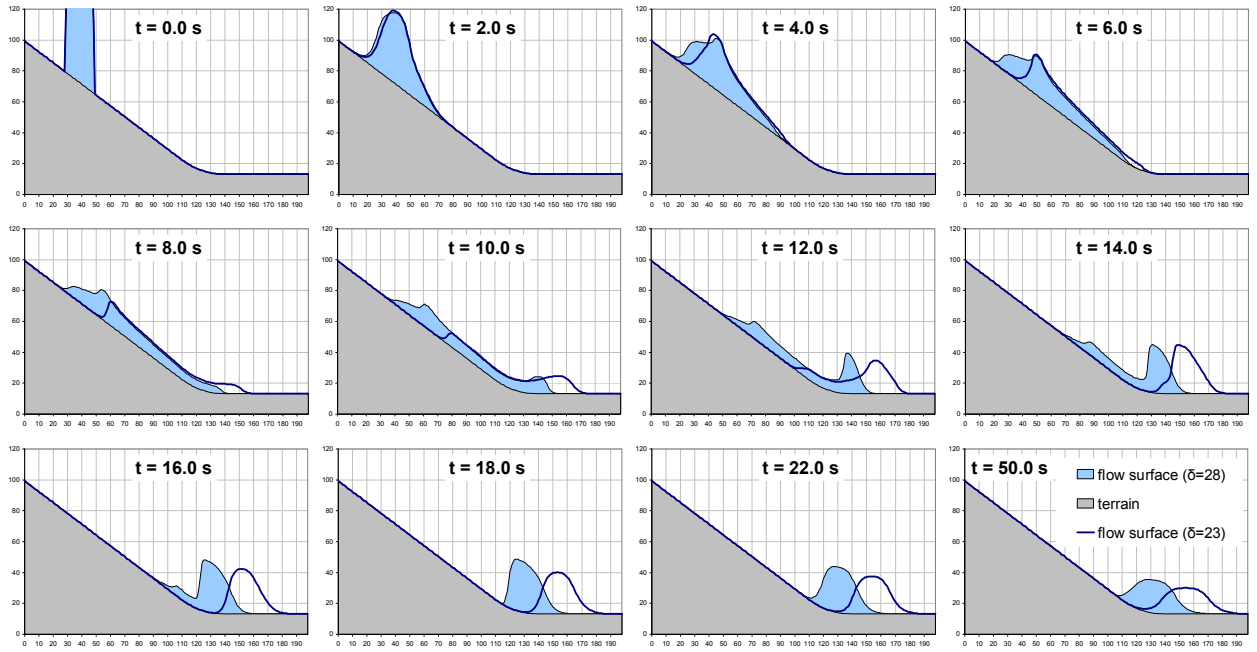

Figure 3: Longitudinal profiles through a debris flow or avalanche running over a simple topography, comparing the influence of different bed friction angles (23° and 28°).

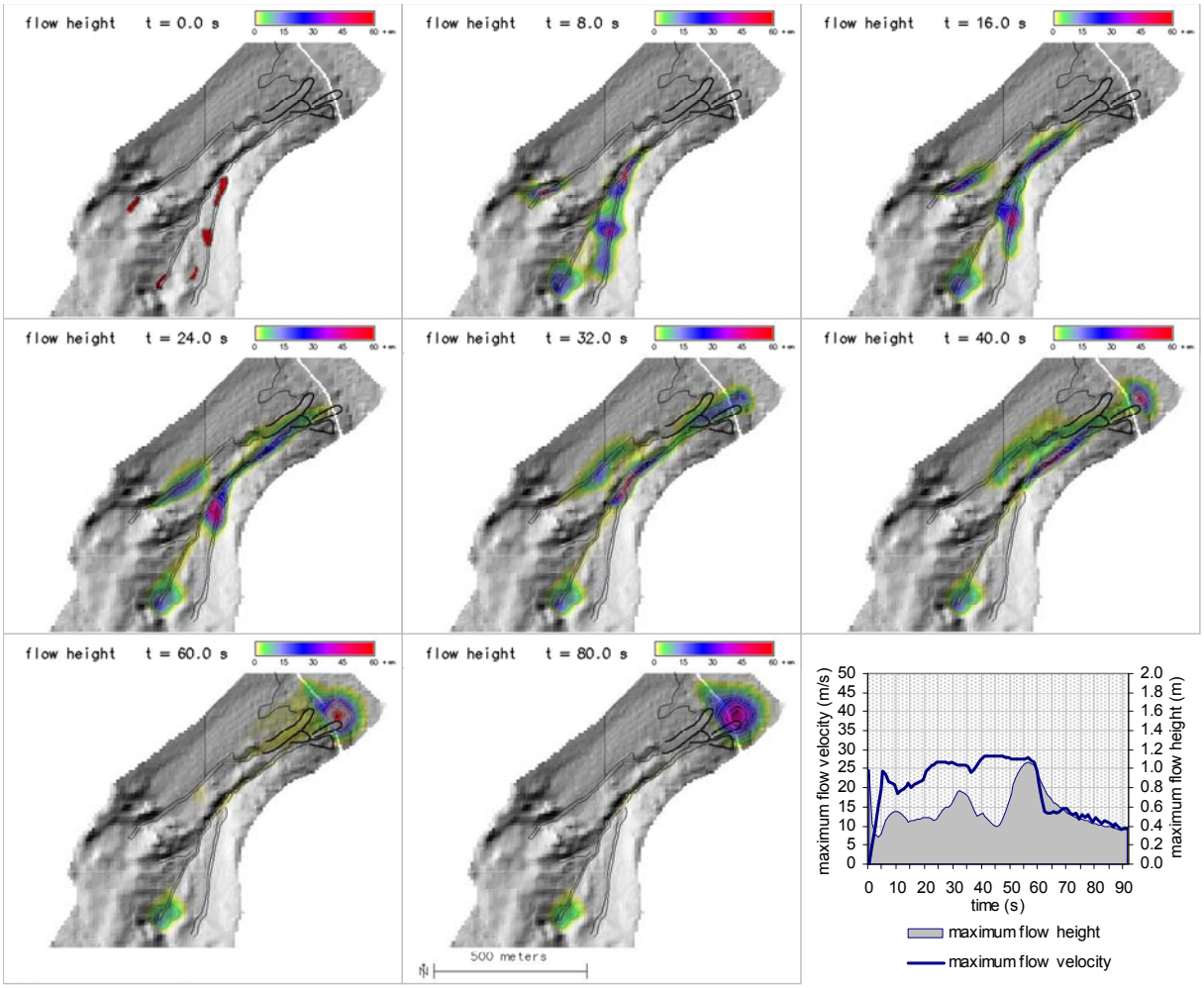

Figure 4: Debris flow runout over a real topography with a bed friction angle δ = 33°. Spatio-temporal distribution of flow depth and time series of maximum flow depth and velocity. Black lines indicate observed delineation of debris flow mobilization (fine) and deposition (bold).

Whilst varying the angle of internal friction φ between 32° and 37° showed only a minor influence on the runout behaviour, a decrease of bed friction angle σ from 28° to 23° led to a significant increase of runout length (Figure 3). These results and the spatial patterns of the motion of the flow are in line with those shown by Wang et al (2004).

The model was then applied to a real study catchment near Mendoza in the Argentine Andes (spatial resolution: 5 m; the DEM was derived by stereo-matching of aerial photos and satellite imagery, the starting areas were mapped from an orthophoto). The runout length was in best accordance to field observations when using a bed friction angle σ = 33°, which is a rather high value compared to those used for other studies. The spatial patterns of deposition indicated a degree of lateral spreading which was not observed in the field (Figure 4), a phenomenon which may be caused by insufficient representation of topographic details by the elevation model on the one hand, and by using a too coarse spatial resolution (in order to keep the computation time at an acceptable level) on the other hand.

Discussion and preview

The first version of *r.avalanche* presented in this paper succeded in simulating flow phenomena over simple topographies without major changes of flow direction. For more complex topographic conditions, however, it fails. The future steps of program development shall be:

(1) to select and adapt a sound method for modelling rapid granular flows over arbitrary topographies. The method shall be extended by incorporating particle entrainment, which can have important implications for the runout behaviour of granular flows, and and the role of pore fluid. The differential formulation of the model will be derived analytically, using and extending the existing models;

(2) to devise an appropriate numerical scheme (including shock capturing) for solving the equations derived in (1). Numerical solutions of the analytical model for arbitrary topography will be elaborated and implemented into GRASS GIS, analogous to the present version of *r.avalanche*;

(3) to evaluate the quality of the developed approach by comparing it to existing methods and models (DAN, SAMOS) and to validate the results with data from past snow avalanches and debris flows. One particularly interesting case would be the Nomash River Landslide, where McDougall & Hungr (2005) showed the large impact of entrainment on runout. Finding suitable values for the bed friction angle for different types of terrain would be an essential step towards enabling class A predictions with *r.avalanche*.

Furthermore, a more efficient way of data management during the computation in order to decrease the computation time would facilitate computations at higher spatial resolutions.

In the present version, the execution of *r.avalanche* relies on text files and command lines. For the future, a user interface facilitating data management and replacing *r.avalanche.sh* would be desirable.

References

Cannata, M 2007, RiskBox: Natural Hazards and Risks Analysis within the GIS GRASS. Oral presentation at the FOSS4G conference, Victoria, Canada.

Chau, KT & Lo, KH 2004, 'Hazard assessment of debris flows for Leung King Estate of Hong Kong by incorporating GIS with numerical simulations.' *Natural Hazards and Earth System Sciences* 4, pp. 103-116.

Gamma, P 2000, dfwalk – Ein Murgang-Simulationsprogramm zur Gefahrenzonierung. *Geographica Bernensia* G66, Bern. In German.

Iverson, RM 1997, 'The physics of debris flows.' *Reviews of Geophysics* 35, pp. 245-296.

McDougall, S & Hungr, O 2004, 'A Model for the Analysis of Rapid Landslide Motion across Three-Dimensional Terrain.' *Canadian Geotechnical Journal* 41, pp. 1084-1097.

McDougall, S & Hungr, O 2005, 'Dynamic modeling of entrainment in rapid landslides.' *Canadian Geotechnical Journal* 42, pp. 1437-1448.

Mergili, M. & Fellin, W. 2007, 'GRASS GIS and modelling of natural hazards: an integrated approach for debris flow simulation.' *OSGeo* 3 (FOSS4G 2007 Proceedings), pp. 53-59.

Mergili, M, Fellin, W, Moreiras, SM & Stötter, J submitted, 'Simulation of debris flows in the Central Andes based on Open Source GIS: Chances, limitations and parameter. sensitivity'. Submitted to *Natural Hazards*.

Perla, R, Cheng, TT & McClung, DM 1980, 'A Two-Parameter Model of Snow Avalanche Motion.' *Journal of Glaciology* 26, pp. 197-207.

Pudasaini, SP 2003, Dynamics of Flow Avalanches Over Curved and Twisted Channels. Theory, Numerics and Experimental Validation. Dissertation at the Technical University of Darmstadt, Germany.

Pudasaini, SP & Hutter, K 2007, Avalanche Dynamics: Dynamics of rapid flows of dense granular avalanches. Springer, Berlin Heidelberg New York.

Rickenmann, D 1999, 'Empirical Relationships for Debris Flows.' *Natural Hazards* 19, pp. 47-77.

Savage, SB & Hutter, K 1989, 'The motion of a finite mass of granular material down a rough incline.' *Journal of Fluid Mechanics* 199, pp. 177–215.

Takahashi, T, Nakagawa, H, Harada, T & Yamashiki, Y 1992, 'Routing debris flows with particle segregation.' *Journal of Hydraulic Research* 118, pp. 1490–1507.

Vandre, BC 1985, 'Rudd Creek debris flow', in Bowles, DS (ed.), Delineation of landslide, flashflood, and debris flow hazards in Utah. Utah Water Research Laboratory, Utah State University, Logan, Utah.

Voellmy, A 1955, 'Über die Zerstörungskraft von Lawinen.' *Schweizerische Bauzeitung* 73, pp. 159-162, 212-217, 246-249, 280-285. In German.

Wang, Y, Hutter, K & Pudasaini, SP 2004, 'The Savage-Hutter theory: A system of partial differential equations for avalanche flows of snow, debris, and mud.' *ZAMM - Journal of Applied Mathematics and Mechanics / Zeitschrift für Angewandte Mathematik und Mechanik* 84, pp. 507-527.

Wichmann, V 2006, Modellierung geomorphologischer Prozesse in einem alpinen Einzugsgebiet. Abgrenzung und Klassifizierung der Wirkungsraeume von Sturzprozessen und Muren mit einem GIS. *Eichstaetter Geographische Arbeiten* 15, Eichstätt. In German

Appendix 3: Manuals

The following manuals shall facilitate the use of *r.debrisflow* and *r.avalanche*. They can be downloaded from

www.uibk.ac.at/geographie/personal/mergili/scripts

The program files, detailed descriptions of the background of the models, and a test dataset can be obtained from this website, too.

A3.1 MERGILI, M. 2008: *r.debrisflow* Version 1.3. A model framework for simulating potential initiation and movement of debris flows based on GRASS GIS. User's manual.

A3.2 MERGILI, M. 2008: *r.avalanche* Version 1.1. A model framework for simulating the motion of granular flows based on GRASS GIS. User's manual.

r.debrisflow Version 1.3

A model framework for simulating mobilization and movement of debris flows

based on GRASS GIS

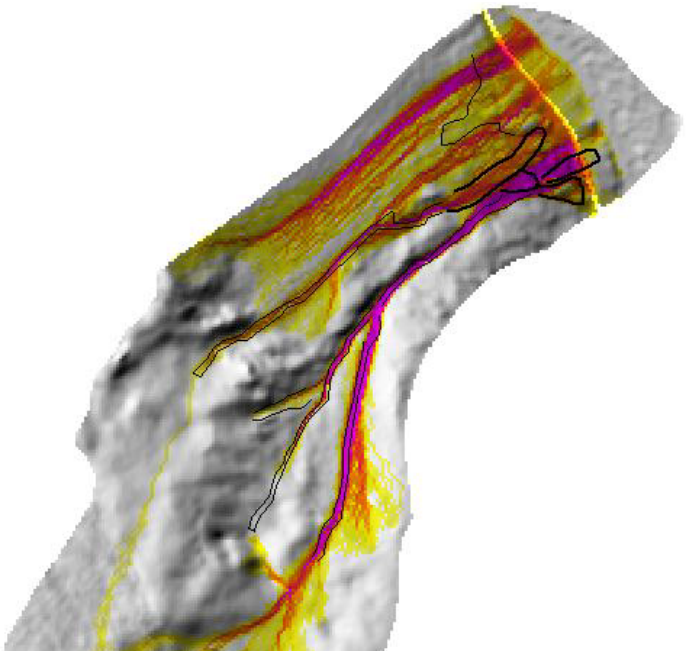

A.3.1 User's manual for r.debrisflow

by Martin Mergili

Institute of Geography, University of Innsbruck, Austria
www.uibk.ac.at/geographie/personal/mergili
martin.mergili@uibk.ac.at

July 2008

r.debrisflow is a GIS-supported model framework for simulating the potential spatial patterns of debris flow initiation, movement, and deposition. It is physically-based in general, but includes some empirical-statistical components. *r.debrisflow* is designed as a raster module for the software *GRASS*. The scientific concepts behind *r.debrisflow* are summarized in Section 4.2.

r.debrisflow, the present document (including a description of the background of the model), and a test dataset can be downloaded from

www.uibk.ac.at/geographie/personal/mergili/scripts

In contrast to most of the other *GRASS* raster modules, management of the data and the parameters (input and output) is not done by adding parameters to the *r.debrisflow* command, but by an additional shell script (*r.debrisflow.sh*) with various functionalities, including derivation of secondary input parameters from primary ones. This is required due to the complexity of the model framework.

Every user is encouraged to report encountered bugs or errors to

martin.mergili@uibk.ac.at.

Furthermore, the developer would be grateful for receiving comments regarding

- experiences with the program, shortcomings, recommendations for improvements (scientific concepts, ease of use);
- parameters chosen for certain study areas;
- interest in cooperation in application and further development.

The model, as applicable with *GRASS*, is running under the *GNU General Public License* (www.gnu.org). *r.debrisflow* has been created with the purpose to be useful for modelling of debris flows. It has been developed with care, and much emphasis has been put on ensuring its scientific value. Nevertheless, every user has to be aware that it is only a computer program created by a human being, which may contain technical and topical errors and shortcomings. No responsibility can be taken by the developer for any types of deficiencies in the program or in the present document, or for the consequences of such deficiencies.

System requirements

r.debrisflow was developed and tested under *Fedora Core 6* with *GRASS 6.2.1*. It probably works on most other *UNIX* systems as well as with other versions of *GRASS*. The module itself should also be usable under *cygwin*, but the related shell script *r.debrisflow.sh* (compare below) would probably not work.

Please make sure to have a proper installation of *GRASS* before installing *r.debrisflow*. In case of doubt, please consult www.grass.itc.it.

Test dataset

A test dataset is provided together with the program, consisting of some text files and a *GRASS* location with the name *test_location*. All data is packed in the file *testdata.zip*.

test_prec.txt and *test_temp.txt* contain precipitation and temperature data in the format described below, while *test_param.txt* is the required parameter file. *test_ctrlpoints.txt* contains the control points (compare below). Table 1 shows the names of the raster and vector maps.

Table 1: Names of the maps of the test dataset

name of the map	description
test_mask	mask for study catchment (raster)
test_elev	elevation map at 5 m resolution (raster)
test_elev10	elevation map at 10 m resolution (raster)
test_soilclass	soil classes (raster)
test_soildepth	soil depth (raster)
test_landcover	land cover classes (raster)
test_hydcl	hydrological surface classes at 5 m resolution (raster)
test_hydcl10	hydrological surface classes at 10 m resolution (raster)
test_chanw	width of flow channel(s) at 5 m resolution (raster)
test_chanw10	width of flow channel(s) at 10 m resolution (raster)
test_road	road (object at risk; raster)
test_snowdepth	depth of snow cover (raster)
test_dinitdef	predefined depth of debris flow initiation (raster)
test_dscourdef	predefined maximum depth of entrainment (raster)
test_init_observed	observed patterns of debris flow initiation (line vector)
test_depd_observed	observed patterns of deposition from debris flow (line vector)

The test dataset is suitable to run *r.debrisflow* at spatial resolutions of 5 m or 10 m. Please note that the reclass tables described below are suitable for the soil and land cover classes in the test dataset – for other datasets, they have to be modified.

File management

The file system behind *r.debrisflow* consists of two parts:

- a *GRASS* mapset with all the spatially distributed input information as raster or vector maps, and
- a folder named *r.debrisflow*, which may be stored at any location in your `home` directory. The internal structure of the folder *r.debrisflow* may not be manipulated, otherwise some of the functionalities will fail.

The directory *r.debrisflow* contains the following subdirectories:

tools

The tools directory hosts the scripts required for installing and running *r.debrisflow*:

- *main.c*: the source code for *r.debrisflow*;
- *r.debrisflow.sh*: a shell script facilitating data input, management, and output (compare below);
- *install.sh*: a shell script helping to compile the source code (*main.c*).

data

It contains the input files of the meteorological data, the parameter file, and the file with control points (compare below), and a file for scaling the legends of the resulting maps to be displayed. The subfolder /recl contains reclass tables (for deriving secondary parameters from input datasets), the subfolder /colors contains colour tables for display.

temp

The temp directory contains temporary files created during the execution of *r.debrisflow.sh*. Its content shall not be manipulated manually, but only using the functionalities of *r.debrisflow.sh*.

results

It contains some simulation results (summary file, documentation file; compare below). However, the main results are stored as rasters in the active *GRASS* mapset.

docs

The docs directory contains this manual.

Installation

r.debrisflow has to be added to the *GRASS* raster library as a new module, based on the source code of the file *main.c*. For performing this task, log in as super user (su). call the script *install.sh* in the folder r.debrisflow/tools:

```
cd dir/r.debrisflow/tools
sh install.sh
```

dir may be any location in your home directory. The following prompt is displayed:

```
Full path to GRASS source (slashes at be-
ginning and end):
```

Here, enter the path to the location where GRASS is installed, for example

```
/usr/gissoft/grass-6.2.2/
```

The Makefile is created, and compilation and installation are run automatically, so that *r.debrisflow* is ready to use.

Please note that you have to change to the tools directory as described above – if just entering

```
sh dir/r.debrisflow/tools/install.sh
```

an error message will display and *r.debrisflow* will not be installed.

Data management

r.debrisflow uses text files and rasters with predefined names as input. The shell script *r.debrisflow.sh* serves for creating these datasets, and for generating secondary datasets from primary information (e.g. hydraulic conductivity from grain size class). It must be run from within the used *GRASS* mapset:

```
cd dir/r.debrisflow/tools
sh r.debrisflow.sh
```

r.debrisflow.sh offers the following modules:

```
1 --> Parameter and data input
2 --> Preparation of parameters
3 --> Execution of simulations
4 --> Post-processing of model output
5 --> Display of results
6 --> Removal of result files
7 --> Cleaning of file system
8 --> Exit
```

By entering a number, the corresponding module is executed.. The modules are described in detail below. *r.debrisflow.sh* has to be called from within the *GRASS* mapset with all the required raster maps.

Parameter and data input

Module 1 consists of a sequence of prompts for input data and parameters. If no input is given for a prompt (by just pressing *ENTER*), the dataset specified earlier is kept. The numbers behind the prompts denote the modes of simulation (compare Section 4.2) for which the corresponding dataset is required.

```
--> Catchment map (boolean): |1|2|3|4|5|6|
```

Boolean raster map defining the catchment of interest (identified by cell values of *1*, areas out of the catchment are defined by *0* or *no data*).

```
--> Elevation map (m): |1|2|3|4|5|6|
```

Raster map of elevation (meters).

```
--> Soil depth map (m): |1|2|3|4|5|6|
```

Raster map of soil depth (in meters). If soil depth is not known, it should be set to a high value. For bedrock, it has to be set to *0*.

```
--> Hydrological surface classes map (inte-
ger): |1|2|3|4|5|6|
```

Integer raster map of the distribution of the hydrological surface classes (*1* for defined flow channel, *2* for multiple flow channel or unconcentrated overland flow). Care has to be taken that the cell size of the map corresponds to the cell size of the simulation it shall be used for. Particularly the defined channels (class *1*) have to be clean and continuous.

```
--> Channel width map: |1|2|3|4|5|6|
```

Raster map denoting total width of flow channel(s) for each cell, connected to the hydrological surface classes: *1* (defined flow channel): width of the flow channel; *2* (multiple channels or unconcentrated overland flow): ratio between sum of width of all flow channels crossing a cell and cell width, perpendicular to the steepest slope. The advantage of this approach is to be largely independent from cell size, at least for quite uniform distributions of channels.

Also here, the cell size has to correspond to the cell size of the simulation it shall be used for. Additionally, it has to fit to the hydrological surface classes map exactly in order to avoid serious problems during simulation.

```
--> Objects at risk map (boolean):
    |1|2|3|4|5|6|
```

Boolean raster map denoting objects at risk (*1* for presence of potential objects at risk like roads or buildings, else *0* or *no data*).

```
--> Soil classes map (integer): |1|2|3|4|5|
```

Integer raster map with predefined soil classes (compare *Module 2*: Preparation of parameters). The numbers of the classes may be chosen freely, but must fit to the corresponding reclass tables (compare Table 3).

```
--> Land cover classes map (integer):
    |1|2|3|4|
```

Integer raster map with predefined land cover classes (compare *Module 2*: Preparation of parameters). The numbers of the classes may be chosen freely, but must fit to the corresponding reclass tables (compare Table 3).

```
--> Estimated depth of mobilization of soil
    map (m): |6|
```

Raster map showing the patterns of estimated potential debris flow initiation (depth in meters).

```
--> Estimated depth of entrainment of soil
    map (m): |5|6|
```

Raster map showing the patterns of estimated potential depth of entrainment by debris flows (meters).

```
--> Snow depth map (m): |1|2|3|4|
```

Raster map denoting depth of snow cover (meters).

Table 2: Input parameters (single values) for *r.debrisflow*

variable	description	unit	examples of value(s)
γ_g	grain specific weight of soil	N m^{-3}	26,500 for quartzitic soil
u_1	exponent for weighting of slope angle for surface runoff random walk	exponent	3
u_2	exponent for weighting of slope angle for debris flow runout random walk	exponent	4
p_r	percolation through rock (ratio compared to effective rainfall plus snow melt)	ratio	0.0–1.0
ST_1	factor for calibration of critical runoff formula	factor	1.0
ST_2	factor for calibration of potential sediment load formula	factor	0.005 – 0.01
ST_3	factor for calibrating detachment by surface runoff	factor	0.1 cell sizes
ST_4	factor for calibrating deposition from surface runoff		factor
C_{min}	minimum sediment concentration for development of debris flow	ratio	0.45
C_{max}	maximum sediment concentration for development of debris flow in cohesive soil	ratio	0.55
–	minimum depth of unstable or detached soil for initiation of debris flow	m	various
–	minimum number of adjacent failed cells for development of debris flow	integer	depends on cell size
–	minimum volume of unstable or detached soil for development of debris flow	m^3	various
–	factor for computing μ (compare Eq. 35)	factor	0.13
–	exponent for computing μ (compare Eq. 35)	exponent	-0.25
–	lower threshold for μ	coefficient	0.045 – 0.15
–	upper threshold for μ	coefficient	0.3
M/D	mass-to-drag ratio	m	75
–	slope threshold for entrainment/deposition	deg	15
–	velocity threshold for entrainment/deposition	m s^{-1}	10
–	maximum depth of debris flow deposit	m	5 – 15
–	options for distribution of material deposited from debris flow	integer	1 for wedge-shaped towards the front, 2 for even
–	Minimum slope angle for initiation of debris flows	deg.	20 – 30

Table 3: Spatially distributed input parameters of *r.debrisflow*, specified in *Module 1* or automatically created in *Module 2* of r.*debrisflow.sh*, respectively

shortcut	description	unit	derived from	name of reclass table dir/r.debrisflow/data/recl/	modes of simulation 1	2	3	4	5	6
catchment	definition of catchment of interest	boolean	specified as input in *Module 1*		x	x	x	x	x	x
elevation	elevation above sea level	m			x	x	x	x	x	x
soildepth	depth of soil	m			x	x	x	x	x	x
soilclass	class of soil	integer			x	x	x	x	x	
landcovclass	class of land cover	integer			x	x	x	x	x	
hsc	hydrological surface class	integer			x	x	x	x	x	x
chanwidth	width of flow channel	m, ratio			x	x	x	x	x	x
riskobj	definition of objects potentially at risk	boolean			x	x	x	x	x	x
dinitdef	depth of debris flow initiation	m								x
dscourdef	maximum depth of entrainment	m							x	x
snow	depth of snow cover	m				x	x	x	x	
soil	presence of soil	boolean	soildepth		x	x	x	x	x	x
alpha	local slope angle	deg.	elevation		x	x	x	x	x	x
my	friction coefficient for runout	coeff.			x	x	x	x	x	x
icp	interception capacity of the vegetation	m	land-covclass	recl_lcv_icp4_min.txt recl_lcv_icp4_max.txt	x	x	x	x		
croot	root cohesion	N m^{-2}		recl_lcv_croot_min0.txt recl_lcv_croot_max0.txt	x	x	x		x	
droot	rooting depth	m		recl_lcv_droot_min1.txt recl_lcv_droot_max1.txt	x	x	x		x	
nman_add	vegetation surcharge for Manning's *n*	summand		recl_nman_add_min3.txt recl_nman_add_max3.txt	x	x		x		
textclass	texture class of soil	integer	soilclass	recl_soil_class0.txt	x	x	x	x	x	
d30	d30 grain diameter of soil	m		recl_soil_d305.txt	x	x		x		
d50	d50 grain diameter of soil	m		recl_soil_d505.txt	x	x		x		
d90	d90 grain diameter of soil	m		recl_soil_d905.txt	x	x		x		
skeleton	skeleton content of soil (> 2 mm)	ratio		recl_soil_s3.txt	x	x	x	x	x	
gammad	dry specific weight of soil	N m^{-3}		recl_soil_gammad0.txt	x	x	x	x	x	
csoil	soil cohesion	N m^{-2}		recl_soil_c0.txt	x	x	x		x	
phi	soil angle of internal friction	deg.		recl_soil_phi1.txt	x	x	x		x	
nman_bas	basic value for Manning's *n*	summand		recl_nman_bas_min3.txt recl_nman_bas_max3.txt	x	x		x		
pref	factor for preferential (macropore) flow, to be multiplied with infiltration capacity	factor		recl_soil_pref_min1.txt recl_soil_pref_max1.txt	x	x	x	x		
thetar	soil residual water content	ratio	textclass	recl_hyd_thetar3.txt	x	x	x	x		
thetas	soil saturated water content	ratio		recl_hyd_thetas2.txt	x	x	x	x	x	
psi	matric suction at wetting front	m		recl_hyd_psi5.txt	x	x	x	x		
k	soil hydraulic conductivity	m s^{-1}		recl_hyd_k9.txt	x	x	x	x		

The remaining four required input datasets are the names of files which have to exist in the

```
dir/r.debrisflow/data
```

directory. In each of the files, each line has to consist of a label (first column) and a value (second column). The content of the label only serves for enhancing readability, it has no influence on the simulation, but it may not contain tabulators. It is important, however, that it does exist and is separated from the actual value by a tabulator, as only the part of the file after the tabulator is used. Please consult the example files (starting with ***example_***) as reference.

`--> Precipitation file (mm): |1|2|3|4|`

File with precipitation values (from measured data or hypothetical). header information:

- first line: elevation of rain gauge (meters);
- second line: duration of basic time step (seconds);
- third line downwards: precipitation values (mm), sum of one time step per line.

`--> Temperature file (°C): |1|2|3|4|`

File with temperature values (from measured data or hypothetical). Header information:

- first line: elevation of thermometer (meters);
- second line: daily minimum temperature (°C);
- third line: daily maximum temperature (°C);
- forth line: temperature for computing snow melt (°C);
- fifth line: critical temperature (rainfall/snowfall boundary, °C);
- sixth line: vertical gradient for daily minimum temperature (°C m^{-1});
- seventh line: vertical gradient for daily maximum temperature (°C m^{-1});
- eighth line: degree day factor for snow melt (m $°C^{-1}$).
- Ninth line downwards: temperature values, one time step per line.

Temperature is only relevant when including snow melt or when it is lower than the critical temperature separating rainfall and snow fall. If the raster map of snow depth is 0 m over the entire catchment, the specified values have no influence on the results of the simulation as long as the exceed the critical temperature.

```
--> Parameter file: |1|2|3|4|5|6|
```

File with list of parameters for simulation, one per line. The parameters have to be specified in a defined order (Table 2).

In the folder `dir/r.debrisflow/data/`, a file with example parameters (*example_param.txt*) is provided.

```
--> Legend file: |1|2|3|4|5|6|
```

File with user-specified values serving as maxima for the display of the output maps.

In the folder `dir/r.debrisflow/data/`, an example for a legend file (*example_legend.txt*) is provided. The order shown in this file has to be kept for all legend files

```
--> File with coordinates of control points:
    |1|2|3|4|
```

File with coordinates of some specific points for which some variables are documented for each time step. Each line contains one coordinate – first line the x coordinate of the first point, second line the y coordinate of the first point, third line the x coordinate of the second point, etc. Please note that, if you do not wish to specify control points, the file has to exist, anyway (otherwise, *r.debrisflow* will produce an error message), but may be empty.

Preparation of parameters

No user inputs are required for this module, which serves for the automatic derivation of secondary input parameter maps from the maps specified in *Module 1*. A slope raster map is derived from the elevation model (*r.slope.aspect*), and a boolean presence of soil map is derived from the soil depth map. Secondary parameter maps are derived from the land cover and soil classes using reclass tables (compare Table 3; *r.reclass*). All the reclass tables have to be stored under

```
dir/r.debrisflow/data/asc/
```

and must exactly be named as shown in Table 3. All the reclass tables must correspond to the following pattern:

```
original value_1 = derived value_1
original value_2 = derived value_2
...
original value_n = derived value_n
end
```

for example

```
1 = 34
3 = 5
...
10 = 37
end
```

All numbers must be left-aligned and all equal signs have to stand in one column.

The numbers before the `.txt` extension of the reclass files denote the factor with which the original derived values have to be multiplied before writing them into the reclass table. This is necessary because the *r.reclass* module of *GRASS* is not able to cope with non-integer values. After reclassification, the magnitude of the derived raster maps is corrected automatically.

For parameters with *max* or *min* at the end of the name of the reclass table, the pixel values of the created raster map are randomly distributed between the minimum and the maximum values. If this is not desired, the maxima and minima have to be identical.

Example reclass tables are stored in the abovementioned directory, but the tables have to be modified for each study area, except the tables for the hydraulic parameters, which refer to grain size classes according to the following key: *1*=S; *2*=LS; *3*=SL; *4*=SCL; *5*=SC; *6*=L; *7*=CL; *8*=SIL; *9*=C; *10*=SICL; *11*=SI; *12*=SIC.

It is possible to skip *Module 2* and instead create all the parameter maps manually. In this case, please note that the naming conventions have to be met exactly in order to ensure the functionality of the simulation (compare Table 3).

Execution of simulations

Prompts for mode of simulation and cell size are displayed:

```
--> Mode of simulation (integer):
--> Cell size (m):
```

The options for the mode of simulation are described in Section 4.2 (the corresponding number has to be entered). The cell size has to be chosen in accordance with the input datasets and the required level of detail. For test simulations it is recommended to choose larger cell sizes in order to reduce computing time.

After specifying these two parameters, the *GRASS* raster module *r.debrisflow* is called by pressing *ENTER*. Additionally to an array of raster maps, a summary file (*summary.txt*) and a documentation file (*doc.txt*) are written and stored in the

```
dir/r.debrisflow/results/
```

directory. The summary file contains global values (particularly volumes) for each basic time step. The documentation file contains values for the coordinates specified as control points (*ctrlpoints.txt*), for each short time step (compare Table 4 for the names of the variables).

Please note that if you wish to run *r.debrisflow* manually, not from within *r.debrisflow.sh*, you have to copy

the input files to the `dir/r.debrisflow/temp/` directory as ***prec.txt*** (precipitation), ***temp.txt*** (temperature, ***param.txt*** (parameter file), and ***ctrlpoints.txt*** (control points). These files shall not contain labels, but only the values.

Post-processing of model output

All the resulting raster maps are cleaned (cells outside of the defined catchment are set as no data), and the sediment balance from debris flows is computed. For the modes of simulation ***1*** and ***4***, the sediment balance from surface runoff as well as the sediment concentration for each time step and the maximum sediment concentration are computed. Some of the major resulting maps are prepared for display (compare below). In order to ensure comparable legends, a maximum value is assigned to each type of legend (depth of wetting front; factor of safety; sediment concentration; failure, detachment, and entrainment; deposition; sediment balance; debris flow index; depth and velocity of surface runoff; depth of load). The legend file has to be stored in `dir/r.debrisflow/data/` and to be specified during the data and parameter input (compare above) The color tables have to be stored in `dir/r.debrisflow/data/colors`.

Furthermore, three prompts do appear when calling the module. Each task is accepted by typing ***1***, or denied by typing ***0***.

`--> Calculate statistics (boolean) ?`

> Maximum values of runoff velocity, runoff depth, and load depth over the entire event are computed. Please note that the option is not applicable to all modes of simulation (***1***, ***2***, and ***4*** for the runoff variables, ***1*** and ***4*** for load depth).

Table 4: Output from *r.debrisflow* (after running *Module 4*). r=raster map, s=summary file, d=documentation file

shortcut	description	unit	versions			time steps	mode of simulation					
			r	s	d		1	2	3	4	5	6
vflow	flow velocity of surface runoff	m s^{-1}	x		x	all	x	x		x		
vflow_max	maximum flow velocity	m s^{-1}	x			–	x	x		x		
dflow	depth of surface runoff	m	x		x	all	x	x		x		
dflow_max	maximum depth of surface runoff	m	x			–	x	x		x		
dload	depth of sediment load of surface runoff	m	x		x	all	x			x		
dload_max	maximum depth of load	m	x			–	x			x		
streampower	stream power (as additional information)	N m^{-1} s^{-1}	x			all	x	x		x		
deltaddetw	detachment by surface runoff (short time step)	m			x	–	x			x		
ddetw	cumulative detachment by surface runoff	m	x	x		all	x			x		
ddetw_val	detachment by surface runoff (basic time step)	m	x			all	x			x		
deltaddepf	deposition from surface runoff (short time step)	m			x	–	x			x		
ddepf	cumulative deposition from surface runoff	m	x	x		all	x			x		
ddepf_val	deposition from surface runoff (basic time step)	m	x			all	x			x		
dbudget_wat	cumulative sediment balance from water flow	m			x	all	x			x		
dbudget_wat_val	sediment balance from water flow (time step)	m			x	all	x			x		
csed	sediment concentration of surface runoff	ratio	x			all	x			x		
csed_max	maximum sediment concentration	ratio	x			–	x			x		
dwfront_chan	depth of wetting front below flow channel(s)	m	x			pre-last	x	x	x	x		
dwfront_int	depth of wetting front between channel(s)	m	x			pre-last	x	x		x		
fos	factor of safety below flow channel(s)	ratio	x			last	x	x	x		x	
dfailpot	potential depth of slope failure	m	x	x		last	x	x	x		x	
dinit_fail	depth of debris flow initiation from slope failure	m	x	x		last	x	x	x		x	
dinit_detw	depth of debris flow initiation from detachment by surface runoff	m	x	x		last	x			x		
dinit	total depth of debris flow initiation	m	x			last	x	x	x	x	x	
dscour	depth of entrainment by debris flow	m	x	x		last	x	x	x	x	x	x
ddepd	depth of deposition from debris flow	m	x	x		last	x	x	x	x	x	x
dbudget_deb	sediment balance from debris flow	m	x			last	x	x	x	x	x	x
idepG	indicator for entrainment or deposition by debris flow according to the two-parameter friction model	integer	x			last	x	x	x	x	x	x
idepR	indicator for debris flow incidence according to RICKENMANN (1999) equation	integer	x			last	x	x	x	x	x	x
rcoef	runoff coefficient	ratio		x		all	x	x	x	x		
deltat	length of short time step	s		x		all	x	x	x	x	x	x

`--> Extract values for time steps (boolean) ?`

This option is only applicable for the modes of simulation *1* and *4*. Raster maps of detachment, deposition, and sediment balance for each time step are extracted from the rasters of cumulative values written by the simulation.

`--> Export maps to ascii (boolean) ?`

The resulting raster maps are exported as ascii rasters in order to be usable with other GIS software products like ArcGIS. The resulting files are stored in `dir/r.debrisflow/results/asc`.

In the output rasters, the display during program execution, and in the summary and documentation files, every variable is addressed by a shortcut (Table 4). The names of the resulting raster maps have the prefix *r_*. Depths (raster maps and documentation file) start with *d*. The volumes depicted in the display during simulation and in the summary file have the prefix *vol_* instead of *d*. The number at the end of the raster map names indicates the time step. Rasters, except those of runoff and sediment transport variables, are only written for the pre-last (depth of wetting front) or last time step (all other variables).

For example, the raster *r_ddepd20* shows the depth of deposition from debris flow for each pixel at the end of time step 20, while *vol_depd* indicates the volume deposited from debris flow over the entire study area.

Display of results

Some of the major resulting maps can be displayed using this module. The following parameters have to be specified:

`--> Azimuth of the sun for shaded relief map:`

All maps are displayed with a shaded relief as background, the azimuth of which has to be specified (in decimal degrees; recommended: 315).

`--> Export maps to jpg (1/0):`

The displayed maps can be automatically stored as `jpg` graphics in `dir/r.debrisflow/results/jpg`. If you wish to do so, please specify *1*, else *0*.

`--> Height of monitor in pixels:`

Please specify the height of the monitor for display – a value between 500 and 800 is recommended, depending on the size of your monitor.

`--> Observed patterns of debris flow initiation (line vector):`

A line vector map with areas of debris flow initiation observed in the field may be specified, if available, for facilitating the evaluation of the model results.

`--> Observed patterns of debris flow deposition (line vector):`

A line vector map with areas of debris flow deposits observed in the field may be specified, if available, for facilitating the evaluation of the model results.

A monitor opens, and a prompt with instructions appears in the terminal. The maps are displayed in a defined sequence – please enter the number of steps to move forward or backward, or *exit* to quit. If you have moved a defined number of steps fore- or backwards and would like to apply the same action again, you can just press *ENTER* to do so.

If you have chosen to export the maps as `jpg`, no prompts appear, but all maps are displayed and exported automatically, and the module is terminated.

Please note that the size of the monitor and the placement of some of the elements of the maps (legend, bar scale) are not suitable for all map width to height ratios. It may happen that some of the placement options have to be changed in the shell script *r.debrisflow* itself in order to design satisfactory layouts.

Removal of result files

All results (rasters and text files produced by *r.debrisflow* and *Module 4*) are deleted. All temporary files created in the modules *1* and *2* are kept, so that new simulations may be performed immediately.

Cleaning of file system

All temporary rasters and text files created by the modules *1* and *2* are deleted. They must be re-run in order to perform new simulations.

Exit

r.debrisflow.sh is exited and the default cell size is restored

r.avalanche

Version 1.1

A model for simulating runout of granular flows (debris flows and snow avalanches)

based on GRASS GIS

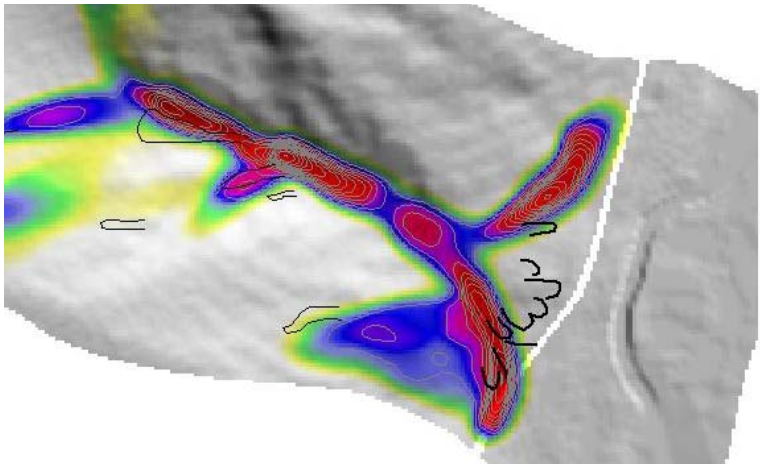

A3.2 User's manual for r.avalanche

by Martin Mergili

Institute of Geography, University of Innsbruck, Austria
www.uibk.ac.at/geographie/personal/mergili
martin.mergili@uibk.ac.at

July 2008

r.avalanche is a GIS-supported model framework for simulating the motion of granular flows like debris flows or snow avalanches over inclined surfaces. *r.avalanche* is designed as a raster module for the software *GRASS GIS*. The scientific concepts behind *r.avalanche* are summarized in Section 4.3.

r.avalanche, the present document (including a description of the background of the model), and a test dataset can be downloaded from

www.uibk.ac.at/geographie/personal/mergili/scripts

In contrast to most of the other *GRASS* raster modules, management of the data and the parameters (input and output) is not done by adding parameters to the *r.avalanche* command, but by an additional shell script (*r.avalanche.sh*) with various functionalities, including input of data and parameters as well as post-processing and display of the results.

Every user is encouraged to report encountered bugs or errors to

martin.mergili@uibk.ac.at.

Furthermore, the developer would be grateful for receiving comments regarding

- experiences with the program, shortcomings, recommendations for improvements (scientific concepts, ease of use);
- parameters chosen for certain study areas;
- interest in cooperation with application and further development.

The model, as applicable with *GRASS*, is running under the *GNU General Public License* (www.gnu.org). *r.avalanche* has been created with the purpose to be useful for modelling of debris flows. It has been developed with care, and much emphasis has been put on ensuring its scientific value. Nevertheless, every user has to be aware that it is only a computer program created by a human being, which may contain technical and topical errors and shortcomings. No responsibility can be taken by the developer for any types of deficiencies in the program or in this document, or for the consequences of such deficiencies.

System requirements

r.avalanche was developed and tested under *Fedora Core 6* with *GRASS 6.2.1*. It probably works on most other *UNIX* systems as well as with other versions of *GRASS*. The module itself should also be usable under *cygwin*, but the related shell script *r.avalanche.sh* (compare below) would probably not work.

Please make sure to have a proper installation of *GRASS* before installing *r.avalanche*. In case of doubt, please consult www.grass.itc.it.

Test dataset

A test dataset is provided together with the program, consisting of some text files and a *GRASS* location with the name *test_location*. All data is packed in the file *testdata.zip*.

Table 1 shows the names of the raster and vector maps. The test dataset is suitable to run *r.avalanche* at spatial resolutions of 5 m or 10 m.

Table 1: Names of the maps of the test dataset

name of the map	description
test_mask	mask for study area (raster)
test_elev	elevation map at 5 m resolution (raster)
test_elev10	elevation map at 10 m resolution
test_delta	bed friction angle (raster)
test_road	road potentially at risk (raster)
test_dinitdef	depth of flow initiation (raster)
test_init_observed	observed patterns of flow initiation (line vector)
test_depd_observed	observed patterns of deposit from flow (line vector)

File management

The file system *r.avalanche* consists of two parts:

- a *GRASS* mapset with all the spatially distributed input information as raster or vector maps, and
- a folder named *r.avalanche* which may be stored at any location of your `home` directory. The internal structure of the folder *r.avalanche* may not be manipulated, otherwise the functionalities are not more given.

The directory *r.avalanche* contains the following subdirectories:

`tools`

The `tools` directory hosts the scripts required for installing and running *r.avalanche*:

- *main.c*: the source code for *r.avalanche*;
- *r.avalanche.sh*: a shell script facilitating data input, management, and output;
- and *install.sh*: a shell script helping to compile the source code (*main.c*).

`data`

It contains the parameter file (*test_param.txt* as part of the test dataset). The subfolder `/colors` contains colour tables for the display of the results.

Table 2: Input parameters required for running *r.avalanche*

parameter	symbol (unit)	input format	description
catchment	– (boolean)	raster map	catchment of interest map
elev	z (m)	raster map	elevation map
delta	δ (degree)	raster map	basal angle of friction map
riskobj	– (boolean)	raster map	objects at risk (1 = present, 0 = absent)
dinit	*h0* (m)	raster map	starting material map
phi	φ (degree)	value	angle of internal friction of the debris flow material
L	L (m)	value	typical avalanche length (recommended: 1; compare)
H	H (m)	value	typical avalanche depth (recommended: 1; compare Section 4.3)
R	R (m)	value	typical radius of curvature (recommended: 1; compare Section 4.3)
deltatout	Δt_{out} (s)	value	interval between writing output (length of time step)
tmax	t_{max} (s)	value	time of simulation until it stops
vmin	v_{min} (m s^{-1})	value	velocity at maximum flow depth at which simulation stops
xchan1, ychan1	– (m)	values	coordinates of first point in flow channel (for rotating coordinate system); each in one line
xchan2, ychan2	– (m)	values	coordinates of second pt. in flow channel (for rotating coordinate system); each in one line
xmin1, ymin1	– (m)	values	coordinates of lower left corner of area of interest; each in one line
xmax2, ymax2	– (m)	values	coordinates of upper right corner of area of interest; each in one line

`temp`

The `temp` directory contains temporary files created during the execution of *r.avalanche.sh*. Its content shall not be manipulated manually, but only using the functionalities of *r.avalanche.sh*.

`results`

It contains some simulation results (summary file, profile file). However, the main results are stored as rasters in the active *GRASS* mapset.

`docs`

The `docs` directory contains this manual.

Installation

r.avalanche has to be added to the *GRASS* raster library as a new module, based on the source code of the file *main.c*. For performing this task, call the script *install.sh* in the folder `r.avalanche/tools`:

```
cd dir/r.avalanche/tools
sh install.sh
```

`dir` may be any location in your `home` directory. The following prompt is displayed:

```
Full path to GRASS source (slashes at be-
ginning and end):
```

Here, enter the path to the location where GRASS is installed, for example

```
/usr/gissoft/grass-6.2.2/
```

The Makefile is created, and compilation and installation are run automatically, so that *r.avalanche* is ready to use.

Please note that you have to change to the tools directory as described above – if just entering

```
sh dir/r.avalanche/tools/install.sh
```

an error message will display and *r.avalanche* will not be installed.

Data management

r.avalanche uses text files and rasters with predefined names as input. The shell script *r.avalanche.sh* serves for creating these datasets.

r.avalanche.sh offers the following modules:

```
1 --> Parameter and data input
2 --> Execution of simulations
3 --> Post-processing of model output
4 --> Display of results
5 --> Removal of result files
6 --> Cleaning of file system
7 --> Exit
```

When entering a number, the corresponding module is executed. *r.avalanche.sh* has to be called from within the *GRASS* mapset with all the required raster maps.

Parameter and data input

Module 1 consists of a sequence of prompts for input of data and parameters (Table 2). If no input is given for a prompt (by just pressing *ENTER*), the dataset specified earlier is kept.

`--> Catchment map (boolean):`

Boolean raster map defining the catchment of interest (identified by cell values of *1*, areas out of the catchment are defined by *0* or *no data*).

`--> Elevation map (m):`

Raster map of elevation (meters).

`--> Bed friction angle map:`

Raster map of bed friction angle (decimal degrees).

`--> Objects at risk map (boolean):`

Boolean raster map denoting objects at risk (*1* for presence of potential objects at risk like roads or buildings, else *0* or *no data*).

`--> Estimated depth of mobilization of soil map (m):`

Raster map showing the patterns of estimated initiation of the debris flow or snow avalanche (depth in meters).

`--> Parameter file:`

File with list of parameters for the simulation. The parameters have to be specified in a defined order (compare Table 2 and *test_param.txt*).

Execution of simulations

A prompt for cell size displays:

`--> Cell size (m):`

The cell size has to be chosen in accordance with the input datasets and the required level of detail. For test simulations it is recommended to choose larger cell sizes in order to reduce computing time. However, results have shown that the chosen cell size may have a considerable influence on the simulation results.

After specifying the cell size, the *GRASS* raster module *r.avalanche* is called by pressing *ENTER*. Additionally to an array of raster maps, a summary file (*summary.txt*) and a profile file (*profile.txt*) are written and stored in the

`dir/r.avalanche/results/`

directory. The summary file contains global values (time step length, maximum depth and velocity of the flow, and flow volume) for each time step. The profile file contains a profile of flow depth along the predefined flow channel for each time step.

Please note that if you wish to run *r.avalanche* manually, not from within *r.avalanche.sh*, you have to copy the parameter file to the `dir/r.avalanche/temp/` directory as *param.txt*. This file shall not contain labels, but only the values.

Post-processing of model output

All the resulting raster maps are cleaned (cells outside of the defined catchment are set to no data) and a color table is assigned to the flow depth map for each time step. The colour tables are stored in `dir/r.avalanche/data`.

Furthermore, three prompts do appear when calling the module. Each task is accepted by typing *1*, or denied by typing *0*.

`--> Maximum flow depth for display (cm):`

The flow depth which should serve as maximum for colouring the maps to be displayed (compare below) has to be specified in full centimetres.

`--> Interval of contour lines for display (m):`

Contour lines of flow depth (not of ground elevation!) are shown on the maps during display (compare below). The interval between these contours has to be specified here.

`--> Export maps to ascii (boolean) ?`

If *1* is entered, the resulting raster maps are exported as ascii rasters in order to be usable with other GIS software products. The resulting files are stored in `dir/r.avalanche /results/asc`. Please enter *0* if you do not wish to export the maps.

In the output rasters, the displays during program execution, and in the summary and documentation files, every variable is addressed by a shortcut (Table 3). The names of the resulting raster maps have the prefix *r_*. The number at the end of the raster map names indicates the time step. For example, the raster *r_dflow0020* shows the flow depth at the end of time step 20. Attention: These time steps are different from those used for the computation itself (compare Section 4.3).

Display of results

A sequence of flow depth maps over all time steps can be displayed using this module. The following parameters have to be specified:

`--> Azimuth of the sun for shaded relief map:`

All maps are displayed with a shaded relief as background, the azimuth of which has to be specified (in decimal degrees; recommended for most areas: 315).

`--> Interval for export of maps to jpg:`

The displayed maps can be automatically stored as `jpg` graphics in `dir/r.avalanche/results /jpg`. If you wish to do so, please specify an integer number larger than *0*, else *0*. The number you enter defines the interval of output – for example, if you enter *4*, the map from every 4th time step is exported.

`--> Height of monitor in pixels:`

Please specify the height of the monitor for display – a value between 500 and 800 is recommended, depending on the size of your monitor.

`--> Observed patterns of debris flow initiation (line vector):`

A line vector map with areas of debris flow initiation observed in the field may be specified, if available, for facilitating the evaluation of the model results.

--> Observed patterns of debris flow deposition (line vector):

A line vector map with areas of debris flow deposits observed in the field may be specified, if available, for facilitating evaluation of the model results.

A monitor opens, and a prompt with instructions appears in the terminal. The maps are displayed in a defined sequence (over all time steps forward) – please enter the number of steps to move forward or backward, or *exit* to quit. If you have moved a defined number of steps fore- or backwards and would like to apply the same action again, you can just press *ENTER* to do so.

If you have chosen to export the maps as `jpg`, no prompts appear, but all maps are displayed and exported automatically.

Please note that the size of the monitor and the placement of some of the elements of the maps (legend, bar scale) are not suitable for all map formats. It may happen that some of the placement options have to be changed in the shell script *r.avalanche* itself in order to design satisfactory layouts.

The text on the display is partly copied from the `summary.txt` file in the `dir/r.avalanche/results/` directory – please do not rename or remove this file before the display of the maps is completed.

Removal of result files

All results (rasters and text files produced by *r.avalanche* and Module *3*) are deleted. All temporary files created in *Module 1* are kept, so that new simulations may be performed immediately.

Cleaning of file system

All temporary rasters and text files created in *Module 1* are deleted. *Module 1* must be re-run in order to perform new simulations.

Exit

r.avalanche.sh is exited and the default cell size is restored

Table 3: Output from *r.avalanche* (after running Module 4). r=raster map, s=summary file, p=profile file

shortcut	description	unit	versions			time steps
			r	s	p	
dflow	flow depth	m	x		x	all
vx	flow velocity in x direction	m s^{-1}	x			all
vy	flow velocity in y direction	m s^{-1}	x			all
dflow_max	maximum flow depth over all time steps	m	x			–
hmax	maximum flow depth over all cells	m		x		all
vmax	maximum flow velocity over all cells	m s^{-1}		x		all
vol	flow volume	m^3		x		all
vol_riskobj	flow volume on object at risk (road, etc.)	m^3		x		all
deltat	length of time step	s		x		all
tsum	time elapsed since start of simulation	s		x		all
cfl	Courant-Friedrichs-Levy condition (comp. Section 4.3)	–		x		all

Appendix 4: Curriculum vitae

Name:	Martin Mergili
Date of birth:	30.10.1979
Place of birth:	Linz, Austria
Marital status:	single
Academic title:	Mag. rer.nat.
Residence:	Beethovenstraße 4, A-6020 Innsbruck
Email:	martin.mergili@uibk.ac.at
Website:	www.uibk.ac.at/geographie/personal/mergili
Mother:	Edith Mergili, *1951; profession: masseuse
Father:	Walter Mergili, 1944 – 2007

Pre-university education

09.1986 – 07.1990	Primary school, Linz, Austria
09.1990 – 07.1994	Secondary school, Linz, Austria
09.1994 – 06.1999	Technical school for Engineering, Linz, Austria

10.2000 - 04.2005 Diploma study of geography at the University of Innsbruck

Thematic fields of specialization: Geoecology, geomorphology, climatology

Methodical fields of specialization: Geoinformatics (particularly remote sensing and numerical modelling)

Diploma thesis:	The Vegetation of Grootbos Nature Reserve (Western Cape, South Africa): GIS-based Mapping and Numerical Analysis
02.2002	Finishing undergraduate studies
09.2002 – 05.2003	Study visit at the University of Lapland, Rovaniemi, Finland: participation in the Arctic Studies Program
02.2004	Study visit in Sri Lanka (Tropical Ecology Excursion)
09.2004 – 11.2004	Study visit in South Africa (Stellenbosch University and Grootbos Nature Reserve)
04.2005:	Finishing graduate studies

since 10.2005 Doctoral studies of natural sciences (branch geography) at the University of Innsbruck

Thesis:	Integrated modelling of debris flows with Open Source GIS: Numerical simulations of triggering, mobilization, and runout of debris flows for selected study areas along the Trans-Andean road corridor Mendoza – Valparaíso.
04.2006 – 05.2006	Study visit at Mendoza and Santiago de Chile for acquiring data and establishing contacts with local research organisations
09.2006 – 12.2006	Study visit in Argentina/Chile for field investigations and data acquisition

Internships (4 weeks each)

07.1995 Construction site internship, Universale Bau, Linz, Austria

07.1997 Office internship City of Linz, Water Department, Linz, Austria

08.1999 City of Linz, Water Department, Linz, Austria

07.2001	Government of Upper Austria, Digital Spatial Information System, Linz, Austria
08.2003	Government of Upper Austria, Cultural Assets Information System, Linz, Austria

Grants

since 2002	various grants from the University of Innsbruck (Faculties of Natural Sciences and Office for International Relations) and the Province of Upper Austria
10.2005 – 09.2007	'Doktoratsstipendium aus der Nachwuchsförderung der LFU'

Jobs

10.2003 – 01.2008:	Lecturer and teaching assistant in cartography, GIS, remote sensing, soil and vegetation sciences
07.2005 – 08.2006	Project collaborator at the alpS Centre for Natural Hazard Management, Innsbruck. Activities: GIS-based modelling in the fields of ecology, hydrology and natural hazards
02.2007 – 12.2007	Researcher at the Institute of Mountain Research, Austrian Academy of Sciences, Innsbruck
since 02.2008	Leader of the project "Debris Flows as Natural Hazards Along the Trans-Andean Corridor Mendoza – Valparaíso" (funded by the Tyrolean Science Funds)

Further activities

10.1999 – 09.2000	Civilian service at the ambulance service of the Red Cross organization, Bad Hall, Upper Austria
10.2000 – 04.2002	Voluntary service at the ambulance service of the Red Cross organization, Bad Hall, Upper Austria

Publications (those listed in App. 2 are excluded)

ERHARD, A., STEINICKE, E., HENZINGER, E. & MERGILI, M. 2007: Von den Quellen des Nils zum Mount Kenya. Eindrücke einer geographischen Exkursion durch Uganda und Kenia im Februar 2006. Institute of Geography, University of Innsbruck. In German.

GEITNER, C., MERGILI, M., STÖTTER, J., LAMMEL, J., MORAN, A., OBERPARLEITER, C. & MEIßL, G. in press: Modelling of Runoff Peaks in small Alpine Catchments in Consideration of Area properties and System Conditions. Springer.

MERGILI, M. 2005: The Vegetation of Grootbos Nature Reserve. GIS-based Mapping and Numerical Analysis. Masters thesis at the University of Innsbruck.

MERGILI, M. 2008: The Vegetation of Grootbos Nature Reserve. Fynbos and Forest Ecosystems at the Southernmost Tip of Africa. Verlag Dr. Müller, Saarbrücken. 176 pp.

MERGILI, M., GEITNER, C., MORAN, A. & STÖTTER, J. 2006: SOILSIM, a GIS-based framework for data-extensive modelling of the spatial distribution of soil hydrological characteristics in small alpine catchments. In: STROBL, J., BLASCHKE, T. & GRIESEBNER, G. (eds.): Angewandte Geoinformatik 2006 - Beiträge zum 18. AGIT-Symposium Salzburg, 444-453.

MERGILI, M., LAMMEL, J., MORAN, A., OBERPARLEITER, C., GEITNER, C. & STÖTTER, J. 2006. SYCOSIM - a GIS-based tool for assessing extreme runoff events of small alpine catchments using open source software. *Geophysical Research Abstracts* 8

MERGILI, M. & PRIVETT, S. 2008: Vegetation and vegetation-environment relationships on Grootbos Nature Reserve (Western Cape, South Africa). *Bothalia* 38: 89-102.